frontiers | Research Topics

Recent advances in unconventional natural gas

Edited by
Yu Song, Guijie Sang, Ang Liu and Long Fan

Published in
Frontiers in Earth Science

ISSN 1664-8714
ISBN 978-2-8325-2792-4
DOI 10.3389/978-2-8325-2792-4

About Frontiers

Frontiers is more than just an open access publisher of scholarly articles: it is a pioneering approach to the world of academia, radically improving the way scholarly research is managed. The grand vision of Frontiers is a world where all people have an equal opportunity to seek, share and generate knowledge. Frontiers provides immediate and permanent online open access to all its publications, but this alone is not enough to realize our grand goals.

Frontiers journal series

The Frontiers journal series is a multi-tier and interdisciplinary set of open-access, online journals, promising a paradigm shift from the current review, selection and dissemination processes in academic publishing. All Frontiers journals are driven by researchers for researchers; therefore, they constitute a service to the scholarly community. At the same time, the *Frontiers journal series* operates on a revolutionary invention, the tiered publishing system, initially addressing specific communities of scholars, and gradually climbing up to broader public understanding, thus serving the interests of the lay society, too.

Dedication to quality

Each Frontiers article is a landmark of the highest quality, thanks to genuinely collaborative interactions between authors and review editors, who include some of the world's best academicians. Research must be certified by peers before entering a stream of knowledge that may eventually reach the public - and shape society; therefore, Frontiers only applies the most rigorous and unbiased reviews. Frontiers revolutionizes research publishing by freely delivering the most outstanding research, evaluated with no bias from both the academic and social point of view. By applying the most advanced information technologies, Frontiers is catapulting scholarly publishing into a new generation.

What are Frontiers Research Topics?

Frontiers Research Topics are very popular trademarks of the *Frontiers journals series*: they are collections of at least ten articles, all centered on a particular subject. With their unique mix of varied contributions from Original Research to Review Articles, Frontiers Research Topics unify the most influential researchers, the latest key findings and historical advances in a hot research area.

Find out more on how to host your own Frontiers Research Topic or contribute to one as an author by contacting the Frontiers editorial office: frontiersin.org/about/contact

Recent advances in unconventional natural gas

Topic editors

Yu Song — China University of Mining and Technology, China
Guijie Sang — University of Strathclyde, United Kingdom
Ang Liu — The Pennsylvania State University (PSU), United States
Long Fan — University of Alaska Fairbanks, United States

Citation

Song, Y., Sang, G., Liu, A., Fan, L., eds. (2023). *Recent advances in unconventional natural gas*. Lausanne: Frontiers Media SA. doi: 10.3389/978-2-8325-2792-4

Table of contents

frontiers | Frontiers in Earth Science

TYPE Original Research
PUBLISHED 04 January 2023
DOI 10.3389/feart.2022.1062580

OPEN ACCESS

EDITED BY
Yu Song,
China University of Mining and Technology, China

REVIEWED BY
Bo Zhao,
Taiyuan University of Technology, China
Liu Xueying,
Huaqiao University, China
Xin-Bo Zhao,
Qingdao University of Technology, China

*CORRESPONDENCE
Di Wu,
wudi202@126.com

SPECIALTY SECTION
This article was submitted to Economic Geology, a section of the journal Frontiers in Earth Science

RECEIVED 06 October 2022
ACCEPTED 01 December 2022
PUBLISHED 04 January 2023

CITATION
Yu Y, Liu J, Yang Y, Wu D, Zhai W and Miao F (2023), Experimental study on coal seam permeability enhancement and CO_2 permeability caused by supercritical CO_2.
Front. Earth Sci. 10:1062580.
doi: 10.3389/feart.2022.1062580

Experimental study on coal seam permeability enhancement and CO_2 permeability caused by supercritical CO_2

Yongjiang Yu[1], Jingjing Liu[1], Yuntao Yang[1], Di Wu[2]*, Wenbo Zhai[2] and Feng Miao[2]

[1]School of Mining, Liaoning Technical University, Fuxin, China, [2]School of Mechanics and Engineering, Liaoning Technical University, Fuxin, China

Permeability is one of the most important parameters for characterizing fluid flow and production from reservoirs. In this paper, experimental studies on the percolation, permeability, and adsorption of supercritical CO_2 in coal seams were carried out, taking into account the effects of injection pressure and temperature, comparing the changes in longitudinal wave velocity of specimens before and after the tests, and analyzing the permeability effect of supercritical CO_2 on raw coal specimens. The test results showed that when the volume stress was 36 MPa, the permeability of supercritical CO_2 in coal increased by 93%, on average, compared with that of CO_2. The modified D-R model was used to fit the adsorption data, and it was found that the excess adsorption capacity of supercritical CO_2 by coal decreased with increased pressure, with a maximum value of approximately 8 MPa. When the temperature increased by 10°C, the adsorption capacity decreased by 8.3%, on average. In the subcritical CO_2 state, the trend of excess CO_2 adsorption in coal was consistent with that of absolute adsorption, which was 16% higher than that of excess adsorption, on average. After the action of supercritical CO_2, the propagation velocity of the longitudinal wave in the sample decreased significantly, indicating that supercritical CO_2 can effectively promote the development of pores and fractures in the coal sample, with an obvious anti-reflection effect on the coal seam and the best permeability enhancement effect at 35°C.

KEYWORDS

supercritical CO_2, permeability, adsorption capacity, longitudinal wave velocity, permeability enhancement

Introduction

As coal resources continue to decrease, efficient mining of coal-bed methane becomes important (Jia et al., 2012). China's coal-bed methane resources are mainly located 1,500-3,000 m underground, and existing coal-bed methane mining technology is limited by factors such as high temperature and high ground stress in deep coal seams, although these characteristics

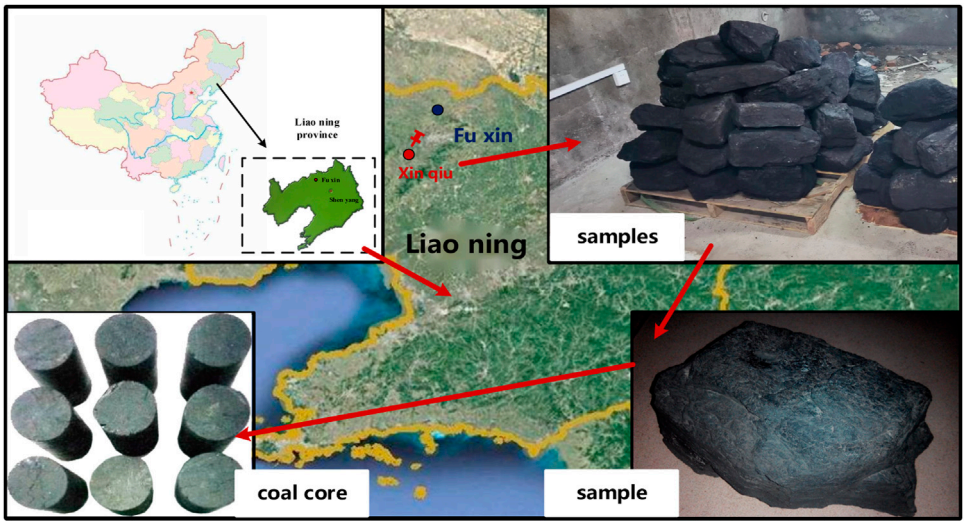

FIGURE 1
Coal samples.

are not universal (Feng, 2008). In recent years, methods for the recovery of enhanced stored coal-bed methane using CO_2 (CO_2 - ECBM) have received increasing attention (Reucroft and Patel, 1986; Reucroft and Sethuraman, 1987; Qin, 2005; Wu and Zhao, 2005). This method is based on good fluidity and zero surface tension of supercritical CO_2, which can not only significantly improve the recovery of coal-bed methane but also store CO_2 in coal seams to reduce the greenhouse effect.

In recent years, many scholars have studied the seepage and adsorption properties of coal on CO_2. (Xu et al., 2017) explored the sensitivity of the response of coal rock permeability to changes in stress by testing CO_2 in the coal seam and found that the greater the stress, the less sensitive the corresponding force of coal sample permeability. Through the CO_2 isothermal adsorption test, it has been found that the CO_2 isothermal adsorption curve reaches a maximum value near the critical pressure (7.38 MPa) and then gradually decreases with increased adsorption pressure (Wu et al., 2019; Wu et al., 2021; Miao et al., 2022). Ma et al. (2015) studied the adsorption capacity of coal for different gases and found that the capacity for adsorption of CO_2, CH_4, and N_2 decreased sequentially. Tang et al. (2004) confirmed the superiority of CO_2 in competitive adsorption with CH_4 through the experimental study of adsorption isotherms of CO_2–CH_4 binary gas. He et al. (2018) studied the expansion deformation of CO_2 adsorption of coal bodies of different coal grades and concluded that expansion deformation decreased with increased coal grades under the same amount of CO_2 adsorption. By comparing multiple adsorption models, it was found that the modified D-R model could better describe the trend of supercritical CO_2 adsorption in coal (Sakurovs et al., 2007; Richard et al., 2008; Wu et al., 2018a). Sun et al. (2013) studied the seepage law of coal under the action of supercritical CO_2 and demonstrated that, after the action of supercritical CO_2, honeycomb-like pore cracks appeared in coal samples and permeability was significantly improved. In a CH_4 experiment in supercritical CO_2-flooded coal, it was found that the injection of supercritical CO_2 into the coal seam can improve the recovery of CH_4 and effectively seal in CO_2 (Yang et al., 2012; Liang et al., 2014; Wu et al., 2018b).

Scholars at home and abroad have carried out studies of CO_2 seepage and adsorption in coal seams, with results indicating that when the temperature exceeds 31.8°C and the pressure exceeds 7.38 MPa, CO_2 becomes supercritical and supercritical CO_2 has a specific anti-permeability effect on coal seams (Wang and Liang, 2019). Therefore, in this study, nine coal samples from the Xinqiu Mine Area, Fuxin City in the Liaoning Province, China, were tested. Seepage and adsorption experiments of supercritical CO_2 injection of raw coal specimens under different injection pressures and temperatures were performed, and the anti-permeability effect of supercritical CO_2 on the specimens was studied by comparing the changes in longitudinal wave velocity and permeability before and after supercritical CO_2 injection.

Coal sample preparation and test device

Coal sample preparation

Coal samples were taken from the Xinqiu Mine Area, Fuxin City, Liaoning Province. Coring equipment was used to drill the

TABLE 1 Basic physical parameters of the specimen.

Sample	L/mm	D/mm	m/g
M01	100.2	50.1	258.06
M02	99.8	50.0	256.87
M03	100.3	50.1	258.06
M04	100.1	50.1	257.16
M05	99.8	50.0	256.87
M06	100.2	50.1	258.06
M07	99.9	50.0	255.07
M08	99.8	50.0	255.01
M09	100.0	50.1	257.88

core perpendicular to the bedding direction of the coal seam; the core was then cut into 50 mm*100 mm standard cylindrical specimens. The inclination of the end face was less than 0.1°, as shown in Figure 1. Nine samples with apparent integrity and no visible cracks were selected. The samples were placed in a drying oven at 105°C for 24 h and then covered with cling film after cooling. The specific parameters of the coal samples are shown in Table 1.

Experimental device

Permeability experimental device

Permeability measurement was achieved using the steady-state method. The experimental apparatus used to measure permeability is shown in Figure 2. The device included a gas supply, data acquisition, temperature control, and core holder systems. The core holder system included a triaxial core holder, pressure kettle, and flow meter. The gas supply system included high-pressure gas cylinders, booster pumps, air compressors, pressure pumps, and vacuum pumps that provided pressure for the CO_2 phase transition to a supercritical state. The data acquisition system consisted of a TP700 data logger and many pressure transducers, each with an accuracy of 0.01 MPa. The temperature control system consisted of a water bath container and many temperature transducers with an accuracy of 0.1°C. The injection pressure was at least 5 MPa lower than the confining pressure to reduce the possibility of hydraulic fracturing within the shales and leakage of liquid from the gap between the rubber sleeve and the sample (Zhang and Yu, 2019).

Adsorption experimental device

The experimental apparatus used to measure adsorption is shown in Figure 3. The device included a gas supply system, data acquisition system, temperature control system, and adsorption system. The adsorption system included two high-pressure adsorption chambers, and the pressure of the adsorption tank was 0 ~ 60 MPa; other systems were the same as the permeability experimental device. Unlike the seepage experimental apparatus, the adsorption experimental apparatus did not require confining pressure and axial pressure on shale specimens.

Permeability experiment

Permeability model

Based on the stable upstream pressure (p_1, MPa), downstream pressure (p_2, MPa), and volumetric flow rate of the gas (Q, m^3/s), the gas permeability was obtained from the expression (Zhao and Yu, 2017):

$$K = \frac{2Qp_0\mu_g LZ}{A(p_1^2 - p_2^2)Z_a}. \quad (1)$$

where K is the permeability, 10^{-15} m^2; p_0 is the standard atmospheric pressure, 0.1 MPa; L is the length of the coal sample, cm; A is the cross-sectional area of the coal sample, cm^2; Z is the compressibility factor under the experimental

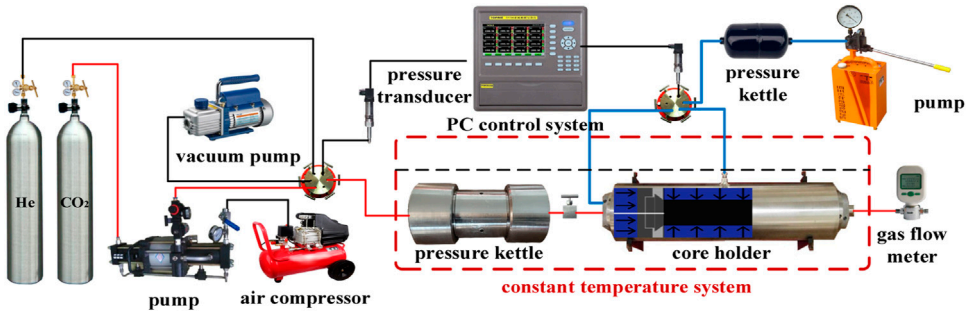

FIGURE 2
Permeability experimental device.

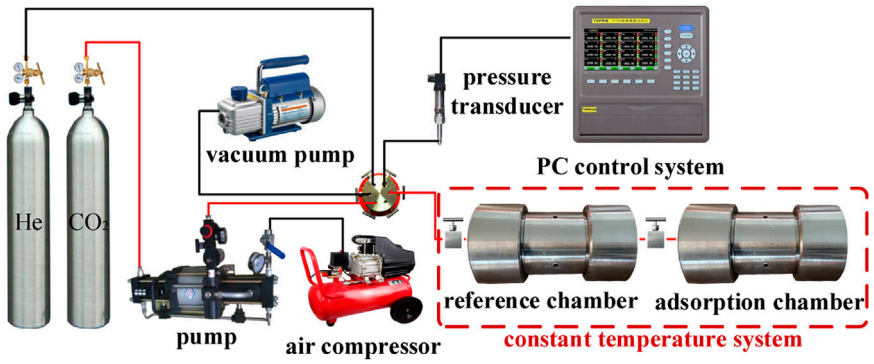

FIGURE 3
Adsorption experimental device.

TABLE 2 Permeability experiment program.

Sample	Temperature/°C	Confining pressure/MPa	Axial pressure/MPa	Pore pressure/MPa
M01	35	12	12	4–7; 8–11
M02	45	12	12	4–7; 8–11
M03	55	12	12	4–7; 8–11

conditions; and Z_a is the compressibility factor at the experimental temperature.

Permeability experiment program and steps

The permeability experiments were divided into three groups according to temperature, including 35, 45, and 55°C. The volumetric stress in the experiment was 36 MPa, the CO_2 injection pressure was 4–7 MPa, and the supercritical CO_2 injection pressure was 8–11 MPa. The experimental program is shown in Table 2. The specific steps were as follows:

1) The test device was connected and confirmed to be airtight. The sample was sealed with a heat shrink sleeve and put into the core holder. The water bath tank temperature was set to 35°C, and the volume stress was set to 36 MPa. After the temperature and pressure stabilized, the pore pressure was adjusted to 4 MPa by feeding CO_2, and test data were recorded after allowing the flow to stabilize. Three sets of data were collected for each experimental group, and the average value was calculated.
2) After testing at one observation point, the CO_2 injection pressure was gradually increased until 11 MPa, according to the experimental protocol.
3) The coal sample was replaced according to the experimental protocol, and the test temperature was increased to 45°C and then 55°C, in turn. Steps 1) and 2) were repeated, and the coal sample permeability under different test conditions was calculated using the collected data.

Permeability experiment results and discussion

As shown in Figure 4, under the same volumetric stress, pore pressure and temperature had significant effects on the permeability of coal samples. The permeability of coal samples increased with increased pore pressure at the same temperature, and the permeability increased exponentially before the supercritical state. After the critical pressure was exceeded, the permeability had an obvious linear growth trend. By comparing the permeability of coal samples under the two carbon dioxide phase states, it was found that when the carbon dioxide reached the supercritical state, permeability was significantly improved. Comparing permeability at the three temperatures, it was found that coal permeability was highest and had the smallest decrease in permeability over time at 35°C. These results indicate that the volume of pores and cracks in the coal body was limited. With increased temperature, the expansion of the coal body

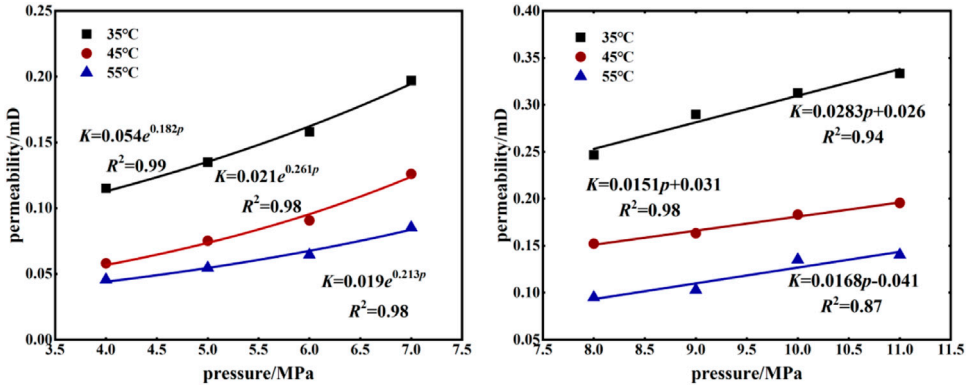

FIGURE 4
Change curves of permeability with an injection of CO_2 and SC-CO_2 pressure.

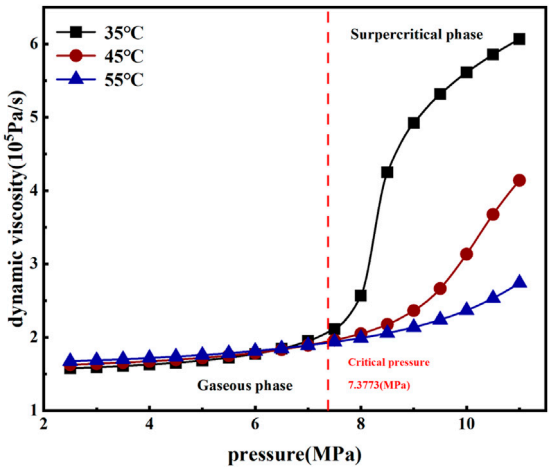

FIGURE 5
Dynamic viscosity of CO_2 varies with pressure.

skeleton gradually increases. However, due to the compressive and restrictive effects of effective stress on pore cracks, the volume of pores and fractures gradually decrease with increased expansion of the coal skeleton. The expansion of the coal skeleton will not increase indefinitely with increased temperature. As temperature increases, the rate of change of the expansion of the coal skeleton gradually decreases; i.e., the rate of change of the volume of pores and fractures will gradually decrease. On the other hand, permeability is also related to gas dynamic viscosity. From Eq. 1, the permeability is proportional to the dynamic viscosity of the gas. As shown in Figure 5, comparing the dynamic viscosity of carbon dioxide at three temperatures, it was clear that the dynamic viscosity of CO_2 increased with increasing temperature before the supercritical state. The dynamic viscosity of CO_2 at 35°C was significantly higher than that at 45°C and 55°C, although, with increased temperature, the viscosity of supercritical CO_2 will decrease significantly. The expansion of clay minerals in the coal body plays a leading role in this process (Wu et al., 2018b); therefore, the decrease of permeability will gradually slow down.

Adsorption experiment

Adsorption capacity model

After measuring the pressure in the adsorption system before and after adsorption equilibrium, the adsorption amount was calculated based on the change in the number of substances converted using the gas state equation. A known amount of adsorption gas was injected into the reference chamber and the adsorption chamber, and after stabilization, the reference chamber pressure, p_1, and the adsorption chamber pressure, p_2, were recorded. Using the gas compressibility factor equation of state: $pV = ZnRT$, the amount of gas in the reference chamber, n_1, and the amount of gas in the adsorption chamber, n_2, were calculated. The valve between the adsorption chamber and the reference chamber was opened, the final equilibrium pressure, p0, was recorded, and the gas factor state equation was used to calculate the total amount of gas, n_0, in the adsorption system. The adsorption amount of the gas at this pressure is then: $n_{ad} = n_1 + n_2 - n_0$, and the excess adsorption amount V_{ad} of CO_2 per unit mass of coal was calculated using (Eq. 2).

$$V_{ad} = 22.4 \times 10^3 n_{ad} / G_c. \quad (2)$$

In Eq. 2, G_c is the total mass of the coal sample, g.

TABLE 3 Adsorption experiment program.

Sample	Temperature/°C	Pore pressure/MPa
M04	35	1–11
M05	45	1–11
M06	55	1–11

Adsorption experiment program and steps

Experiments were divided into three groups according to temperatures of 35, 45, and 55°C. The CO_2 pressure was gradually increased from 0 MPa to 11 MPa for a total of 11 pressure measurement points, each with a balanced time of not less than 24 h (Tang et al., 2018). The experimental program is shown in Table 3. The specific steps are as follows:

1) Coal samples that had undergone a 35°C seepage test were placed in an adsorption tank, which was heated to 35°C, and then placed in a water bath tank. Helium gas was introduced to bring the pressure in the test system to 11 MPa. Stability of gas pressure was observed for 24 h to ensure the test system was airtight.
2) The volume of free space was measured. Helium gas was passed in to achieve a pressure of 2–3 MPa, and the aforementioned steps were repeated two times. Measurement of free space volume was repeated three times. The difference between the test values of free space volume in the adsorption chamber was less than 0.1 cm^3.
3) The vacuum pump was turned on to remove excess gases from the system and vacuum treatment continued for at least 12 h. When the data logger consistently displayed the same data, vacuum treatment was complete.
4) The reference chamber was filled with CO_2 gas, and the reference chamber pressure after stabilization was recorded. The balance valve between the reference chamber and the adsorption chamber was opened and kept open for 12 h, and the final balance pressure was recorded. When the adsorption test of one measurement point was completed, introduction of CO_2 gas was continued to allow the pressure in the test system to reach 2 MPa, and the aforementioned process was repeated. The test pressure measurement point was 11 MPa, and when the pressure in the test system reached 11 MPa, testing of the group was complete.
5) The test temperature and test specimen were changed and steps 3) and 4) were repeated. The amount of CO_2 gas adsorption under different temperature conditions was calculated.

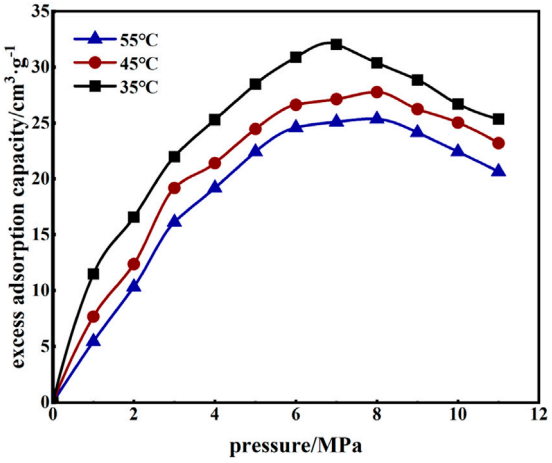

FIGURE 6
Change curves of excess CO_2 adsorption with pore pressure.

Adsorption experiment results and discussion

As shown in Figure 6, under different temperature conditions, the excess adsorption of CO_2 by coal samples first increased with the increase of pore pressure. Then, when the pressure reached 6 MPa, the excess adsorption increase decreased significantly, and, at 7–8 MPa, the excess adsorption reached the maximum and then decreased with increased pore pressure. When the temperature was increased from 35°C to 45°C and then 55°C, the maximum excess adsorption of CO_2 in coal samples decreased from 31.96, to 27.86, and 25.6 cm^3/g, respectively.

From the test data, it was found that for every 10°C increase in temperature, the excess adsorption volume decreased by an average of 8.3%. These data demonstrate that with increased temperature, the CO_2 molecules had more energy which, when free from the bondage of the adsorption site, resulted in a decreased amount of adsorption.

In the coal sample adsorption CO_2 test, the Langmuir adsorption model is commonly used. However, when CO_2 reaches a supercritical state, the Langmuir adsorption model fits poorly, and even the fit result does not converge. Therefore, the Sakurovs modified D-R model (Sakurovs et al., 2007) was used in this study, as it can be applied to the adsorption of supercritical CO_2 by converting the adsorption pressure to density and adding a correction coefficient. The specific model is as follows:

$$V_{ad} = V_0\left(1 - \frac{\rho_g}{\rho_a}\right)\exp\left\{-D\left[\ln\left(\frac{\rho_a}{\rho_g}\right)\right]^2\right\} + k\rho_a, \quad (3)$$

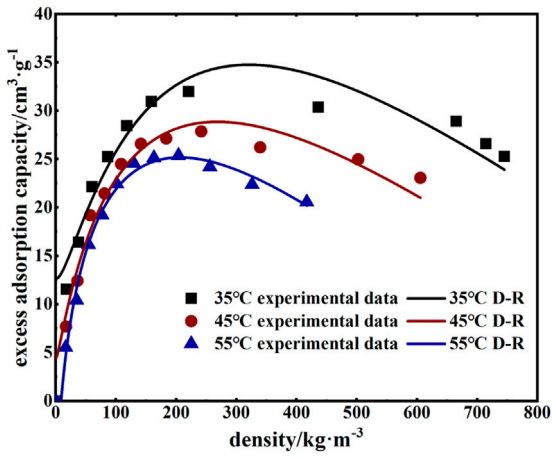

FIGURE 7
D–R model fitted curves of excess CO_2 adsorption.

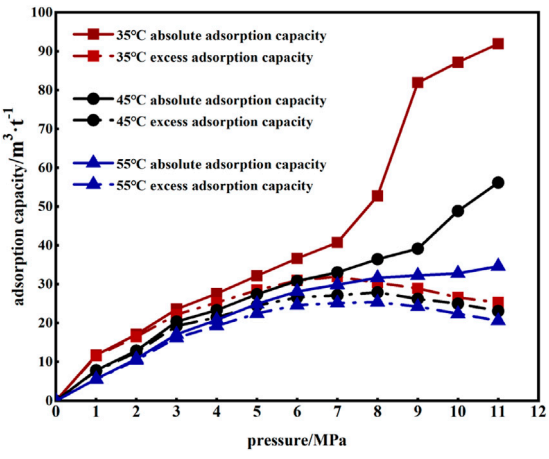

FIGURE 8
Change curves of CO_2 adsorption with pore pressure.

TABLE 4 D-R model fitting parameters.

Temperature/°C	V_0/cm³·g⁻¹	D	k	R^2
35	34.74	0.194	0.012	0.95
45	28.84	0.132	0.004	0.97
55	25.14	0.078	0.008	0.99

where V_0 is the maximum excess adsorption under ideal conditions, cm³/g; ρ_g is the density of the adsorbed gas at the corresponding temperature and pressure, kg/m³; ρ_a is the adsorption phase density, and the current common value is 1028 kg/m³ (Li et al., 2014); D and k are constants. The experimental data were collated and then fit using the model mentioned previously; the results are shown in Figure 7 and Table 4.

The fit results demonstrated that the modified D-R model better described the adsorption of supercritical CO_2 by coal, with a coefficient of determination R^2 that was greater than 0.95 and increased with increasing temperature. The temperature was increased from 35°C to 45°C and then 55°C, corresponding to maximum excess adsorption of 34.74, 28.84, and 25.14 cm³/g, respectively; supercritical CO_2 density of 317, 266, and 199 kg/m³, respectively; and supercritical CO_2 pressure of 7–9 MPa.

Due to the high test pressure, the excess adsorption does not reflect the true adsorption of CO_2 in coal (Yang et al., 2011). Therefore, the absolute adsorption amount V_{ap} was used in this study to describe the amount of CO_2 adsorption in coal and was calculated as follows (Moffat and Weale, 1955):

$$V_{ap} = \frac{V_{ad}}{\left(1 - \rho_a/\rho_g\right)}. \quad (4)$$

Under different temperature conditions, the excess adsorption of CO_2 and the absolute adsorption amount of coal changed with pore pressure, as shown in Figure 8. When CO_2 did not reach the supercritical state, the excess adsorption of CO_2 and absolute adsorption under different temperature conditions were consistent, and the absolute adsorption was increased by an average of 16% compared with the excess adsorption (Figure 8).

When CO_2 reached a supercritical state, the excess adsorption amount began to decrease with increased pore pressure. In contrast, the absolute adsorption amount increased with increased pore pressure, and the lower the temperature, the more obvious the increase. The supercritical CO_2 pressure was 8–11 MPa, and the absolute adsorption amount was increased by an average of 214%, 79%, and 41% compared with the excess adsorption amount, respectively.

Supercritical CO_2 permeability enhancement results and discussion

To better explore the permeability enhancement effect of supercritical CO_2 on raw coal samples, the permeability calibration test was applied before and after CO_2 treatment, and the change in ultrasonic wave velocity before and after CO_2 treatment was assessed.

Permeability enhancement test

The permeability enhancement effect of supercritical carbon dioxide on coal was analyzed by comparing the N_2 permeability of coal samples before and after permeability enhancement. The specific test plan is shown in Table 5, and the experimental steps are

TABLE 5 Permeability enhancement experiment program.

Sample	Temperature/°C	Axial pressure/MPa	Confining pressure/MPa	Time/h
M07	35	12	12	24
M08	45	12	12	24
M09	55	12	12	24

TABLE 6 Comparison of P-wave velocity V_P before and after being subjected to supercritical CO_2.

Temperature/°C	35	45	55
Before V_P/(km·s^{-1})	2.13	2.07	2.10
After V_P/(km·s^{-1})	1.92	1.93	1.98
ΔV_P/(km·s^{-1})	0.21	0.14	0.12

the same as those described in the *Permeability experiment program and steps* section. The experimental results are shown in Figure 8.

As shown in Figure 8, the permeability of coal samples before and after permeability enhancement increased exponentially as the pore pressure increased. After using supercritical CO_2 to increase the permeability of coal samples, the permeability of coal samples under the same pore pressure conditions was significantly improved, with an average increase of 53.34%. The greater the pore pressure, the greater the permeability of coal samples, indicating that supercritical CO_2 had a good permeability enhancement effect on coal samples.

Changes in ultrasonic wave velocity

A non-metal detector was used to measure the propagation velocity of longitudinal waves in coal samples before and after the test, as shown in Table 6. After the action of supercritical CO_2, the propagation rate of longitudinal waves in the coal sample was significantly slower, and the wave velocity decreased as humidity increased (Table 6). The propagation speed of ultrasonic waves was different in different media; specifically, the propagation speed of solid media was significantly more than that of gaseous media. After the test, the wave velocity slowed, indicating that the coal sample had either a new pore crack or expansion of the original pore crack after the supercritical CO_2 action; the lower the temperature, the more obvious the effect. The aforementioned results show that supercritical CO_2 promoted the development of coal-like pore fractures, improved the pore connectivity in the coal sample, changed the seepage path of the fluid in the coal sample, and increased the permeability of the sample. Additionally, supercritical CO_2 at 35°C had the best enhancement effect on coal sample permeability.

Conclusion

1) Under the condition of constant volume stress, pore pressure and temperature had a significant impact on the permeability of the coal seam. When the pore pressure was fixed, the permeability decreased with increased temperature; when the temperature was fixed, the permeability increased with increased pore pressure. The injection of supercritical CO_2 increased permeability by an average of 93% compared to the permeability of coal samples after CO_2 injection.
2) Using the modified D-R model, the adsorption data were fitted and the maximum amount of excess adsorption of CO_2 by coal was found to be 7–9 MPa. The temperature was increased from 35°C to 45°C and then 55°C, corresponding to maximum excess adsorption of 34.74, 28.84, and 25.14 cm^3/g, respectively. For every 10°C increase in temperature, excess adsorption decreased by an average of 8.3%.
3) Excess and absolute adsorption of carbon dioxide in coal were assessed. When the CO_2 did not reach the supercritical state, the excess adsorption amount and the absolute adsorption amount change trends were consistent, and the absolute adsorption amount was increased by an average of 16% compared with the excess adsorption amount. When CO_2 reached a supercritical state, the excess adsorption amount began to decrease with increased pressure, and the absolute adsorption amount increased with increased pressure; the lower the temperature, the more obvious the effect.
4) In comparing the changes in coal sample permeability before and after supercritical CO_2 action, it was found that after supercritical CO_2 was injected into the coal sample, the pore cracks inside the sample were further developed and permeability increased by an average of 53.34%. These data

indicate that supercritical CO_2 had a good permeability enhancement effect on the coal seam.

5) Using a non-metallic detector to measure the change in ultrasonic wave velocity of coal samples before and after supercritical CO_2 action, it was concluded that supercritical CO_2 at 35°C had the best permeability enhancement effect on coal samples.

Data availability statement

The original contributions presented in the study are included in the article/Supplementary Material; further inquiries can be directed to the corresponding author.

Author contributions

YY: conceptualization. JL: data curation, writing—original draft, software. YY: investigation. DW: project administration. WZ: investigation. FM: investigation.

Funding

This study was supported by the National Natural Science Foundation of China (51974147).

Conflict of interest

The authors declare that the research was conducted in the absence of any commercial or financial relationships that could be construed as a potential conflict of interest.

Publisher's note

All claims expressed in this article are solely those of the authors and do not necessarily represent those of their affiliated organizations, or those of the publisher, the editors, and the reviewers. Any product that may be evaluated in this article, or claim that may be made by its manufacturer, is not guaranteed or endorsed by the publisher.

References

Feng, Z. (2008). *Low permeability of coal seam gas extraction the- ory and application*. China, Beijing: Science Press.

He, W., Liang, W., Zhang, B., Li, Z., and Li, L. (2018). Experimental study on swelling characteristics of CO_2 adsorption and storage in different coal rank China. *Journal of China Coal Society*. 43 (5), 1408–1415.doi:10.13225/j.cnki.jccs.2017.1138

Jia, C., Zheng, M., and Zhang, Y. (2012). Unconventional hydrocarbon resources in China and the prospect of exploration and development China. *Petroleum Exploration and Development*. 39 (2), 129–136.doi:10.1016/s1876-3804(12)60026-3

Li, Q., Ni, X., Wang, Y., and Gang, S. (2014). The experi- mental study on the adsorption/desorption of carbon dioxide in the coal under supercritical condition China. *Coal Geology & Exploration*. 42 (3), 36–39.

Liang, W., Zhang, B., Han, J., and Yang, D. (2014). Experi- mental study on coal bed displacement and recovery by super crit-ical carbon dioxide injection China. *Journal of China Coal Society*. 39 (8), 1511–1520.

Ma, L., Li, B., Deng, J., Li, B., and Hu, A. (2015). On the characteristic fea- tures of the adsorption capacity of the coal for the singular compo- nent gases of CH_4, CO_2, N_2 under regular pressures China. *Journal of Environment and Safety*. 15 (2), 64–67.

Miao, F., Wu, D., Liu, X., Xiao, X., Zhai, W., and Geng, Y. (2022). Methane adsorption on shale under *in situ* conditions: Gas-in-place estimation considering *in situ* stress. *Fuel* 308, 121991. doi:10.1016/j.fuel.2021.121991

Moffat, D. H., and Weale, K. E. (1955). Sorption by coal of methane at high pressures China. *Fuel* 34, 449–462.

Qin, Y. (2005). Advances in overseas geological research on coalbed gas: Origin and reservoir characteristics of coalbed gas China. *Frontiers in Earth Science*. 12 (3), 289–298.

Reucroft, P. J., and Patel, H. (1986). Gas-induced swelling in coal. *Fuel* 65 (6), 816–820. doi:10.1016/0016-2361(86)90075-x

Reucroft, P. J., and Sethuraman, A. R. (1987). Effect of pressure on carbon dioxide induced coal swelling. *Energy fuels*. 1 (1), 72–75. doi:10.1021/ef00001a013

Sakurovs, S., Day, S., Weir, S., and Duffy, G. (2008). Temperature dependence of sorption of gases by coals and charcoals. *International Journal of Coal Geology*. 73 (3/4), 250–258. doi:10.1016/j.coal.2007.05.001

Sakurovs, R., Day, S., Weir, S., and Duffy, G. (2007). Application of a Modified Dubinin–Radushkevich Equation to Adsorption of Gases by Coals under Supercritical Conditions. *Energy fuels*. 21, 992–997. doi:10.1021/ef0600614

Sun, K., Wu, D., Su, A., Chen, Z., Ren, S., Yue, L., et al. (2013). Coupling experimental study of coal permeability with pore pressureeffective volume stresstemperature under supercritical carbon dioxide action China. *Chinese Journal of Rock Mechanics and Engineering*. 32 (S2), 3760–3767.

Tang, J., Wang, X., Lu, Y., Ao, X., and Han, S. (2018). Experimental study on time effect and deformation anisotropy of shale and coal under CO_2 China. *Journal of China Coal Society*. 43 (8), 2288–2295.

Tang, S., Tang, D., and Qi, Y. (2004). Binary-component gas adsorption isotherm experiments and their significance to ex- ploitation of coalbed methane China. *Earth Science* (2), 219–223.

Wang, L., and Liang, W. (2019). Experimental study on crack propa- gation of coalrock mass under supercritical CO2 fracturing China. *Coal Science Technology*. 47 (2), 65–70.

Wu, D., Miao, F., Liu, X., Xiao, X., and Zhai, W. (2021). Prediction of high-pressure adsorption of CH4 and CO2 in shale. *International Journal of Greenhouse Gas Control*. 110, 103440. doi:10.1016/j.ijggc.2021.103440

Wu, D., Liu, X., Sun, K., Xiao, X., and Xin, L. (2018). Experiments on supercritical CO2 adsorption in briquettes. *Energy Sources, Part A: Recovery, Utilization, and Environmental Effects* 41 (8), 1005–1011. doi:10.1080/15567036.2018.1523258

Wu, D., Liu, X., Liang, B., Sun, K., and Xiao, X. (2018). Experiments on Displacing Methane in Coal by Injecting Supercritical Carbon Dioxide. *Energy fuels*. 32 (12), 12766–12771. doi:10.1021/acs.energyfuels.8b03172

Wu, S., and Zhao, W. (2005). Analysis of effective stress in adsorbed methane-coal system China. *Chinese Journal of Rock Mechanics and Engineering*. 24 (10), 1674–1678.

Wu, S., Tang, D., Song, L. I., and Li, X. (2019). Effect of temperature and pressure on energy parameters of methane supercritical adsorp- tion China. *Coal Science. Technology*. 47 (9), 60–67.

Xu, J., Chen, Y., Jiang, C., Li, C., and Zeng, C. (2017). Test on carbon dioxide permeability in coal seam China. *Ministry of Environment, Forest and Climate Change*. 44 (4), 10–13.

Yang, Z., Qin, Y., Gao, D., and Chen, R. (2011). Differences between apparent and true adsorption quantity of coalbed methane under supercritical conditions and their geological significance China. *Natural gas in India* 31 (4), 13–16.

Yang, T., Nie, B., Yang, D., Zhang, R., and Zhao, C. (2012). Experimental research on displacing coal bed methane with supercritical CO2. *Safety. Science*. 50 (4), 899–902. doi:10.1016/j.ssci.2011.08.011

Zhang, C., and Yu, Q. (2019). Breakthrough pressure and permeability in partially water-saturated shales using methane-carbon dioxide gas mixtures: An experimental study of Carboniferous shales from the eastern Qaidam Basin, China. *Bulletin* 103 (2), 273–301. doi:10.1306/07111818018

Zhao, Y., and Yu, Q. (2017). CO 2 breakthrough pressure and permeability for unsaturated low-permeability sandstone of the Ordos Basin. *Journal of Hydrology* 550, 331–342. doi:10.1016/j.jhydrol.2017.04.050

frontiers | Frontiers in Earth Science

TYPE Original Research
PUBLISHED 04 January 2023
DOI 10.3389/feart.2022.1054787

OPEN ACCESS

EDITED BY
Chaojun Fan,
Liaoning Technical University, China

REVIEWED BY
Qiming Huang,
Shandong University of Science and Technology, China
Bin Xiao,
Liaoning Technical University, China
Nan Fan,
Taiyuan University of Technology, China

*CORRESPONDENCE
Shuai Zhang,
zhang578803683@126.com

SPECIALTY SECTION
This article was submitted to Economic Geology,
a section of the journal
Frontiers in Earth Science

RECEIVED 27 September 2022
ACCEPTED 08 November 2022
PUBLISHED 04 January 2023

CITATION
Zhang S (2023), A regionally verified method for fusion indexes of gas outbursts in adjacent seams within close coal seam groups.
Front. Earth Sci. 10:1054787.
doi: 10.3389/feart.2022.1054787

A regionally verified method for fusion indexes of gas outbursts in adjacent seams within close coal seam groups

Shuai Zhang[1,2]*

[1]State Key Laboratory of Gas Disaster Monitoring and Emergency Technology, Chongqing, China, [2]China Coal Science and Industry Group Chongqing Research Institute Co., Ltd., Chongqing, China

To effectively solve the problem of regional verification of gas outbursts adjacent to close coal seam groups, a method of regional verification and index fusion of the working face was proposed to promote the general idea of advanced detection, index fusion, and the determination of the critical values, inspection, and verification. Based on the engineering background of Xiaotun Coal Mine and advanced geological exploration, drilled holes were arranged in key locations and consisted of small intervals between layers, thickened coal seams, and geological structural belts. Moreover, fusion indexes were selected according to the statistical analysis of laboratory tests and on-the-spot measurements, which can be used to determine that the critical value of the residual gas content of the fusion indexes of the six adjacent upper coal seams is 8 m^3/t and K_1 is 0.50 ml/g.$min^{1/2}$. The results illustrate that the method for measuring residual gas content and the fusion index of the K_1 value during the effect test of regional prevention measures is convenient and effective for advanced regional verification of adjacent coal seams, which can also provide a reference and guiding significance for the regional verification of adjacent coal seams of gas outbursts under similar conditions.

KEYWORDS

***W-K1* relationship model, index fusion of the region and working face, regional verification, adjacent coal seam, gas outburst**

Introduction

Coal and gas outbursts are some of the most harmful natural disasters in coal mine production (Wang et al., 2020a; Li et al., 2020; Kong et al., 2022). However, regional verification is the last link in the regional four-in-one comprehensive prevention measures for gas outbursts and is a significant checkpoint for controlling and preventing coal and gas outburst accidents (State Administration of Coal Mine Safety, 2019). Before the excavation is conducted in the adjacent coal seam with a normal distance of less than 5 m from the outburst danger zone of the coal seam, regional prevention measures for gas outbursts must be examined for the corresponding areas of the coal seam with gas outbursts in Article 29 of the 2019 edition of the Detailed Rules for the Prevention and Control of Coal and Gas Outbursts. However, determining whether to conduct regional

verification is not clearly specified. Recently, scholars have investigated and discussed the regionally verified method of close coal seam groups of gas outbursts. Fan et al. (Fan, 2012), Li and Yanbin (2010), and others proposed that when excavating activities are conducted in close coal seams of gas outbursts, and after implementing regional prevention measures for coal seams of gas outbursts with close proximity and verifying their effectiveness, the regional verification may not be performed for the lower adjacent layer with a layer spacing greater than 2 m. However, the upper adjacent layer must be verified with reference to the method of regional verification of the working face of the coal seam of the gas outburst (Zhang et al., 2020). Similarly, the method for joint regional verification of the excavation working face of the close coal seam groups of gas outbursts was proposed by Hao et al. (Gui et al., 1048), which added the method of measuring the drilled holes cutting index K_1 and S values for coal seams of gas outbursts and the joint arrangement of drilled holes in the range of up and down adjacent coal seams of gas outbursts at a distance of less than 5 m that filled the gap in the verification of the joint area (Wang, 2019a; Wang, 2019b). Xu (2016) and others proposed the method of joint regional verification of coal seams of gas outbursts with an interlayer spacing of less than 5 m, which was conducted in the $0116^{1}15$ working face of Pinggou Coal Mine during development of safe mining of the working face. In addition, the continuous regional verified method was proposed on the basis of deep hole fixed-point sampling (Cheng, 2018), which improved the work efficiency of regional verification. However, this method is only applicable in mining the working face of the coal seam and the close distance thick coal seam, and it is difficult to popularize the verification of the adjacent coal seam of gas outbursts.

Recently, the regionally verified method of close coal seams adjacent to coal seams of gas outbursts was based on the regionally verified method of mining working faces (Jia, 2022). The verification of the area adjacent to the coal seam of gas outbursts in the excavation face is used as an example; gas control has become a major factor restricting safe and efficient production in coal roadway excavation in high-gas mines (Yang and Liao, 2023). A total of 15 through-layer drilled holes need to be arranged for each cycle to control the 8–10 m ahead of the excavation when the verification of the adjacent coal seam of the gas outburst area is conducted. Consequently, several problems exist consisting of the volume of large drilled holes and construction difficulty, low verification efficiency, high gangue content in the orifice contact powder, large tested index error, and extended time (Fan et al., 2022). These problems affect the efficient production of mining the working face of close coal seam groups with gas outbursts.

However, in most areas of southwest China, problems also exist in mining adjacent coal seam groups of gas outbursts, which results in the verification of adjacent coal seams of gas outbursts with an interlayer spacing less than 5 m and a series of the afore-mentioned problems. In this paper, a regional verification method for adjacent outburst coal seams is proposed on the basis of the fusion of regional and working face indicators, which can be used to effectively prevent coal and gas outburst accidents and thereby improve the production efficiency of the mining working face.

A proposed regionally verified method for fusion indexes of adjacent coal seams of gas outbursts

General idea

The general idea is to use advanced detection, index fusion, the determination of critical value, inspection, and verification to conduct regional verification of adjacent coal seams of gas outbursts.

Advanced detection, that is, of coal and rock conditions, can be done by using the coal road strip through horizontal control of the roadway and investigation of the hydrogeological conditions of the mines and pre-extraction drilled holes, which are advantageous in seeking key factors, including small interlayer spacing, coal seam thickening, and geological structure, and thus provide a basis for the fusion indexes of tested drilled hole arrangement.

Index fusion includes measuring the residual gas content of adjacent coal seams of gas outbursts and the K_1 value of the drilled hole cutting gas desorption index during the test of effectiveness of the prevention measures of regional gas outbursts, which can determine whether the regional measures are effective and the degree of the outburst danger of coal seams.

The critical values thus obtained are used to measure the critical value of the fusion index through comprehensive analysis by combining laboratory tests and on-the-spot measurements.

Proposed method

During tunneling of the gas drainage in the floor roadway, the coal and rock conditions of the roadway horizontal control, hydrogeological conditions, and holes drilled for gas drainage in the corresponding strip area are comprehensively analyzed to accurately determine the occurrence of coal seams. During the inspection of regional outburst prevention measures, a measured point is arranged at a certain distance along the roadway extraction direction or mining direction of the working face to determine the residual gas content of the fusion index and the K_1 value of the drill cutting gas desorption index. According to the investigated critical value and regional verification standard, the regional verification method of adjacent outburst coal seams for regional advanced verification and working face index fusion is established. Each inspected and tested point is prioritized in the

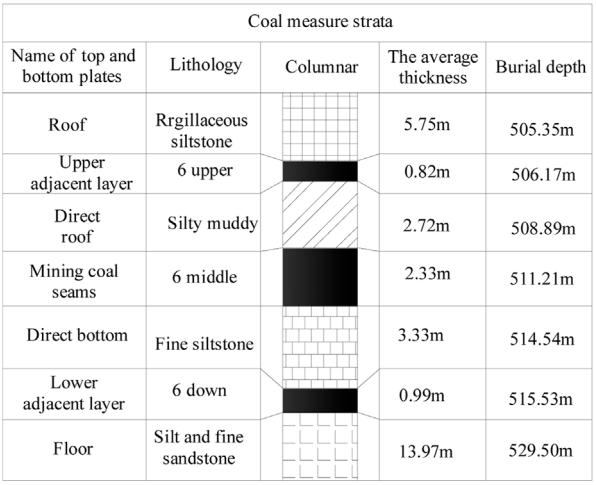

FIGURE 1
Comprehensive histogram of measured coal strata.

key position area of abnormal structures including smaller interval, thickened coal seam, fault, and fold, and the points are appropriately increased (the tested point must control the two walls of the fault and the axis of the fold).

The regionally verified method of fusion indexes

Xiaotun Coal Mine in Guizhou Province works with close-range coal seams with gas outbursts. The excavation working faces of the 16 middle and 14 transport roadways was used as testing sites, and the roadway was excavated along the direction of middle coal seam 6. The upper overlying coal seam 6 is characterized by a coal seam spacing of 1.7–9.1 m, an average coal seam spacing of 2.7 m, a coal seam thickness of 0.52–1.14 m, and an average coal seam thickness of 0.82 m. Additionally, the lower underlying coal seam 6 is characterized by a coal seam spacing of 0.9–8.4 m, an average coal seam spacing of 3.3 m, a coal seam thickness of 0.12–3.46 m, and an average coal seam thickness of 0.99 m. In addition, the upper, middle, and lower layers of coal seam 6 are all identified as coal seams of the gas outburst, and the comprehensive histogram of the measured coal strata is shown in Figure 1.

The floor gas drainage roadway of the 16 middle and 14 transport roadways is arranged with through-layer grid drilled holes with a width of 5 m × 5 m, which is beneficial for the pre-extraction 6 middle coal roadway strip of the coal seam, and regional prevention measures are taken of the gas outburst in the upper and lower layers of coal seam 6 of the corresponding area. After a period of pre-extraction, the middle, upper, and lower layers of coal seam 6 adjacent to the upper and lower sides will be tested for the effect of regional measures. Before excavation of the 16 middle and 14 transport roadways, regional verification of the upper, middle, and lower layers of coal seam 6 will be conducted. Moreover, the regionally verified method of the upper and lower layers of coal seam 6 is conducted with reference to the regionally verified method of the excavation working face of the coal seam of the gas outburst, which includes 3 groups arranged in the excavation direction of the 16 middle and 14 transport roadways using the air coal drill for a total of 15 through-bed drilled holes. These holes are drilled into the upper and lower layers of coal seam 6 per cycle. Consequently, strips of the upper layer of coal seam 6 corresponding to the area of 8–10 m in front of the excavation face and 2–4 m of the 16 middle and 14 transport roadways are controlled by this method. However, this is characterized by the difficult construction of regionally verified drilled holes and a large amount of engineering of drilled holes, drilled hole cuttings with a lot of gangue, and a low accuracy of regionally verified indicators; these problems have seriously restricted the safe and efficient excavation operation of the excavation working face in the 16 middle and 14 transport roadways (Hu et al., 2008; Jiang et al., 2018; Yang et al., 2019).

Advanced geological exploration

In the outer section of the 16 middle and 14 transport roadways (200–410 m) (the mileage is based on the opening point of the 16 middle and 14 transport roadways) of the tested area, 293 pre-extraction drill holes were placed in the construction area of the floor drainage roadway. Figure 2 shows the occurrence of coal seams in the tested area of the 16 middle and 14 transport roadways according to the coal and rock in the regional pre-extraction drilled holes.

The representative upper coal seam is characterized by a relatively close distance to the middle coal seam and an interlayer spacing of less than 5 m. At 270 m and 410 m of the 16 middle and 14 transport roadways, upper coal seam 6 is relatively close to middle coal seam 6. Furthermore, the area where the coal seam is thickened on upper coal seam 6 occurs at 280 m, 320 m, and 365 m and there is a small fault in the upper coal seam at a distance of 340 m.

Determination of regionally verified fusion indicators

Selection of regionally verified fusion indicators

(1) Selection of regional fusion indicators

According to Article 69 of the Detailed Rules for the Prevention and Control of Coal and Gas Outbursts, if the regional prevention measures of gas outbursts for pre-extracted coal seam gas are adopted, the effect of the regional outburst prevention measures must be checked. In addition, the residual gas pressure or other tested residual gas pressure can also be used (this selection should comply with the procedures required by article 57 of these rules)

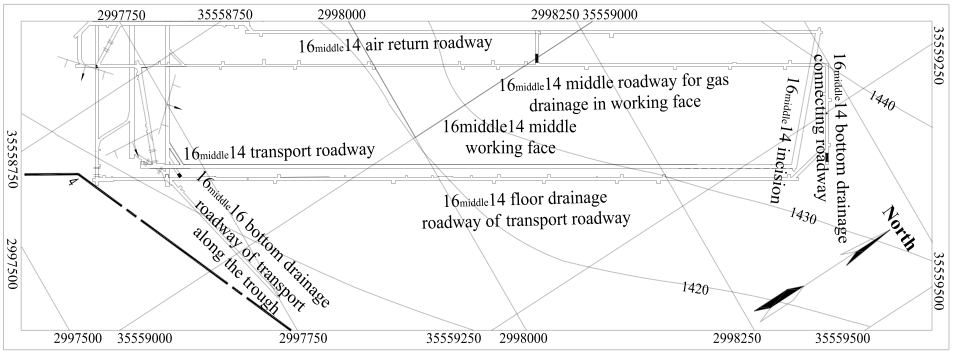

FIGURE 2
Occurrence of coal seams in the tested area.

according to the site conditions and considering that the residual gas content index is preferred as the inspection index and indicates that validated indicators and methods are tested.

Therefore, the residual gas content index is used as the regional index of the fusion index for the verification of the adjacent coal seam region of gas outbursts when the effect of the regional prevention measures of gas outbursts is tested.

Selection of the working face fusion index

Presently, the prediction methods of the working face consist of the cuttings index, compound index, and R value index methods. Among them, the key tested indicators are the index of the gas desorption of drilled hole cuttings, the volume of drilled hole cuttings, and the initial velocity of gas emissions of the drilled holes.

The index of the cutting volume refers to the slag discharge volume of 1 m drilled holes with a diameter of φ42 mm of the spiral drilled pipe. However, in Xiaotun Coal Mine area, the tested drill holes of the prevention measures of regional gas outbursts are generally constructed with tools at a diameter of φ75 mm or φ94 mm. Moreover, the critical value of the amount of cuttings has not been investigated due to the different size of the drilling tool and the amount of slag discharge. Therefore, this indicator is not suitable for simultaneous measurement of residual gas content, which should not be taken as the fusion index of the working face in the verification of the adjacent layer area.

The initial velocity index of the gas emission from the hole requires that the initial velocity q is measured within 2 min after the drill is suspended. In addition, the drilled depth of the tested drill holes is generally tens of meters and the drill pipe cannot be withdrawn within 2 min. Therefore, this index is not suitable for the simultaneous measurement of residual gas content, which also should not be taken as the fusion index of the working face in the verification of adjacent layer areas.

The measurement of the gas desorption index of drilled hole cuttings and the residual gas content index are both selected for the measurement of drilled hole cuttings, which can be simultaneously measured. Consequently, the gas desorption index of drilled hole cuttings is the fusion index of the working face during the verification of the adjacent layer area.

In conclusion, the cutting gas desorption index is selected as the regionally verified fusion index of the working face in the adjacent coal seam of a gas outburst when the effect of the regional prevention measures are tested.

Determination of the critical value of regionally verified fusion indexes

Determination of the critical value of regional fusion indexes

The coal in upper coal seam 6 in Xiaotun Coal Mine is high metamorphic anthracite coal, and the effect of regional prevention measures of gas outbursts is tested by the residual gas content index, whose critical value is the 8 m^3/t recommended in the Detailed Rules for the Prevention and Control of Coal and Gas Outbursts. After nearly 15 years of on-site practice, it was proven that the gas dynamic phenomenon and abnormal gas outburst never occur when the residual gas content of upper coal seam 6 dropped below 8 m^3/t, which illustrates that the reference value of 8 m^3/t is safe and reliable for testing the effect of the measures (Zhang, 2009; Zhang, 2014; Zhang et al., 2016; Lv, 2018; Wang et al., 2020b).

Determination of the critical value of the fusion indexes of the working face

1) Determination of the experimental threshold

The coal samples of upper coal seam 6 and the relatively soft coal samples of the non-obvious soft layer were collected by the grooving method, and only 2 coal samples were collected due to the few exposed locations of upper coal seam 6. These samples were tested in the laboratory and the measured results of the adsorption constant and industrial analysis indexes are shown in Table 1 (dry coal samples were used for this coal sample collection and site inspection).

TABLE 1 Tested results of experimental parameters including the gas adsorption constant and industrial analysis indexes of upper coal seam 6.

Coal seam	Sites of collection	Industrial analysis (%)			TRD (g/cm^3)	ARD (g/cm^3)	Porosity	Gas adsorption constant	
		M_{ad}	A_d	V_{daf}				a (m^3·kg^{-1})	b (MPa^{-1})
Upper 6	K0+350 m of 14 middle 16	1.55	29.30	9.77	1.77	1.70	3.95	33.918	1.677
	16 middle 07 outside of 5 m upward from the slope leveling point	1.42	29.85	7.86	1.68	1.61	4.30	33.898	1.693

The coal samples with a particle size of 1–3 mm were selected to investigate the relationship between the experimental gas pressure and the K_1 value of the drilled hole cutting desorption index. The balanced pressures were set to 0.30, 0.5, 0.75, 1.00, 1.25, and 1.50 MPa. Then, two coal samples were tested in the laboratory under different balanced pressures and the K_1 value of the drilled hole cutting desorption index was obtained.

The results of the K_1 value were fitted according to different balanced pressure conditions. The relationships of the power exponential relationship between the gas pressure P and the K_1 value were fitted as shown in Eqs 1, 2.

$$K_1 = 0.8724P^{0.8539},\ R^2 = 0.9875 \tag{1}$$

$$K_1 = 0.7704P^{0.7706},\ R^2 = 0.9902 \tag{2}$$

where K_1 is the gas desorption index of the drilled hole cuttings, ml/g.min$^{1/2}$; and P is the gas pressure of the coal seam, MPa.

According to the theory of Langmuir gas adsorption, the relationship between the gas content W and the gas pressure P is shown in formula (3) (Bai et al., 2019).

$$W = \frac{ab(P+0.1)}{1+b(P+0.1)} \times \frac{100-A_d-M_{ad}}{100} \times \frac{1}{1+0.31M_{ad}} + \frac{\pi(P+0.1)}{\gamma P_a}, \tag{3}$$

where W is the gas content of the coal seam, m^3/t; a and b are the coal seam gas adsorption constants, respectively, m^3·kg^{-1}, MPa^{-1}; M_{ad} is the coal seam moisture, %; and A_d is the coal seam ash, %.

Simultaneously, for Eqs 1–3, the relationships between the gas content W of the coal seam and the value of the desorption index K_1 of the drilled hole cuttings can be established in upper coal seam 6 as shown in Eqs 4, 5.

$$W = \frac{ab\left(\left(\frac{K_1}{0.8724}\right)^{\frac{1}{0.8539}}+0.1\right)}{1+b\left(\left(\frac{K_1}{0.8724}\right)^{\frac{1}{0.8539}}+0.1\right)} \times \frac{100-A_d-M_{ad}}{100} \times \frac{1}{1+0.31M_{ad}} + \frac{\pi\left(\left(\frac{K_1}{0.8724}\right)^{\frac{1}{0.8539}}+0.1\right)}{\gamma P_a} \tag{4}$$

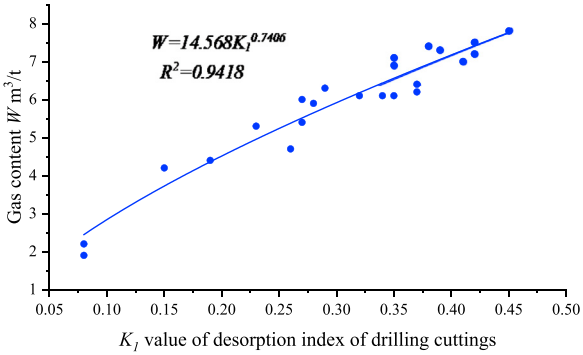

FIGURE 3
Regression fitted curve of the K_1 value and gas content in upper coal seam 6.

$$W = \frac{ab\left(\left(\frac{K_1}{0.7704}\right)^{\frac{1}{0.7706}}+0.1\right)}{1+b\left(\left(\frac{K_1}{0.7704}\right)^{\frac{1}{0.7706}}+0.1\right)} \times \frac{100-A_d-M_{ad}}{100} \times \frac{1}{1+0.31M_{ad}} + \frac{F\left(\left(\frac{K_1}{0.7704}\right)^{\frac{1}{0.7706}}+0.1\right)}{\gamma P_a} \tag{5}$$

According to the relationship model, the W-K_1 value is established by the experimental parameters of measurement, the gas desorption index K_1 values of drilled hole cuttings are 0.56 and 0.51 ml/g.min$^{1/2}$, respectively, and the smaller value of 0.51 ml/g.min$^{1/2}$ is selected as the critical laboratory value when the residual gas content of the regional fusion index is 8 m^3/t.

2) Determination of the critical value in on-the-spot tests

During the effect test of the 16 middle and 11 transport roadways (mileage K0+360–750 m), 26 groups of the seam desorption index K_1 values of drilled hole cuttings were followed in upper coal seam 6.

The fitted curve has the highest fit with the power exponential function using the reflection of the drawn discrete point graph, the

removed points with large dispersion, and the fitted relationship between gas content and cutting desorption as shown in Figure 3. The fitted relationship is shown in formula (6).

According to the fitted formula of the field investigation, the value of K_1 of the desorption index of the drilled hole cuttings is 0.50 ml/g.min$^{1/2}$ when the calculated gas content is 8 m^3/t.

Analysis of the desorption index K_1 values of the drilled hole cuttings calculated from laboratory tests and on-the-spot investigation showed that the critical values of K_1 are 0.51 ml/g.min$^{1/2}$ and 0.50 ml/g.min$^{1/2}$, respectively. In addition, to ensure safe production in the mine and reduce the outflow of gas from the adjacent layers to the excavation space, the minimum value should be selected as the critical value of the regionally verified index K_1 value in the upper coal seam area. Finally, 0.50 ml/g.min$^{1/2}$ was selected as the critical value of the regionally verified indexes of upper coal seam 6 of Xiaotun Coal Mine.

Inspection and verification

In areas with complex geological structures or pre-drained gas areas of coal seams where non-directional drill holes are used, at least two regional verifications should be conducted for every 30 m of advance of the anti-burst measurement (State Administration of Coal Mine Safety, 2019). Combined with the above-mentioned outburst coal seam mining working face and the inspection effect of regional measures and verified requirements, the requirements for the drilled hole arrangement to determine the fusion indexes during the regional verification of the gas outburst area on upper coal seam 6 of Xiaotun Coal Mine are as follows:

1) When regional verification of the coal seam adjacent to upper coal seam 6 is conducted in the coal road strip area of middle coal seam 6, the arrangement of drilled holes requires at least two inspection and tested points every 30 m along the coal roadway strip. This is favorable to determine the residual gas content index and gas desorption index of drilled hole cuttings in upper coal seam 6. Furthermore, tested drill holes should be arranged areas with a small interval, thickened coal seam, and complex geological structure.
2) When the working face area of middle coal seam 6 is regionally verified against the area adjacent to upper coal seam 6 of gas outbursts and the mining area does not exceed 120 m, the arrangement of the drilled holes requires that at least two inspection and tested points are arranged at intervals of 30 m along the advancing direction of the coal face. Otherwise, at least three inspection and tested points should be arranged at intervals of 30 m along the advancing direction of the coal face, which is favorable for the measurement of the residual gas content index and drilled hole cutting gas desorption index of upper coal seam 6. In addition, the location of the tested drilled holes should be arranged in areas with small interlayer spacing, thickened coal seams, and complex geological structures.

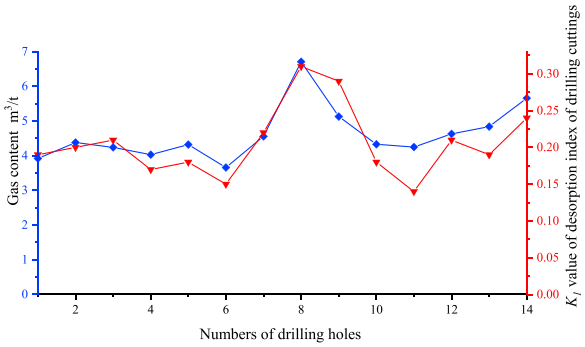

FIGURE 4
Measured results of regionally verified fusion indexes in upper coal seam 6.

Field applications

Field applications were conducted in the 16 middle and 14 transport roadways (410–620 m); two inspection and tested points were arranged at every interval of 30 m and there were a total of 14 groups of inspection points. The results of the fusion index are shown in Figure 4.

According to the regional verification of the 16 middle and 14 transport roadways of 410–620 m, the maximum residual gas content measured by the fusion index is 6.71 m^3/t and the maximum K_1 value of the drilled hole cutting gas desorption index is 0.31 ml/g.min$^{1/2}$; these values do not exceed the specified critical values of 8 m^3/t and 0.50 ml/g.min$^{1/2}$. More importantly, there are no dynamic phenomenon consisting of jet holes, jacking drilled holes, and abnormal gas emissions from adjacent layers during tunneling, which showed safe and efficient tunneling of 16 middle and 14 transport roadway. Therefore, in the tested area, the drilled length of the regional verified drill holes was reduced by 8700 m with a reduced construction cost of more than 500000 Yuan. Moreover, the average excavation speed increased from approximately 90 m/month to 150 m/month with the increase in the average excavation speed by 1.6 times.

Conclusions

1) Through laboratory tests and on-the-spot statistical analysis, the W-K_1 relationship model was established and the critical value of K_1 was determined to be 0.50 ml/g.min$^{1/2}$ when the gas content in upper coal seam 6 was 8 m^3/t.
2) The layout requirements for the regionally verified drill holes and the judgment principle of regionally verified results for the fusion indexes of upper coal seam 6 in Xiaotun Coal Mine were established.
3) The method of regional verification and index fusion of the working face was proposed to adhere to the general idea of

advanced detection, index fusion, determination of the critical values, inspection, and verification, which also showed that the method was feasible and effective through inspection and verification. Moreover, the method provides a new idea and method for the regional verification of mining working faces in similar mining areas in Guizhou Province, and also provides practical experience and a scientific basis for the formulation of relevant industrial normative clauses for the regional verification of close coal seam groups adjacent to coal seams of gas outbursts.

Data availability statement

The original contributions in this study are included in the article/Supplementary Material, and further inquiries can be directed to the corresponding author.

Author contributions

SZ, as an industry expert and writer, completed the overall content of the paper and related experiments.

Funding

This work was financially supported by the National Key R&D Program (2017YFC0804206) and the projects from Chongqing Research Institute, China Coal Science and Industry Group (2022ZDXM07).

Conflict of interest

SZ was employed by the China Coal Science and Industry Group, Chongqing Research Institute Co., Ltd.

Publisher's note

All claims expressed in this article are solely those of the authors and do not necessarily represent those of their affiliated organizations, or those of the publisher, the editors, and reviewers. Any product that may be evaluated in this article, or claim that may be made by its manufacturer, is not guaranteed or endorsed by the publisher.

References

Bai, G., Zhou, X., and Shiping, W. (2019). Numerical simulation and application of increasing gas drainage by CO_2 injection in low permeability coal seam[J]. *Coal Field Geol. Explor.* 47 (03), 77–84. doi:10.3969/j.issn.1001-1986.2019.03.013

Cheng, J. (2018). *Investigation on the occurrence mechanism and joint outburst prevention method of close seam group [D]*. China: Anhui University of technology.

Fan, C., Wen, H., Li, S., Bai, G., and Zhou, L. (2022). Coal seam gas extraction by integrated drillings and punchings from the floor roadway considering hydraulic-mechanical coupling effect. *Geofluids* 2022, 1–10. doi:10.1155/2022/5198227

Fan, X. (2012). Discussion on the regionally verified method of close coal seam of gas outburst [J]. *Coal Eng.* (10), 45–47.

Gui, H., Wen, G., and Zhang, G. *A joint area verified method for driving face of close coal seam of gas outburst [P]*. Cn104806291a, 2015-07-29.

Hu, Q., Zhou, S., and Zhou, X. (2008). Mechanical mechanism of coal and gas outburst process [J]. *Acta coal Sin.* 33 (12), 1368–1372.

Jia, Y. (2022). Research on local comprehensive outburst prevention measures for coal roadway driving faces in outburst coal seams [J]. *China Coalbed Methane* 19 (02), 36–39.

Jiang, X., Fan, S., and Cheng, Z. (2018). Comprehensive gas control mode of three zone linkage based on combined up and down well extraction [J]. *Coal Sci. Technol.* 46 (6), 107–113. doi:10.13199/j.cnki.cst.2018.06.018

Kong, B., Cao, Z., Sun, T., Qi, C., and Zhang, Y. (2022). Safety hazards in coal mines of Guizhou China during 2011–2020. *Saf. Sci.* 145, 105493. doi:10.1016/j.ssci.2021.105493

Li, Y., and Yanbin, H. (2010). Analysis on the regional verification and effect test method of coal seam of gas outburst in Jiaozuo mining area [J]. *Coal mine Saf.* 41 (11), 86–88.

Li, H., Ma, J., Wang, Z., Wang, W., and Liu, Y. (2020). A gas outburst prevention and control strategy for single thick coal seams with high outburst risk: a case study of hudi coal mine in qinshui basin. *Energy Sci. Eng.* 8 (7), 2471–2491. doi:10.1002/ese3.680

Lv, G. (2018). Investigation on the method of determining the critical value of gas content for the effect inspection of regional prevention measures of gas outburst [J]. *Coal Eng.* 50 (8), 105–108.

State Administration of Coal Mine Safety (2019). *Detailed rules for prevention and control of coal and gas outbursts [M]*. Beijing: Coal Industry Press.

Wang, L., Lu, Z., Chen, D., Liu, Q., Chu, P., Shu, L., et al. (2020). Safe strategy for coal and gas outburst prevention in deep-and-thick coal seams using a soft rock protective layer mining. *Saf. Sci.* 129, 104800. doi:10.1016/j.ssci.2020.104800

Wang, F., Liang, Y., Sun, Z., Li, L., and Li, X. (2020). Determination of the sensitivity index and its critical value for outburst risk prediction: A case study in fuxiang mine, China. *Adsorpt. Sci. Technol.* 38 (9-10), 502–527. doi:10.1177/0263617420963735

Wang, S. (2019). Study the critical value of outburst effect inspection index in the case of regional gas predrainage. *IOP Conf. Ser. Earth Environ. Sci.* 358 (2), 022007. doi:10.1088/1755-1315/358/2/022007

Wang, W. (2019). Determination of gas emission radius based on drilled cuttings index method [J]. *Inn. Mong. Coal Econ.* (09), 142–143.

Xu, T. (2016). Discussion on the regionally verified method of the working face of the close coal seam groups of gas outburst [J]. *Energy Technol. Manag.* 41 (2), 59–66.

Yang, S., and Liao, Y. (2023). Research on gas grading control method of coal roadway heading face in high gas mine[M]. *Adv. Geol. Resour. Explor.*, 237–242. CRC Press.

Yang, F., Zheng, J., and Wang, L. (2019). Study on gas overrun control technology in mining working face of close seam group [J]. *Coal Sci. Technol.* 47 (5), 126–131. doi:10.13199/j.cnki.cst.2019.05.020

Zhang, Y., Lv, G., and Liu, H. (2016). Investigation on the critical value of gas content in gas outburst prediction index of outburst coal seam area [J]. *Coal Sci. Technol.* 44 (11), 82–87. doi:10.13199/j.cnki.cst.2016.11.016

Zhang, E., Zhu, Q., and Liu, Y. (2020). Comprehensive prediction and verification of coal seam outburst risk [J]. *J. North China Univ. Sci. Technol.* 17 (04), 19–26+42.

Zhang, Z. (2009). *Gas geology [M]*. Xuzhou: China University of mining and Technology Press.

Zhang, Z. (2014). Determination of the critical value of the gas content in the test indexes of pre-drainage effect of coal seam of gas outburst [J]. *Coal Sci. Technol.* 42 (4), 39–42. doi:10.13199/j.cnki.cst.2014.04.011

frontiers | Frontiers in Earth Science

TYPE Original Research
PUBLISHED 06 January 2023
DOI 10.3389/feart.2022.1040147

OPEN ACCESS

EDITED BY
Yu Song,
China University of Mining and Technology, China

REVIEWED BY
Dong Duan,
Taiyuan University of Technology, China
Hongwei Yang,
North China University of Science and Technology, China

*CORRESPONDENCE
Xiang Fu,
334823023@qq.com

SPECIALTY SECTION
This article was submitted to Economic Geology,
a section of the journal
Frontiers in Earth Science

RECEIVED 09 September 2022
ACCEPTED 22 September 2022
PUBLISHED 06 January 2023

CITATION
Fu X, Liu H, Sha H, Wang Z and Liu X (2023), Micro-Porosity and gas emission characteristics of thermally contacted metamorphic coal by igneous intrusion. *Front. Earth Sci.* 10:1040147. doi: 10.3389/feart.2022.1040147

Micro-Porosity and gas emission characteristics of thermally contacted metamorphic coal by igneous intrusion

Xiang Fu[1]*, Hongda Liu[1], Huihui Sha[1], Zhiquan Wang[2] and Xuan Liu[1]

[1]College of Mining, Liaoning Technical University, Fuxin, China, [2]College of Safety Science and Engineering, Liaoning Technical University, Fuxin, China

In order to quantitatively characterize the pore structure of thermally contacted metamorphic coal by igneous intrusion and investigate the intrinsic connection between the pore and dispersion properties of coal, the samples of metamorphic coal from different locations of Daxing Coal Mine were collected and processed. The correlative analysis on pore characteristics, including pore area, perimeter, shape factor and fractal dimension of pores with different sizes, were carried out by using scanning electron microscopy (SEM) and pore-fracture analysis system (PCAS). The results show that the porosity of macro- and meso-pores and the number of pores in the metamorphic coal are larger than those of the normal coal. The total length of pores per unit area and the average shape factor increase, and the connectivity of pore is raised, resulting in an enhanced gas release capacity (increased V_1) within the first one second. The proportion of gas emission in the first one second of metamorphic coal is much higher than that of other coals. The decrease of pore volume and specific surface area of micropores makes the adsorption capacity weaker, which results in a decrease in the total amount of emission - smaller Δp value, and earlier inflection point and faster attenuation on the emission curve, namely an increased α value. In addition, the V_1, α value and volatile content satisfy the quadratic nonlinear and linear relationships, respectively. In the prediction of outburst risk of thermally contacted metamorphic coal, it is more reasonable to use the V_1 index to characterize the gas release rate.

KEYWORDS

initial velocity of gas emission, coal and gas outburst, thermally contacted metamorphic coal, pore structure, PCAS

Introduction

China's northeast region is rich in coal resources, but igneous intrusion is common Igneous rock activity in Tiefa Daxing Coal Mine is much developed, which has direct correlation with coal and gas outbursts, and fire disasters. Therefore, the impact area of igneous rock on safe mining has become a significant issue.

Coal is a porous medium with dual structure of pores and fractures. The characteristics of pore structure have a controlling role in the behaviors of gas storage and transport (adsorption, diffusion and seepage), which will directly determine the gas emission of coal. The investigation on pore characteristics has a crucial role in the prevention of coal and gas outburst (Fu et al., 2017). Coal seams are subjected to different degrees of metamorphism by igneous intrusion, which changes the microstructure and macroscopically, as well as the adsorption and dispersion characteristics (Fan et al., 2022; Zhou et al., 2022). As a result, the gas outburst risk of coal seams is changed. The metamorphism raised by igneous intrusion includes regional metamorphism, contacted metamorphism, and dynamic metamorphism. Due to the different period and mode of metamorphism, the regional metamorphism has obvious influence on coal seam zoning. The large scope of the action, the stable assignment of the metamorphic zone. Contacted metamorphic coal has small scope of action and unstable assignment of metamorphic zone, and is easy to form highly metamorphic coal (Arora et al., 2017; Fan et al., 2021; Teicherta et al., 2022).

The effect of soluble organic matter on the specific surface area pore volume, average pore size and porosity of coal has been researched (Yang et al., 2018). Some scholars concluded that the porosity of coal seam shows a change pattern of increasing and then decreasing as the distance to igneous rocks gets closer (Wang, 2015; Zhang et al., 2019). Li et al. studied the microscopic pore characteristics of coal by combining SEM-PCAS with gas adsorption methods (Li et al., 2022). Temperature has a significant transforming effect on the pore structure of coal, especially the macropore and microporous structure (Zhao et al., 2021). The quantitative analysis is also limited to the pore volume statistics.

Previous studies have verified that the initial velocity of gas emission increases with the degree of metamorphism (Liu and Wang, 2013; Song et al., 2019). The initial velocity of gas emission is experimentally related to the specific surface area of coal as a primary function (Luo, 1989; Wang et al., 2021). The larger the pore specific surface area, the smaller the initial velocity of gas emission (Wang et al., 2020). There is also a primary function between the specific surface area of micropores and the initial velocity of gas emission, and the initial velocity of gas emission decreases exponentially with the degree of metamorphism (Zhao et al., 2017). In conclusion, it is believed that the initial velocity of gas emission increases with the degree of metamorphism. Chinese scholars have used Δp (ie, Δp10-60, representing the emission amount from 10 s to 60 s) to characterize the gas emission rate of coal when carrying out the above researches. Although the Δp indicator has high practical value in field application, it is impossible to describe the microscopic characteristics of the release velocity curve in the first 60 s when conducting in-depth scientific research. Some literatures have mentioned that this indicator may have missed the outburst prediction in metamorphic coal by igneous intrusion. However, there are few literatures on the contacted metamorphic coal.

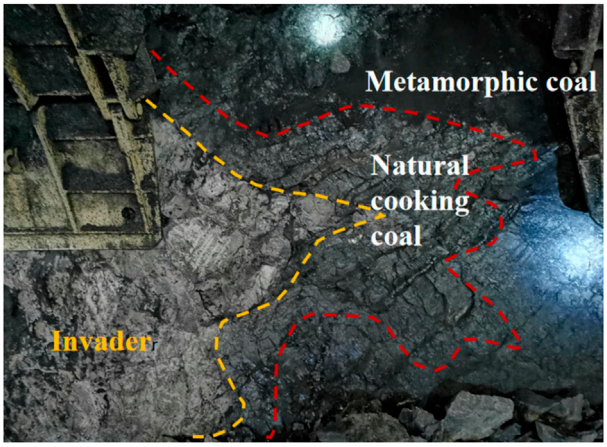

FIGURE 1
Thermally contacted metamorphic coal.

The scale, shape, structure, number, fractal and other factors of pore-fracture directly affect the gas emission characteristics of coal, and can also in turn infer and verify the coal microstructure. Pore-fracture analysis system (PCAS) is a special software for identifying and quantitatively analyzing pore systems and fracture systems, and PCAS has been successfully applied in quantitative identification and structural analysis of pore-fractures in geotechnical soils and shale pore-fractures (Liu et al., 2011; Lin et al., 2016; Wang et al., 2016; Liu et al., 2017; Wang et al., 2017; Zhao et al., 2020). In this paper, the microscopic characteristics of 5 coal samples of No. 9 coal in Daxing Coal Mine were researched and analyzed by using scanning electron microscope (SEM) and pore fracture analysis system (PCAS), and the emission velocity curve in the first 60 s were measured and described. The internal relationship between the microscopic characteristics of thermally contacted metamorphic coal and the macroscopic performance of the emission characteristics will be revealed to provide guidance for prevention of the gas disaster resulted from igneous rock intrusion.

Collection and description of coal samples

Collection of coal samples

The experimental coal samples was selected from the No. 9 coal seam in the North 2# mining area of Daxing Coal Mine.

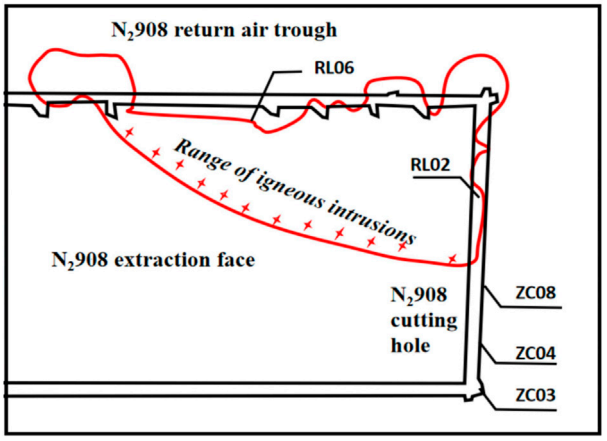

FIGURE 2
Location of sampling coals.

The coal seam is 4 m thick, with local basal shallow faience intrusions - mostly existing as a rock wall or a bed of intrusion along the top and bottom plate and locally engulfing the coal seam to form a coal-free zone, as shown in Figure 1. The gabbro intrusions in $N_2$908 panel have been uncovered many times near the in-seam roadway and the open cut. Hence, they are the ideal sampling sites. 5 coal samples were collected this time, and the sampling locations are shown in Figure 2.

Industrial analysis of coal samples

The industrial analysis data of the coal samples is listed in Table 1. The coal distancing 8 m from the intrusion is characterized by the moisture of 4.46%, fixed carbon of 40.58%, ash of 10.11% and volatile matter of 44.85%. The change trend is not obvious. In the range of 0.4 m–5.5 m, the internal moisture of coal was heat gasified by the high temperature baking effect during the intrusion of igneous rocks, and the moisture content of all coal samples is lower than that of normal coal samples, with the lowest ~1.58%. The ash content of coal with igneous intrusion increases from 10.11% to 19.29% compared to that of normal coal. As the distance from igneous intrusion decreases, the volatile content decreases from 44.85% to 8.89%, and the metamorphic area is obviously lower than normal coal. Due to the decrease of water and volatile matter, the percentage of fixed carbon increases, from 47.19% at 5.5 m to 69.55% at 0.4 m.

Pore characteristics of contacted metamorphic coal samples

Observation of pore shape in coal samples using SEM

The SEM model Jsm-7800f was used to observe the pore shape in coal samples. The collected coal block was processed to be cubic samples with a size of 5 mm × 5 mm × 5 mm. The surface of these coal samples were coated with a layer of gold with a thickness of 5–10 nm to enhance the conductivity of the surface. Then the coated coal samples were put into the sample chamber, and evacuated it to 10~3 Pa. The magnification of 500–100000 times were selected to observe the images. Problems of differences in scanned images caused by different scanning positions can be solved by using multi-point scanning.

The primary low-metamorphic coal in the No. 9 coal seam in the North Second Mining Area of Daxing Coal Mine has good homogeneity and integrity, as shown in Figure 3A. There are few 1um-level pores in this area, and pores can be seen above the magnification of 10,000. Pores are seen in all coal samples, but more in metamorphic coals, as shown in Figure 3B. Fast metamorphism rate is a significant external factor for the development of pores. Thermally contacted metamorphism is characterized by high temperature, low pressure, short time, fast metamorphism rate, and obvious gas generation peak. The solidified hydrocarbon-rich components in coal are easy to soften, flow and gasify, resulting in well development of the pores. A series of small-scale parallel fissures appear in the uniform vitrinite of metamorphic coal, which do not penetrate the entire sample, are perpendicular to the bedding without crossing the bedding plane. They are arranged in parallel at equal intervals and are not connected to each other, proving that

TABLE 1 Industrial analysis of coal samples.

Test coal samples	Distance from intruder Distance(m)	Water content Mad (%)	Volatile matter Vdaf (%)	Ash Ad (%)	Fixed carbon FCad (%)
High metamorphic coal (6#)	0.4	1.74	9.42	19.29	69.55
High metamorphic coal (2#)	1.5	1.58	8.89	16.36	73.17
Medium metamorphic coal (4#)	3.5	2.71	33.28	10.38	53.63
Low metamorphic coal (3#)	5.5	2.78	34.74	15.29	47.19
Low metamorphic coal (8#)	8	4.46	44.85	10.11	40.58

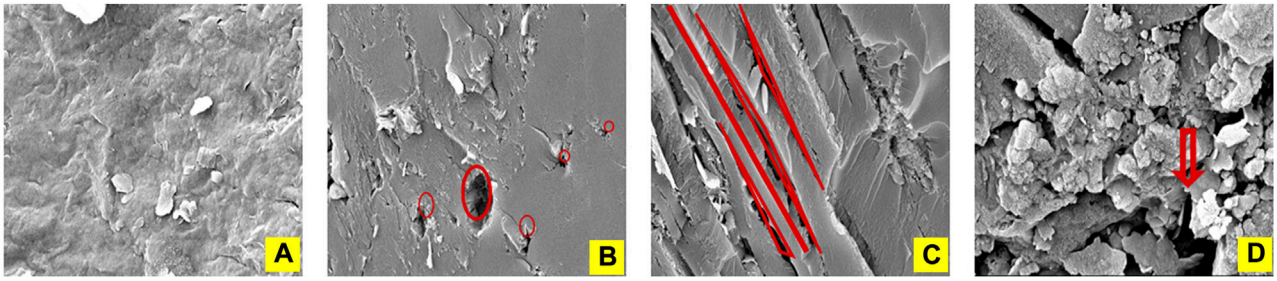

FIGURE 3
Types of coal pores at the test site.

these fissures are endogenous fissures in the process of coal metamorphism. As shown in Figure 3C, the shape of the hydrostatic fractures can be classified as plate shape. Breccia pores are distributed in all coal samples, but more developed in metamorphic coals with complex and changeable shapes and good connectivity, as shown in Figure 3D. Illite is present in the breccia pores of metamorphic coals (Hwang and Pini, 2019).

Binarization of SEM images

The SEM images were analyzed by using PCAS, and the image unit radius was set to 1 pixel (pix) and the minimum analysis area was 5 pix. Coal pores were divided into four categories: micropores (<10 nm), small pores (10–100 nm), mesopores (100–1000 nm) and macropores (>1000 nm) (Huoduote, 1966). Due to the irregularity of the pore shape, on the SEM plane images, the circular area was used to classify the pores: micropores (<78.5 nm^2), small pores (78.5–7850 nm^2), and mesopores (7850–785000 nm^2) and macropores (>785000 nm^2) (Li et al., 2022). This method can better identify small, medium and large pores, but the accuracy of identifying micropores is poor even with a maximum 100000-fold SEM image. The images were binarized, as shown in Figure 4.

Figure 4A and Figure 4B belong to thermally contacted metamorphic coal samples, the surface is mainly polycondensation cracks or pores in endogenous fissures, and the surface is filled with minerals. The fractal picture shows that the fissures are curved, non-directional, and have different lengths, irregular shape. Figure 4C is a coal sample damaged by shear stress structure, which is filled with minerals in the later stage, and the surface is honeycomb-like distribution. Figure 4D and Figure 4E are normal coal samples without obvious damage, and the surface is relatively continuous flat. Figure 4F is more complicated to damage, reflecting in pores caused by endogenous evanescent condensation and condensation, and compressive fractures caused by tectonic stress damage.

Characterization of pore by PCAS method

Geometric characteristics of pores in coal

According to the characteristics of adsorption loops, pores in coal are generally divided into cylindrical, slit, wedge and ink bottle shapes. For the binarized images of SEM, the morphological characteristics of pores should include three independent characteristics, namely pore shape (overall outline, such as roundness), angularity (curvature of corners and edges of pores) and pores surface roughness, as shown in Figure 5. The three represent the spatial variation of the pore profile at different dimensional scales. The following attempts to quantitatively characterize individual pores and regional pore aggregates by using different methods.

Fourier series can be used to describe the morphological characteristics of pores (roundness, angularity, roughness) (Kandasami and Murthy, 2017; Barone and Sen, 2018; Wenjuan et al., 2018; Ren et al., 2021). The Fourier series equation describing the boundary contour of the stack pores is:

$$R(\theta) = a_0 + \sum_{m=1}^{\infty} (a_m \cos)m\theta) + b_m \sin(\theta)) \quad (1)$$

Where a_m and b_m are the Fourier coefficients; and m is the frequency; $R(\theta)$ is a function of the azimuth angle θ ($0^\circ \le \theta \le 360^\circ$), indicating the distance from the center of the pore to its contour boundary, which is obviously a periodic function; a_0 is the average radius of the pores.

$$a_0 = \frac{1}{2\pi} \int_0^{2\pi} R(\theta) d(\theta) \quad (2)$$

$$a_m = \frac{1}{\pi} \int_0^{2\pi} R(\theta) \cos(m\theta) d(\theta) \quad (3)$$

$$b_m = \frac{1}{\pi} \int_0^{2\pi} R(\theta) \sin(m\theta) d(\theta) \quad (4)$$

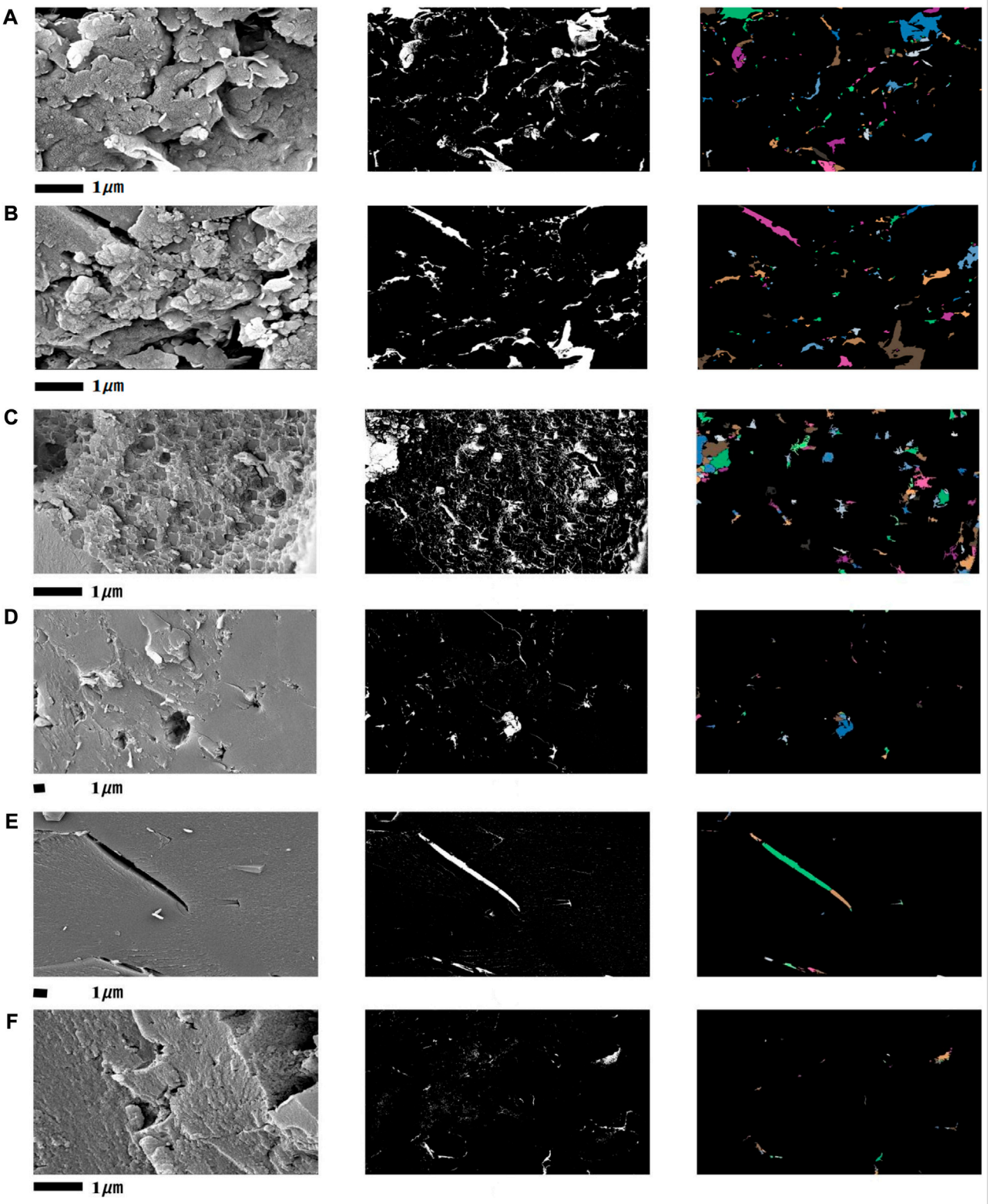

FIGURE 4
SEM and parametric processing of pictures.

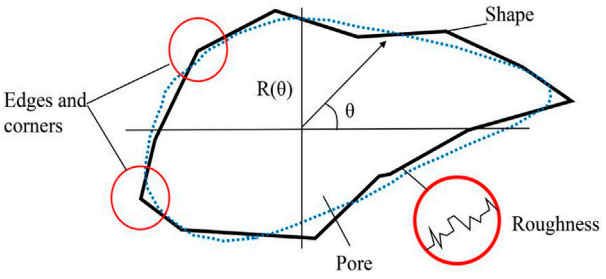

FIGURE 5
Schematic diagram of overall shape, angularity and surface roughness of pores.

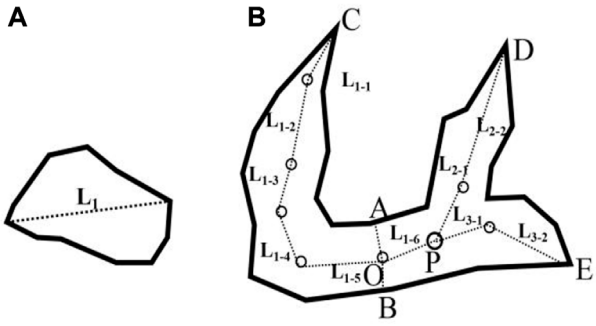

FIGURE 6
Calculation of the total length of the hole (crack) gap.

Since $R(\theta)$ and θ are discrete variables, the above integral expressions can be listed in the form of summation. The area of the pore contour in Figure 5 can be described as:

$$A = \int_0^{2\pi} \frac{1}{2} R^2(\theta) d(\theta) = \pi \left[a_0^2 + \frac{1}{2} \sum_{m=1}^{\infty} a_m^2 + b_m^2 \right] \quad (5)$$

Among them, a_0 is the average equivalent radius of the circle, that is, the boundary is surrounded by boundary lines of equal area. Therefore, the Fourier index α of the pore morphology characteristic is defined as:

$$\alpha = 1 + (\alpha_s + \alpha_r + \alpha_t) \quad (6)$$

$$\alpha_s = \frac{1}{2} \sum_{m=1}^{m=n_1} \left[\left(\frac{a_m}{a_0} \right)^2 + \left(\frac{b_m}{a_0} \right)^2 \right] \quad (7)$$

$$\alpha_r = \frac{1}{2} \sum_{m=n_1+1}^{m=n_2} \left[\left(\frac{a_m}{a_0} \right)^2 + \left(\frac{b_m}{a_0} \right)^2 \right] \quad (8)$$

$$\alpha_t = \frac{1}{2} \sum_{m=n_2+1}^{m=\infty} \left[\left(\frac{a_m}{a_0} \right)^2 + \left(\frac{b_m}{a_0} \right)^2 \right] \quad (9)$$

Eqs. 7, 8, and Eq. 9 define the Fourier shape index, angularity index, and surface texture index of pore morphology, which are functions of m. The larger m is, the closer $R(\theta)$ in Eq. 2 is to the real boundary of the pores, and the Fourier indices of Eqs. 7, 8, and Eq. 9 can better reflect the morphological characteristics of the pores.

Total length of holes (cracks) in studied area

The length of the simple hole (crack) can be represented by the long axis L_1, and the length of the complex hole (crack) is represented by multiple continuous broken lines. Hole (crack) gap bifurcations or intersections are individually marked as nodes, such as point P in Figure 6B. Complex holes (cracks) can be simplified as graphs (graph theory term for discrete mathematics), where C, D, and E are the vertices of the graph, and PD, PE, and PC are the edges of the graph. The total length of the hole (crack) in the area after the graph is calculated can be expressed as:

$$L_a = \sum_{K=1}^{p} \left(\sum_{j=1}^{m} \sum_{i=1}^{n} L_{j-i} \right) \quad (10)$$

Where L_a is the total length of the pores in the region, pix (pixels); L_{j-i} is the length of the i-th line segment in the j-th side, pix; i, j, k are the serial numbers of line segments, edges, and complex pores, respectively; n, m, p are the number of line segments, edges, and complex pores, respectively.

The total pore length comprehensively characterizes the degree of pore development and pore shape. The total length L_a of regional pores (cracks) is related to the shape of a single pore (crack), and is also determined by the shape and number of pores (cracks). The larger the L_a value, not only means that the pores are relatively developed, but also the probability of pore connectivity is higher, and the gas flow resistance is smaller.

Shape factor of pores

Under the same pore volume, due to the different pore surface characteristics and shapes, the specific surface area may vary greatly, showing the difference in the gas adsorption capacity on the macroscopic level. However, due to the difference in the pore shape, the porosity and specific surface area cannot be directly determined. The ability of the coal to release gas. In the coal micro-pore system, pores and fissures cannot be strictly distinguished, especially for severely damaged coal. Therefore, in certain cases, the two can be treated equally and described by the shape factor.

The ratio of the square of the pore contour perimeter l to the pore contour area is defined as the shape factor of the pores, namely:

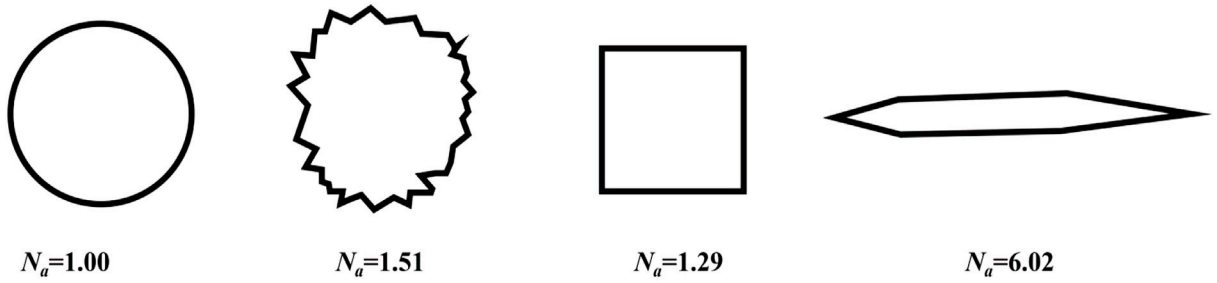

FIGURE 7
Shape factors for different geometries.

$$N_a = \frac{l^2}{4\pi S} \tag{11}$$

where N_a is the shape factor of the pores; l is the perimeter of the pore contour, pix; S is the pore contour area, pix^2 (pixel^2).

For binarizated images of coal pores, the shape factor of pores represents the perimeter of a certain area of pores, which depends on the circularity and rough edges of the pores. The larger the value, the narrower the pores and the rougher the boundary. The larger the N_a, the greater the probability that the pores (cracks) are connected to each other. The ideal circular N_a value is shown in Figure 7.

Equation. 11 is suitable for describing the shape characteristics of a single pore (crack), and statistical methods can be used to describe the group characteristics of pores (cracks). If the total perimeter and total area of pores (cracks) in the specific area are known, the average shape factor N_0 of the pores can be obtained, and the N_0 value can characterize the performance characteristics of the pores (cracks) in the specific area. The larger the value of N_0, the larger pore contour perimeter (representing the specific surface) in the region, and the better interconnectivity between the pores, in the same region of pore profile area (representing the pore volume).

$$N_o = \frac{\left(\sum_{i=1}^{i=n} l_i\right)^2}{4\pi \sum_{i=1}^{n} S_1} \tag{12}$$

Where N_0 is the average shape factor of the pores; L_i is the perimeter of the i-th pore contour, pix; S_i is the i-th pore area, pix^2.

Binarization quantitative analysis of coal pore characteristics

The PCAS analysis can accurately identify all pores larger than 5 pixels in the electron microscope image through the algorithm, then use image analysis software to calculate fractal, and obtain porosity, shape factor, fractal dimension, and finally calculate the total length of pores.

Pore volume based on PCAS analysis

The parameters such as pore area, perimeter, shape factor, and fractal dimension are counted according to macropores, mesopores, small pores, and micropores, respectively, as shown in Figure 8. The number of pores is counted according to the unit area of 1220000pi.

For metamorphic coal and non-metamorphic coal samples, no obvious difference is found in the porosity and pore number of small pores. Statistics show that the macropores and mesopores of 2# and 6# metamorphic coal samples and the number of pores is generally larger than those of the other coal samples, indicating that the thermal contacted metamorphic coal samples have more macropores and mesopores than the other coal samples.

The fractal dimension reflects the validity of the space occupied by the coal matrix and is used to measure the irregularity of the coal. The statistical results show that there is no obvious regularity in the change of fractal dimension with the degree of metamorphism of the five coal samples.

The total length of the macropores of the 2# and 6# coal samples of metamorphic coal is more than 78806200 nm, which is 31% higher than that of normal coal samples. The total length of mesoporous pores reaches more than 628019000 nm, which is 29% higher than the average value of other coal samples.

The shape factors of each coal sample were statistically analyzed and compared. As shown in Figure 9, the shape factors of macropores, mesopores and small pores are 3.8–4.3, 3.47–3.88, 2.2–2.8, respectively, and the average values are 4.01, 3.65, and 2.53, respectively. The average shape factor of large pores of non-metamorphic coal samples is 3.89, and the average shape factor of large pores of metamorphic coal is 4.12, which is 7.5% higher than the former. The average shape factor of mesopores in non-metamorphic coal samples is 3.62, and the

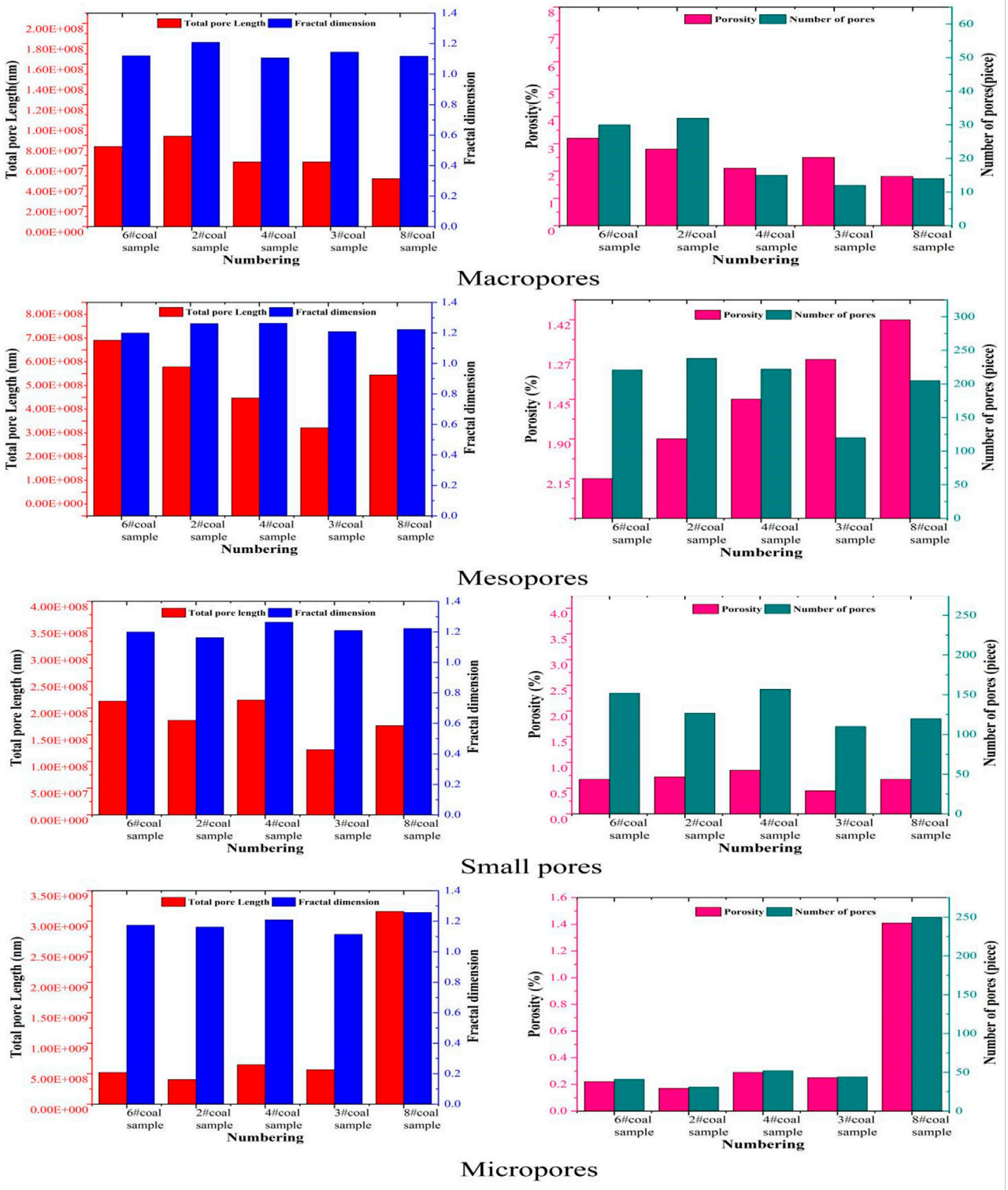

FIGURE 8
PCAS analysis of each coal sample.

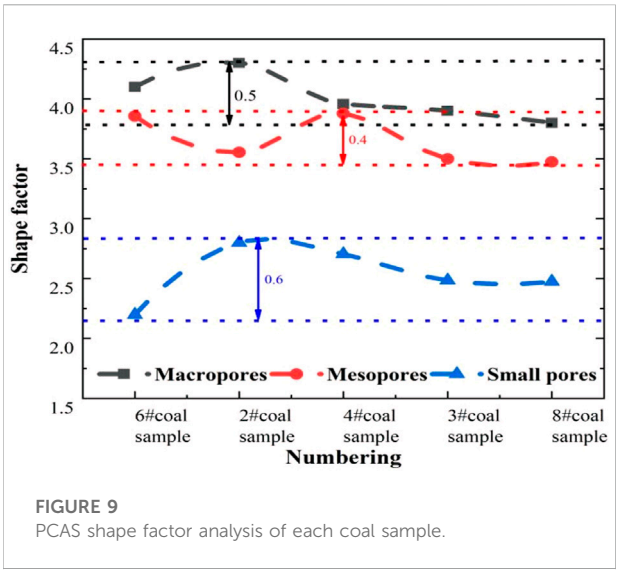

FIGURE 9
PCAS shape factor analysis of each coal sample.

average shape factor of mesopores in metamorphic coal is 3.71, an increase of 2.4% compared with the former. For metamorphic coal and non-metamorphic coal, the average shape factors of the pores are 2.50 and 2.55, respectively, and there is no significant difference between the two. It shows that the macropore and mesopore shape factor values of thermal contacted metamorphic coal samples have a certain increase, that is, for the same pore volume, the probability of inter-pore connectivity increases significantly, which is more conducive to the movement of methane molecules.

Determination of micropores by nitrogen adsorption at low temperature

It is difficult to distinguish pores below 5 nm by using SEM images of 100,000 times, so the specific surface area and micropore pore volume were determined by low-temperature nitrogen adsorption method. The specific surface area analyzer was used to compare the surface area and microvolume volume by conducting a low-temperature nitrogen adsorption test (Zhao et al., 2016), and the results are listed in Table 3 (Qiang, 2017).

The specific surface area of coal is proportional to the amount of adsorption (Zhu et al., 2021), and its value mainly depends on the micropore system. The degree of development of micropores determines the adsorption capacity of methane on coal. The measured specific surface area of metamorphic coal is only 38.7% that of normal coal, and the pore volume of micropores is only 32.9% that of normal coal. Due to thermal contacted metamorphism, the pore volume and specific surface area of the microporous system are greatly reduced, and the gas adsorption capacity is weakened.

Comparative tests on coal emission characteristics

Methods and instruments of measurement

Under a certain gas pressure, the coal reaches adsorption equilibrium, and then it is quickly released to the external low-pressure space. The measured gas release speed is the gas emission rate. Coal particles in free state are not subjected to mechanic stress, and the micropore (crack) system remains in a natural state and is basically stable. The experiments on the gas emission rate were carried out using the developed WT-1A gas emission velocity measuring apparatus. The sensor response speed is 10 ms, the sampling frequency is 1000Hz, and 2 coal samples can be tested at one time. The gas source uses standard gas with a purity of 99.99%. The coal samples were crushed and dried. Coal samples of 5 g with a particle size of 0.25–0.5 mm were screened and loaded into the instrument. After degassing for 90 min, they were inflated for 90 min at a pressure of 0.1 MPa, and measured in a venting space with a pressure close to vacuum.

Measured results of gas emission amount and rate

The measured gas emission curve is shown in Figure 10. On the whole, there is little difference in the cumulative emission of all coal samples, but the curves are very different in the three stages of gas emission. In the first stage, the emission rate of all samples increases sharply, and the gas emission rate reaches the maximum value in an instant. The emission rate of the 2# coal sample closest to the intrusive body increases significantly. The emission amount reaches 4.45 ml/g in 1s, reaching 94% of the emission amount in 60 s. The 3#, 4#, 8# coal samples grow relatively slowly. In the second stage, an inflection point appears in the emission curve, and the increase in emission slows down significantly. The 2# and 6# coal samples have a fast decay rate, from 0.3 ml/g to 0.01 ml/g, and the inflection point appears earlier than other coal samples. The cumulative emission of 2# and 6# coal samples at the end of this stage account for 99% of the total emission in 60 s, and the emission amount is overtaken by the 3# coal sample. The gas emission of 3#, 4# and 8# coal samples still maintain a relatively rapid growth rate. In the third stage, the emission rate of coal samples stabilizes and the growth rate slows down. The emission amount of 2# and 6# coal samples only accounts for 1% of the total emission amount in the first 60 s. Generally speaking, in the first stage, the proportion of the 2# and 6# coal samples in the total emission is much higher than that of the other coal samples. In the second and third stages, the cumulative emission of the 2# and 6# coal samples is much lower than that of the other coal samples.

TABLE 2 Statistical comparison of PCAS of coal samples with different grades of pores.

Content		Sort	Content		Sort
Porosity	Macropore	6#>2#>3#>4#>8#	Pore length	Macropore	2#>6#>4#>3#>8#
	Mesopore	6#>2#>4#>8#>3#		Mesopore	6#>2#>8#>4#>3#
	Small pore	4#>2#>8#>6#>3#		Small pore	4#>6#>2#>8#>3#
Number of pores	Macropor	2#>6#>4#>8#>3#	Fractal dimension	Macropor	6#>2#>3#>8#>4#
	Mesopore	2#>4#>6#>8#>3#		Mesopore	4#>2#>8#>3#>6#
	Small pore	4#>6#>2#>8#>3#		Small pore	4#>8#>3#>6#>2#

TABLE 3 Characteristic parameters of microporous pores.

Projects and units	Metamorphic coal	Normal coal
Average volatile matter (%)	14.16	37.63
Specific surface area (m^2/g)	6.04	15.6
Micropore pore volume (ml^3/g)	1.88	5.72

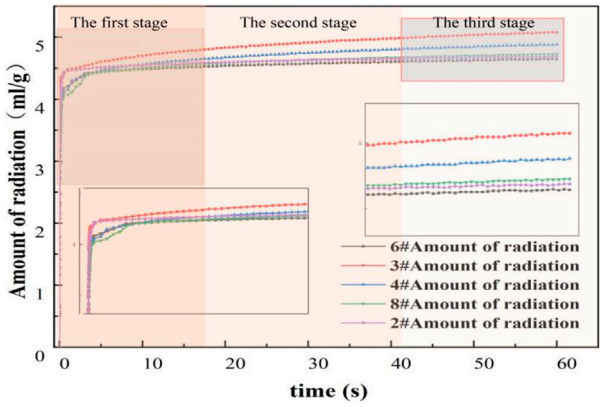

FIGURE 10
Gas emission curve of raw coal.

In the experiment, the pressure difference inside and outside the coal particles and the concentration gradient difference are the driving forces for the flow of methane molecules in the coal particles. The gas emission rate depends on the coal adsorption capacity and the resistance of methane molecules to move. The more developed the micropores, the greater the adsorption capacity of methane, the greater the number of stored methane molecules, the more gas sources in the emission process, and the greater the cumulative emission amount. Due to the small particle size of the experimental coal sample, the short migration route of methane molecules and the fast overall release rate, the emission amount in 0–60s can largely reflect the total amount of emission. Δp is basically equivalent to the gas emission from 0 to 60s in application (Fu, 2006). Taking the distance from the intrusive body as the abscissa, the two parameters and the volatile content were plotted as a curve, as shown in Figure 11. Different from the conclusions of most literatures, whether it is the Δp value or the accumulated amount of gas released from 0 to 60 s, the trend is not monotonically decreasing with the increase of the intrusion distance, and even has an increasing trend. The reasons for this are further analyzed below. Referring to the results of PCAS analysis and low-temperature nitrogen adsorption method, the micropore volume and specific surface area of each coal sample were compared and analyzed with the total emission in 0–60 s, the average volatile content and the specific surface area of thermal contacted metamorphic coal are 14.16% and 6.04 m^2/g, which are much smaller than 37.63% and 15.6 m^2/g of normal coal. Its micropore volume is 1.88 ml^3/g, much smaller than 5.72 ml^3/g of normal coal. The emission amount of metamorphic coal in 0–60s is 4.67 ml/g, while that of normal coal is 4.9 ml/g. Tthe average value of the total emission of normal coal in 0–60 s is larger than that of metamorphic coal in terms of macroscopic performance. PCAS analysis shows that normal coal does not develop macropores and mesopores, but has large specific surface area, high micropore porosity, larger methane adsorption capacity, and more gas sources during the release process. The farther away from the intrusive body, the higher the volatile matter, the larger the Δp value, the better the continuation of the emission process, and the slower the decay.

The increase in ash content caused by thermal contacted deterioration is also another reason for the decrease in the total emission from 0 to 60 s. Non-coal minerals occupy a part of the volume of raw coal, but its effective pores are very few. Observation of coal SEM shows that pyroxene, quartzite, illite, feldspar and other crystals are filled in the primary pores, blocking the gas migration channel.

The above PCAS analysis shows that thermal contacted metamorphic coal has small specific surface area, low microporosity, smaller methane adsorption capacity, fewer stored methane molecules, and relatively fewer gas sources during the release process, and the closer it is to the intrusion, the lower the volatile matter, the smaller the total emission. However, the porosity, total pore length, and pore number of the macropores and mesopores of thermally contacted metamorphic

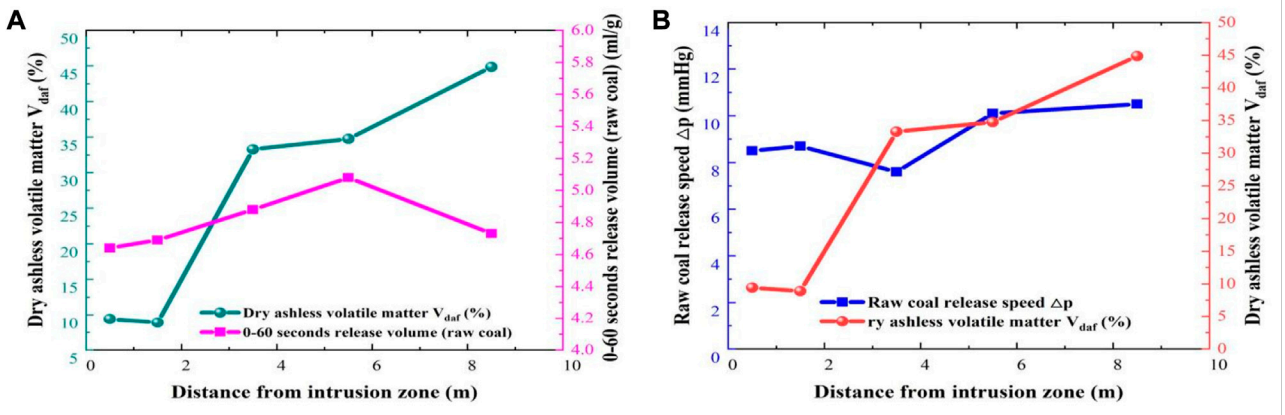

FIGURE 11
Variation of Δp value and total gas emission in 0–60s of coal in igneous rock intrusive zone.

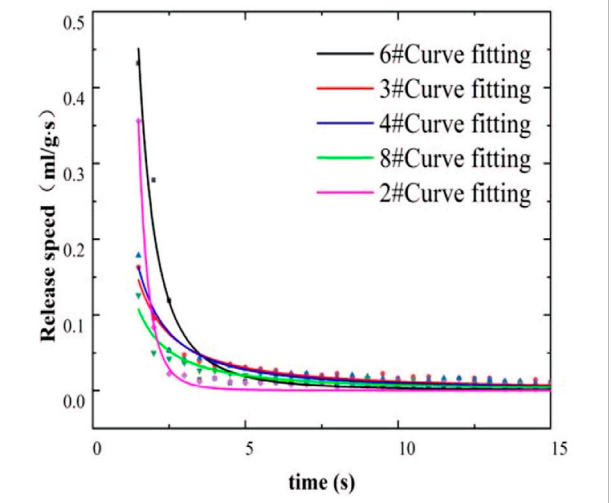

FIGURE 12
Curve of gas emission velocity of raw coal.

coal are larger than those of normal coal. It has more developed migration channels, and methane molecules have little resistance to movement, resulting in a violent gas emission in a few seconds before the test, followed by a rapid decay.

Mathematical characterization of gas emission from metamorphic coal

The gas emission velocity curve of the raw coal can well conform to $Vt=V_1t^{-\alpha}$, and the fitted curve is shown in Figure 12 (Fu, 2006; Zhao et al., 2022; Zhu et al., 2022). The V_1 is defined as the gas emission velocity in the first second, and the α is defined as the attenuation coefficient. The curve of V_1 *via* V_{daf} is shown in Figure 13, with fitting formula of Eq. 13, and $R^2$of 0.98. The V_1 value of the 2# and 6# coal samples is significantly larger than that of the other coal samples. With the increase of volatile matter, the V_1 decreases monotonically, satisfying the quadratic nonlinear relationship.

$$V_1 = 0.62 - 0.02V_{daf} + 2.4 \times 10^{-4}V_{daf}^2 \quad (13)$$

The relationship of α value and the volatile content are fitted linearly, as shown in Figure 14. The fitted formula is shown in Eq. 14. The value of α decreases linearly with the increase of volatile content.

$$\alpha = 2.6 - 0.04V_{daf} \quad (14)$$

Microscopic interpretation of gas emission from the metamorphic coal

When the covering layer of the coal seam is thin, the shallow intrusive bodies such as rock walls, dykes, and rock beds contact or intrude into the coal seam. Because of their high temperature, volatile matter and pressure, and the coal undergoes thermal contacted metamorphism. After the water and volatiles are gasified and released, the coal is rapidly cooled and transformed into natural coke and highly metamorphic coal. This rapid heating process is similar to the coking process. On the one hand, the gasification of volatiles causes the formation of pores in the coal body, on the other hand, the gasification of volatiles escapes to form more throats or pores to connect the pores with each other. Rapid cooling makes these structures fully retained, resulting in the development of macropores and mesopores with complex, long - narrow pore shape, and greater connectivity. For the same gas content, the gas release

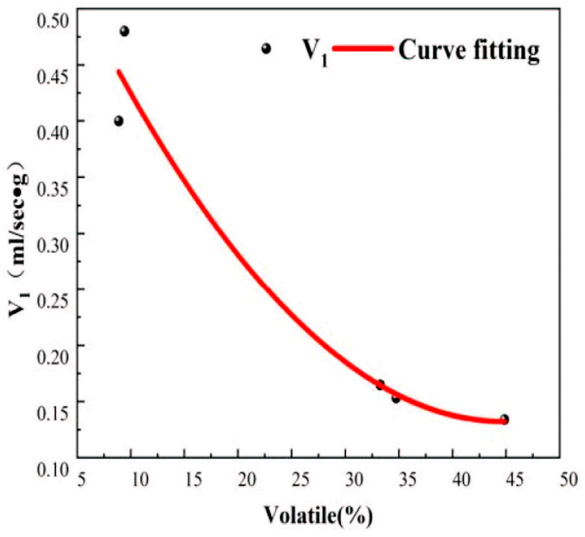

FIGURE 13
Fitting curve of V_1 value of coal sample in igneous intrusion zone.

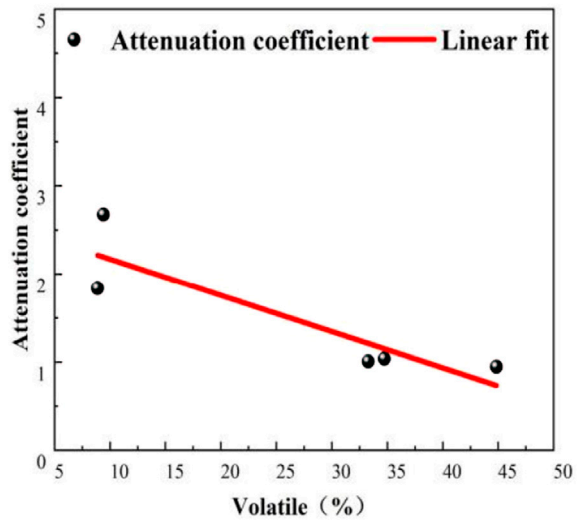

FIGURE 14
Fitting curve of attenuation coefficient values of coal samples in igneous intrusion zone.

rate is faster in a short period of time (0–1 s), the V_1 value is larger, and the inflection point decays earlier (within 2 s), which increases the amount of released gas in the second and third stages. In the cooling process after thermal contacted metamorphism, re-compaction causes the micropores to shrink, and the micropore volume and specific surface decrease, resulting in a decrease in the adsorption capacity. This is manifested as a smaller Δp value. On the contrary, the normal coal sample has stronger adsorption capacity and can store more methane molecules, but the development of macropores and mesopores is relatively poor, and it cannot escape quickly within a few seconds. The decay is slow, but more gas can be released within 0–60 s, showing a larger Δp value.

When coal and gas outbursts occur, the gas release capacity in a very short period of time will play a more significant role in promoting the outbursts. In actual production, if the Δp value is used to characterize the gas emission rate of thermally contacted metamorphic coal, there may be a phenomenon that the Δp value does not exceed the critical value, but still has outstanding danger. In particular, when thermally contacted metamorphic coal is affected by tectonic stress and is in a high stress and high gas pressure area, the microporous system can still store enough methane molecules, and it is very prone to outburst during mining. Therefore, it is more reasonable to use the V_1 index to measure the gas emission rate of thermally contacted metamorphic coal.

Conclusion

1) As the distance from the igneous rock intrusion decreases, the volatile matter and water content tend to decrease, and the ash content gradually increases. The direct contacted position generates natural coke and high metamorphic coal.
2) The PCAS analysis on porosity and pore quantity index of thermal contacted metamorphic coal show that there is no obvious difference of small pores between metamorphic coal and normal coal, while the large and medium pores in metamorphic coal are generally larger than the that of normal coals. The pore volume and specific surface area of micropores decrease significantly, and the adsorption capacity is weakened. The total pore length and average shape factor of macropores and mesopores in per unit area of thermally contacted metamorphic coals increase compared with normal coals, indicating better connectivity among pores.
3) V_1 and volatile matter conform to a parabolic equation, and V_1 decreases monotonically with the volatile matter. The decay coefficient α value has a linear relationship with the volatile matter, and the α value decreases linearly with the volatile matter.
4) Micropore shrinkage in thermal contacted metamorphic coal leads to a decrease in the total amount of gas emission and Δp value in 0–60 s but the development of macropores and mesopores will form more throat pores, and initially sharp increase of the emission amount. And the emission amount within 1 s accounts for the total amount of emission is larger than other samples. The inflection point appears earlier, the attenuation is faster, and the gas emission ability is enhanced within a few seconds, namely the V_1 value increases.

5) In field applications, it is more reasonable to use the V_1 index, the gas emission velocity in the first second, to characterize the gas emission rate of thermally contacted metamorphic coal.

Data availability statement

The original contributions presented in the study are included in the article/Supplementary Material, further inquiries can be directed to the corresponding author.

Author contributions

XF, as an industry expert, guided and completed the overall content of the paper and provided relevant experimental conditions. HL is the main writer of the paper, and is responsible for completing the sampling, SEM experiments, gas emission experiments and data analysis. HS assisted in the completion of the SEM experiment and the gas emission experiment, and assisted in the completion of the relevant data processing. ZW provided guidance on scanning electron microscopy and microscopic analysis as an instructor, and provided great support for the completion of the thesis. XL completed the fractalization of SEM images, applied computer software to carry out PCAS analysis, and researched and analyzed the data.

Funding

This research was financially supported by the National Natural Science Foundation of China (Grant Nos. 52174117, 52004117), and the project supported by the discipline innovation team of Liaoning Technical University (Grant No. LNTU20TD-30).

Acknowledgments

The author(s) would like to thank all editors and reviewers for their comments and suggestions.

Conflict of interest

The authors declare that the research was conducted in the absence of any commercial or financial relationships that could be construed as a potential conflict of interest.

Publisher's note

All claims expressed in this article are solely those of the authors and do not necessarily represent those of their affiliated organizations, or those of the publisher, the editors and the reviewers. Any product that may be evaluated in this article, or claim that may be made by its manufacturer, is not guaranteed or endorsed by the publisher.

Supplementary material

The Supplementary Material for this article can be found online at: https://www.frontiersin.org/articles/10.3389/feart.2022.1040147/full#supplementary-material

References

Arora, A., Dutta, S., Gogoi, B., and Banerjee, S. (2017). The effects of igneous dike intrusion on organic geochemistry of black shale and its implications: Late Jurassic Jhuran Formation, India. *Int. J. Coal Geol.* 178, 84–99. doi:10.1016/j.coal.2017.05.002

Barone, A., and Sen, M. K. (2018). A new Fourier azimuthal amplitude variation fracture characterization method: Case study in the Haynesville Shale. *Geophysics* 83, WA101–WA120. doi:10.1190/geo2017-0030.1

Fan, C., Wen, H., Sun, H., Zhou, L., Zhang, X., Zhu, C., et al. (2022). Experimental investigation on the effect of loading and unloading on coal permeability with different sediment beddings. *Lithosphere*, 2022, 9949201. doi:10.2113/2022/9949201

Fan, C., Yang, L., Wang, G., Huang, Q., Fu, X., and Wen, H. (2021). Investigation on coal skeleton deformation in CO2 injection enhanced CH4 drainage from underground coal seam. *Front. Earth Sci. (Lausanne).* 9, 766011. doi:10.3389/feart.2021.766011

Fu, H., Tang, D., Xu, T., Xu, H., Tao, S., Li, S., et al. (2017). Characteristics of pore structure and fractal dimension of low-rank coal: A case study of lower jurassic XiShanYao coal in the southern junggar basin, NW China. *Fuel* 193 (1), 254–264. doi:10.1016/j.fuel.2016.11.069

Fu, X., (2006). Experimental study on gas instantaneous release velocity index V_1 under minimum outburst pressure. *Coal Mine Safety* (09), 4–6.

Huoduote, B. B. (1966). *Coal and gas outburst*. Editor S.-Z. Song and Y.-A. Wang (Beijing: China Industry Press).

Hwang, J., and Pini, R. (2019). Supercritical CO_2 and CH_4 uptake by illite-smectite clay minerals. *Environ. Sci. Technol.* 53 (19), 11588–11596. doi:10.1021/acs.est.9b03638

Kandasami, R. K., and Murthy, T. G. (2017). Manifestation of particle morphology on the mechanical behaviour of granular ensembles. *Granul. Matter* 19 (2), 21–13. doi:10.1007/s10035-017-0703-z

Li, X., Xia, M., Dong, X., Long, R., Liu, Y., Huang, Y., et al. (2022). High mechanical properties of stretching oriented poly(butylene succinate) with two-step chain extension. *Polymers* 47 (05), 1876–1889. doi:10.3390/polym14091876

Lin, Q., Jiajia, Y., Jian, Z., and Zhigang, C. (2016). Microstructure study on intact clay behavior subjected to cyclic principal stress rotation. *Procedia Eng.* 143, 991–998. doi:10.1016/j.proeng.2016.06.088

Liu, B., Yi, L. U., Liu, C., Gu, K., and Shu, R., (2017). Extraction technology of sandy soil microstructure during compression. *J. Eng. Geol.*, 25, 968–974. doi:10.13544/j.cnki.jeg.2017.04.010

Liu, C., Shi, B., Zhou, J., and Tang, C. (2011). Quantification and characterization of microporosity by image processing, geometric measurement and statistical methods: Application on SEM images of clay materials. *Appl. Clay Sci.* 54 (1), 97–106. doi:10.1016/j.clay.2011.07.022

Liu, J., and Wang, Z. (2013). The effect of coal metamorphism on the initial velocity of gas release. *J. Liaoning Tech. Univ. Sci. Ed.* 32 (06), 745–748. doi:10.3969/j.issn.1008-0562.2013.06.006

Luo, Z. (1989). Study on the relationship between coal specific surface area and coal and gas outburst. *Chin. J. Coal* (01), 44–54. doi:10.1007/BF02005959

Qiang, Bi (2017). Study on coal spontaneous combustion characteristics and prevention technology under the condition of igneous rock intrusion in Daxing Mine. *Liaoning Tech. Univ.*. Doctoral dissertation, 150.

Ren, J., Mao, X., and Fu, S. (2021). Image-based flow decomposition using empirical wavelet transform. *J. Fluid Mech.* 906, A22. doi:10.1017/jfm.2020.817

Song, Y., Yang, S., Xu, Q., Cai, J., Hu, X., Sang, N., et al. (2019). Effect of low-temperature oxidation of coal with different metamorphic degrees on coal quality characteristics and outburst comprehensive index. *Process Saf. Environ. Prot.*, 132, 142–152. doi:10.1016/j.psep.2019.10.009

Teicherta, Z., Ebleb, C. F., Bosea, M., and Williamsa, L. B. (2022). Effects of contact metamorphism on the lithium content and isotopic composition of kerogen in coal. *Chem. Geol.* 602, 120885. doi:10.1016/j.chemgeo.2022.120885

Wang, F., (2015). Research on the influence of magmatic intrusion on coal properties in Daxing Coal Mine. *Coal Sci. Technol.* 43 (12), 61–65+71. doi:10.13199/j.cnki.cst.2015.12.013

Wang, H., Li, T., Zou, Q., Cheng, Z., and Yang, Z. (2020). Influences of path control effects on characteristics of gas migration in a coal reservoir. *Fuel* 267, 117212. doi:10.1016/j.fuel.2020.117212

Wang, H., Yong, Z., Zhang, X., Ran, B., Yang, D., Luo, C., et al. (2016). Depositional environment and micropore characteristics of the ediacaran doushantuo formation black shale in western hubei, China. *Arabian J. Geosciences* 9 (5), 1–13. doi:10.1007/s12517-016-2408-8

Wang, K., Peng, C., Pan, J., Wan, X., Zheng, D., and Lv, R. (2017). Pore structure characteristics of coal-bearing organic shale in Yuzhou coalfield, China using low pressure N-2 adsorption and FESEM methods. *J. Pet. Sci. Eng.* 153, 234–243. doi:10.1016/j.petrol.2017.03.043

Wang, W., Hong, L., Gao, D., Lun, J., et al. (2021). Filling characteristics of the micropores in coals with different metamorphic degrees. *AIP Adv.*, 11, 125016. doi:10.1063/5.0070299

Wenjuan, S., Wang, L., and Tutumluer, E. (2018). Image analysis technique for aggregate morphology analysis with two-dimensional fourier transform method. *Transp. Res. Rec.* 2267 (1), 3–13. doi:10.3141/2267-01

Yang, Y., Sun, J., Li, Z., Zhang, X., Liu, L., Yan, D., et al. (2018). Influence of soluble organic matter on mechanical properties of coal and occurrence of coal and gas outburst. *Powder Technol.* 332, 8–17. doi:10.1016/j.powtec.2018.03.053

Zhang, Y., Chen, L., Zhao, J., Deng, J., and Yang, H. (2019). Evaluation of the spontaneous combustion characteristics of coal of different metamorphic degrees based on a temperature-programmed oil bath experimental system. *J. Loss Prev. Process Industries* 60, 17–27. doi:10.1016/j.jlp.2019.03.007

Zhao, B., Wen, G., Nian, J., Ma, Q., Fan, C., Lv, X., et al. (2022). Numerical simulation study on the multi-physical field response to underground coal and gas outburst under high geo-stress conditions. *Minerals* 12, 151. doi:10.3390/min12020151

Zhao, D., Guo, Y., Wang, G., Jiao, W., Liu, J., Hai, Y., et al. (2020). Quantitative characterization of nano-scale pores in shale reservoirs of Wufeng-Longmaxi formation based on image processing. *Fresenius Environ. Bull.* 29 (5), 3992–3999.

Zhao, J., Xu, H., Tang, D., Mathews, J. P., Li, S., and Tao, S. (2016). A comparative evaluation of coal specific surface area by CO2 and N2 adsorption and its influence on CH4 adsorption capacity at different pore sizes. *Fuel* 183 (1), 420–431. doi:10.1016/j.fuel.2016.06.076

Zhao, L., Qin, Y., Cai, C., Xie, Y., Wang, G., Huang, B., et al. (2017). Control of coal facies to adsorption-desorption divergence of coals: A case from the xiqu drainage area, gujiao cbm block, North China. *Int. J. Coal Geol.*, 171, 169–184. doi:10.1016/j.coal.2017.01.006

Zhao, S., Chen, X., Li, X., Qi, L., and Zhang, G. (2021). Experimental analysis of the effect of temperature on coal pore structure transformation. *Fuel* 305, 121613. doi:10.1016/j.fuel.2021.121613

Zhou, L., Zhou, X., Fan*, C., and Bai, G. (2022). Coal permeability evolution triggered by variable injection parameters during gas mixture enhanced methane recovery. *Energy* 252, 124065. doi:10.1016/j.energy.2022.124065

Zhu, H., Huang, C., Ju, Y., Bu, H., Li, X., Yang, M., et al. (2021). Multi-scale multi-dimensional characterization of clay-hosted pore networks of shale using FIBSEM, TEM, and X-ray micro-tomography: Implications for methane storage and migration. *Appl. Clay Sci.* 213, 106239. doi:10.1016/j.clay.2021.106239

Zhu, Z., Wu, Y., and Han, J. (2022). A prediction method of coal burst based on analytic hierarchy process and fuzzy comprehensive evaluation. *Front. Earth Sci.* 9, 834958. doi:10.3389/feart.2021.834958

frontiers | Frontiers in Earth Science

TYPE Original Research
PUBLISHED 09 January 2023
DOI 10.3389/feart.2022.1083489

OPEN ACCESS

EDITED BY
Yu Song,
China University of Mining and Technology, China

REVIEWED BY
Quanzhong Guan,
Chengdu University of Technology, China
Bo Zhao,
Taiyuan University of Technology, China
Lei Zhang,
China University of Mining and Technology, China

*CORRESPONDENCE
Zhijia Zhang,
lntukyxyzzj@163.com

SPECIALTY SECTION
This article was submitted to Economic Geology, a section of the journal Frontiers in Earth Science

RECEIVED 29 October 2022
ACCEPTED 01 December 2022
PUBLISHED 09 January 2023

CITATION
Lan T, Zhang Z, LE QB, Liu Y and Wang S (2023), Study on the influence of the tectonic evolution of Shuangyashan Basin on gas occurrence and extraction in mines.
Front. Earth Sci. 10:1083489.
doi: 10.3389/feart.2022.1083489

Study on the influence of the tectonic evolution of Shuangyashan Basin on gas occurrence and extraction in mines

Tianwei Lan, Zhijia Zhang*, QUY BAO LE, Yonghao Liu and Shunxiang Wang

College of Mining, Liaoning Technical University, Fuxin, China

The formation and later evolution of coal-bearing basins in eastern Heilongjiang are controlled by multi-phase tectonic movements, and the Shuangyashan Basin is tectonically located at the southern end of the Sanjiang Basin in the northeast. The paper focuses on the regional geological and tectonic evolution of the Shuangyashan Basin and its influence on the gas occurrence law and extraction difficulty of the Jixian Coal Mine. The study determined that the gas occurrence of the mine in the Suibin-Jixian depression basin has regional aggregation and caprock sealing characteristics. The gas pressure and content of the 9# Coal Seam were measured in the underground test, and the results showed that the 9# coal seam is a hard-to-extract coal seam with low permeability. Aiming at the issue of hard-to-extract gas in 904 Working Face of 9# Coal Seam which is affected by depression basin and derived secondary tectonic conditions, numerical calculation and analysis of gas extraction effect of working face with different extraction parameters were carried out by COMSOL software, the results showed that: negative extraction pressure has less influence on gas extraction effect under basin conditions; when 113 mm diameter borehole is used for gas extraction, gas pressure decreases to 0.72 MPa; when the spacing of extraction borehole is 2 m, the gas pressure is reduced by 20%; when the coal seam permeability is increased by 10 times to more than 0.015 mD, the gas pressure is reduced by more than 50%. The optimized gas extraction scheme with 113 m diameter, 2 m borehole spacing, and 15 kPa negative pressure was proposed for the test working face, and combined with supercritical CO_2 fracturing and permeability enhancement technology. Under underground measurement, the coal seam gas content was reduced by 39.7% compared to the original gas extraction scheme. It can be seen that the reasonable gas extraction scheme and coal seam pressure relief and permeability enhancement technology can significantly improve the gas extraction rate, and the extraction effect is remarkable.

KEYWORDS

tectonic evolution, depression basin, low permeability coal seam, gas extraction, supercritical CO2 fracturing

1 Introduction

Coal seam gas is a product of geological action (Dazhen et al., 2021). The regional tectonic background and its evolution control the formation and distribution of coalbed methane accumulation zones (Liu et al., 2022). The mine structure controls the gas zoning characteristics, and the working face structure determines the local gas enrichment area and outburst dangerous area (Zhang et al., 2022a). As a typical geological tectonic, the basin is formed under the action of crustal tectonic movement. The stratum is squeezed or stretched, a downward bending fracture occurs, and its internal structure is damaged to varying degrees. Under the influence of basin conditions, regional coalfields will be in the scope of certain closed-type tectonic traps, which are mostly reserved with low permeability hard-to-extract coal seams (Liu et al., 2021). In addition, the thickness of the overlying strata in the depression basin increases, which acts as a sealing cap for the gas occurrence in the lower coal seams, effectively blocking the gas migration and diffusion, resulting in a sharp increase in the gas content of the coal seams. Liu Li et al. proposed the gas occurrence characteristics of Cambrian-Ordovician shale in the Tarim Basin. The research results enriched the theory of marine shale gas accumulation and provided theoretical guidance for the "three depressions and four uplifts" model of marine shale (LIU et al., 2018). He Shuxian et al. discussed the influence of fracture development characteristics on gas quantity under the conditions of the Sichuan Basin. The study found that fracture development provides a channel for gas desorption, and the free gas content in the fracture development section accounts for more than 55% of the total gas content (He et al., 2022a). Therefore, there is an urgent need to extract the gas generated during coal mining under basin conditions. The coal permeability is directly related to the extraction efficiency and attainment time of coal seam gas under basin conditions (Zou et al., 2022). Domestic and foreign scholars simulated the transient changes of coal permeability by proposing the intrinsic constitutive equation on the scale of fractured coal (Abouloifa et al., 2021), proposed a new coal seam permeability measurement method based on considering the equivalent scale characteristics of coal matrix-fracture structure, effective stress, and matrix adsorption-induced strain permeability evolution model, and verified the reliability of the new method by comparing with field test data (Guo et al., 2021). For other gas extraction parameters, Huihuang Fang used the Hudi Coal Mine in the Qinshui Basin as the study area to analyze the overlying load differences in gas pressure distribution and factors affecting the effective extraction radius and found that extraction time, extraction borehole diameter, extraction negative pressure, permeability and effective extraction radius were exponentially related based on COMSOL simulation (Fang et al., 2022).

Many studies have been done by domestic and foreign scholars on the characteristics of gas occurrence in basin conditions and optimization of gas seepage characteristics and extraction parameters in mines, and a lot of results have been achieved. However, there are few studies on gas extraction in which the gas occurrence is characterized by regional aggregation and caprock sealing due to the influence of the depression basin. Based on the regional geological and tectonic evolution of the Shuangyashan basin and the study of the gas occurrence law and extraction difficulty of the Jixian Coal Mine, this paper determines that the coal seam belongs to the hard-to-extract coal seam with low permeability, and proposes the gas extraction technology and gas extraction optimization scheme by applying supercritical CO_2 fracturing to pressure relief and permeability enhancement. The research results provide theoretical and technical guidance for coal seam gas extraction technology under basin conditions.

2 Analysis of tectonic evolution of the Shuangyashan Basin and its influence on mine gas occurrence

2.1 Tectonic evolution of the Shuangyashan Basin

The tectonic framework of the coal-bearing basin group in eastern Heilongjiang is a product of the overlapping of the Paleo-Asian Ocean tectonic domain and the Marginal-Pacific tectonic domain and the transformation to the Marginal-Pacific tectonic domain (Zhao et al., 2022). Basin formation and later evolution are controlled by multi-phase tectonic movements, which are the main driving force for the development of the Eastern Basin Group. The coal-bearing basin is a dustpan-shaped structure in the longitudinal section, which is deep in the south and shallow in the north, steep in the south, and gentle in the north. Jixi Basin, Boli Basin, and Sanjiang Basin are distributed in order from south to north in their structural positions. Shuanghua Basin and Shuangyashan Basin are formed at the southern end of the Sanjiang Basin due to the Huanan Uplift, as shown in Figure 1A.

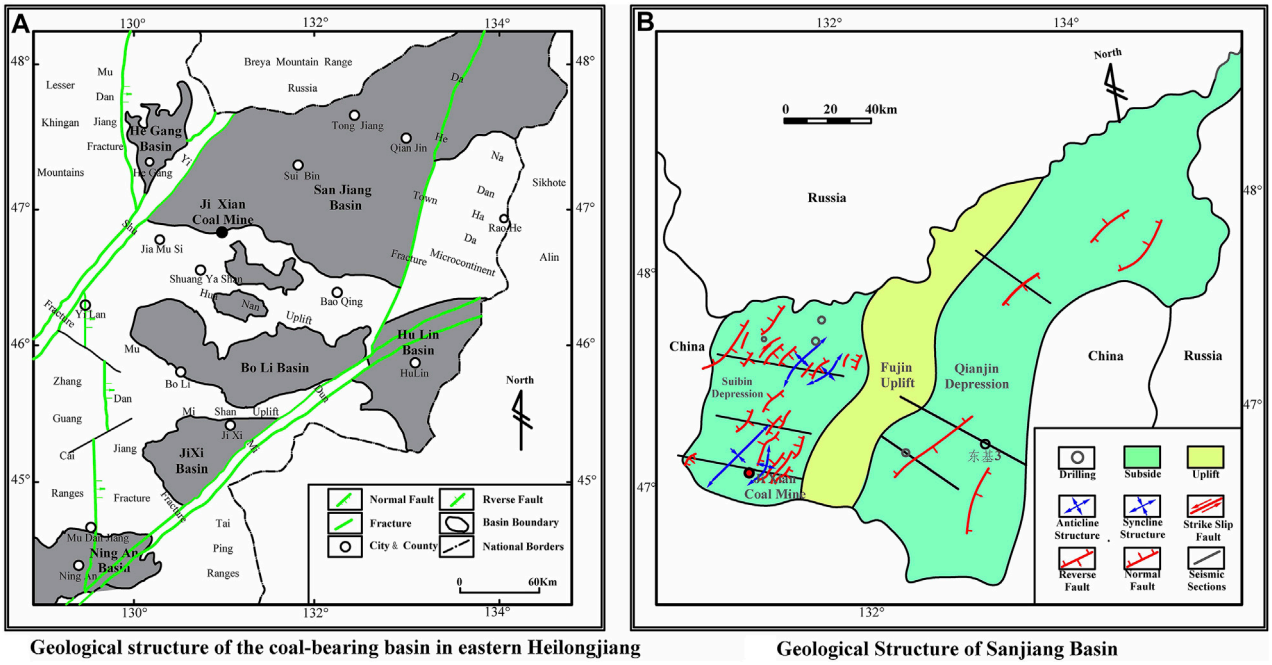

FIGURE 1
Structural evolution of eastern Heilongjiang Basin.

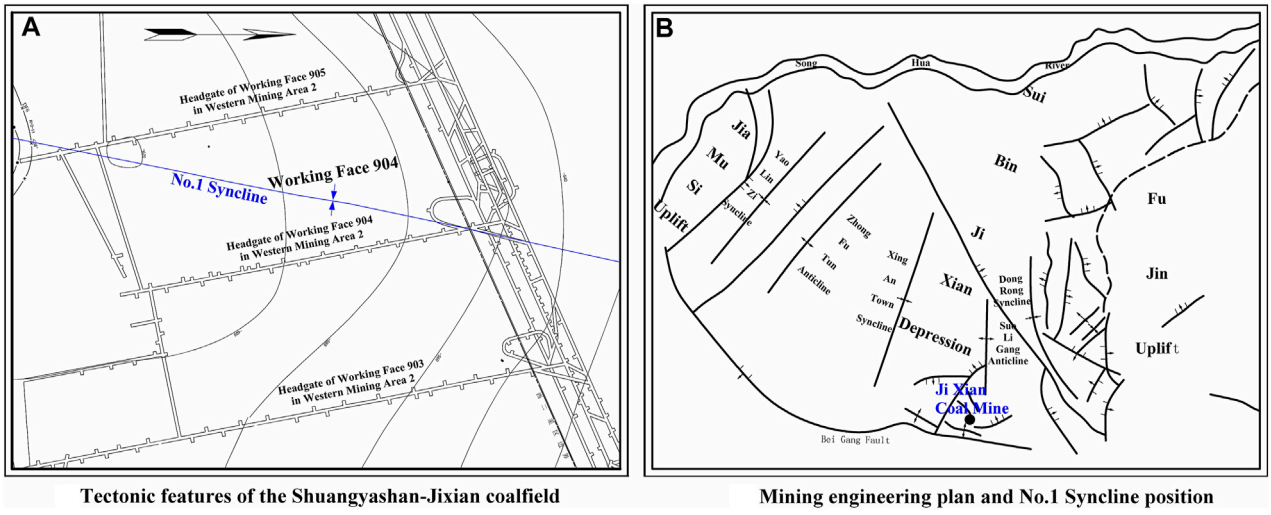

FIGURE 2
Structural features of Jixian Coalfield and mining engineering plan of study area.

The Sanjiang Basin is mainly spreading in a north-easterly direction, consisting of the Suibin Depression, the Fujin Uplift, and the Qianjin Depression from west to east (GUO and WANG, 2008), as shown in Figure 1B. In the late Early Cretaceous, the Suibin Depression underwent strong alluvial-fold deformation, with massive uplift and intense denudation of the basin, a process that probably continued until the Paleogene rift, and since the Cenozoic, the Suibin Depression has undergone weak extension and subsidence, resulting in the present-day tectonic landscape. It can be seen that the Suibin Depression in the Sanjiang Basin generally shows the basin characteristics of superposition of multi-

phase extrusion and extensional deformation, while the Shuangyashan-Jixian coalfield in the study area is located at the edge of the Suibin Depression basin.

2.2 Geological and tectonic evolution of the Jixian Coalfield

The Jixian Coalfield is located in the Suibin-Jixian Depression Basin, which ranges from the Jiamusi Uplift in the west to the Fujin Uplift in the east. The coal measure strata are generally a north-dipping syncline structure, with steep western flanks and gentle eastern flanks. Secondary structures are developed in each uplift zone and depression zone. In the southern part of the Suibin-Jixian Depression, there are the Dongrong Syncline, Suoligang Anticline, Xinganzhen Syncline, Zhongfutun Anticline, and Yaolinzi Syncline, which play a controlling role in the tectonic framework of the Jixian Coalfield. The Sujiadian-Bijiashan Fault on the southwestern edge of the coalfield is obliquely connected with the near east-west Beigang Fault, forming an "arc structure" in the local area. Jixian coal mine is located in the south of the Jixian coalfield, which is part of the Shuangyashan Jixian coalfield, as shown in Figure 2A.

2.3 Analysis of the coal seam gas occurrence in the Jixian Mine

Jixian Coal Mine is located in the north wing of the Jixian Syncline between the Soligang Anticline and the Jixian Anticline in the depression zone. The thickened coal seam in the center of the depression basin forms a good caprock sealing to the gas enrichment area below (Wang et al., 2021a), leading to a further increase in gas content. At the same time, due to the influence of the latitudinal tectonic system, the area is subjected to north-south extrusion. The Beigang Fault lifts the southern wing of the Jixian Syncline, weathering, and denudation, while the northern wing is preserved, forming a monoclinic structure with strata striking nearly east-west and small folds developing locally due to the cutting of the fault. The complex geological and tectonic conditions in the wellfield play a controlling influence on the regional accumulation of gas in the mine.

The mineable coal seam in Ji Xian Wellfield is Chengzihe Group, the main mining nine# coal seam, the depth of the coal seam buried is 689 m; and the roof and floor of the coal seam are more stable, with mostly fine sandstone and siltstone of poor permeability, which plays an obstructive and sealing role in the migration of gas. With the increase of mining depth, the high gas area has appeared underground, the measured gas content has been as high as 14.72 m^3/t, and the absolute gas emission from the working face has been as high as 20 m^3/min.

Under the influence of the geological and tectonic conditions of the Suibin-Jixian Depression Basin, the Jixian mining area is subject to greater radial extrusion stress, the fissures of the coal rock body are compressed and dense, the permeability is significantly reduced, the gas is difficult to migrate in the vertical direction, blocking the communication fissure channels between the deep coal seam gas and the surface, which plays a closed role in the coal seam gas, resulting in deep coal seam with high gas content.

3 Gas parameter test and occurrence characteristics analysis of working face

3.1 West mining area 2 904 working face general situation

To better analyze the gas occurrence characteristics of the Jixian Coal Mine under the conditions of the Suibin-Jixian Depression Basin, the 904 Working Face of the 9# coal seam in the West Mining Area 2 of the Jixian Coal Mine was selected as the research area. The 904 Working Face is located at the -450 m level of the mine, geographically located in the eastern part of the West Mining Area 2. The northern part of the Working Face is the West No. Two mining area track downhill, the southern part is the Beigang Fault, the western part is the West No. Two Mining Area 905 Preparation Working Face, and the eastern part is the West No. Two Mining Area 903 Goaf. 904 Working Face mining engineering plane diagram is shown in Figure 2B. The No. One Syncline of the Jixian Mine is located in the West Mining Area 2, with an axial direction of nearly north-south and an axial length of about 1.6 km, and the No. 904 Working Face is located in the southern central axis of the No. One Syncline.

3.2 Testing of gas parameters at working face 904 in west mining area 2

Based on the influence of the above depression basin conditions on the characteristics of mine gas occurrence, the researchers conducted underground tests on the basic parameters of 9 # coal seam gas in the 904 Working Face of the West Mining Area 2 of Jixian Coal Mine, mainly including gas pressure, gas content, borehole flow attenuation coefficient, permeability coefficient, and other indicators. The test results are shown in Table 1.

According to the underground test results, it can be seen that the 9# coal seam studied in this paper has a poor pore development degree, the ultimate adsorption a value of gas is 26.237 m^3/t, the permeability coefficient of the coal seam is 0.06 $m^2/(MPa^2 \bullet d)$, the maximum gas pressure of the coal seam at the measurement point is 0.22 MPa, and the 9#coal seam is determined to be the hard-to-extract coal seam with low permeability.

TABLE 1 Test results of gas parameters at working face of nine# Coal Seam in West Mining Area 2.

Testing/Sampling location	Test parameters	Test value	
150 m in front of the setup room of 904 Working Face	Gas adsorption constant	a (m3/t)	26.237
		b (MPa−1)	0.335
904 Working Face middle roadway	Residual gas content of coal seam (m3/t)	3.67	
904 Working Face middle roadway	The maximum gas pressure of the coal seam at the measurement point (MPa)	0.22	
450 m from the headgate of 906 Working Face	Borehole gas flow decay coefficient (d−1)	0.2142	
450 m from the headgate of 905 Working Face	Coal seam permeability coefficient m2/(MPa2·d)	0.06	
50 m in front of the setup room of 904 Working Face	Gas release initial velocity index	7.1	
150 m in front of the setup room of 904 Working Face		7.9	

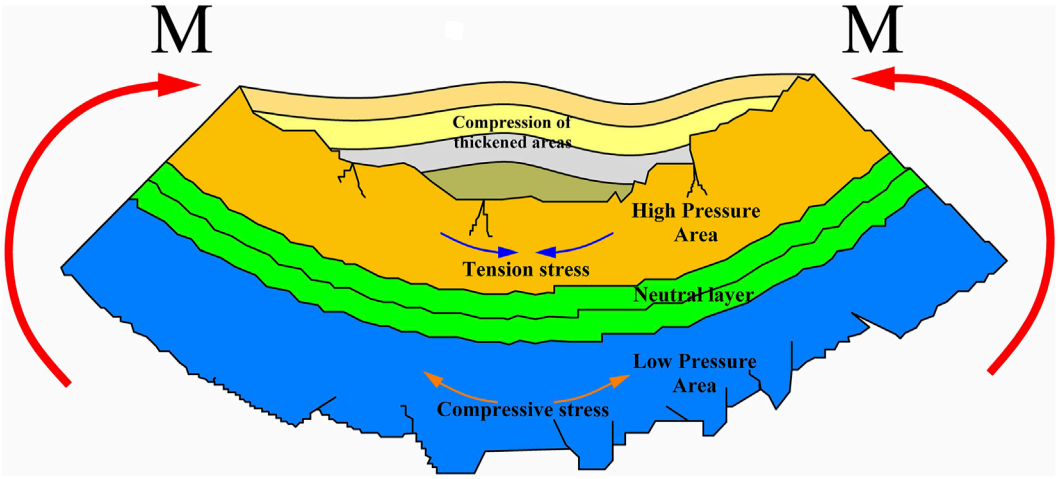

FIGURE 3
Schematic diagram of pressure zoning of the synclinal structure.

3.3 Analysis of gas occurrence characteristics in the working face

Under the influence of the regional depression basin conditions, secondary derivative structures exist at the working face of the Jixian Coal Mine, resulting in the regional aggregation characteristics of the mine gas occurrence. According to Figure 2B, taking 904 Working Face in the West Mining Area 2 as an example, during the formation of the Suibin-Jixian Depression Basin, No. One Syncline structure was derived from the working face, resulting in shearing of the coal seam as a soft layer and bending of the surrounding rocks as a hard layer, the primary surface of the coal seam was damaged by splitting under shearing and plastic sliding along the syncline axis, and the interlayer sliding further damaged the primary structure of the coal seam, metamorphosing it into an extremely soft or loose tectonic coal (Zhang et al., 2022b), which increases the adsorption capacity of the coal body and traps more gas in the coal seam.

Under the action of tectonic stress, the two wings of the No.1 Syncline structure of the 904 Working Face and the axis are above the neutral layer as a high-pressure zone, and below the neutral layer forms a relatively low-pressure zone, as shown in Figure 3. The non-uniformity of the stress state on both sides bounded by the neutral layer determines the zoning characteristics of the gas in the working face (Yuan et al., 2020). In addition, the upper compression thickening of the syncline makes the fractures and pores in the coal-rock mass compacted, reducing the lower gas seepage and escape; the lower layer of syncline structure produces tensile fracture or fracture surface under the action of tension, and the joints and micropores in the coal body are expanded. The expansion of space reduces the desorption pressure and forms a good gas accumulation space, which is helpful for the

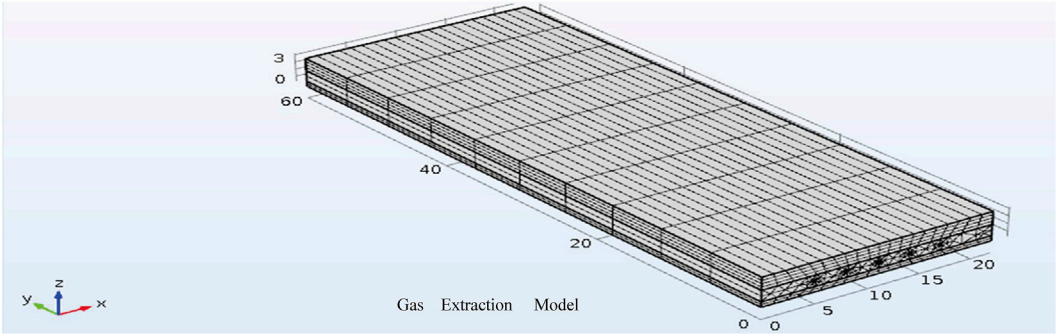

FIGURE 4
Gas extraction model diagram.

TABLE 2 Numerical simulation base parameters of the original extraction scheme.

Parameters	Numerical value	Parameters	Numerical value
Coal seam thickness H1	1.5 m	Length of working face	194 m
Direct floor thickness H2	0.7 m	Strike length	410 m
Direct roof thickness H3	1.7 m	Gas pressure (av. value)	1.09 MPa
Slippage factor b	0.76 MPa	Gas dynamic viscosity μg	1.84×10−5 Pa s
Sealing length	10 m	Borehole length	140 m、60 m
The dip angle of coal seam	9°	Porosity	0.063
Permeability	0.0015mD	Borehole spacing	3 m
Langmuir pressure constant PL	2.985 MPa	coefficient of horizontal pressure	0.8、1.5
Langmuir volume parameter VL	0.026237 m3/kg	Gas desorption References temperature Tt	300 K
Coal seam gas content	4.5 m3/t (2.3–6.6 m3/t)	Borehole distance from coal seam floor h1	0.8 m
Overlying strata stress	17 MPa–18.5 MPa (680m–730 m)	Biot effective stress coefficient α	0.92

desorption of adsorbed gas in coal seams. Therefore, the depression basin not only affects the gas content of the mining area but also derives the secondary structure of the working face under the condition of the depression basin, which together affects the zoning of the gas content in the mining area and the difference of the gas content in the working face.

4 Simulation analysis of gas pre-drainage effect on working face

4.1 Establishment of a numerical model of the extraction system

According to the test results of the underground gas parameters of the 904 Working Face in the West Mining Area 2, gas pre-drainage must be carried out in the 904 Working Face in the West Mining Area 2. To better test the effect of gas pre-drainage in the working face, the corresponding extraction system model was established using COMSOL software according to the layout of the working face and the layout of extraction boreholes, with the model size of 60 m x 25 m x 3 m, as shown in Figure 4.

Based on the original gas extraction scheme for the 904 Working Face in the West Mining Area 2 of the Jixian Coal Mine, the base parameters for the numerical simulation were determined, as shown in Table 2.

The simulation specifically investigates the effect of different extraction parameters (extraction negative pressure, borehole diameter, borehole spacing, and permeability) on the gas extraction effect of the working face, and a total of four sets of extraction parameters are designed for the comparison scheme (only the corresponding extraction parameters are changed,

TABLE 3 Comparison scheme of different gas extraction parameters.

Parameters Group	Scheme 1	Scheme 2	Scheme 3	Scheme 4
	Extraction negative pressure/kPa	Borehole diameter/mm	Borehole spacing/m	Permeability increase multiplier
1	15	64	1	10
2	20	94	2	20
3	25	113	3	50
4	30	130	4	100

other parameters are the same as the original scheme). The numerical simulation parameters of the comparison scheme are shown in Table 3.

According to the ⟪Interim Provisions for Coal Mine Gas Extraction to Meet Standards⟫: "If the coal seam gas content or pressure at the depth of the initial coal seam outburst is not examined, the coal seam gas pressure is reduced to less than 0.74 MPa" Using 0.74 MPa as the extraction requirement for the study of gas pre-extraction.

4.2 Effect of different extraction parameters on gas pre-drainage in working face

4.2.1 Effect of negative extraction pressure on the effectiveness of gas extraction

The extraction negative pressure and the coal seam gas pressure form the pressure gradient in the coal body together, which provides the power for the gas flow (Wang et al., 2021b). The practice has proved that too high or too low extraction negative pressure will seriously affect the extraction effect. Only by combining the characteristics of coal seam gas occurrence can we determine a reasonable negative pressure interval suitable for the extraction of this coal seam. Figure 5A shows the gas pressure curves of different extraction negative pressures from extraction to 360 days. It can be seen from the diagram that when the negative pressure of extraction increases or decreases, the gas pressure value does not change. It shows that the change in extraction negative pressure is not the main factor affecting the effect of gas extraction in the depression basin.

4.2.2 Effect of borehole diameter on gas extraction

The diameter of the extraction borehole is an important indicator for improving the efficiency of gas extraction. Large-diameter boreholes increase the exposed area of the coal body and increase the extent of the pressure relief zone around the borehole, resulting in more fissures and providing channels for the flow of coal seam gas (Li et al., 2020). However, in the actual extraction process of underground gas, increasing the diameter of the borehole can lead to difficulties in construction and sealing. As can be seen from Figure 5B, the gas pressure at the same location decreases as the diameter of the borehole increases under the same conditions of gas extraction. This indicates that the larger the diameter of the extraction borehole, the better the gas extraction effect. The gas pressure was 0.765 MPa and 0.747 MPa for borehole diameters of 64 mm and 94 mm respectively, which did not meet the extraction requirements. The gas pressures for 113 mm and 130 mm boreholes were 0.720 MPa and 0.718 MPa respectively, which met the extraction requirements. The decrease in gas pressure from 64 mm to 94 mm is greater than the decrease in gas pressure from 113 mm to 130 mm, indicating that the effect of increasing the diameter of the borehole on gas extraction is reduced to a certain extent. Under the condition of meeting the extraction requirements, it is suggested to adjust the borehole diameter to 113 mm.

4.2.3 Effect of borehole spacing on gas extraction

Different borehole spacing affects the gas extraction flow rate and effective gas extraction area (Wei et al., 2019), which in turn affects the gas extraction effect. A reasonable borehole arrangement can effectively utilize the optimum radius of the borehole (Zhang et al., 2019) in the gas extraction process and significantly improve the gas extraction efficiency. Figure 5C shows the gas pressure curves for different borehole spacing for 360 days of extraction time. The gas pressure in the vicinity of the extraction borehole rises as the spacing of the boreholes increases. The smaller the spacing of the boreholes, the faster the gas pressure around the borehole drops and the better the extraction effect. However, the gas pressure is still high at the distance from the borehole. In the original scheme, the gas pressure is 0.737 MPa when the borehole spacing is 3 m. When the borehole spacing is 2 m, the gas pressure is 0.593 MPa, and the gas pressure decreases greatly. Therefore, it is suggested that the borehole spacing be adjusted to 2 m, and the gas extraction effect will be better.

4.2.4 Effect of permeability on gas extraction

As one of the key parameters in the process of gas migration, the coal seam permeability has a direct impact

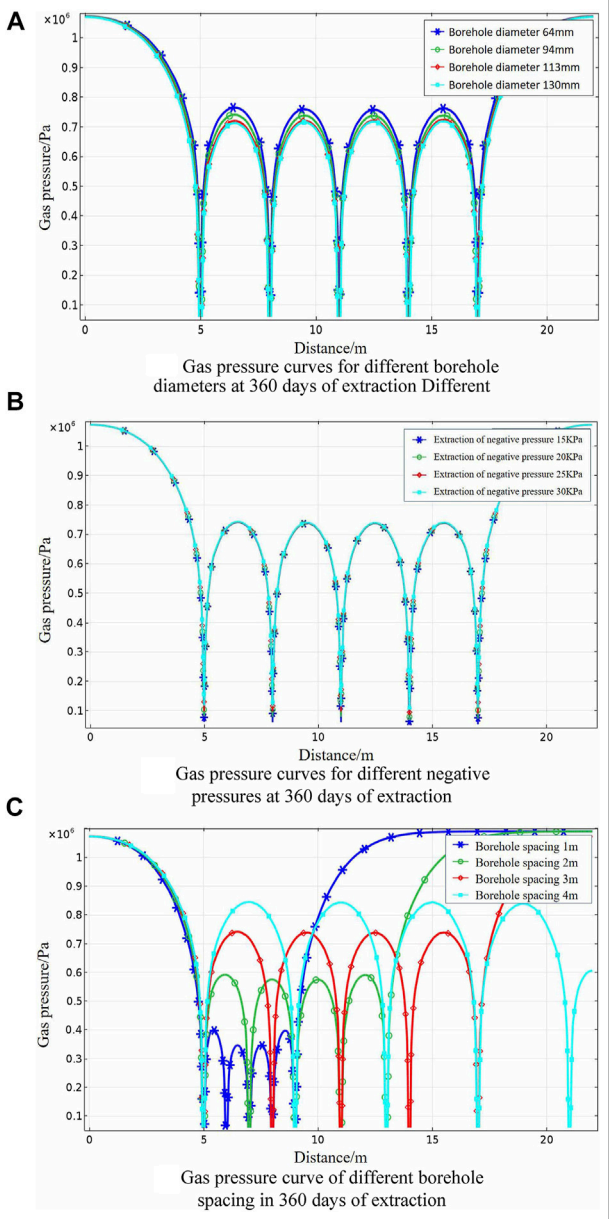

FIGURE 5
Influence curve of different extraction parameters on gas pre-extraction effect in working face.

on the effect of gas extraction (Jing et al., 2020; Fu et al., 2022; Vasilenko et al., 2022). Figure 6 shows the gas pressure curves at 50, 100, 200, and 365 days of gas extraction at the working face when the coal seam permeability is increased by different multiples. Comparing the gas pressure curves for different permeability at the same time, we can see that the larger the permeability, the faster the gas pressure drops and the better the extraction effect. At different times and with the same permeability, the gas pressure decreases gradually as the extraction time increases.

4.3 Gas extraction optimization scheme

Analyze the influence of gas extraction parameters on the extraction effect of the working face, combined with the gas occurrence of the working face, and propose the optimization scheme of gas extraction parameters and boreholes arrangement: adjusting the negative pressure of extraction to 15 KPa; and using 113 m diameter, double rows of parallel holes with depths of 60 m and 140 m respectively for gas extraction of the working face. The boreholes are spaced at 2 m. Both sides of the working face are drilled parallel to each other as pre-extraction boreholes for the pre-extraction boreholes of gas from the nine# coal seam. When the pre-extraction working face becomes the mining working face, the pre-extraction borehole is used for the extraction while the mining borehole unloads the coal seam for gas extraction. Take the 904 working face as an example, the specific gas extraction boreholes optimization layout is shown in Figure 7.

5 Research on coal seam pressure relief and permeability enhancement techniques and gas extraction scheme

5.1 Research on coal seam pressure relief and permeability enhancement technology

According to the numerical simulation results of gas extraction under different permeability conditions, based on the application of a gas extraction optimization scheme, for the hard-to-extract coal seam with low permeability at 904 Working Face, increasing coal seam permeability can substantially improve gas extraction efficiency. At present, the pre-fracturing and permeability enhancement technologies applied underground are hydraulic fracturings, chemical blasting, and airburst fracturing. The residual fracturing fluid produced by hydraulic fracturing will cause serious harm to the environment (Yost et al., 2017), and traditional chemical blasting will have a potential risk of ignition to the gas. Therefore, airburst fracturing technology is most suitable for coal seam permeability enhancement in the gas extraction process. Among them, the supercritical CO_2 airburst pressure relief technology is widely used in the field of low permeability and hard-to-extract coal seam penetration due to its large blasting range, high permeability coefficient, and strong adaptability (Wang et al., 2021c; He et al., 2022b). In this paper, the supercritical CO_2 airburst fracturing technology was used to unload and increase the permeability of 904 Working Faces in the second west mining area of the Jixian Coal Mine, and the effect of coal seam permeability increase was measured underground.

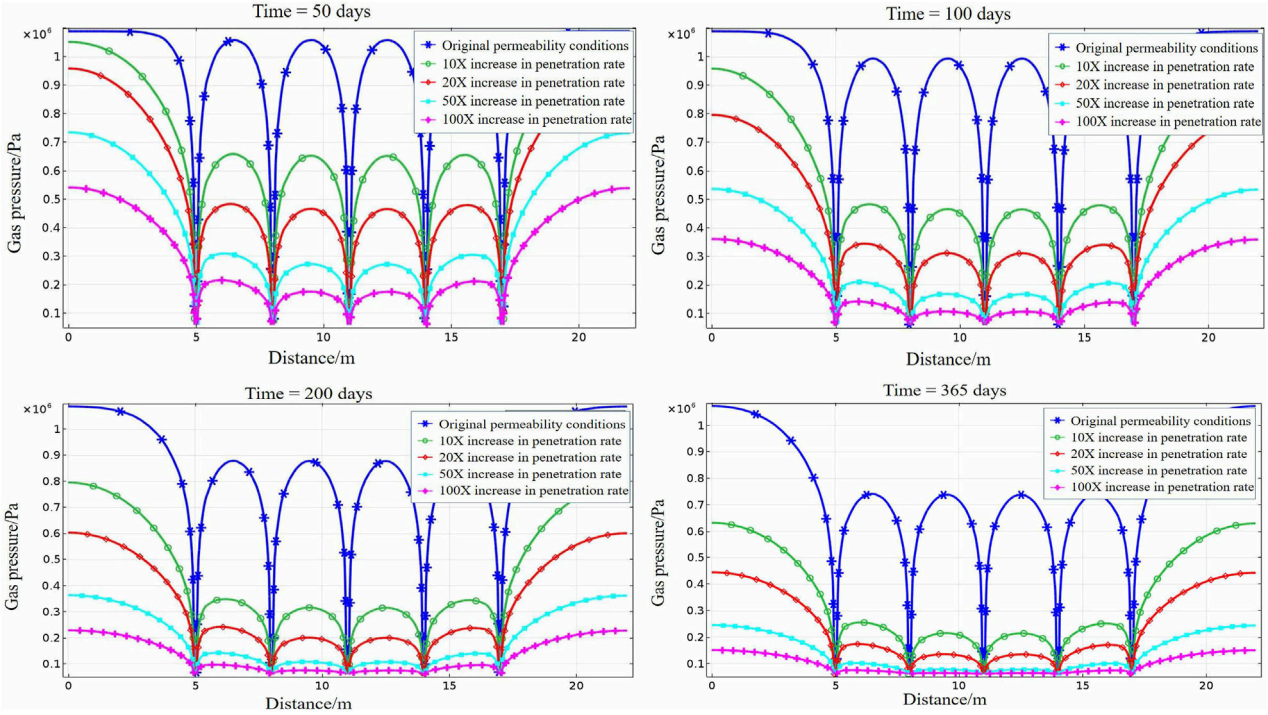

FIGURE 6
Gas extraction effect curve of different permeability increase times under different extraction times.

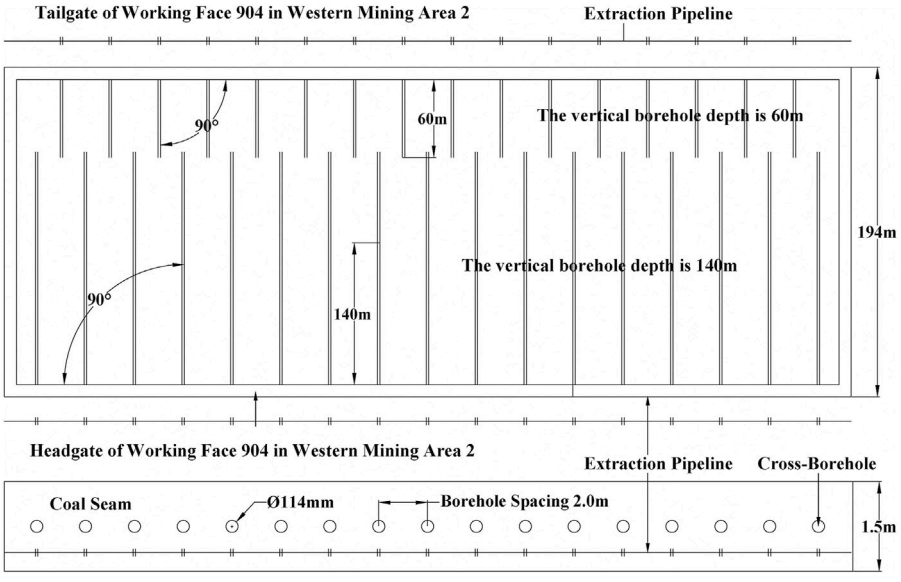

FIGURE 7
The 904 working face gas extraction borehole optimization layout diagram.

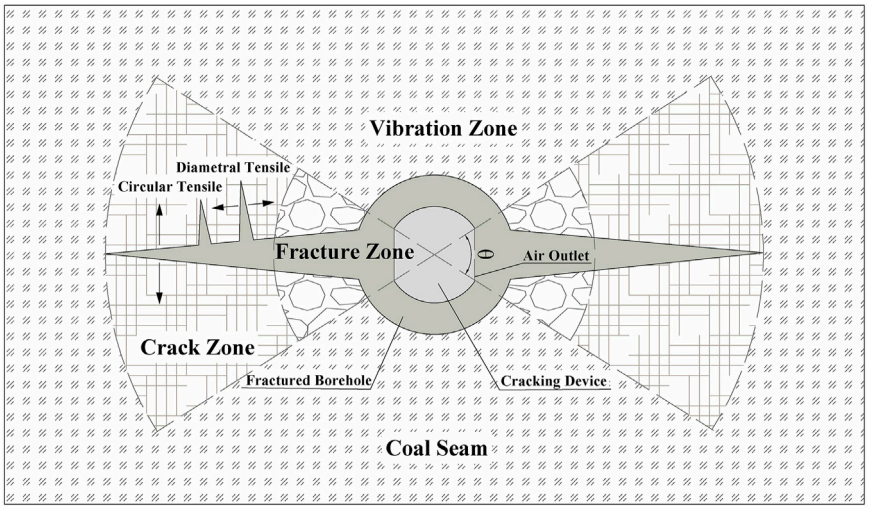

FIGURE 8
Comparison diagram of fracturing effect of supercritical CO_2 in underground test borehole.

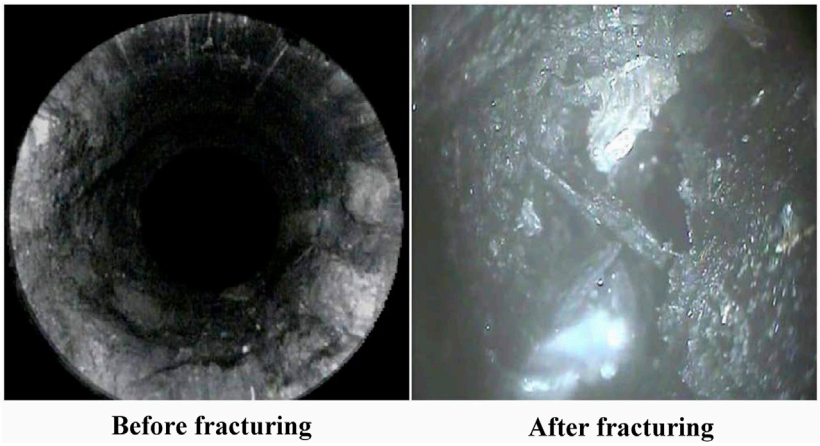

FIGURE 9
Test borehole gas content measurement results comparison chart.

5.2 Supercritical CO_2 airburst fracturing principle and damage range

Supercritical carbon dioxide is injected into the blasting pipe, and the heating pipe is quickly excited by the initiator, after detonation in a supercritical state carbon dioxide will be rapidly vaporized, with its increasing expansion pressure to reach the ultimate strength of the fixed pressure shear plate, shear plate break, high-pressure gas released from the energy drainage head, along the fracture surface or natural fractures quickly spread, to achieve directional fracture blasting (Sun et al., 2021), from the center of the source outward in turn to form a crack zone, fracture zone, and vibration zone, the damage range as shown in Figure 8.

5.3 Effect of supercritical CO_2 airburst fracturing technology in the underground working face

Multiple series blasting with ZLQ-38/300 and ZLQ-38/600 fracturing devices underground with CO_2 weight of 0.17 kg and 0.26 kg respectively. The diameter of the construction borehole is 50 mm. Three boreholes were

TABLE 4 Working face gas content determination.

Parameter scheme	Boreholes number	Gas loss amount (m3/t)	Gas desorption amount (m3/t)	Gas residual amount (m3/t)	Gas content (m3/t)
Original gas extraction	1–1	0.96	1.89	3.02	5.87
	1–2	0.89	1.79	3.06	5.97
	1–3	0.92	1.65	3.24	5.79
Gas extraction optimization	2–1	0.84	1.13	2.56	5.01
	2–2	0.76	0.99	2.42	4.97
	2–3	0.86	1.24	2.76	4.85
CO2 cracking permeability enhancement	3–1	0.79	0.87	1.98	3.61
	3–2	0.67	0.78	1.87	3.42
	3–3	0.73	0.91	1.85	3.59

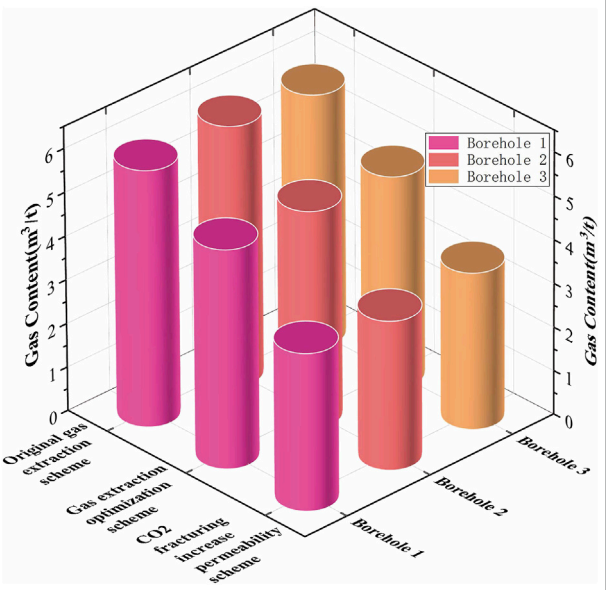

FIGURE 10
Comparison diagram of gas content measurement results.

constructed in the middle roadway of the 904 Working Face for testing. The borehole spacing was 10 m, and the distance between the fracturing devices and the borehole wall was 12 mm. The multi-section fracturing device series blasting method was implemented. The effect of liquid CO_2 fracturing in the underground working face is shown in Figure 9. After blasting, the borehole collapses in the hole, the hole wall is rough, and there are more broken coal blocks.

After using the supercritical CO_2 fracturing technology to relieve the pressure and increase the permeability of the coal seam in the 904 working face, the gas extraction optimization scheme was used to extract the gas from the 904 working face. After the gas desorption in the underground site was completed, the gas parameters of the three test boreholes were measured. The measured results were compared with the original gas extraction scheme and the gas content measured by the gas extraction optimization scheme. The specific data is shown in Table 4.

Based on Table 4, a comparison graph of gas content measurement results is obtained as shown in Figure 10, which shows that the coal seam gas content is reduced by 15.83% by applying the optimized gas extraction scheme compared to the original gas extraction scheme. The gas content of the coal seam with supercritical CO_2 fracturing and permeation technology was reduced by 28.4% compared to the coal seam without supercritical CO_2 fracturing and permeation technology, and by 39.7% compared to the original gas extraction scheme before the gas extraction optimization scheme was applied. The gas extraction optimization program improves the efficiency of gas extraction in the mine; The application of supercritical CO_2 fracturing technology can significantly improve the permeability of the hard-to-extract with low permeability coal seams.

6 Conclusion

1) By analyzing the tectonic evolution of the Shuangyashan Basin and the multi-phase extrusion and extensional deformation characteristics of the Suibin-Jixian Depression, it is determined that the tectonic activity has a controlling effect on the tectonic pattern of the coalfield and the coal seam gas occurrence in the Jixian Coal Mine, and the gas occurrence in the mine has the characteristics of partition aggregation and caprock sealing, and the low permeability of nine# coal seam is hard to be extracted.
2) Applying the numerical calculation method, the analysis of the gas extraction scheme for 904 Working Face of nine# coal seam in Jixian Coal Mine shows that: coal seam permeability,

borehole diameter, and borehole spacing have significant effects on gas extraction effect. The gas extraction optimization scheme of extracting negative pressure of 15 KPa, borehole diameter of 113 m, spacing of 2 m, and parallel boreholes with lengths of 60 m and 140 m in the two lanes is proposed.

3) We proposed a supercritical CO_2 fracturing permeability enhancement technology for low-permeability coal seams and implemented a tandem blasting method with multiple fracturing devices. Through underground measurements, the gas content of the coal seam was reduced by 39.7% compared with the original gas extraction scheme. The reasonable gas extraction scheme and coal seam pressure relief and permeability enhancement technology can significantly improve the gas extraction rate. The research results provide new ideas for the development of gas extraction technology under basin conditions.

Data availability statement

The original contributions presented in the study are included in the article/supplementary material, further inquiries can be directed to the corresponding author.

Author contributions

LT is responsible for theoretical guidance, ZZ is responsible for numerical simulation and experimental data processing, QL is responsible for theoretical analysis, YL and SW are responsible for downhole testing.

Funding

This work was financially supported by the LiaoNing Revitalization Talents Program (XLYC2007042), Liaoning Provincial Education Department Basic Scientific Research Project (Key Project)(LJKZ0325), and the National Natural Science Foundation of China (51604139).

Acknowledgments

We would like to thank all editors and anonymous reviewers for their comments and suggestions.

Conflict of interest

The authors declare that the research was conducted in the absence of any commercial or financial relationships that could be construed as a potential conflict of interest.

Publisher's note

References

Abouloifa, Najib, Vandamme, Matthieu, and Dangla, Patrick (2021). Modeling transient variations of permeability in coal seams at the reservoir scale. *J. Nat. Gas Sci. Eng.* 88 (2021), 103796. doi:10.1016/j.jngse.2021.103796

Dazhen, T. A. N. G., Shuguang, Y. A. N. G., and Shuling, T. A. N. G. (2021). Advance on exploration–development and geological research of coalbed methane in the Junggar Basin. *J. China Coal Soc.* 468, 2412–2425. doi:10.13225/j.cnki.jccs.CB21.0717

Fang, Hui-Huang, Zheng, C. S., Qi, N., Xu, H. J., Liu, H. H., Huang, Y. H., et al. (2022). Coupling mechanism of THM fields and SLG phases during the gas extraction process and its application in numerical analysis of gas occurrence regularity and effective extraction radius. *Petroleum Sci.* 19, 990–1006. doi:10.1016/j.petsci.2022.01.020

Fu, J., Li, B., Ren, C., Li, J., Wang, Z., Wu, X., et al. (2022). Coupling between damage evolution and permeability model with the adsorption effect for coal under gas extraction and coal mining conditions. *Energy fuels.* 3618, 10813–10831. doi:10.1021/acs.energyfuels.2c01758

Guo, Haijun, Tang, H., Wu, Y., Wang, K., and Xu, C. (2021). Gas seepage in underground coal seams: Application of the equivalent scale of coal matrix-fracture structures in coal permeability measurements. *Fuel* 288 (2021), 119641. doi:10.1016/j.fuel.2020.119641

Guo, Shao-bin, and Wang, Hong-liang (2008). Sequence stratigraphic characteristics and hydrocarbon prospect of mesozoic formation in Suibin depression, Sanjiang Basin. *Petroleum Explor. Dev.* 35, 44–51. doi:10.1016/s1876-3804(08)60007-5

He, Shun, Qin, Q., Qin, Z., and Zhou, J. (2022). Natural fracture development characteristics and their relationship with gas Contents— A case study of wufeng–longmaxi formation in luzhou area, southern sichuan basin, China. *ACS omega* 738, 34066–34079. doi:10.1021/acsomega.2c03318

He, Wei, Lian, H., Liang, W., Wu, P., Jiang, Y., and Song, X. (2022). Experimental study of supercritical CO2 fracturing across coal–rock interfaces. *Rock Mech. Rock Eng.*, 1–12. doi:10.1007/s00603-022-03070-9

Jing, Zhenhua, Balucan, R. D., Underschultz, J. R., Pan, S., and Steel, K. M. (2020). Chemical stimulation for enhancing coal seam permeability: Laboratory study into permeability variation and coal structure examination. *Int. J. Coal Geol.* 219, 103375. doi:10.1016/j.coal.2019.103375

Li, Hong, Liu, Y., Wang, W., Liu, M., Ma, J., Guo, X., et al. (2020). The integrated drainage technique of directional high-level borehole of super large diameter on roof replacing roof extraction roadway: A case study of the underground zhaozhuang coal mine. *Energy Rep.* 6, 2651–2666. doi:10.1016/j.egyr.2020.09.013

Liu, Dameng, Yao, Yanbin, and Wang, Hui (2022). Structural compartmentalization and its relationships with gas accumulation and gas production in the Zhengzhuang Field, southern Qinshui Basin. *Int. J. Coal Geol.* 259 (2022), 104055. doi:10.1016/j.coal.2022.104055

Liu, Junjun, Xie, J., Wang, F., Yang, B., Liu, Y., Fu, C., et al. (2021). Experiment investigation on gas flow characteristics of coal considering the integrity of coal samples. *Geomatics, Nat. Hazards Risk* 121, 2984–3000. doi:10.1080/19475705.2021.1987342

Liu, Luofu, Wang, Y., Chen, Y., Shen, B., and Gao, X. (2018). Gas occurrence and accumulation characteristics of Cambrian–Ordovician shales in the Tarim Basin, northwest China. *Acta Geol. sinica-. Engl. Ed.* 925, 1948–1958. doi:10.1111/1755-6724.13687

Sun, Keming, Chen, P., Zhang, S., Li, K., and Zhang, X. (2021). Numerical investigation of fracturing of coal with cleats caused by supercritical CO2 explosion. *ACS omega* 626, 16854–16868. doi:10.1021/acsomega.1c01450

Vasilenko, Tatyana, Kairillov, A., Islamov, A., Doroshkevich, A., Ludzik, K., Chudoba, D. M., et al. (2022). Permeability of a coal seam with respect to fractal features of pore space of fossil coals. *Fuel* 329 (2022), 125113. doi:10.1016/j.fuel.2022.125113

Wang, Fuwei, Chen, D., Wang, Q., Du, W., Chang, S., Wang, C., et al. (2021). Quantitative evaluation of caprock sealing controlled by fault activity and hydrocarbon accumulation response: K gasfield in the xihu depression, east China sea basin. *Mar. Petroleum Geol.* 134, 105352. doi:10.1016/j.marpetgeo.2021.105352

Wang, Kang, Pan, Hongyu, and Zhang, Tianjun (2021). Experimental study of prefabricated crack propagation in coal briquettes under the action of a CO2 gas explosion. *ACS omega* 638, 24462–24472. doi:10.1021/acsomega.1c02850

Wang, Zhiming, Hurter, S., You, Z., Honari, V., Sun, Y., and Zhang, S. (2021). Influences of negative pressure on air-leakage of coalseam gas extraction: Laboratory and CFD-DEM simulations. *J. Petroleum Sci. Eng.* 196 (2021), 107731. doi:10.1016/j.petrol.2020.107731

Wei, Pan, Huang, C., Li, X., Peng, S., and Lu, Y. (2019). Numerical simulation of boreholes for gas extraction and effective range of gas extraction in soft coal seams. *Energy Sci. Eng.* 75, 1632–1648. doi:10.1002/ese3.377

Yost, Erin E., Stanek, John, and Burgoon, Lyle D. (2017). A decision analysis framework for estimating the potential hazards for drinking water resources of chemicals used in hydraulic fracturing fluids. *Sci. Total Environ.* 574, 1544–1558. doi:10.1016/j.scitotenv.2016.08.167

Yuan, Y. U. A. N., Tang, Y., and Cao, D. (2020). Coalbed methane enrichment regularity and major control factors in the Xishanyao formation in the Western part of the Southern Junggar Basin. *Acta Geol. sinica-. Engl. Ed.* 942, 485–500. doi:10.1111/1755-6724.14339

Zhang, Chaolin, Xu, J., Peng, S., Li, Q., and Yan, F. (2019). Experimental study of drainage radius considering borehole interaction based on 3D monitoring of gas pressure in coal. *Fuel* 239, 955–963. doi:10.1016/j.fuel.2018.11.092

Zhang, Hao, Xu, L., Yang, M., Deng, C., and Cheng, Y. (2022). Pressure relief mechanism and gas extraction method during the mining of the steep and extra-thick coal seam: A case S tudy in the yaojie No. 3 coal mine. *Energies* 1510, 3792. doi:10.3390/en15103792

Zhang, Kaizhong, Zou, A., Wang, L., Cheng, Y., Li, W., and Liu, C. (2022). Multiscale morphological and topological characterization of coal microstructure: Insights into the intrinsic structural difference between original and tectonic coals. *Fuel* 321 (2022), 124076. doi:10.1016/j.fuel.2022.124076

Zhao, Xueqin, Lv, C., Jiang, Y., Zhu, H., Wang, F., and Chai, P. (2022). Geological characteristics of the mesozoic unconformities in eastern Heilongjiang, NE China: Implications for the mesozoic continental margin evolution of northeast asia. *Front. Earth Sci. (Lausanne).* 10, 1248. doi:10.3389/feart.2022.850324

Zou, Guangui, Zhang, Q., Peng, S., She, J., Teng, D., Jin, C., et al. (2022). Influence of geological factors on coal permeability in the Sihe coal mine. *Int. J. Coal Sci. Technol.* 91, 6–13. doi:10.1007/s40789-022-00475-3

frontiers | Frontiers in Earth Science

TYPE Original Research
PUBLISHED 09 January 2023
DOI 10.3389/feart.2022.1036165

OPEN ACCESS

EDITED BY
Chaojun Fan,
Liaoning Technical University, China

REVIEWED BY
Qingyi Tu,
Anhui University of Science and Technology, China
Lipeng He,
Chongqing University, China
Xin Ding,
Liaoning Technical University, China

*CORRESPONDENCE
Bo Zhao,
zhaobo91@cqu.edu.cn

SPECIALTY SECTION
This article was submitted to Economic Geology, a section of the journal Frontiers in Earth Science

RECEIVED 04 September 2022
ACCEPTED 20 September 2022
PUBLISHED 09 January 2023

CITATION
Shang S, Zhang Q, Zhao Y, Diao Y, Yin J, Che Y, Kang X and Zhao B (2023), Experimental research of the geo-stress evolution law and effect in the intact coal and gas outburst process. *Front. Earth Sci.* 10:1036165. doi: 10.3389/feart.2022.1036165

Experimental research of the geo-stress evolution law and effect in the intact coal and gas outburst process

Shaoyong Shang[1], Qinghua Zhang[2,3,4], Yinghua Zhao[1], Yong Diao[1], Jiakuan Yin[1], Yuheng Che[2,3], Xiaotong Kang[1] and Bo Zhao[2]*

[1]CHN Energy Yulin Energy Qing Longsi Colliery, Yulin, Shanxi, China, [2]State Key Laboratory of the Gas Disaster Detecting Preventing and Emergency Controlling, Chongqing, China, [3]China Coal Technology and Engineering Group Chongqing Research Institute, Chongqing, China, [4]Anhui University of Science and Technology, Huainan, Anhui, China

Coal and gas outbursts are a potentially fatal hazard that must be managed when mining gassy coal seams. Mining-induced stress plays an important role in outbursts, while elastic potential is accumulated to provide energy for an outburst. In this study, a large-scale true triaxial (LSTT) apparatus was developed to conduct experiments and to understand the outburst mechanism and mining-induced geo-stress evolution law. In the LSTT experiments, coal and gas outbursts resulted from both stress and gas pressure and occurred in a limited balance area. Under the action of mining-induced stress, surrounding rock and coal are compressed. Thus, a large amount of elastic potential is accumulated to provide energy for a coal and gas outburst. Mining-induced stress promotes the development and expansion of the fracture in the coal body, which results in coal wall deformation and damage. The four types of coal wall instability are bodily movement of coal wall, layered separation of coal wall, collapse of coal wall, and break of coal wall. This study develops a classification scheme and management strategies for outbursts.

KEYWORDS

gas outburst, mining-induced stress, mass distribution characteristics, outburst instability models, geo-stress evolution law

Introduction

Coal and gas outbursts are complicated dynamic disasters. They are potentially indiscoverable lethal hazards that must be focused on carefully when mining gassy coal seams (Litwiniszyn, 1985; Skoczylas, 2012; Lei et al., 2022; Zhang et al., 2022; Zou et al., 2022). China is rich in coal, but short of gas and oil. Consequently, for a long time, coal has played a central role in China's primary energy production and consumption structure (Yuan, 2016). In the last 20 years, China has averaged 50 pairs of coal mine outbursts and more than 300 outburst accidents every year. Gas and coal and rock mass become more

complex as the mining depth, geo-stress, gas pressure and content increase, as ground temperature rises with depth, and as the coupling geo-stress increases (Fan et al., 2017; Fan et al., 2019; Zhou et al., 2019).

The mechanism of a coal and gas outburst has been extensively studied by means of theoretical analysis, laboratory test, numerical simulation, and field tests in major coal-producing countries (Aguado and Nicieza, 2007). Outburst mechanisms can be summed up in several aspects, as follows: outburst center hypothesis, unified instability theory of outburst and rock burst, rheological hypothesis, spherical shell instability hypothesis and combination hypothesis (Wang et al., 2017; Jin et al., 2018; Sun et al., 2018). It has been widely considered that the combination hypothesis can well describe the whole outburst process. It is also generally believed that geo-stress and gas pressure provide energy sources for the occurrence and development of an outburst, and the physical and mechanical properties of the coal and rock reflect the ability of coal and rock to resist destruction (An and Cheng, 2014; Jiang et al., 2015; Guo et al., 2016; Yin et al., 2016; Wang et al., 2018a; Wang et al., 2019; Zhao et al., 2020). The complex mining conditions in a deep mine (e.g., high geo-stress, gas pressure, and ground temperature) lead to the new characteristics of a coal and gas outburst, such as high energy, high intensity, and difficulty to prevent and control. At the same time, it presents obvious coupling characteristics of coal, rock, and gas dynamic disaster (Aguado and Nicieza, 2007; Xue et al., 2014; Chunli et al., 2015; Hu et al., 2015; Zhai et al., 2016; Fan et al., 2021). The outburst mechanism was recently studied using experimental technology (Li et al., 2017; Wang et al., 2017; Wang et al., 2018b; Ding and Yue, 2018; Yang et al., 2018).

Researchers have recently developed different scale simulation test systems (according to different research objectives). Zhao et al. (2016) explored the geo-stress and the way it impacts the outburst and stated the influence of geo-stress and gas content on outburst under different mining depths. A small-scale coal and gas outburst device has been developed, and the control of coal and gas outburst in gas-enriched areas and the related research on coal and gas outburst spallation have been carried out with this device (Tu et al., 2016). In the study of the permeability distribution of a coal body affected by mining, the changes of permeability from the area not affected by mining activities to the coal wall area of the working face in front of the mining are successively divided into decreasing area, increasing area, and sudden increasing area (An and Cheng, 2014). Xue et al. (2011) analyzed the influence of water content on coal and gas outbursts and stated that the intensity of a coal and gas outburst is negatively correlated with the water content of a coal body. Fisne et al. and Nie et al. discussed the relationship between the outburst and geological parameters, and the outburst's strength, particle size distribution, and failure of the pore shape of the outburst coal were studied (Zhang et al., 2022). They also studied how the variation of stress in a stress concentration area has an important influence on protrusion. Li et al. (2017) made several groups of simulation tests on an outburst and studied the influence of the exposed area of gas-containing coal on the outburst, especially in the case of uncovering coal. Liu and Cheng (2014) simulated coal and gas outburst accidents due to the change of the stress environment when uncovering coal underground. They then discussed the evolution law of stress in the process of coal and gas outburst, and the influence of structural factors on a coal and gas outburst. Peng et al. (2012) considered that failure condition and law of coal with different strengths under stress-gas pressure. Taking Tianfu Sanhui No. 1 Mine as the engineering background, the process of coal and gas outburst under mining conditions was simulated based on the similarity theory experiment, and the space-time evolution law of air pressure in the outburst process was analyzed (Xu et al., 2010). Fedorchenko and Fedorov (2012) demonstrated the development law of acoustic signal and the development of a crack during an outburst. PFC3D and FLAC3D have been used to analyze the control of protrusion by effective stress in different zones, and the different stages of crack burst were discussed (Zhao et al., 2022a). Lu et al. and Xu et al. analyzed the desorption of adsorbed gas in the process of outburst, from the microscopic view (Lu et al., 2011). It is considered that the cause of coal and gas outburst is the failure and instability of the coal body that is caused by the gas pressure gradient, and the free gas is involved in the process of coal and gas outburst in the form of work done by expansion (Xie et al., 2017; Zhao et al., 2022b). The first condition for adsorbed gas to participate in the outburst work is to quickly transform into free gas during the burst. The process of adsorbed gas in an outburst involves the desorption of adsorbed gas from the pore surface, diffusion of gas in the pore, and seepage of gas in a fracture system (Ding et al., 2019; Fan et al., 2020; Liu et al., 2020; Jianshe et al., 2021; Liu et al., 2021; Zhao et al., 2022c; Zhou et al., 2022; Zhu et al., 2022).

When coal-gas mixture meets a fire source in a roadway, it can lead to a gas explosion, coal dust explosion, and so on, which can seriously endanger the miners' safety and cause huge economic loss. The coal and gas outburst mechanism has been studied extensively in major coal-producing countries by means of theoretical analysis, laboratory test, numerical simulation, and field tests. However, experimental data are still limited. Therefore, mining-induced stress monitoring, observation, and evolution require further research—direct observations are especially lacking. Therefore, in this paper we will examine mining-induced stress in outbursts using a self-developed large-scale true triaxial (LSTT) apparatus. Using the

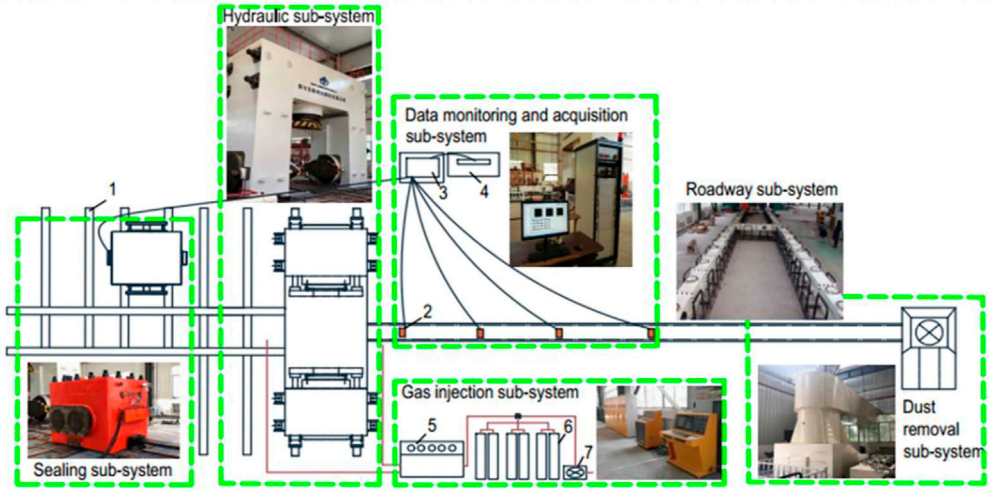

FIGURE 1
Schematic diagram of the outburst simulating device (LSTT).

TABLE 1 Coal-like material ratios.

Coal-like material ratios, %					Uniaxial compressive strength (MPa)	Firmness coefficient	Elasticity modulus (MPa)	Density (g/cm^{3})	Porosity (%)	Adsorption constant	
Cement	Sand	Water	Active carbon	Coal						a	b
7	5.5	8.5	0.84	78.16	1.1~1.5	0.188	62.1~113	1.39~1.40	5.36	33.97	1.62
Raw coal					1.5	0.18~0.25	1,230	1.4	5.48	32.5	1.56

LSTT apparatus, we launch an outburst experiment to replay the outburst accident at Dingji coal mine, Anhui Province, China. Even when gas extraction reaches the standard, coal and gas outburst accidents dominated by stress can still occur from time to time. This has seriously restricted the safe mining of coal. Therefore, it is of great significance to study the coupling mechanism of stress, gas, and coal; the coal and gas outburst mechanism; and prevention theory under the condition of high ground stress in deep mining.

Experimental

Experimental apparatus

It is of great value to reduce the number of deep coal and gas outburst accidents through research with high similarity in the laboratory. Analysis of experimental data can lead to a deeper understanding of the stages of gestation, excitation, development, and termination of a deep coal and gas outburst. It can also provide data to support the discussion of the mechanism of a deep coal and gas outburst. The outburst simulating device consists of a pathway sub-system, hydraulic sub-system gas, injection sub-system, roadway sub-system, data monitoring and acquisition sub-system, and dust removal sub-system (as shown in Figure 1). The vertical loading pressure of the mechanical loading system is 3,000 t. The maximum working pressure is 25 MPa. Meanwhile, the horizontal symmetrical loading pressure is 2000 t, and the maximum working pressure is 16.7 MPa. The external dimensions of the box are 2.2 m × 1.8 m × 1.5 m. A sealing ring is used to seal the box, forming an empty size of 0.8 m × 1.1 m × 1.5 m. The simulated roadway is a square with a section side length of 0.3 m, with sensor installation, and ash removal and observation window,

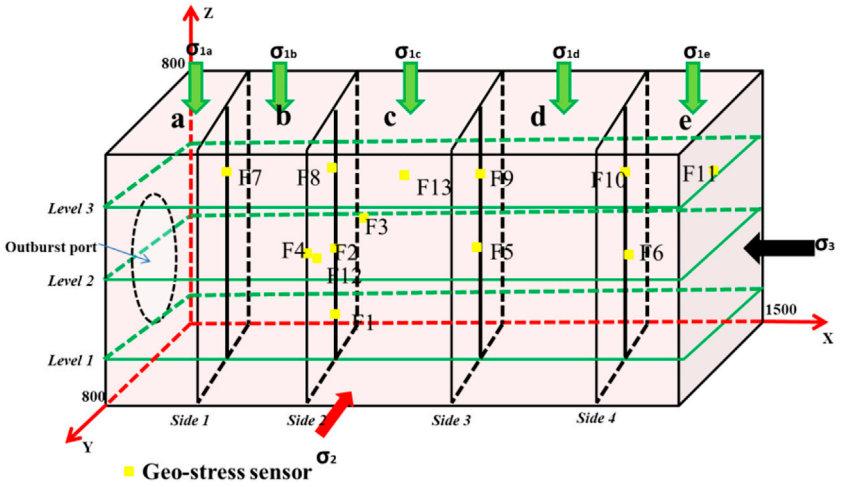

FIGURE 2
Layout of the geo-stress sensors in the container.

TABLE 2 The coordinates of the geo-stress sensors.

Geo-stress sensors	*x*/mm	*y*/mm	*z*/mm
F1	550	400	200
F2	550	400	350
F3	550	100	350
F4	550	700	350
F5	900	400	350
F6	1,300	400	350
F7	200	400	600
F8	550	400	600
F9	900	400	600
F10	1,300	400	600
F11	1,450	400	600
F12	550	700	350
F13	750	400	600

which can resist the impact damage of 6 MPa experimental gas. This setup can simulate a horizontal plane angle of 10°, 20°, and 90°; a vertical plane angle of 10° and 20°, and its combination turn; and a 90° bifurcated roadway layout.

Coal samples and gas source

The test model is the "4•19″ outburst accident of the 1,331 1) transport roadway heading face in Dingji Mine. According to the preliminary analysis of the coal mine field investigation, the direct cause of this accident is that the coal seam of the accident working face is buried 870 m deep, which is a deep mine with large ground stress. This has the basic conditions for the occurrence of gas dynamic disasters, mainly caused by ground stresses such as rock burst, and coal and gas outburst. Pulverized coal, cement, sand, activated carbon and water were selected as the main raw materials to simulate coal materials. The basic parameters of the similar materials are listed in Table 1. The fixed process parameters were determined as follows: the molding pressure is 25 MPa, the loading mode is load loading, there are five pressed layers, the pressure holding time is 30 min, and the curing time is 7 days.

Experimental design

Outburst experiments mainly included collecting basic parameters, loading with similar materials, testing airtightness, linking the chamber with the roadway, and starting the experiment. The experiments are generally divided into non-adsorbent gas and adsorbent gas. In the outburst test, carbon dioxide is generally used as the test gas to ensure the experimental safety. In our experiment, carbon dioxide was selected as the adsorption gas, with an adsorption time of about 15 days. We assumed that the materials reached adsorption equilibrium when the adsorption equilibrium was determined by pressure-retaining adsorption for 3 days.

To facilitate sensor positioning, a three-dimensional axis is established with the lower left-hand corner of the direction of the protruding mouth as the origin of the coordinates. The *X*-axis is perpendicular to the protruding mouth, the *Y*-axis is parallel to the protruding mouth, and the vertical direction is the *Z*-axis. The coordinates of the vertices of the box are (0,0,0), (1500,0,0), (0,800,0), (0,0,800), (1500,800,0), (1500,0,800), (0,800,800), and (1500,800,800) (Figure 2) (Table 2).

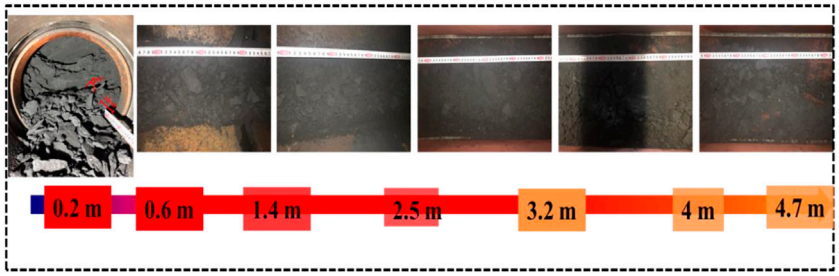

FIGURE 3
Characteristics of the areas of ejected coal masses.

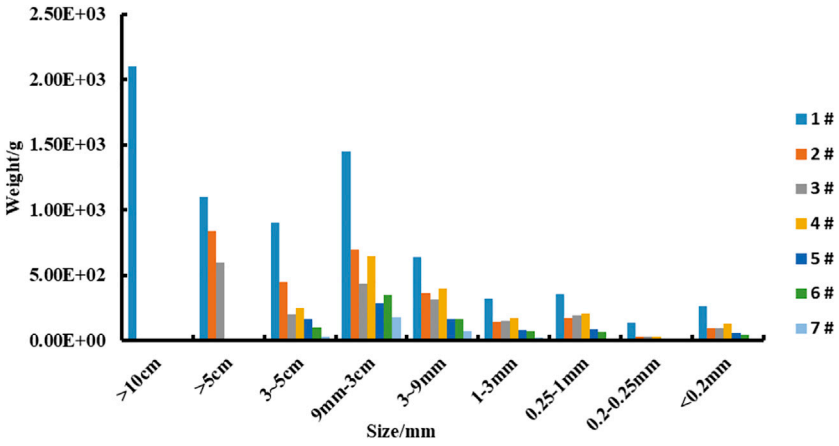

FIGURE 4
Size distribution in different regions.

Results and discussion

Experimental results

After the outburst, the complete coal body is broken under the action of geo-stress, and a large amount of broken coal is thrown into the simulated roadway under the action geo-stress and gas pressure, which is consistent with the outburst site. After the thrown broken coal runs for several meters in the roadway under the action of gas airflow, the samples are accumulated in the simulated roadway after energy depletion. In the test, the pressure hole is wedge-shaped and semicircular with a large mouth and a small cavity, with a width of about 0.3 m and a depth of about 0.4 m. Figure 3 shows that the broken coal is piled up in the roadway, and a large number of broken coal samples are piled up near the outburst mouth. At the same time, a relatively large volume of broken coal is piled up within 2 m from the outburst mouth. The pulverization degree of the protruding coal body shows two characteristics: the pulverization rate of the coal body near the outburst mouth is small, and the pulverization degree of the coal body far from the protruding mouth is high. In the area where pulverized coal is relatively concentrated in the simulated roadway, the pulverization rate of coal is relatively large. This may be related to the higher collision frequency of particles in the area with higher pulverized coal mass distribution in the process of pulverized coal and gas flow transport (Figure 4).

Stress distribution in front of the working face

From the energy accumulation stage to the initiation stage in the process of outburst, the coal and rock mass system gradually evolves from the equilibrium state to the sudden instability process, which results from the non-linear features of the coal and rock mass system (material non-linearity and geometric non-linearity). Instability usually occurs in the limited balanced

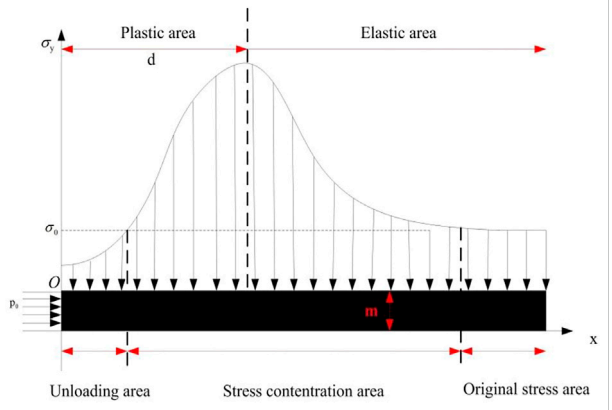

FIGURE 5
Stress distribution in front of the working face.

area of supporting pressure in front of the coal wall. Therefore, stress-strain status research facilitates the exploration of the deformation failure mechanism in the outburst. Previous research suggests that there are unloading areas, stress concentration areas, and original stress areas in front of a working face. The area from coal wall to stress peak is always called a limited balance area (d), as shown in Figure 5.

A unit width of dx, height of m (coal seam thickness), is under triaxial stress. The stress status is shown in Figure 6. Based on $\sum F_x = 0$, we can build the balance equation:

$$\sigma_x m - \left(\sigma_x + \frac{d\sigma_x}{dx}dx\right)m + 2\left(c_1 + f_1\sigma_z\right)dx + 2m\left(c_2 + f_2\sigma_y\right)dx = 0 \tag{1}$$

where σ_x $\sigma_x + d\sigma_x$ is the stress in the direction of the x-axis; σ_y, σ_z is the stress in the direction of the y-axis and z-axis, respectively; c_1 is the cohesion between coal and roof/floor; f_1 is the angle of internal friction; c_2 is the cohesion of coal; and f_2 is the angle of internal friction of coal.

This is simplified as:

$$2\left(c_1 + mc_2 + f_1\sigma_z + mf_2\sigma_y\right) - m\frac{d\sigma_x}{dx} = 0 \tag{2}$$

Ignoring the shear stress τ_{xy}, we can regard $\sigma_x\sigma_y$, and σ_z as principal stresses. Therefore, in the limited balance area, the stress meets the Molar-coulomb criterion, as follows:

$$\sigma_x = \frac{\sigma_t}{\sigma_c}\sigma_z - \sigma_c \tag{3}$$

where σ_c is the uniaxial compressive strength of coal, and σ_t is the uniaxial tensile strength of coal.

Substitute Eq. 3 into Eq. 2:

$$\frac{d\sigma_z}{dx} - \frac{2f_1\sigma_c}{m\sigma_t}\sigma_z = \frac{2\sigma_c}{m\sigma_t}\left(c_1 + mc_2 + mf_2\sigma_y\right) \tag{4}$$

Supposing that the coal wall is subjected to a counterforce p_0, substitute $\sigma_x|x = 0 = p_0$ into Eq. 4:

$$\left[\frac{\sigma_c}{\sigma_t}p_0 + \sigma_c + \frac{1}{f_1}\left(c_1 + mc_2 + mf_2\sigma_y\right)\right]e^{\frac{2f_1\sigma_c}{m\sigma_t}x} - \frac{1}{f_1}\left(c_1 + mc_2 + mf_2\sigma_y\right) = \sigma_z \tag{5}$$

and substitute $\sigma_x|x = 0 = p_0$ into Eq. 3:

$$\left[p_0 + \sigma_t + \frac{1}{f_1}\frac{\sigma_t}{\sigma_c}\left(c_1 + mc_2 + mf_2\sigma_y\right)\right]e^{\frac{2f_1\sigma_c}{m\sigma_t}x} - \frac{1}{f_2}\frac{\sigma_t}{\sigma_c}\left(c_1 + mc_2 + mf_2\sigma_y\right) - \sigma_c = \sigma_x \tag{6}$$

The area from coal wall to stress peak is defined as a limited balance area (d), and the stress in the peak σ_z is equal to $K_\sigma r_s H$. We can calculate the plastic zone width (d).

$$\frac{m\sigma_t}{2f_1\sigma_c}\ln\left[\frac{K_\sigma r_s H + \frac{1}{f_1}\left(c_1 + mc_2 + mf_2\sigma_y\right)}{\frac{\sigma_c}{\sigma_t}P_0 + \sigma_c + \frac{1}{f_1}\left(c_1 + mc_2 + mf_2\sigma_y\right)}\right] = d \tag{7}$$

where K_σ is the stress concentration factor, r_s is the bulk density of overlying strata, and H is the mining depth.

Stress evolution rules during the process of an outburst

The outburst process is divided into four stages: preparation, initiation, development, and termination. After an outburst occurs, coal is thrown out from the coal wall, and

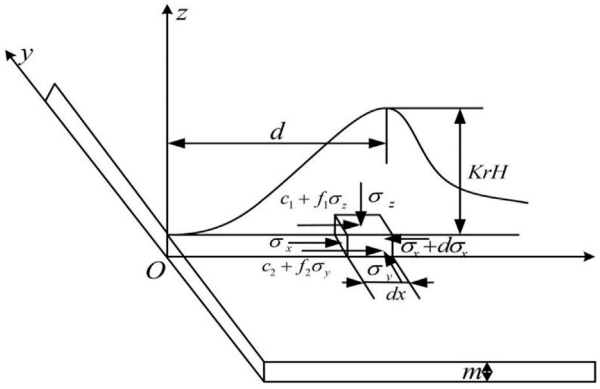

FIGURE 6
Stress distribution in the limited balance area.

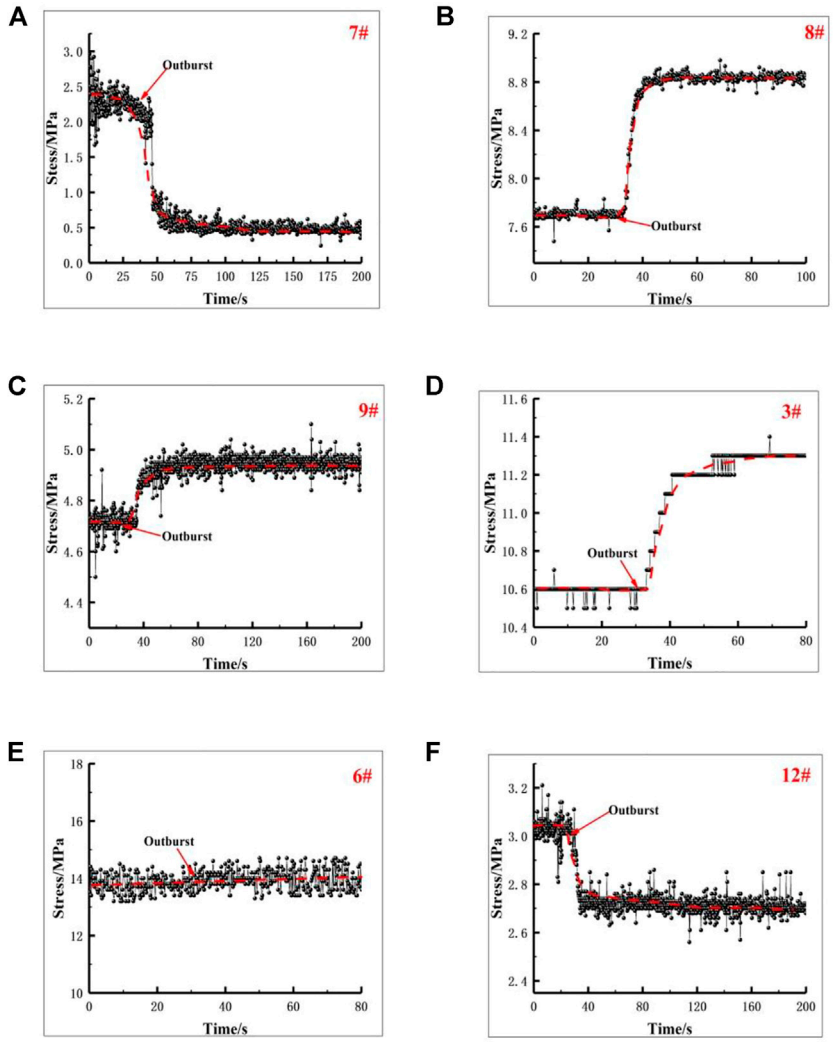

FIGURE 7
The stress evolution rule in the process of an outburst.

an initial outburst hole is formed on the coal wall. Geo-stress around the coal wall may be redistributed, and the stress state is variable depending on conditions (as shown in Figure 7). After the outburst, the vertical stress near the hole wall rapidly decreases (as shown in Figure 7A) and geo-stress decreases from 2.5 MPa to 0.5 MPa. However, vertical stress far from the hole wall gradually increases (as shown in Figures 7B–D). Stress sensor #8 shows that the geo-stress increased from 7.7 MPa to 8.8 MPa (as shown Figure 7B). Stress sensor #9 shows that the geo-stress increased from 4.7 MPa to 5.9 MPa (Figure 7C). Stress sensor #3 shows that the geo-stress increased from 10.6 MPa to 11.3 MPa (as seen in Figure 7D). The high geo-stress makes the coal near the coal hole wall reach a plastic state in a short time, the peak of the tangential stress shifts to the deep part, and radial stress rapidly decreases. The failure occurrence rule in a coal wall is developed from the position of exposed surface of coal wall to the deep part, and upward and downward from the vertical center of the coal seam. However, Figure 7E shows that the original stress remained stable throughout the original stress region. We conclude that the coal hole wall, which is exposed as a result of the outburst, had higher geo-stress. Horizontal stress near the outburst hole quickly decreased from 3.1 MPa to 2.8 MPa (as shown in Figure 7F). Stress evolution demonstrates the coal damage rules. Ejected coal, in the center, was caused by vertical stress but damaged coal, at the bottom and roof of the coal wall, was caused by shear stress.

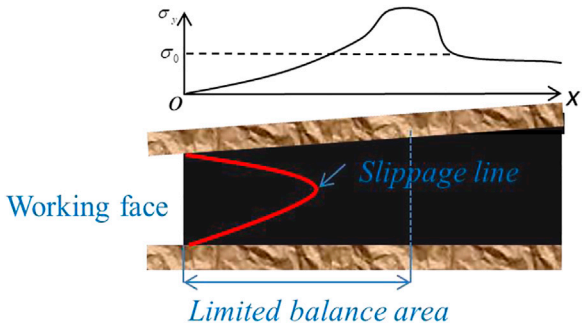

FIGURE 8
Bodily movement of the coal wall.

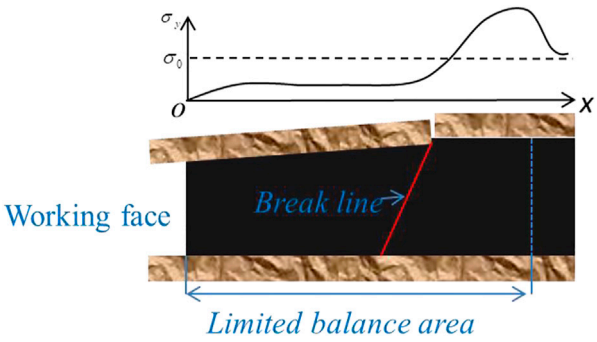

FIGURE 10
Collapse of the coal wall model.

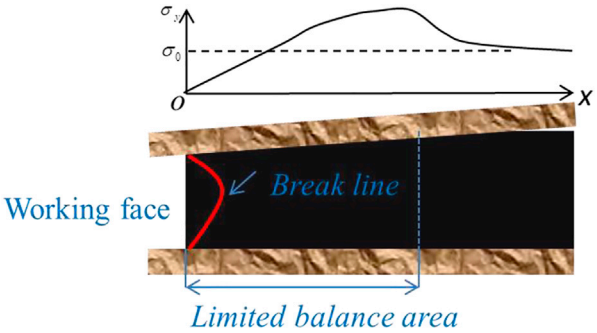

FIGURE 9
Layered separation of the coal wall.

Outburst instability models of a coal wall

We have analyzed the process of initial mining from the coal wall, the stress distribution in the limited balance area, and the stress evolution rules. The failure occurrence rule in the coal wall was developed from the position of the exposed surface of the coal wall to the deep part, and upward and downward from the vertical center of the coal seam. Based on the stress evolution rules during the process of an outburst, the following four basic types of coal wall instability are given: 1) bodily movement of coal wall, 2) layered separation of coal wall, 3) collapse of coal wall model, and 4) break of coal wall model. The typical condition for this instability model is that the overburden load of the coal seam is large enough and the roof of the coal seam is hard. In this way, the width of the limiting balance zone of the coal seam becomes longer and the roof is not easily broken (as shown in Figure 8). A wider ultimate balance zone of supporting pressure is related to the greater shear strain of the coal wall. The capacity of the coal seam to resist the external force of the horizontal direction toward the mining space is extremely weakened, and the cracks in the coal seam are gradually expanded. In addition, the high-pressure gas in the coal seam can cause an overall movement of the sliding line of some coal bodies or may even throw the coal away from the wall. A side-falling model is a common form of instability, which occurs in coal seams with high brittleness and strength. The depth of the coal wall may be very small, which will not cause a coal and gas outburst. However, when the depth of the sides is larger, it is best to change to a coal wall extrusion model (Figure 9).

Collapse of the coal wall may frequently occur in a coal mining face. The typical instability condition is that the roof of the coal seam in front of the face has a fracture structure. Residual strength rapidly decays after coal wall collapse. The action of gas pressure, high-speed failure, and extrusion or ejection to the mining space lead to the initial launch of the outburst (Figure 10). The typical conditions for the break of the coal wall model are that the working face enters soft coal from hard coal or that the stone door is cracked. The hard coal seam exposed in front of the working face will bear high vertical support pressure and horizontal thrust exerted by the weak coal seam inside, which results in a huge elastic potential energy in the coal seam. If disturbed, a lot of elastic potential energy may be released (Figure 11).

Effect of mining-induced stress on outburst

Mining-induced stress and gas pressure play different roles at different stages of an outburst. Mining-induced stress plays an important role in the process of a coal and gas outburst. Under the action of ground stress, surrounding rock and coal are compressed. Therefore, a large amount of elastic potential is accumulated to provide energy for a coal and gas outburst. Mining-induced stress promotes the development and expansion of the fracture in the coal

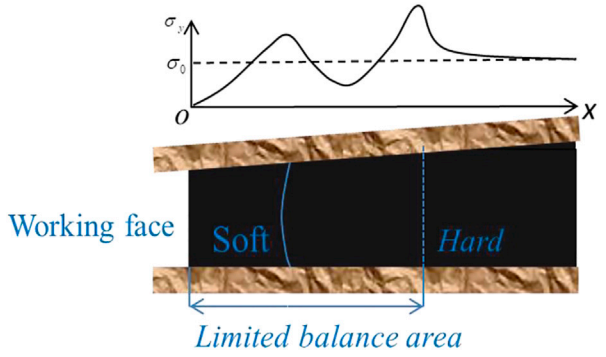

FIGURE 11
Break of the coal wall model.

body, which results in deformation and damage. Permeability is also impacted by mining-induced stress. High mining-induced stress coupled with low permeability results in a high gas pressure gradient.

As mining depth increases, geo-stress plays an increasingly important role in coal and gas outburst disasters. The distribution of the stress field in the process of a coal and gas outburst plays a crucial role in the gestation and excitation of a coal and gas outburst and determines the occurrence and development process of a gas outburst to a certain extent. The influence of geo-stress on a coal and gas outburst is mainly manifested in the plastic failure stage of the coal body. The plastic failure of the coal body under the action of stress leads to a series of conditions, such as strain field, gas migration field, and mechanical property field of coal body change. On one hand, the stress field affects the compressed coal skeleton and makes the coal accumulate an elastic potential. On the other hand, when the local stress exceeds the strength limit of the coal body, it will cause the coal body to crack or even destabilize, which results in the initial failure of the coal.

The failure of coal under the action of geo-stress is a necessary but not sufficient condition for an outburst. When the coal fails under the action of geo-stress and the gas pressure cannot cause the crack to expand and destroy, then the damaged coal will not be thrown out and a protrusion will not occur. The gas pressure will then gradually disappear, and the coal and rock mass near the crack will be stable under the support of spherical and radial stresses. If the gas pressure can continue to act on the fracture tip after the coal body is destroyed under the action of geo-stress, then the initial fracture develops continuously, and the gas pressure can make the destroyed coal and rock mass throw out. A coal and gas outburst will then inevitably occur.

Conclusion

In this paper, the influence of stress on a coal and gas outburst is studied by means of theoretical analysis and physical experiment, based on stress-dominated physical simulation test and parameter response of several physical fields. We analyzed mining-induced stress evolution rules in the outburst process. Mining-induced stress plays an important role in the process of a coal and gas outburst.

1) In the test, the pressure hole is wedge-shaped and semicircular with a large mouth and a small cavity, with a width of about 0.3 m and a depth of about 0.4 m. The broken coal is piled up in the roadway, and a large number of broken coal samples are piled up near the outburst mouth. At the same time, a relatively large volume of broken coal is piled up within 2 m from the outburst mouth.
2) An outburst occurs in a limited balance area. Under the action of mining-induced stress, surrounding rock and coal are compressed. Therefore, a large amount of elastic potential is accumulated to provide energy for a coal and gas outburst. Mining-induced stress promotes the development and expansion of a fracture in the coal body, which results in deformation and damage. Four typical types of coal wall instability are given: bodily movement of coal wall, layered separation of the coal wall, collapse of the coal wall model, and a break of the coal wall model.

Data availability statement

The original contributions presented in the study are included in the article/Supplementary Material; further inquiries can be directed to the corresponding author.

Author contributions

All authors listed have made a substantial, direct, and intellectual contribution to the work and approved it for publication.

Funding

This work was supported by the Joint Fund for Regional Innovation and Development (U21A20110), Chongqing Research Program of Technical Innovation and Application Development (cstc2019jscx-gksbX0076), Guizhou Science and Technology Plan Project (Guizhou scientific and technological cooperation support (2021) General 398), and Major Special

Topics of China Coal Technology Engineering Group Chongqing Research Institute (2021ZDZX05).

Conflict of interest

The authors declare that the research was conducted in the absence of any commercial or financial relationships that could be construed as a potential conflict of interest.

Publisher's note

All claims expressed in this article are solely those of the authors and do not necessarily represent those of their affiliated organizations, or those of the publisher, the editors and the reviewers. Any product that may be evaluated in this article, or claim that may be made by its manufacturer, is not guaranteed or endorsed by the publisher.

References

Aguado, M. B. D., and Nicieza, C. G. (2007). Control and prevention of gas outbursts in coal mines, Riosa-Olloniego coalfield, Spain. *Int. J. Coal Geol.* 69, 253–266. doi:10.1016/j.coal.2006.05.004

An, F. H., and Cheng, Y. P. (2014). An explanation of large-scale coal and gas outbursts in underground coal mines: The effect of low-permeability zones on abnormally abundant gas. *Nat. Hazards Earth Syst. Sci.* 14, 2125–2132. doi:10.5194/nhess-14-2125-2014

Chunli, Y., Yiliang, Z., Xiangchun, L., Yangyang, M., and Feifei, Z. (2015). Gas concentration distribution law in the roadway after coal and gas outburst. *Appl. Mech. Mat.* 713-715, 314–318. doi:10.4028/www.scientific.net/amm.713-715.314

Ding, X., Xiao, X. C., Lv, X. F., Wu, D., and Xu, J. (2019). Mechanical properties of bump-prone coal with different porosities and its acoustic emission-charge induction characteristics under uniaxial compression. *Adv. Civ. Eng.* 2019, 1–18. doi:10.1155/2019/7581061

Ding, Y., and Yue, Z. Q. (2018). An experimental investigation of the roles of water content and gas decompression rate for outburst in coal briquettes. *Fuel* 234, 1221–1228. doi:10.1016/j.fuel.2018.07.143

Fan, C., Elsworth, D., Li, S., Zhou, L., Yang, Z., and Song, Y. (2019). Thermo-hydro-mechanical-chemical couplings controlling CH 4 production and CO 2 sequestration in enhanced coalbed methane recovery. *Energy* 173, 1054–1077. doi:10.1016/j.energy.2019.02.126

Fan, C. J., Yang, L., Wang, G., Huang, Q. M., Fu, X., and Wen, H. O. (2021). Investigation on coal skeleton deformation in CO2 injection enhanced CH4 drainage from underground coal seam. *Front. Earth Sci. (Lausanne).* 9, 766011. doi:10.3389/feart.2021.766011

Fan, C., Li, S., Elsworth, D., Han, J., and Yang, Z. (2020). Experimental investigation on dynamic strength and energy dissipation characteristics of gas outburst-prone coal. *Energy Sci. Eng.* 8 (4), 1015–1028. doi:10.1002/ese3.565

Fan, C., Li, S., Luo, M., Du, W., and Yang, Z. (2017). Coal and gas outburst dynamic system. *Int. J. Min. Sci. Technol.* 27, 49–55. doi:10.1016/j.ijmst.2016.11.003

Fedorchenko, I. A., and Fedorov, A. V. (2012). Gas-dynamic stage of the coal and gas outburst with allowance for desorption. *J. Min. Sci.* 48, 15–26. doi:10.1134/s1062739148010030

Guo, H. J., Cheng, Y. P., Ren, T., Wang, L., Yuan, L., Jiang, H. N., et al. (2016). Pulverization characteristics of coal from a strong outburst-prone coal seam and their impact on gas desorption and diffusion properties. *J. Nat. Gas Sci. Eng.* 33, 867–878. doi:10.1016/j.jngse.2016.06.033

Hu, Q. T., Zhang, S. T., Wen, G. C., Dai, L. C., and Wang, B. (2015). Coal-like material for coal and gas outburst simulation tests. *Int. J. Rock Mech. Min. Sci.* 74, 151–156. doi:10.1016/j.ijrmms.2015.01.005

Jiang, C. L., Xu, L. H., Li, X. W., Tang, J., Chen, Y. J., Tian, S. X., et al. (2015). Identification model and indicator of outburst-prone coal seams. *Rock Mech. Rock Eng.* 48, 409–415. doi:10.1007/s00603-014-0558-0

Jianshe, L., Zhao, W., Zhou, J., Yan, Z., Wang, K., Xu, C., et al. (2021). Influence of deep magma-induced thermal effects on the regional gas outburst risk of coal seams. *Int. J. Coal Sci. Technol.* 8 (6), 1411–1422. doi:10.1007/s40789-021-00452-2

Jin, K., Cheng, Y. P., Ren, T., Zhao, W., Tu, Q. Y., Dong, J., et al. (2018). Experimental investigation on the formation and transport mechanism of outburst coal-gas flow: Implications for the role of gas desorption in the development stage of outburst. *Int. J. Coal Geol.* 194, 45–58. doi:10.1016/j.coal.2018.05.012

Lei, Y., Cheng, Y. P., Wang, L., Ren, T., and Li, Q. Y. (2022). Potential infrasonic tremors in coal seam systems: Implications for the prediction of coal and gas outbursts. *Fuel*, 326, 125000. doi:10.1016/j.fuel.2022.125000

Li, H., Feng, Z. C., Zhao, D., and Duan, D. (2017). Simulation experiment and acoustic emission study on coal and gas outburst. *Rock Mech. Rock Eng.* 50, 2193–2205. doi:10.1007/s00603-017-1221-3

Litwiniszyn, J. (1985). A model for the initiation of coal-gas outbursts. *Int. J. Rock Mech. Min. Sci. Geomechanics Abstr.* 22, 39–46. doi:10.1016/0148-9062(85)92592-6

Liu, Q. Q., and Cheng, Y. P. (2014). Measurement of pressure drop in drainage boreholes and its effects on the performance of coal seam gas extraction: A case study in the jiulishan mine with strong coal and gas outburst dangers. *Nat. Hazards (Dordr).* 71, 1475–1493. doi:10.1007/s11069-013-0957-7

Liu, T., Lin, B., Fu, X., and Liu, A. (2021). Mechanical criterion for coal and gas outburst: A perspective from multiphysics coupling. *Int. J. Coal Sci. Technol.* 8 (6), 1423–1435. doi:10.1007/s40789-021-00447-z

Liu, Y. B., Ba, Q. B., He, L. P., Shen, K., and Xiong, W. (2020). Study on the rock-breaking effect of water jets generated by self-rotatory multinozzle drilling bit. *Energy Sci. Eng.* 8, 2457–2470. doi:10.1002/ese3.679

Lu, T. K., Zhao, Z. J., and Hu, H. F. (2011). Improving the gate road development rate and reducing outburst occurrences using the waterjet technique in high gas content outburst-prone soft coal seam. *Int. J. Rock Mech. Min. Sci.* 48, 1271–1282. doi:10.1016/j.ijrmms.2011.09.003

Peng, S. J., Xu, J., Yang, H. W., and Liu, D. (2012). Experimental study on the influence mechanism of gas seepage on coal and gas outburst disaster. *Saf. Sci.* 50, 816–821. doi:10.1016/j.ssci.2011.08.027

Skoczylas, N. (2012). Coal seam methane pressure as a parameter determining the level of the outburst risk – laboratory and *in situ* research/ciśnienie złożowe jako parametr określający stan zagrożenia wyrzutami metanu I skał – badania laboratoryjne I kopalniane. *Archives Min. Sci.* 57, 861–869. doi:10.2478/v10267-012-0056-8

Sun, H., Cao, J., Li, M., Zhao, X., Dai, L., Sun, D., et al. (2018). Experimental research on the impactive dynamic effect of gas-pulverized coal of coal and gas outburst. *Energies* 11, 797. doi:10.3390/en11040797

Tu, Q. Y., Cheng, Y. P., Guo, P. K., Jiang, J. Y., Wang, L., and Zhang, R. (2016). Experimental study of coal and gas outbursts related to gas-enriched areas. *Rock Mech. Rock Eng.* 49, 3769–3781. doi:10.1007/s00603-016-0980-6

Wang, C. J., Yang, S. Q., Yang, D. D., Li, X. W., and Jiang, C. L. (2018). Experimental analysis of the intensity and evolution of coal and gas outbursts. *Fuel* 226, 252–262. doi:10.1016/j.fuel.2018.03.165

Wang, F., He, J., Liang, Y., Luo, Y., Liao, Z., and Li, L. (2018). Study on the permeability characteristics of coal containing coalbed methane under different loading paths. *Energy Sci. Eng.* 6, 475–483. doi:10.1002/ese3.221

Wang, F., Liang, Y., and Zou, Q. (2019). Correlation between coal and gas outburst risk and adsorption properties of coal seams. *Energy Sci. Eng.* 7, 974–985. doi:10.1002/ese3.326

Wang, G., Li, W., Wang, P., Yang, X., and Zhang, S. (2017). Deformation and gas flow characteristics of coal-like materials under triaxial stress conditions. *Int. J. Rock Mech. Min. Sci.* 91, 72–80. doi:10.1016/j.ijrmms.2016.11.015

Xie, G., Yin, Z., Wang, L., Hu, Z., and Zhu, C. (2017). Effects of gas pressure on the failure characteristics of coal. *Rock Mech. Rock Eng.* 50, 1711–1723. doi:10.1007/s00603-017-1194-2

Xu, J. A., Peng, S. J., Zhang, D. D., Yang, H. W., and Tao, Y. Q. (2010). Analysis on the effect of gas pressure on coal and gas outburst disaster. *Disaster Adv.* 3, 442–446.

Xue, S., Wang, Y. C., Xie, J., and Wang, G. (2011). A coupled approach to simulate initiation of outbursts of coal and gas - model development. *Int. J. Coal Geol.* 86, 222–230. doi:10.1016/j.coal.2011.02.006

Xue, S., Yuan, L., Wang, Y. C., and Xie, J. (2014). Numerical analyses of the major parameters affecting the initiation of outbursts of coal and gas. *Rock Mech. Rock Eng.* 47, 1505–1510. doi:10.1007/s00603-013-0425-4

Yang, D. D., Chen, Y. J., Tang, J., Li, X. W., Jiang, C. L., Wang, C. J., et al. (2018). Experimental research into the relationship between initial gas release and coal-gas outbursts. *J. Nat. Gas Sci. Eng.* 50, 157–165. doi:10.1016/j.jngse.2017.12.015

Yin, G. Z., Jiang, C. B., Wang, J. G., Xu, J., Zhang, D. M., and Huang, G. (2016). A new experimental apparatus for coal and gas outburst simulation. *Rock Mech. Rock Eng.* 49, 2005–2013. doi:10.1007/s00603-015-0818-7

Yuan, L. (2016). Control of coal and gas outbursts in huainan mines in China: A review. *J. Rock Mech. Geotechnical Eng.* 8, 559–567. doi:10.1016/j.jrmge.2016.01.005

Zhai, C., Xiang, X. W., Xu, J. Z., and Wu, S. L. (2016). The characteristics and main influencing factors affecting coal and gas outbursts in Chinese Pingdingshan mining region. *Nat. Hazards (Dordr).* 82, 507–530. doi:10.1007/s11069-016-2195-2

Zhang, X., Tang, J. P., Pan, Y. S., and Yu, H. H. (2022). Experimental study on intensity and energy evolution of deep coal and gas outburst. *Fuel*, 324, 124484. doi:10.1016/j.fuel.2022.124484

Zhao, B., Cao, J., Sun, H. T., Wen, G. C., Dai, L. C., and Wang, B. (2020). Experimental investigations of stress-gas pressure evolution rules of coal and gas outburst: A case study in Dingji coal mine, China. *Energy Sci. Eng.* 8 (1), 61–73. doi:10.1002/ese3.509

Zhao, B., Wen, G., Ma, Q., Sun, H., Yan, F., and Nian, J. (2022b). Distribution characteristics of pulverized coal and stress–gas pressure–temperature response laws in coal and gas outburst under deep mining conditions. *Energy Sci. Eng.* 10 2205–2223. doi:10.1002/ese3.1129

Zhao, B., Wen, G., Nian, J., Ma, Q., Fan, C., Lv, X., et al. (2022a). Numerical simulation study on the multi-physical field response to underground coal and gas outburst under high geo-stress conditions. *Minerals* 12, 151. doi:10.3390/min12020151

Zhao, P., He, B., Zhang, B., and Liu, J. (2022). Porosity of gas shale: Is the NMR-based measurement reliable? *Petroleum Sci.* 19, 509–517. doi:10.1016/j.petsci.2021.12.013

Zhao, W., Cheng, Y., Jiang, H., Jin, K., Wang, H., and Wang, L. (2016). Role of the rapid gas desorption of coal powders in the development stage of outbursts. *J. Nat. Gas Sci. Eng.* 28, 491–501. doi:10.1016/j.jngse.2015.12.025

Zhou, B., Xu, J., Peng, S., Geng, J., and Yan, F. (2019). Test system for the visualization of dynamic disasters and its application to coal and gas outburst. *Int. J. Rock Mech. Min. Sci. (1997).* 122, 104083. doi:10.1016/j.ijrmms.2019.104083

Zhou, L., Zhou, X., Fan*, C., and Bai, G. (2022). Coal permeability evolution triggered by variable injection parameters during gas mixture enhanced methane recovery. *Energy* 252, 124065. doi:10.1016/j.energy.2022.124065

Zhu, Z., Wu, Y., and Han, J. (2022). A prediction method of coal burst based on analytic hierarchy process and fuzzy comprehensive evaluation. *Front. Earth Sci.* 9, 834958. doi:10.3389/feart.2021.834958

Zou, Q. L., Zhang, T. C., Ma, T. F., Tian, S. X., Jia, X. Q., and Jiang, Z. B. (2022). Effect of water-based SiO2 nanofluid on surface wettability of raw coal. *Energy*, 254, 124228. doi:10.1016/j.energy.2022.124228

frontiers | Frontiers in Earth Science

TYPE Original Research
PUBLISHED 20 January 2023
DOI 10.3389/feart.2022.1084117

OPEN ACCESS

EDITED BY
Long Fan,
University of Alaska Fairbanks,
United States

REVIEWED BY
Kun Zhang,
Henan Polytechnic University, China
Xingzong Liu,
Ludong University, China
Yu Zhang,
Tsinghua University, China

*CORRESPONDENCE
Donglin Dong,
ddl@cumtb.edu.cn
Zilong Guan,
2017029007@chd.edu.cn

SPECIALTY SECTION
This article was submitted to Economic Geology,
a section of the journal
Frontiers in Earth Science

RECEIVED 30 October 2022
ACCEPTED 21 November 2022
PUBLISHED 20 January 2023

CITATION
Tang F, Dong D, Xiao Z and Guan Z (2023), Analysis of failure characteristics of grouting concretion body under the action of water-force coupling.
Front. Earth Sci. 10:1084117.
doi: 10.3389/feart.2022.1084117

Analysis of failure characteristics of grouting concretion body under the action of water-force coupling

Fei Tang[1], Donglin Dong[1]*, Zhen Xiao[2] and Zilong Guan[3]*

[1]Department of Geological Engineering and Environment, China University of Mining and Technology, Beijing (CUMTB), Beijing, China, [2]Hebei Geological Environment Monitoring Institute, Shijiazhuang, China, [3]Institute of Ecological and Environmental Engineering, Power China Northwest Engineering Corporation Limited, Xi'an, China

Cement slurry is widely used in grouting reinforcement of coal mine floor. Under the action of water-force coupling, the floor of abandoned roadway reinforced by cement slurry is prone to damage. The failure characteristics of grouting concretion body under water-force coupling were studied by using RFPA software considering the heterogeneity of rock mass. The numerical simulation results show that the acoustic emission (AE) of numerical samples of the same strength with different lower boundary pressure decreases with the increase of lower boundary pressure, and the acoustic emission of numerical samples of the same lower boundary pressure with different strength increases with the increase of compressive strength. The lower the water pressure at the lower boundary is, the lower the softening degree of the sample is, and the sample is more prone to brittle fracture under external load. The numerical simulation results have important guiding significance for the grouting concretion body protection of coal mine floor in the future.

KEYWORDS

rock mechanics, water-force coupling, stress, acoustic emission, numerical simulation

Introduction

Due to the long geological evolution process and chamber excavation, the supporting pressure of surrounding rock exceeds its peak strength, and there must be a large number of weak planes (such as joints, fractures) in the rock mass (Hyett et al., 1992; Nikbakhtan and Osanloo, 2009; Xiujun et al., 2012). In underground engineering construction, grouting method is often used to strengthen and control, so as to improve the bearing capacity and waterproof performance of surrounding rock and ensure the safety of engineering construction (Tuerkmen and Oezguezel, 2003; He et al., 2005; Zhang et al., 2015a). When the coal mining face is completed, the floor of the abandoned roadway will receive the action of external force and water pressure. Under the action of water-force coupling, grouting concretion body in coal mine floor is prone to cracking and crushing (Meng et al., 2013; Xie et al., 2015).

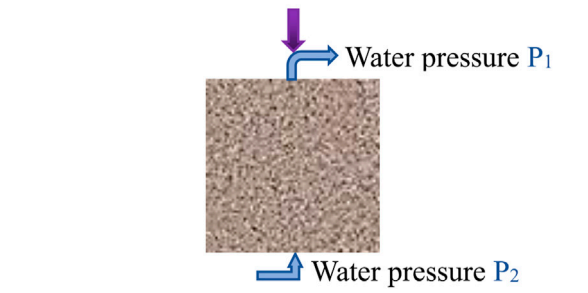

FIGURE 1
Numerical model.

TABLE 1 Physical and mechanical parameters of grouting concretion body.

Parameter	Grouting concretion body
Homogeneity index	3
Young's modulus (GPa)	5.08
Poisson's ratio	0.2
Density (kg/m^3)	2,450
Friction angle (°)	45

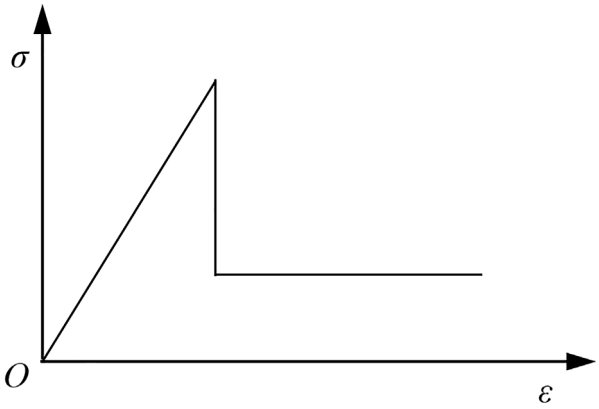

FIGURE 2
Elastic-brittle constitutive relationship of grouting concretion body.

The stability control of weak and broken surrounding rock has always been one of the major problems puzzling the safety and efficient production of coal mines (Zhao et al., 2017; Liu et al., 2018; Wang et al., 2018; Wang et al., 2019; Zhou et al., 2020). Under the influence of high stress, fault fracture zone and weak cementation, the broken degree of surrounding rock is high, and the phenomena of roof fall and floor heave occur frequently (Gao et al., 2004; Pan et al., 2020). The strength and frequency of roadway repair are increased, and grouting reinforcement can improve self-bearing capacity of surrounding rock *in situ*. Grouting reinforcement technology is an efficient roadway support method in the process of coal mining, it is mainly through the injection of a certain slurry material into the surrounding rock to effectively support the roadway. However, groundwater can affect the strength of the grouting concretion body, and even cause roadway damage (Zhang et al., 2015b; Niu et al., 2017; Fan and Ma, 2018; Cai, 2020).

As early as the 1980s, P. D. Evdokimov et al. studied the influence of grouting on shear properties of fractured rock mass (Evdokimov et al., 1970). In the 1990s, Zhou et al. (1993) strengthened and grouted the weakly weathered rock mass near the base surface during the construction of Ertan Arch Dam, and theoretically analyzed the mechanism of rock mass mechanical changes by fracture-damage mechanics method. Zong et al. (2013) carried out the confined grouting reinforcement of cracked rock samples and tested the mechanical properties of grouting reinforced samples by using self-made grouting system. Han et al. (2011) revealed the essence and mechanisms of grouting reinforcement, measured the roughness of structural plane in cracked rock mass, and analyzed the influence of grouting on strength, joint roughness coefficient and stiffness of structural plane through the shear test of structural plane of rupture rock sample around grouting reinforcement. Wang et al. (2007) carried out experimental research on the mechanical properties of post-peak grouting reinforcement samples, and found that the higher the strength of the reinforced solid itself, the higher the strength of the grouting reinforced solid, and the higher the bond strength of the slurry, the higher the strength after grouting. Lei et al. (2015) defined the material parameters of irregular concretion, and analyzed the characteristics of stress and deformation under loads after grouting. Wael et al. (2021) discussed the influence of five different sizes of sand on the ultimate stress (MPa) of hand-mixed cement-grouted sands modified with polymer. Liu et al. (2021) analyzed influences on the performance of cement-based grout used to reform the upper Middle Ordovician limestone in Hanxing mining area. Zhang and Barry (2019) used the finite element method to examine the relative influence of a number of key factors controlling the stability and surface deformations of shallow, horizontal coal mine goafs overlain by sedimentary rock and grouting concretion body. Zhang et al. (2019) compared the microscopic properties of a new borehole sealing material with ordinary cement grout. From the above analysis, it can see that the effect of different water pressures on the fracture characteristics of grouting concretion body has not been studied.

In 1995, Professor Tang proposed the real failure process analysis method, namely the RFPA (Realistic Failure Process Analysis) method (Chen et al., 2021a). This method is based on the basic theory of finite element and fully considers the

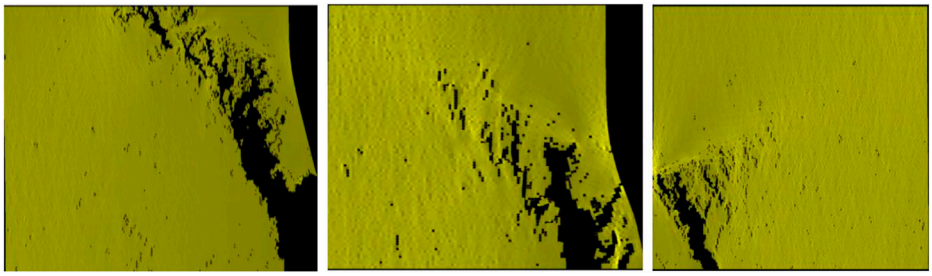

FIGURE 3
Failure modes of water pressure samples with the same strength and different lower boundaries.

characteristics of non-linearity, inhomogeneity and anisotropy that accompany the rock fracture process (Tang et al., 2000; Tang, 2003; Chen et al., 2021b). RFPA is a real fracture process analysis system that uses elastic mechanics as a stress analysis tool and elastic damage theory as a medium deformation analysis module (Chen et al., 2022; Yang, 2004).

In this paper, based on the above research, the failure characteristics of grouting concretion body under water-force coupling are studied by using RFPA software considering the heterogeneity characteristics of rock mass.

Introduction to RFPA-Flow

A brief introduction to the basic principles of RFPA-Flow

1) The seepage process in the rock satisfies the Biot consolidation theory (Tang, 2003; Yang, 2004).

$$\text{Equilibrium equation: } \frac{\partial \sigma_{ij}}{\partial x_{ij}} + \rho X_j = 0 \ \ (i, j = 1, 2, 3) \quad (1)$$

$$\text{Geometric equation: } \varepsilon_{ij} \frac{1}{2}\left(u_{i,j} + u_{i,j}\right) \varepsilon_v = \varepsilon_{11} + \varepsilon_{22} + \varepsilon_{33} \quad (2)$$

$$\text{Constitutive equation: } \sigma_{ij} = \sigma_{ij} - \alpha p \delta_{ij} = \lambda \sigma_{ij} \varepsilon_v + 2G\varepsilon_{ij} \quad (3)$$

$$\text{Seepage equation: } K\nabla^2 p = \frac{1}{Q}\frac{\partial p}{\partial t} - \alpha \frac{\partial \varepsilon_v}{\partial t} \quad (4)$$

where ρ is the density, σ_{ij} is the stress tensor, ε_v is the volume strain, δ is the Kronecker constant, G is the shear modulus, λ is the Lame coefficient, ∇^2 is the Laplace operator.

2) The relationship between permeability and stress-strain function is satisfied in the elastic state of microscopic unit, and the permeability K_f increases after the element is damaged and ruptured, the K_f can be written as:

$$K_f = K_0 e^{-b'} \quad (5)$$

3) The rock structure is non-uniform, and the damage parameters of the unit bodies composing the rock satisfy a certain probability distribution.

Element permeability-damage coupling equation

When the stress state of the meso-element meets a given damage threshold, the element begins to be damaged, and the elastic modulus of the damaged element is:

$$E = (1 - D)E_0 \quad (6)$$

where D is the damage variable, E and E_0 are the elastic modulus of damaged and undamaged elements respectively.

For the element subjected to uniaxial compression, the failure criterion of the element adopts the Mohr-Coulomb criterion, namely:

$$F = \sigma_1 - \sigma_3 \frac{1 + \sin\phi}{1 - \sin\phi} \geq f_c \quad (7)$$

where ϕ is the internal friction angle; f_c is the uniaxial compressive strength.

When the shear stress reaches the Mohr-Coulomb damage threshold, the damage variable D is expressed as follows:

$$D = \begin{cases} 0 & \varepsilon < \varepsilon_{c0} \\ 1 - \dfrac{f_{cr}}{E_0 \varepsilon} & \varepsilon_{c0} < \varepsilon \end{cases} \quad (8)$$

where f_{cr} is the uniaxial compressive residual strength, ε_{c0} is the maximum compressive strain, ε is the residual strain. It can be seen from the test that the damage will cause the permeability coefficient of the rock mass to increase sharply, and the change of the unit permeability coefficient can be described by the following formula:

$$\lambda = \begin{cases} \lambda_0 \partial^{-\beta(\sigma_1 - \partial p)} & D = 0 \\ \xi \lambda_0 \partial^{-\beta(\sigma_1 - \partial p)} & D > 0 \end{cases} \quad (9)$$

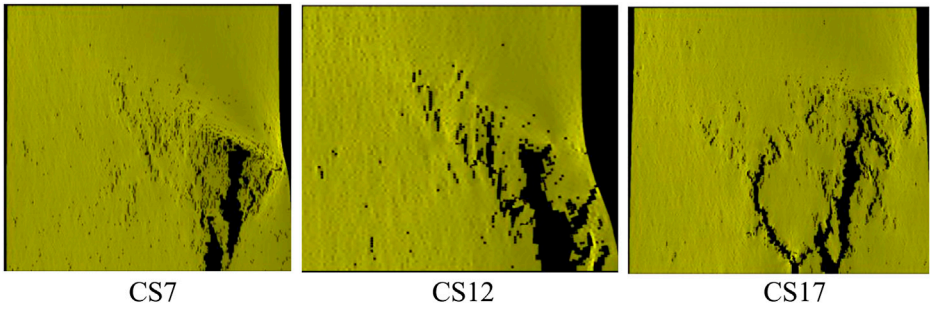

FIGURE 4
Failure modes of samples with different strength under water pressure at the same lower boundary.

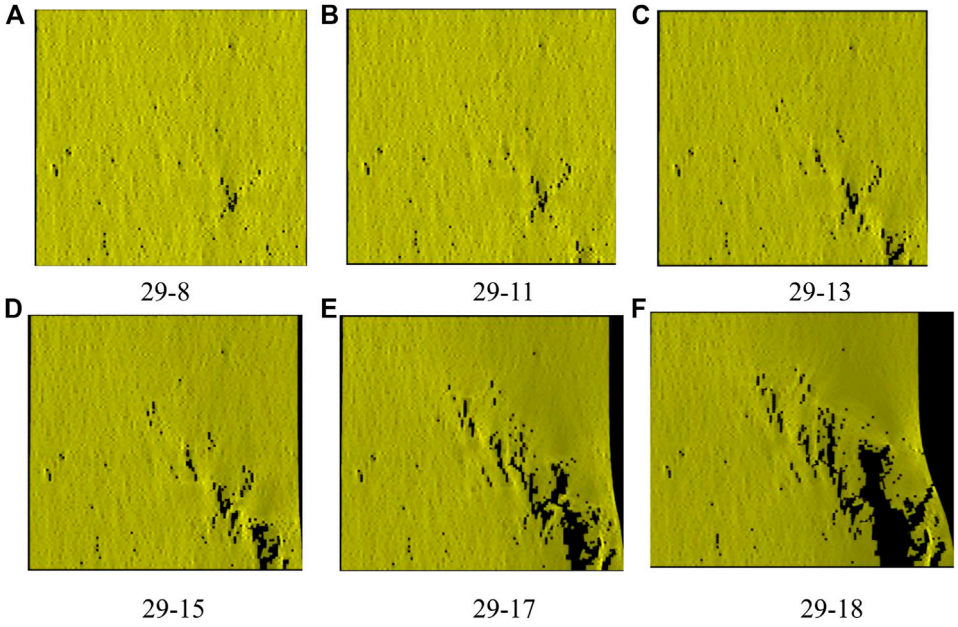

FIGURE 5
Fracture process of WP5 (CS5) sample. Loading step 29-8, Loading step 29-11, Loading step 29-13, Loading step 29-15, Loading step 29-17, Loading step 29-18.

where λ_0 is the initial permeability coefficient, p is the pore pressure, ξ, ∂, β are the increase rate of the permeability coefficient, the pore pressure coefficient and the coupling coefficient, respectively.

Numerical model

The size of the grouting concretion body is 70.7 mm × 70.7 mm, and the numerical model is composed of 202 × 202 mesoscopic units. The mechanical parameters of the unit obey the Weibull distribution. The mechanical model of the grouting concretion body under the action of water-force coupling is simplified into a plane strain problem in RFPA software for research (see Figure 1). The physical and mechanical parameters of grouting concretion body are shown in Table 1. The displacement loading method is adopted, and the displacement increment of each step is 0.005 mm/step. As the grouting concretion body belongs to brittle material, which is compressive but not tensile, the constitutive relationship of grouting concretion body in numerical simulation is simplified to elastic brittleness, as shown in Figure 2.

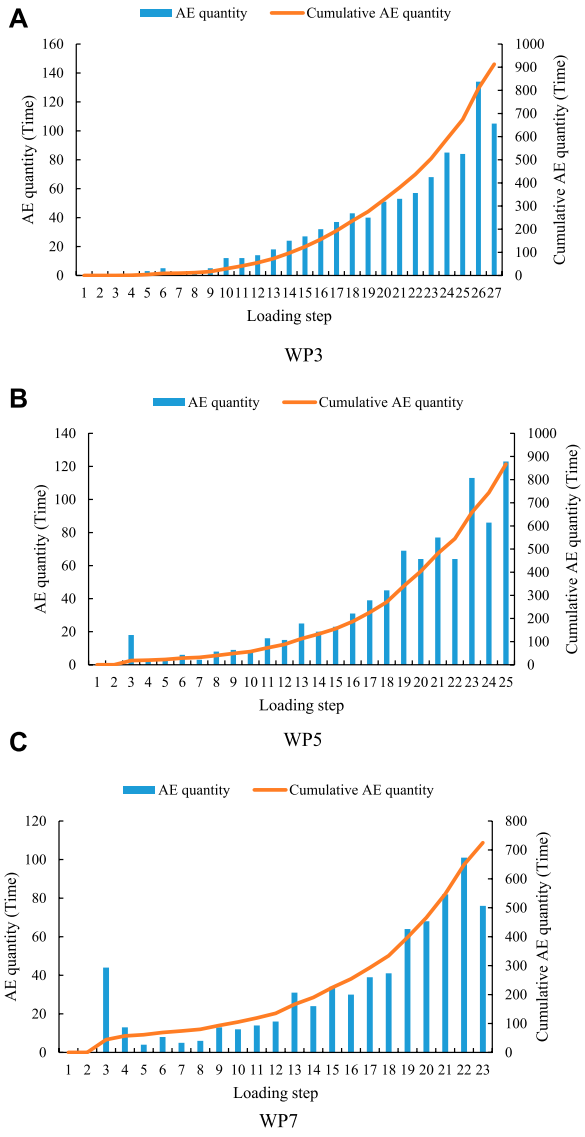

FIGURE 6
Variation trend of AE quantity of water pressure samples with the same strength and different lower boundary.

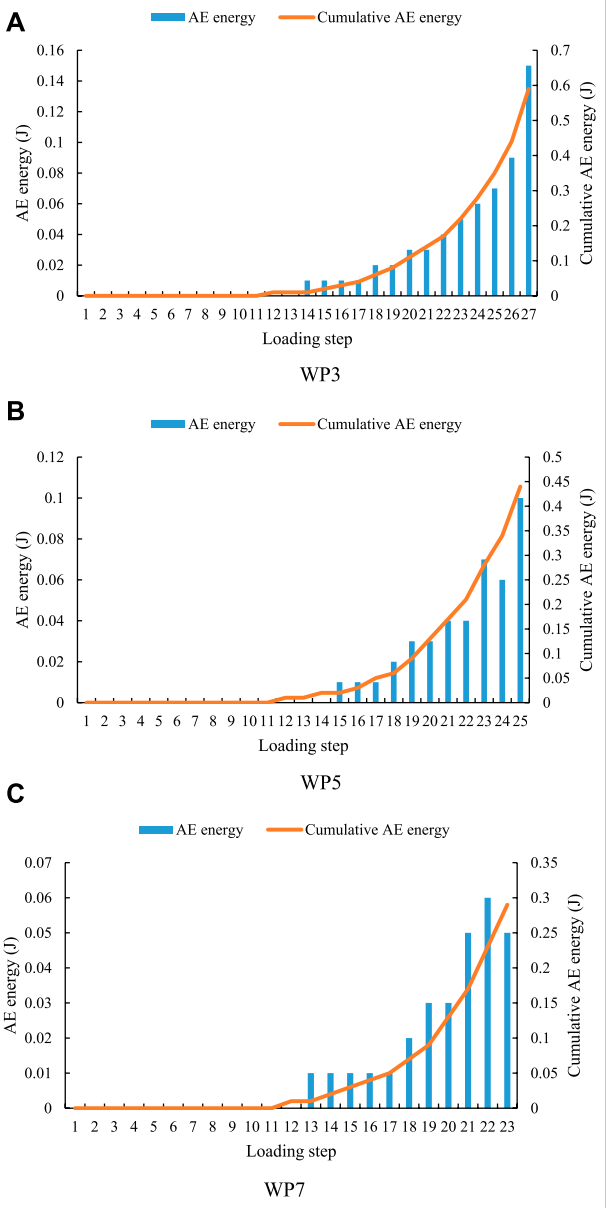

FIGURE 7
AE energy variation trend of water pressure samples with the same strength and different lower boundaries.

TABLE 2 AE values of different lower boundaries water pressure samples with the same strength.

Numerical model	WP3	WP5	WP7
Maximum AE quantity (Time)	134	123	101
Cumulative AE quantity (Time)	913	867	725
Maximum AE energy(J)	0.15	0.1	0.06
Cumulative AE energy(J)	0.59	0.44	0.29

In order to study the influence of different water pressure on the failure characteristics of grouting concretion body, the compressive strength of grouting concretion body is 12.55 MPa, the upper boundary water pressure P_1 is 1 MPa, and the lower boundary water pressure P_2 is 3 MPa, 5 MPa and 7 MPa respectively. Each sample is marked as WP3, WP5 and WP7 respectively. In order to study the failure characteristics of grouting concretion bodies with

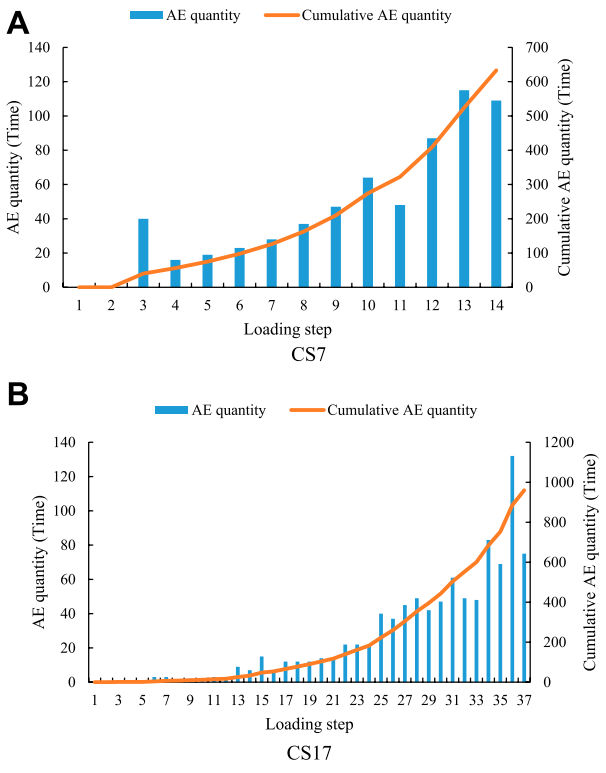

FIGURE 8
Variation trend of AE quantity of samples with different strength under the same lower boundary water pressure.

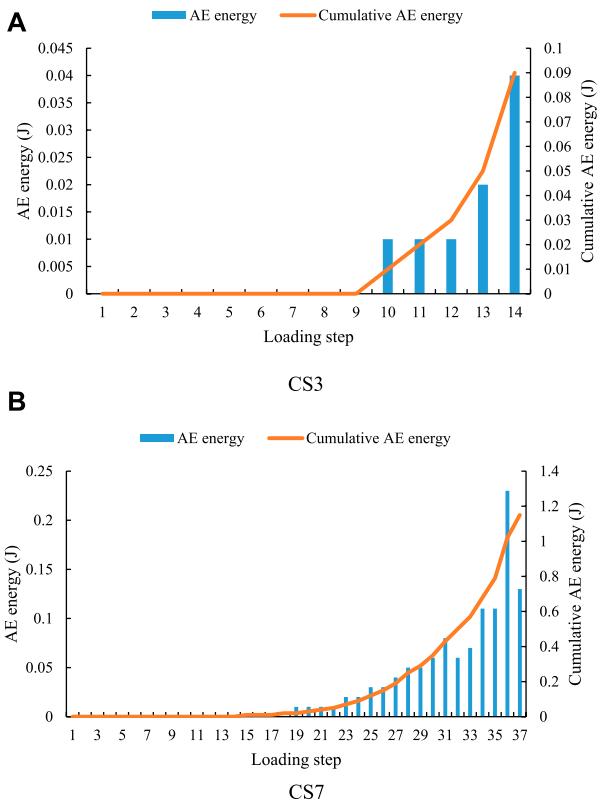

FIGURE 9
Variation trend of AE energy of samples with different strength under the same lower boundary water pressure.

different compressive strengths under the action of water-force coupling, the upper boundary water pressure and the lower boundary water pressure of the numerical model are taken as 1 MPa and 5 MPa respectively, and the compressive strengths of the grouting concretion bodies are 7.55 MPa, 12.55 MPa and 17.55 MPa respectively. Each sample is marked as CS7, CS12 (WP5) and CS17 respectively. Note: In two different comparative tests, WP5 sample and CS12 sample are the same sample.

Numerical simulation results and analysis

Comparative analysis of specimen fracture morphology

Figure 3 shows the failure modes of water pressure samples with the same strength and different lower boundaries. It can be seen from Figure 3 that when the lower boundary water pressure is 3 MPa, the fracture morphology of the sample is the most serious, and a serious fracture zone appears on the right side of the sample. When the water pressure at the lower boundary is 7 MPa, the fracture morphology of the sample is relatively light, and only a macroscopic crack appears in the lower left corner of the sample. When the water pressure at the lower boundary is 5 MPa, the fracture severity of the sample is between the lower boundary water pressure of 3 MPa and 7 MPa, and a serious fracture zone appears in the lower right corner of the sample. The above numerical test phenomenon shows that the smaller the lower boundary water pressure the specimen bears, the more serious the fracture morphology of the specimen. The reason for the above test phenomenon is that the lower the water pressure at the lower boundary is, the lower the softening degree of the sample is, and the sample is more prone to brittle fracture under external load. The greater the water pressure at the lower boundary, the higher the softening degree of the sample, and the sample is more likely to crack in a certain local area under the action of external load.

Figure 4 shows the failure modes of samples with different strength under water pressure at the same lower boundary. As can be seen from Figure 4, when the compressive strength of the sample is 17.55 MPa, the fracture morphology of the sample is the most serious, and multiple macroscopic penetrating fracture zones appear on the right side of the sample. When the compressive strength of the sample is 7.55 MPa, the fracture morphology of the sample is

TABLE 3 AE values of samples with different strength under the same lower boundary water pressure.

Numerical model	CS7	CS12 (WP5)	CS17
Maximum AE quantity (Time)	115	123	132
Cumulative AE quantity (Time)	633	867	960
Maximum AE energy(J)	0.04	0.1	0.23
Cumulative AE energy(J)	0.09	0.44	1.15

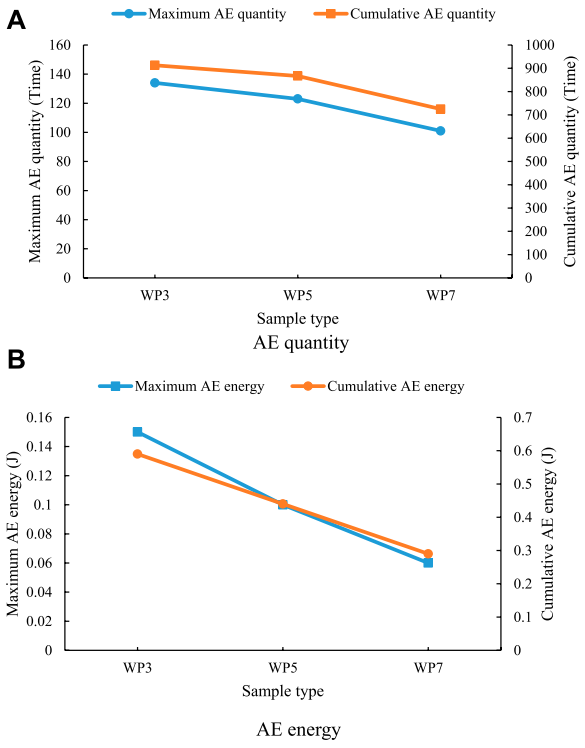

FIGURE 10
AE Comparison Curve of samples with the same compressive strength and different lower boundaries water pressure.

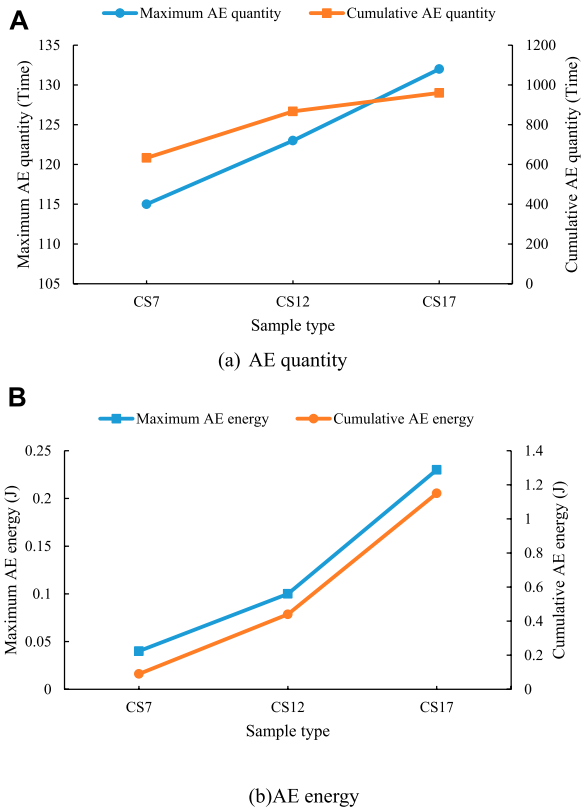

FIGURE 11
AE Comparison Curve of samples with the same lower boundaries water pressure and different compressive strength.

relatively light, and only a macroscopic crack appears in the lower right corner of the sample. When the compressive strength of the sample is 12.55 MPa, the fracture severity of the sample is between the compressive strength of 7.55 MPa and 17.55 MPa. A macroscopic crack also appears in the lower right corner of the sample, and there is a macroscopic penetrating crack in the upper left side of this macroscopic crack. The above numerical test phenomenon shows that the greater the compressive strength of the sample, the more serious the fracture morphology of the sample.

Figure 5 shows the fracture process of WP5 sample (with compressive strength of 12.55 MPa and lower boundary water pressure of 5 MPa). Under the influence of inhomogeneity, the unit with weak strength in the sample first breaks, as shown in Figure 5A,B. Continue to load. Since the water pressure at the lower part of the sample is higher than that at the upper part, the lower part of the sample also breaks, as shown in Figure 5C. Under the combined action of external force and water pressure, the cracks inside the sample and the cracks at the lower boundary of the sample slowly penetrate, as shown in Figure 5D,E. When the external force further increases and exceeds the compressive strength of the rock mass, the crack already penetrated in the lower right corner of the sample further increases and finally forms a macroscopic crack, as shown in Figure 5F.

Comparative analysis of AE parameters

As shown in Figures 6, 7, when the water pressure at the lower boundary is 3 MPa, the AE quantity reaches the maximum of 134 at step 26 (see Table 2), and the AE energy reaches the maximum of 0.15 J at step 27. When the water pressure at the lower boundary is 5 MPa, the AE quantity and energy have two peaks. The AE quantity reached the maximum of 123 at step 25, and the AE energy also reached the maximum of 0.1 J at step 25. At the beginning of the force, the AE quantity shows a sudden rise and fall phenomenon at

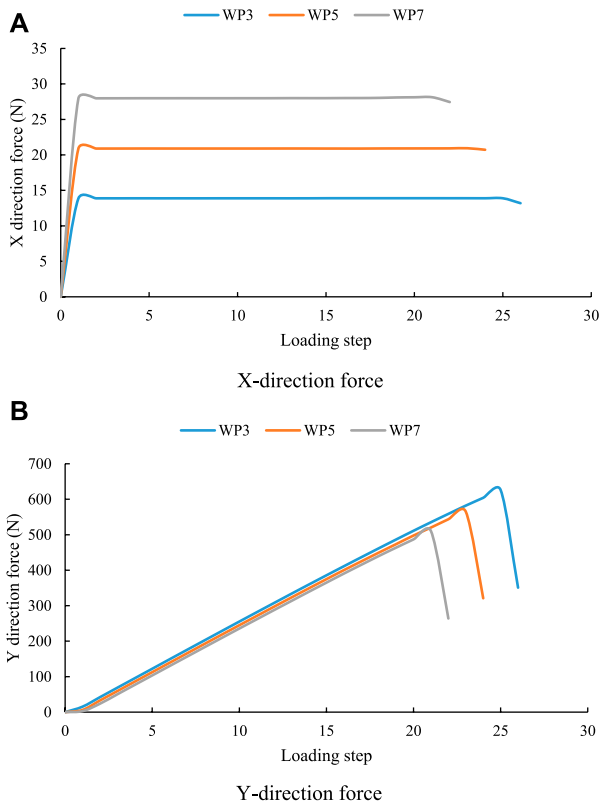

FIGURE 12
Force variation trend of samples with the same strength and different lower boundary water pressure.

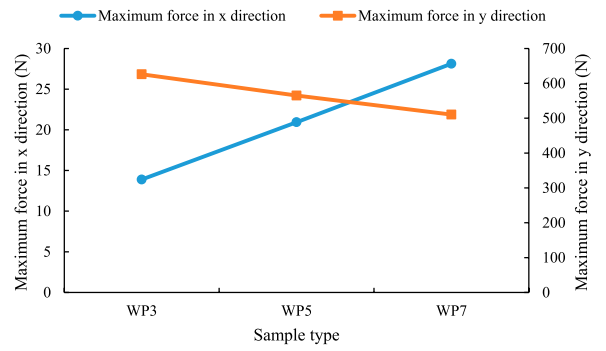

FIGURE 13
Force comparison curve of samples with the same strength and different lower boundary water pressure.

the third step. Moreover, the quantity and energy of AE also appear the first peak at step 23. When the quantity and energy of AE reach the peak for the second time, the sample is completely destroyed. The appearance of the first peak can be used as an early warning, indicating that the sample is about to be completely destroyed.

TABLE 4 Maximum force of lower boundary water pressure samples with the same strength.

Numerical model	WP3	WP5	WP7
Maximum force in x direction (N)	13.89	20.94	28.13
Maximum force in y direction (N)	626.06	565.11	510.37

When the water pressure at the lower boundary is 7 MPa, the AE quantity reaches the maximum value of 101 at step 22, and the AE energy reaches the maximum value of 0.06 J at step 22. At the beginning of the force, the quantity of AE shows a sudden rise and fall phenomenon at the third step. No matter what kind of water pressure the sample is subjected to, the AE cumulative quantity curve and the AE cumulative energy curve are relatively smooth, and there is no obvious jump phenomenon. It can be seen from the above analysis that with the increase of water pressure at the lower boundary, the times when the maximum value of AE quantity and energy occurs are earlier.

As shown in Figures 8, 9, when the compressive strength of the sample is 7.55 MPa, the AE quantity of the sample reaches the maximum of 115 at step 13 (see Table 3), and the AE quantity shows a sudden rise and fall phenomenon at step 3. The AE energy of the sample appears in step 10. Continue loading, and the AE energy reaches the maximum value of 0.04 J in step 14. When the compressive strength of the sample is 17.55 MPa, the AE quantity of the sample reaches the maximum of 132 in step 36, and the AE energy also reaches the maximum of 0.23 J in step 36. Since CS12 and WP5 are the same sample, the variation trend of AE quantity and energy of CS12 sample is shown in sample WP5. It can be seen from the above analysis that with the increase of the compressive strength of the sample, the time when the maximum value of AE quantity and energy occurs is later. This experimental phenomenon shows that the greater the compressive strength of the sample, the stronger the failure resistance of the sample. Under the same external conditions, increasing the water cement ratio of the sample can improve the service time of the sample.

As shown in Figure 10, when the water pressure at the lower boundary is 3 MPa, the maximum AE quantity, cumulative AE quantity, maximum AE energy, and cumulative AE energy are all the largest. When the water pressure at the lower boundary is 7 MPa, the maximum AE quantity, cumulative AE quantity, maximum AE energy and cumulative AE energy are all the minimum. This numerical simulation phenomenon shows that the AE decreases gradually with the increase of the water pressure at the lower boundary. Moreover, the maximum AE energy and the accumulated AE energy obviously decrease linearly.

As shown in Figure 11, when the compressive strength is 7.55 MPa, the maximum AE quantity, cumulative AE quantity, maximum AE energy, and cumulative AE energy are all minimum. When the water pressure at the lower boundary is 17.55 MPa, the

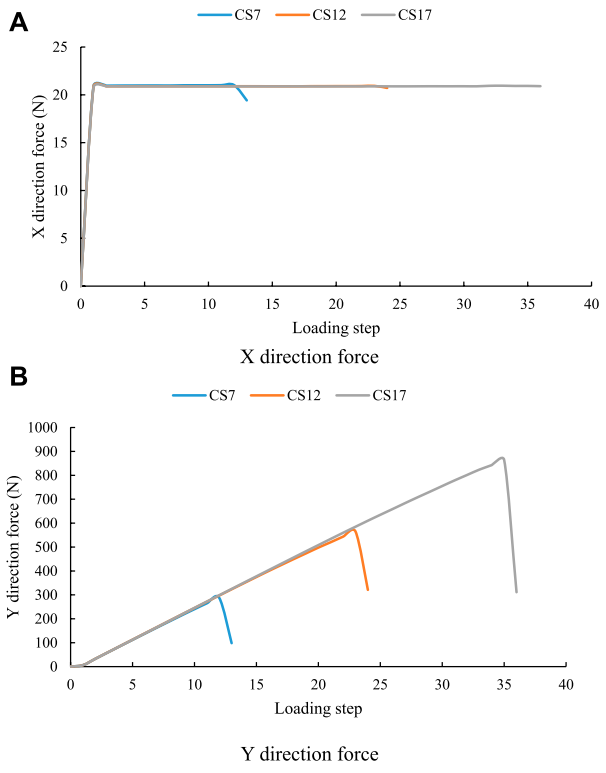

FIGURE 14
Force variation trend of samples with different strength under the same lower boundary water pressure.

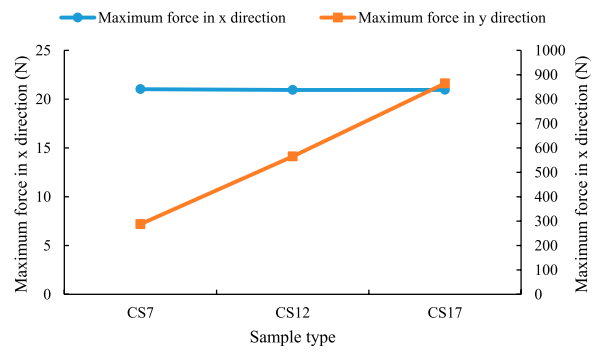

FIGURE 15
Force comparison curves of the samples with different strengths under the same lower boundary water pressure.

maximum AE quantity, the cumulative AE quantity, the maximum AE energy and the cumulative AE energy are all the largest. This numerical simulation phenomenon shows that the AE increases gradually with the increase of compressive strength. Moreover, the maximum AE energy and the accumulated AE energy show a significant increase.

TABLE 5 Maximum force values of samples with different strength under the same lower boundary water pressure.

Numerical model	CS7	CS12 (WP5)	CS17
Maximum force in x direction (N)	21.02	20.94	20.95
Maximum force in y direction (N)	287.59	565.11	864.54

Comparative analysis of force

The force curves in the X direction of the three samples with the same compressive strength and different lower boundary water pressure basically do not change with the increase of external force, and the slope of the force curves in the Y direction of the growth stage is basically the same (see Figure 12). The maximum forces on the X direction of the three samples from large to small are WP3, WP5 and WP7 (see Figure 13), and their values are 13.89 N, 20.94 N and 28.13 N respectively (see Table 4). The maximum forces on the Y direction of the three samples from large to small are WP7, WP5 and WP3, and their values are 626.06 N, 565.11 N and 510.37 N respectively. Regardless of the water pressure at the lower boundary, the force in the Y direction is far greater than that in the X direction. The maximum force in X direction increases linearly with the increase of water pressure, while the maximum force in Y direction decreases linearly with the increase of water pressure.

The force curve in the X direction of the three samples with the same compressive strength and different lower boundary water pressure basically does not change with the increase of external force, and the slope of the force curve in the Y direction of the growth stage is basically the same (see Figure 14). The maximum forces in the X direction of the three samples are basically the same (see Figure 15), and their values are 21.02 N, 20.94 N and 20.95 N respectively (see Table 5). The maximum force values of the three samples in Y direction from small to large are CS7, CS12 and CS17, whose values are 287.59 N, 565.11 N and 864.54 N, respectively. Regardless of the compressive strength of the sample, the force in Y direction is much larger than that in X direction. The maximum force in the X direction has no obvious relationship with the compressive strength of the sample, while the maximum force in the Y direction increases linearly with the increase of compressive strength, and the increase amplitude is very large.

Conclusion

Different lower boundary water pressure and different compressive strength lead to different fracture forms of the samples. However, the force curves in the X direction all show elastic-plastic, and the force curves in the Y direction all show elastic-

brittle. The greater the lower boundary water pressure is, the higher the softening degree of the sample is, and the sample is more likely to crack in a certain local area under the action of external load.

Under the same external conditions, increasing the compressive strength of the sample, that is, increasing the water-cement ratio of the sample, can improve the service life of the sample. However, the brittleness of the samples increases with the increase of the compressive strength, and the brittle fracture morphology of the samples becomes more serious.

The AE values and the maximum force in X direction of the samples with different lower boundary water pressure of the same compressive strength decrease inversely with the lower boundary water pressure. The maximum force in Y direction increases in direct proportion to the lower boundary water pressure.

The AE quantity and the maximum force in Y direction of the samples with different strength under the same lower boundary water pressure increase in positive proportion to the compressive strength of the samples. The maximum force in X direction has no correlation with the compressive strength of the sample, and the maximum force in X direction of the three samples is basically the same.

Data availability statement

The original contributions presented in the study are included in the article/supplementary material, further inquiries can be directed to the corresponding authors.

Author contributions

FT: Writing Original Draft and Data Curation; DD: Review; ZX: Conceptualization; ZG: Funding acquisition.

Funding

This study was supported by the National Natural Science Foundation of China (No. 41972255, 42207084).

Conflict of interest

The author ZG was employed by Power China Northwest Engineering Corporation Limited.

The remaining authors declare that the research was conducted in the absence of any commercial or financial relationships that could be construed as a potential conflict of interest.

Publisher's note

References

Cai, M. F. (2020). Key theories and technonogies for surrounding rock stability and ground control in deep mining[J]. *J. Min. Strata Control Eng.* 2 (3), 5–13. doi:10.13532/j.jmsce.cn10-1638/td.20200506.001

Chen, F., Du, Y-H., Sun, X-M., Ma, T-H., and Tang, C. (2021). Numerical experimental study on influence factors of anchoring force of constant resistance bolt. *Geomat. Nat. Hazards Risk* 12 (1), 424–442. doi:10.1080/19475705.2021.1880490

Chen, F., Wang, X-B., Du, Y-H., and Tang, C. (2021). Numerical analysis of the precursory information of slope instability process with constant resistance bolt. *Sci. Rep.* 11 (1), 21814–21910. doi:10.1038/s41598-021-01387-z

Chen, F., Wang, X-B., Du, Y-H., and Tang, C. (2022). Numerical experiment research on failure characteristics of anchored rock with negative Poisson's ratio bolt[J]. *Front. Earth Sci.* 10, 1–10. doi:10.3389/feart.2022.89975

Evdokimov, P. D., Adamovich, A. N., Fradkin, L. P., and Denisov, V. N. (1970). Shear strengths of fissures in ledge rock before and after grouting. *Hydrotech. Constr.* 4 (3), 229–233. doi:10.1007/bf02376472

Fan, L., and Ma, X. (2018). A review on investigation of water-preserved coal mining in Western China. *Int. J. Coal Sci. Technol. Technol.* 5 (4), 411–416. doi:10.1007/s40789-018-0223-4

Gao, Y., Fan, Q. Z., and Wang, H. (2004). Grouting reinforcement test of rock after peak value of strength and roadway stability control[J]. *Rock Soil Mech.* 25 (1), 21–24. doi:10.16285/j.rsm.2004.s1.005

Han, L., Zong, Y., and Han, G. (2011). Study of shear properties of rock structural plane by grouting reinforcement[J]. *Rock Soil Mech.* 32 (9), 2570–2622. doi:10.16285/j.rsm.2011.09.011

He, M., Xie, H., and Peng, S. (2005). Study on rock mechanics in deep mining engineering[J]. *Chin. J. Rock Mech. Eng.* 24 (16), 2803–2813

Hyett, A. J., Ba Wden, W. F., and Reichert, R. D. (1992). The effect of rock mass confinement on the bond strength of fully grouted cable bolts. *Int. J. Rock Mech. Min. Sci. Geomechanics Abstr.* 29 (5), 503–524. doi:10.1016/0148-9062(92)92634-o

Lei, J. S., Liu, F., and Wang, Q. F. (2015). Diffusion characteristics and reinforcement mechanics of grouting in non-homogeneous soil strata[J]. *Chin. J. Geotechnical Eng.* 32 (12), 2245–2253. doi:10.11779/CJGE201512014

Liu, Q. S., Lei, G. F., Peng, X. X., Lu, C., and Wei, L. (2018). Rheological characteristics of cement grout and its effect on mechanical properties of a rock fracture. *Rock Mech. Rock Eng.* 51, 613–625. doi:10.1007/s00603-017-1340-x

Liu, Z. X., Dong, S., and Wang, H. (2021). Influences on the performance of cement-based grout used to reform the upper Middle Ordovician limestone in Hanxing mining area[J]. *Arabian J. Geosciences* 14 (13), 1–15. doi:10.1007/s12517-021-07512-6

Meng, B., Jing, H., Chen, K., and Su, H. (2013). Failure mechanism and stability control of a large section of very soft roadway surrounding rock shear slip. *Int. J. Min. Sci. Technol.* 23 (1), 127–134. doi:10.1016/j.ijmst.2013.03.002

Nikbakhtan, B., and Osanloo, M. (2009). Effect of grout pressure and grout flow on soil physical and mechanical properties in jet grouting operations. *Int. J. Rock Mech. Min. Sci. (1997).* 46 (3), 498–505. doi:10.1016/j.ijrmms.2008.10.005

Niu, X., Wang, H., and Liu, S. (2017). Application and development trends on grouting reconstruction technology for floor karst aquifers of lower group coal seam in Northern China coal field[J]. *Mine Constr. Technol.* 38 (3), 24–30. doi:10.19458/j.cnki.cn11-2456/td.2017.03.008

Pan, R., Cheng, H., and Wang, L. (2020). Experimental study on bearing characteristics of bolt grouting in shallow fractured surrounding rock of roadway[J]. *Rock Soil Mech.* 41 (6), 1887–1898. doi:10.16285/j.rsm.2019.6448

Tang, C. A. (2003). *Numerical experiments of rock failure process[M]*. Beijing: Science Press. (in Chinese).

Tang, C. A., Liu, H., Lee, P. K. K., Tsui, Y., and Tham, L. G. (2000). Numerical studies of the influence of microstructure on rock failure in uniaxial compression - Part I: Effect of heterogeneity. *Int. J. Rock Mech. Min. Sci. (1997)* 37 (4), 555–569. doi:10.1016/s1365-1609(99)00121-5

Tuerkmen, S., and Oezguezel, N. (2003). Grouting a tunnel cave-in from the surface: A case study on kurtkula irrigation tunnel, Turkey[J]. *Tunn. Undergr. Space Technol. Incorporating Trenchless Technol. Res.* 18 (4), 365–375. doi:10.1016/S0886-7798(03)00007-5

Wael, M., Ahmed Salih, M., and Parveen, S. (2021). Interpreting the experimental results of compressive strength of hand-mixed cement-grouted sands using various mathematical approaches[J]. *Archives Civ. Mech. Eng.* 22 (1), 1–25. doi:10.1007/s43452-021-00341-0

Wang, H., Gao, Y., and Li, S. (2007). Uniaxial experiment study on mechanical properties of reinforced broken rocks pre-and-post grouting[J]. *Chin. J. Undergr. Space Eng.* 3 (1), 27–39.

Wang, Q., Gao, H. K., Yu, H. C., Jiang, B., and Liu, B. (2019). Method for measuring rock mass characteristics and evaluating the grouting-reinforced effect based on digital drilling. *Rock Mech. Rock Eng.* 52, 841–851. doi:10.1007/s00603-018-1624-9

Wang, Q., He, M. C., Yang, J., Gao, H., Jiang, B., and Yu, H. (2018). Study of a no-pillar mining technique with automatically formed gob-side entry retaining for longwall mining in coal mines. *Int. J. Rock Mech. Min. Sci.* 110, 1–8. doi:10.1016/j.ijrmms.2018.07.005

Xie, H., Gao, F., and Yang, J. (2015). Research and development of rock mechanics in deep ground engineering[J]. *Chin. J. Rock Mech. Eng.* 34 (11), 2161–2178. doi:10.13722/j.cnki.jrme.2015.1369

Xiujun, W., Gao, M., and Lv, Y. C. (2012). Evolution of a mining induced fracture network in the overburden strata of an inclined coal seam[J]. *Int. J. Min. Sci. Technol.* 22 (6), 775–779. doi:10.1016/j.ijmst.2012.11.004

Yang, T. (2004). *Seepage characteristic in rock failure: Theory, model and application[M]*. Beijing: Science Press. (in Chinese).

Zhang, C., Chang, J., and Li, S. (2019). Experimental study comparing the microscopic properties of a new borehole sealing material with ordinary cement grout[J]. *Environ. Earth Sci.* 78 (5), 1–11. doi:10.1007/s12665-019-8165-8

Zhang, F., and Barry, L. (2019). A numerical study to assist assessment of the stability of shallow coal mine goafs. *Geotech. Geol. Eng. (Dordr).* 37 (4), 2837–2846. doi:10.1007/s10706-018-00799-5

Zhang, Q. S., Zhang, L. Z., and Liu, R. (2015b). Laboratory experimental study of cement-silicate slurry diffusion law of crack grouting with dynamic water[J]. *Rock Soil Mech.* 36 (8), 2159–2168. doi:10.16285/j.rsm.2015.08.005

Zhang, R., Dai, F., Gao, M. Z., Xu, N., and Zhang, C. (2015a). Fractal analysis of acoustic emission during uniaxial and triaxial loading of rock. *Int. J. Rock Mech. Min. Sci. (1997). Min. Sci.* 79, 241–249. doi:10.1016/j.ijrmms.2015.08.020

Zhao, K., Wang, H., and Xu, W. (2017). Experimental study on seepage characteristics of rock-like materials with consecutive and filling fractures[J]. *Chin. J. Geotechnical Eng.* 39 (6), 1130–1136. doi:10.11779/CJGE201706020

Zhou, D., Zhao, Z., Bo, L., Chen, Y., and Ding, W. (2020). Permeability evolution of grout infilled fractures subjected to triaxial compression with low confining pressure. *Tunn. Undergr. Space Technol.* 104, 103539. doi:10.1016/j.tust.2020.103539

Zhou, W., Yang, R., and Yan, G. (1993). Study on the efficacy of grouting reinforcement of slightly weathered rock masses at the Ertan arch dam abutments [J]. *Chin. J. Rock Mech. Eng.* 12 (2), 138–150.

Zong, Y., Han, L., and Han, G. (2013). Mechanical characteristics of confined grouting reinforcement for cracked rock mass[J]. *J. Min. Saf. Eng.* 30 (4), 483–488.

frontiers | Frontiers in Earth Science

TYPE Original Research
PUBLISHED 20 January 2023
DOI 10.3389/feart.2022.1077652

OPEN ACCESS

EDITED BY
Yu Song,
China University of Mining and Technology, China

REVIEWED BY
Guofa Ji,
Yangtze University, China
Kaizong Xia,
Institute of Rock and Soil Mechanics (CAS), China

*CORRESPONDENCE
Yulin Ma,
hxwyaoyao@163.com

SPECIALTY SECTION
This article was submitted to Economic Geology,
a section of the journal
Frontiers in Earth Science

RECEIVED 23 October 2022
ACCEPTED 21 November 2022
PUBLISHED 20 January 2023

CITATION
Ma Y, Wang D and Zheng Y (2023), Influence of the bedding plane on the propagation of multiple hydraulic fractures.
Front. Earth Sci. 10:1077652.
doi: 10.3389/feart.2022.1077652

Influence of the bedding plane on the propagation of multiple hydraulic fractures

Yulin Ma[1]*, Ding Wang[1] and Yongxiang Zheng[2]

[1]School of Mechanics and Engineering, Liaoning Technical University, Fuxin, China, [2]School of Civil Engineering, Shijiazhuang Tiedao University, Shijiazhuang, China

The presence of bedding planes (BPs) in unconventional shale reservoirs is common and widespread. BPs always affect fracture propagation. The objective of this study was to investigate the impacts of BPs on multiple hydraulic fracturing. The BPs were assumed to be perpendicular to the direction of the fractures. Based on the block distinct element method, we established a numerical model to simulate multiple fracture propagation in reservoirs with BPs. The model considered the fluid partitioning of multiple fractures and the fracture interaction by stress shadow. The numerical simulations clearly showed that the BPs reduced the non-uniform growth of multiple fractures. The results indicated that when hydraulic fractures met BPs, the BPs likely prevented the hydraulic fractures from passing through the formation with a smaller stress contrast. When hydraulic fracturing in a formation containing BPs, the key problem is how to reduce the obstructive effects of the BPs to increase the length of the main fractures.

KEYWORDS

hydraulic fracturing, multiple fracture propagation, bedding planes, block distinct element method, stress inference

1 Introduction

Multiple hydraulic fracturing in horizontal wells can increase the complexity of the fracture network after fracturing and can stimulate reservoirs to exploit hydrocarbon in unconventional reservoirs. This is an important guarantee for the commercial exploitation of shale gas. The main methods of multiple-stage fracturing include sequential fracturing, simultaneous fracturing, and alternating fracturing (Roussel and Sharma, 2011). Simultaneous fracturing is a simple and practical method in which the length of each fracture is not uniform. This is because the fracture is affected by the induced stress of adjacent fractures. The issues of multiple fracture propagation mainly include stress interference between fractures, flow partition of each fracture, and fracture propagation competition.

As for the propagation of multiple fractures, the propagation of every fracture is interactional. Every fracture interacts with other fractures by stress interference. Olson (2008) was one of the earliest to conduct a numerical simulation of multi-fracture propagation. Due to mechanical fracture interaction, he discovered that the fractures at the array's ends had the most freedom to open. Roussel and Sharma (2011) investigated

three fracturing sequences for a typical field in the Barnett Shale. The study demonstrated the potential advantages of alternate fracture sequencing and zipper fracs to improve the performance of stimulation treatments in horizontal wells. Peirce and Bunger (2015) confirmed the phenomenon of inner-fracture suppression because of stress shadowing when the perforation clusters were uniformly distributed. Wu and Olson (2015) and Wu and Olson (2016) developed a novel fracture-propagation model. Stress interaction among multiple hydraulic fractures and fluid flow in the single fracture and the horizontal wellbore were integrated into this model. Salimzadeh et al. (2017) applied a fully coupled three-dimensional finite element model to investigate the interaction between multiple simultaneous and sequential hydraulic fractures. Chen et al. (2018) implemented a three-dimensional numerical model to simulate the simultaneous growth of hydraulic fractures in multi-well fracturing. The above-mentioned studies emphasized multiple fracture propagation. In summary, the critical issues for multiple fracture propagation are the stress shadow, the dynamical fluid partition, and the non-uniform growth of multiple hydraulic fractures. Besides, Xie et al. (2020) proposed a new damage constitutive model related to the Weibull distribution and statistical damage theory. The model considers the shear stiffness degradation, post-peak softening, and residual phase of rock joints in the whole shearing process. Li et al. (2018) examined the effect of the erosion of perforation. The results indicated that the erosion significantly deteriorated the non-uniform growth of multiple fractures. Zeng et al. (2018) studied the propagation of multiple hydraulic fractures in an anisotropic formation.

The research methods for multiple fracture propagation include laboratory experiments and numerical simulation. Many explorations have been made using experimental methods to study the various indicators of the rock (Cao et al., 2016; Wang et al., 2020). The principal numerical methods are the Implicit Level Set Algorithm (ILSA) (Dontsov and Peirce, 2017; Peirce and Bunger, 2015), finite element method (FEM) (Salimzadeh et al., 2017), discrete element method (DEM) (Maxwell, 2016; Zhang and Dontsov, 2018; Zheng et al., 2019a; Zhu et al., 2019), discontinuous displacement method (DDM) (Zou et al., 2016a) and phase field method (Wick et al., 2016). Besides, Xu et al. (2017) applied embedded discrete fracture modeling (EDFM) formulation to reservoir simulators with complex geometries. These numerical simulations were mostly 2D and pseudo-3D models (Tang et al., 2019). More recently, three-dimensional models have been built. Kumar and Ghassemi (2018) presented a fully coupled three-dimensional poroelastic analysis of multiple fracture propagation for horizontal wells. Kresse and Weng (2018) believed that the 3D stress shadow affects multistage fracturing in vertical or deviated wells and in multi-well treatments. In the numerical simulation of multiple fracturing, the aforementioned studies conducted a comprehensive study on the mechanism of multiple fracture propagation under simultaneous fracturing.

In unconventional shale reservoirs, the presence of bedding planes (BPs) is common. However, the influence of BPs has not been comprehensively considered yet. Few studies have considered the influence of the BPs on shale reservoirs. Relevant studies have shown that BPs can affect the propagation of fractures. Zheng et al. (2019a) Zheng et al. (2019b) examined the effect of the bedding plane on a single fracture by using the 3DEC software. The results suggested that the fracture propagation behavior was relevant to the intersection angle between the fracture and bedding, and when the bedding was perpendicular to the fractures, the bedding possibly hindered the fracture propagation. Zou et al. (2016b) conducted a series of numerical simulations to illustrate the influence of anisotropy, associated with the presence of BPs, on the geometry of hydraulic fracture network propagation in shale formations. Tan et al. (2017) performed true triaxial hydraulic fracturing experiments using laminated shale outcrops. The study demonstrated that the distance between the injection point and the bedding plane was also a key factor that affected the fracture propagation results. However, when the BPs that exist in the formation are considered, there are few studies on the simultaneous propagation of multiple fractures. Therefore, the objective of this research was to scrutinize the effects of BPs on multiple hydraulic fracturing to fill the gap.

We applied a 3D block distinct element method considering the stress interference and the flow partition of fractures to calculate the multiple fracture propagation in a formation with BPs. In our study, we investigated the effect of BPs on multiple fracture propagation. The role of BPs on fracture propagation is discussed in detail. Our numerical model is a fully 3-dimensional model that can simulate the spatial features, such as lateral propagation of fractures, that two-dimensional models cannot. The numerical simulations of multiple fracturing in a formation with BPs were conducted to study the effect of BPs. The impacts of *in-situ* stress, the distance from the bedding plane to the wellbore, and bedding number in multi-stage hydraulic fracturing with BPs are discussed in-depth.

2 Numerical model and validation

2.1 The block distinct element method

The numerical modeling has been conducted by the 3D block distinct element method (BDEM) (Cundall, 1988; Hart et al., 1988; Zhang and Dontsov, 2018; Zheng et al., 2019b). In BDEM, the material is modeled using two parts: one part is composed of blocks and the other part is composed of joints. These two parts constitute the discontinuous medium. The deformation characteristics of blocks are described by the stress-displacement

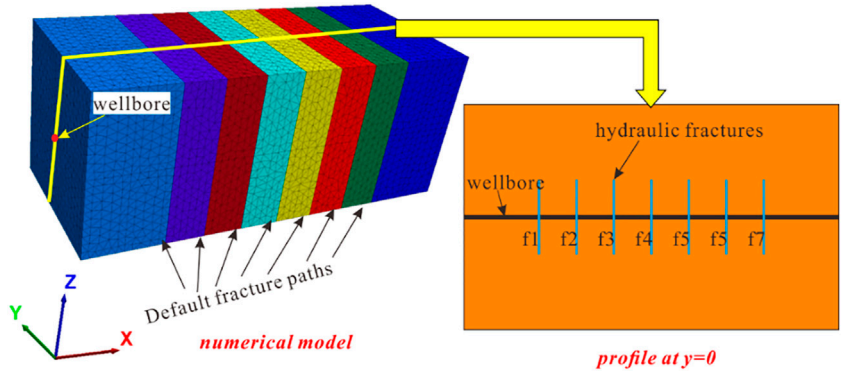

FIGURE 1
Numerical model for multiple hydraulic fractures.

relationship. The stress-displacement relationship is expressed as follows:

$$\begin{Bmatrix} \sigma \\ \tau \end{Bmatrix} = \begin{Bmatrix} K_n & K_{ns} \\ K_{sn} & K_s \end{Bmatrix} \begin{Bmatrix} \delta_s \\ \delta_n \end{Bmatrix} \quad (1)$$

where $K_n = \frac{\partial \sigma}{\partial \delta_n}$, which is the normal stiffness coefficient; $K_s = \frac{\partial \tau}{\partial \delta_s}$, which is the shear stiffness coefficient; $K_{ns} = \frac{\partial \sigma}{\partial \delta_s}$, which is the dilation stiffness coefficient; $K_{sn} = \frac{\partial \tau}{\partial \delta_n}$, which represents the effect of normal displacement on shear stress.

The shear strength of joints is described by the Mohr-Coulomb (M-C) criterion. The contact friction joint model is used in this calculation. This model assumes that the joints have no thickness and that both sides of the blocks are in close contact. One surface is regarded as the target surface, and the other is considered the contact surface. The details of BDEM were introduced and elaborated on in our previous work (Zheng et al., 2019a and Zheng et al., 2019b).

2.2 Validation of the multiple fracturing in the formation without bedding planes

2.2.1 Model description

Some studies (Maxwell, 2016; Zhang and Mack, 2017; Zhang and Dontsov, 2018; Zheng et al., 2019a; Zhu et al., 2019) have used BDEM to simulate hydraulic fracturing. The results of these studies indicated that BDEM could well simulate the propagation of a single fracture and the interaction between hydraulic fracture and natural fracture. Therefore, we did not verify the BDEM simulation for simple crack propagation. We only discussed and verified how to achieve simultaneous fracturing of horizontal wells by BDEM. Studies (see Peirce and Bunger, 2015) have shown that the fracturing fluid pressure in the wellbore is the same regardless of wellbore friction. The pressure boundary is set at the intersection of prefabricated cracks and the wellbore. The pressure is constant in the wellbore. In this way, simultaneous fracturing of multiple fractures can be simulated and flow partition within each fracture can be studied.

TABLE 1 Values of model parameters.

Parameter	Value	Parameter	Value
Elasticity Modulus	20 GPa	Fluid Viscosity	1.5 cp
Poisson's Ratio	0.25	Fluid Density	1,000 kg/m^3
Density of Rock	2,600 kg/m^3	Depth	3,000 m
Joint Friction	20°	Injection Rate	0.05 m^3/s
Joint Cohesion	0 MPa	*In-situ* stress	$\sigma_x = \sigma_y = \sigma_z$=76.518 MPa

The model was established according to Olson (2008). The numerical experiments included only fractures that were initiated from the wellbore, with no natural fractures in the formation. The idealization assumed a horizontal well that provided uniform pressure to seven identical and evenly spaced hydraulic fractures orthogonal to the wellbore trend. The model is shown in Figure 1. Seven prefabricated fracture surfaces (f1–f7) were considered in the formation to simulate seven fractures. The fracture spacing was considered 10 m. The initial fracture size is 20 m. The prefabricated fractures were set as joints. The wellbore was perpendicular to the joints. The horizontal wellbore was located in the middle of the model. The model size of the whole block was 100 m × 50 m × 50 m. The goal of this model was to verify whether BDEM can simulate simultaneous multi-fracture fracturing or not. The existing numerical investigations did not consider the impact of the bedding, thus, the formation model without the bedding was first established. The BDEM was verified by comparison of the model results with those of existing models. To ensure the opening of the crack, the bottom pressure has to be greater than the normal stress of the fracture face. Assume that the

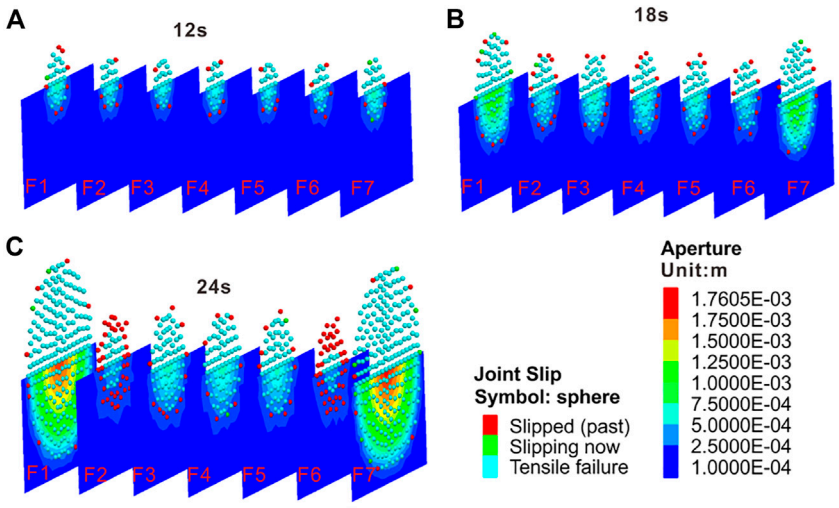

FIGURE 2
Fracture geometry after multiple fracturing. **(A-C)** the fracture morphology at different times.

buried depth of the formation is 3,000 m, the formation is homogenous and uniform, and the stress is uniform. Therefore, the minimum principal stress is 76.5 MPa. Based on this, the bottom pressure was set to 81 MPa. The values of other parameters are presented in Table 1. The mechanical characteristic parameters were selected based on the true triaxial test results of shale taken from Changning in southern Sichuan, China. The elasticity modulus ranged from 16.6 GPa to 25 GPa. The Poisson's ratio ranged from 0.17 to 0.32. Thus, the elasticity modulus was set as 20 Gpa, the Poisson's ratio was set as 0.25, and the density was set as 2,600 kg/m^3. The injection fluid was considered water. Therefore, the fluid density was set as 1,000 kg/m^3. The fluid viscosity was set as 1.5 cp. The injection rate was set as 0.05 m^3/s. This rate is commonly applied in numerical simulation of hydraulic fracturing. Based on the model, the crack propagation and the fluid partition within the fractures were calculated during simultaneous multi-fracture fracturing. The joint model was a weak structural plane and the permeability of the joint was not considered without cracking.

2.2.2 Validation of results

2.2.1.1 The geometry of seven fractures

The propagation of multiple fractures without considering the bedding is shown in Figure 2. We extracted the preset crack paths separately to show the spatial shapes of the fluid-driven cracks. To avoid the incomplete display of the morphology caused by the overlap between the crack faces, only half of the crack faces were intercepted. The different colors on the crack face indicate the aperture of the crack. The dark blue color indicates that fractures are not cracked (for numerical calculation, the initial crack opening in the model was 1e-4 m), and other colors indicate different crack apertures. The red color exhibits the largest crack aperture.

At the same time, to show the geometry of the completely fluid-driven crack, the failure point (Joint Slip in Figure 2) was used to represent the spatial geometry of the fractures. The joint slip indicates fracture cracking at this node. In this way, we obtained the spatial shape of the fractures and the distribution of the fracture aperture from Figure 2. Figures 2A–C depicts the fracture morphology at different times. In summary, the slip points show the spatial position of the crack. The different colors on the plane indicate the width of the crack at different spatial locations.

Individual fractures have the shape of a disk (Figure 2). The largest width of fracture is around the intersection of the wellbore and fracture. With the fluid injection, the fracture propagates outward from the center and becomes larger. Of course, the propagation rates of different fractures are affected by the location. In the early stages of fracturing (Figure 2A, 12s), the fracture shape is approximately the same, the fracture length is small, and the interference between the fractures is small. Thus, each fracture expands independently and does not affect the other fractures. As time passes, the exterior fractures of f1 and f7 gradually become dominant fractures, while the internal fractures of f2–f6 are limited by the stress shadow. When the exterior fractures of f1 and f7 propagate to a certain extent (Figure 2C, 24s), they will interfere with the propagation of the neighboring cracks. In Figure 2C, the joint slip is used to analyze whether or not the crack propagates under the current step. It shows that the slip point is red at the edges of the failure regions of the fractures of f2 and f6. The red points mean that no further damage has occurred at this point. This suggests that the two

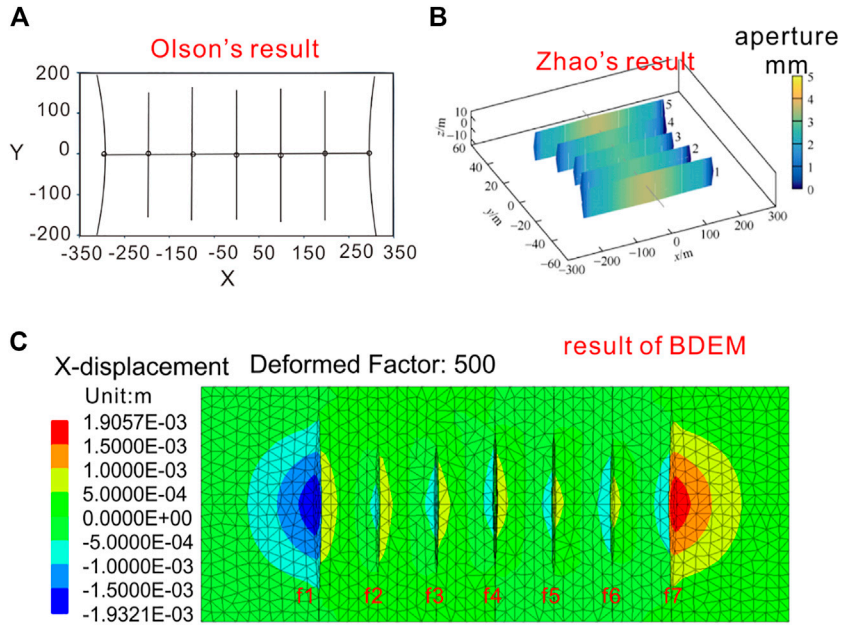

FIGURE 3
Comparison of the model results of simultaneous multi-fracture fracturing with those of Olson (2008) and Zhao et al. (2022). **(A)** Olson's research; **(B)** Zhao's research; **(C)** result of BDEM.

fractures are disturbed by the exterior fractures of f1 and f7 and they fail to propagate outward. The propagation of the exterior crack has suppressed the neighboring fractures of f2 and f6. During simultaneous fracturing, the fractures will interfere with each other, and the exterior fractures are the dominant fractures. The dominant fractures inhibit the propagation of other fractures. The closer the fracture is to the dominant fracture, the greater the impact is.

According to Olson's (Figure 3A) and Zhao's (Figure 3B) research, the fractures at the array's ends have the most freedom to open. The result of BDEM (Figure 3C) is consistent with the results of Olson (2008) and Zhao et al. (2022). This verifies that the calculation method (i.e., the 3D block distinct element method) can simulate multiple fracturing of the horizontal well with great accuracy.

In summary, the exterior cracks of f1 and f7 are dominant cracks. The length and width of the exterior cracks (f1, f7) are larger than those of the inner cracks of f2–f6. Since the fractures propagate vertically, the main displacement of the fracture surface is in the x-direction. Therefore, the contour map of the x-direction displacement was selected to study the change in displacement around the crack. The x-direction displacement on the vertical section (y = 0, where the horizontal well is located) is shown in Figure 3C. The displacement contour map reveals that the exterior cracks of f1 and f7 are dominant cracks. The displacement on both sides of f1 and f7 is the largest and the displacement on both sides of the internal crack is small. It is worth noting that in the exterior crack, the displacement on both sides of the crack is quite different. The absolute value of the left-side displacement of the crack f1 is large, but the absolute value of the displacement on the right side is small. Similarly, the absolute value of the displacement on the right side of the crack f7 is also much larger than that on the left side. Thus, although the exterior crack is a dominant crack, the displacement of the inner side of the crack is small due to the stress interference between the cracks. Olson (2008) concluded that the fractures at the ends of the array had the most freedom to open because they were only opposed by another fracture on one side. The results of this study validated Olson's conclusions. The displacement of the exterior side plays a major role in the cracking of the exterior crack.

2.2.1.2 The fluid partition within seven fractures

Fluid partition is a critical issue for multiple hydraulic fractures. We calculated the fluid partition by the fluid charging rate at the inlet of every fracture. Figure 4 illustrates the fluid partition of every fracture. The fluid partition at the beginning and end of the experiment is compared first. Figure 4A manifests that there is no significant difference in fluid partition among the seven fractures. The charging rates of f1 and f7 are not the biggest. For the idealized mode, the charging rate of every fracture should be the same. Even though the allocated mesh is not completely uniform, the presence of a non-uniform mesh is not an absolute disadvantage. On the contrary, the non-uniform mesh can better simulate the randomness of

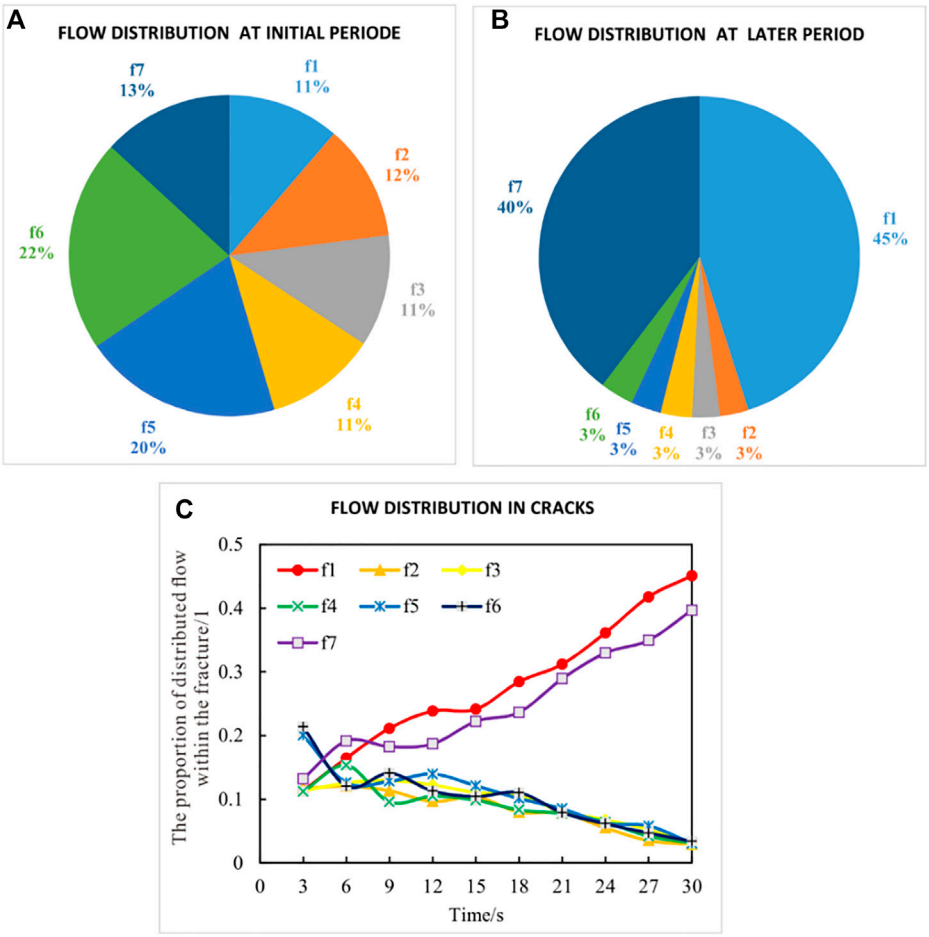

FIGURE 4
Fluid partition in fractures. **(A)** flow distribution at initial period; **(B)** flow distribution at later period; **(C)** flow distribution in cracks.

rock cracking. Therefore, if the mesh is fine enough, the result is more reflective of the authenticity of the rock fracture. In real conditions, if one fracture opens more easily than another for some reasons, it will be able to take fluid preferentially and grow faster than its neighboring cracks. This case can be simulated by the proposed method.

Figure 4A shows that the partition of f5 and f6 is bigger than the others. They are dominated during the initial period. The differences among the seven fractures are not very great. But at the later stage, fractures f1 and f7 are the dominant fractures. Moreover, the total fluid partition of the dominated fracture is more than 85%. This suggests that the fractures may initiate differently for some reasons, such as initial wellbore or perforation conditions. However, the stress interference among fractures is small because the induced stress of short fractures is not large enough to affect neighboring cracks. Consequently, the dominant fractures in the initial period with small stress interference may be replaced by other fractures with large stress inference in the later period. The initial dominance of the dominated fractures of f5 and f6 is replaced by the later dominance of the exterior fractures of f1 and f7.

Why is the domination of initial dominated fractures replaced? The reason is that in the initial period, the stress interference is small and the fractures are similar. With the increase in fracture length, the interference among fractures becomes larger, and the normal stress on interior fractures of f2–f6 increases. As a result, the propagation of the interior fractures is restrained, and the propagation of the exterior fractures is easier. The real-time fluid partition of seven fractures is plotted in Figure 4C. The curves demonstrate that the partition of f1 and f7 increases and that of others decreases with time. Besides, it is obvious that the fluid partition is consistent with fracture propagation. With the same pore pressure, more fluid flows into the exterior fractures.

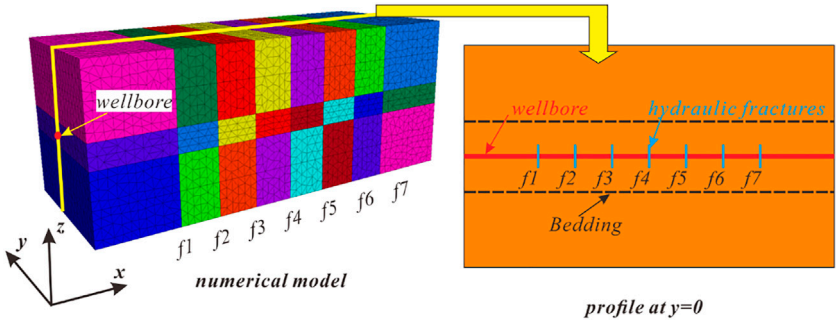

FIGURE 5
The model of multiple hydraulic fracturing considering BPs.

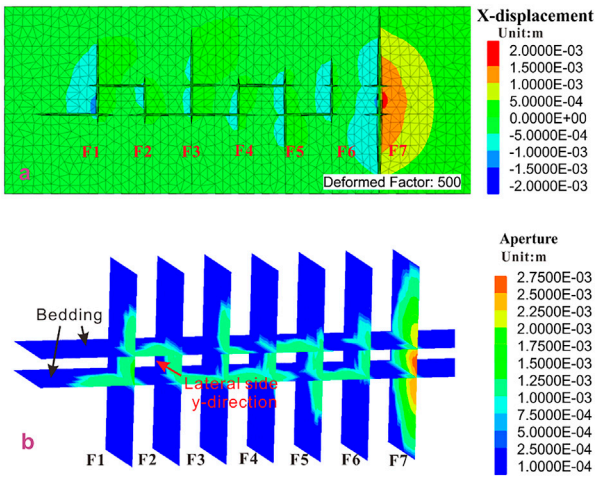

FIGURE 6
Multiple fracture propagation affected by the BPs. **(A)** 2D schematic view; **(B)** 3D schematic view.

2.3 Base case

2.3.1 Model setup

The above section verified the correctness of BDEM predictions in multiple hydraulic fracturing. To study the influence of BPs on the propagation of different fractures, a model considering BPs was established. According to the model described in Figure 1, two horizontal BPs were added above and below the wellbore separately. The BPs were 3 m away from the wellbore. The model is shown in Figure 5. The values of other parameters were consistent with those of Section 2.2.1. There were two assumptions about the BPs. One was that the joint model was a weak structural plane and the permeability of the joint was not considered without cracking. Another one was that the BPs were perpendicular to the direction of the fractures.

2.3.2 Results for the base case

2.3.1.1 The geometry of seven fractures

We first discuss the effect of the BPs on multiple fracturing. The fracture propagation is shown in Figure 6. This figure suggests that BPs have a significant influence on fracture propagation. Compared to Figure 3C, the fractures in Figure 6 are all restricted except for f7. Furthermore, the fluid-driven crack turns into the BPs. The geometry of f1 and f7 is different. The f7 passes through the BPs directly and propagates vertically. The f7 is still the dominant fracture. While the BPs affect the f1, they do not affect the f7. The vertical propagation of f1 is restricted, and the fluid-driven fracture turns into the BPs.

Figure 6A reveals that the f1 passes through the upper bedding plane but not the bottom bedding plane. The f1 propagates along the bottom bedding plane. The geometry of f1 and f7 is different. The BPs have a significant impact on f1 but no impact on f7. The reason for this prediction by numerical simulation is the presence of the non-uniform grid at the intersections of BPs and two fractures. The difference between f1 and f7 results in different crack initiations, leading to different propagation of f1 and f7. In a real rock mass, the crack initiation is still random. At the intersection of fracture f7 and BPs, the fluid-driven crack breaks through the upper and bottom BPs. Then fracture f7 becomes free from the restriction of BPs. However, the f1 does not break through the bottom bedding plane and propagates along with it. Therefore, the f1 is no longer a dominant fracture. As for the interior fractures of f2-f6, their heights are restricted by the BPs. A 3D schematic view is shown in Figure 6B.

In brief, the BPs may hamper the vertical propagation of fracture. When hydraulic fractures can directly cross the BPs, the BPs have little influence on fracture propagation. In contrast, if the hydraulic fractures cannot directly cross the BPs, the BPs will affect the vertical propagation of the crack.

As for the propagation of the interior fractures, the fractures f2, f4, and f6 are more obviously affected by BPs. The two sides, the upper and bottom sides, are restricted. The f2 is the most obvious example. Because the fractures are hindered by two BPs,

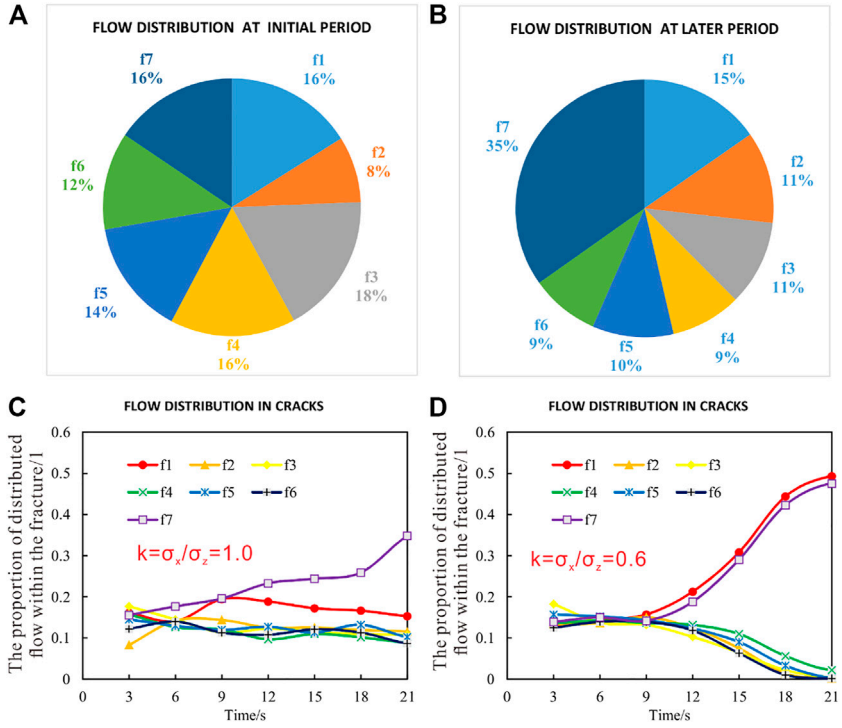

FIGURE 7
Fluid partition in fractures considering the BPs. **(A)** flow distribution at initial period; **(B)** flow distribution at later period; **(C)** flow distribution in cracks when k = 1.0; **(D)** flow distribution in cracks when k = 0.6.

they propagate to the lateral sides (y-direction in Figure 6B) and along BPs. It is important to note that the expansion in the y-direction is different from the previous two-dimensional simulation. Previous two-dimensional or pseudo-three-dimensional simulations could not describe the lateral expansion of cracks. Figure 6B shows that the cracks of f1, f2, f4, and f6 have substantial lateral expansion between the two BPs due to the influence of the bedding. Since the lengths of the surrounding cracks of f2, f4, and f6 are small, the cracks of f3 and f5 extend outward at the end of the bedding. Furthermore, the BPs have also become the main channel for crack propagation. In severe cases, the cracks penetrate along the BPs, leading to the connection between the fractures.

Concisely, the BPs will reduce the competition between the wells, and the competitive advantage between the wells is no longer obvious. Moreover, the BPs will impede the vertical extension of the crack. In this case, the length of the main crack of the hydraulic fracturing is limited, and the effect of the reservoir stimulation is greatly reduced. However, in the practice of shale gas development, the bedded shale is often the most effective shale gas producing layer. According to this theory, shale bedding is an unavoidable problem. We can only utilize the relevant processes and techniques to diminish the influence of the BPs on the simultaneous fracture of multiple fractures in horizontal wells.

2.3.1.2 The fluid partition within seven fractures

Similarly, the partition of flow in each crack during multi-fracture fracturing considering the BPs is analyzed. Figure 7A depicts that the interference between the cracks is small at the initial stage of the fracturing, and the cracks do not meet the BPs. At this time, the flow difference between the cracks is small. Figure 7B displays the fluid partition in the later stage of fracturing. The flow rate of crack f7 is the largest, with a ratio of 35%, and the flow rate of the inner cracks of f2-f6 is 9%–11%, which is much larger than the case when there is no bedding plane. This suggests that the bedding plane reduces the competitive advantage between cracks. Besides, although the crack f1 does not become a dominant crack like f7, the flow rate is still larger than the inner cracks. Figure 7C indicates the flow partition of f1 is greater than the other inner cracks during the fracturing process. This suggests that the crack f1 still has a certain propagation advantage. However, the BPs significantly decrease its expansion advantages.

The uneven fluid distribution in f1 and f7 is because of the minor differences in the grid. The physical reason is the randomness of fracture caused by the structure inside the

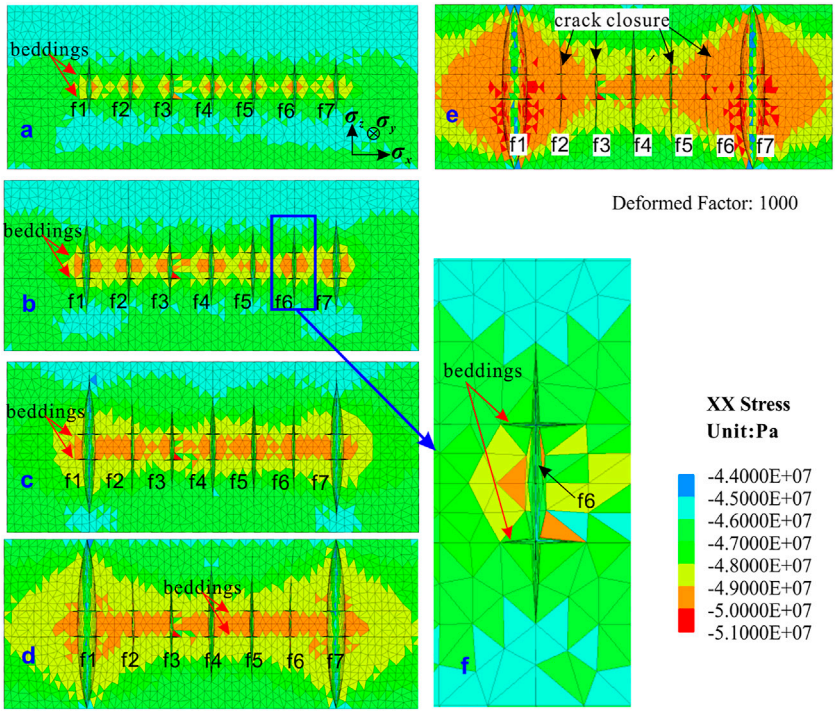

FIGURE 8
The fracture morphology evolution and x stress ($k = \sigma_x/\sigma_z$=0.6). **(A–E)** the fracture morphology at different times.

rock mass in the process of rock fracture. f1 is affected by the BPs during propagation. Thus, it fails to expand outwards. At this condition, f1's expansion is restricted, and the propagation rate is slowed down, resulting in a reduction in fluid injection rate. However, f7 is not influenced by the BPs, and it can continue to expand, so the amount of liquid is larger than that of f1. The advantages and disadvantages of this heterogeneity will be discussed in Section 4.2. Figure 7D exhibits the fluid partition. Comparing Figures 7C,D (*k* represents the state of *in-situ* stress, which will be described in detail in Section 3.1), the results suggest that fracture propagation will become complicated when the stress is uniform. In the case of a larger stress difference, the regularity is stronger. When the stress difference is small, the heterogeneity of the formation is more obvious.

3 Results

3.1 Effect of stress difference

The results of the base case were obtained under uniform *in-situ* stress conditions. However, the *in-situ* stress in a real formation is not uniform. To investigate the effect of BPs on multi-fracture fracturing in horizontal wells under different stress conditions, $k = \sigma_x/\sigma_z$ was defined to represent the state of *in-situ* stress. σ_x is the minimum horizontal principal stress of the formation and σ_z is the vertical *in-situ* stress of the formation. When $k = 1.0$, the ground stress is uniform. When $k > 1.0$, the horizontal stress is greater than the vertical stress, and when $k < 1.0$, the horizontal stress is smaller than the vertical stress. Other parameters remain unchanged. Initially, $k = 0.6$ was selected, and the effect of the BPs on crack propagation was observed when the horizontal stress was smaller than the vertical stress. The fracture morphology evolution is shown in Figure 8. The competitive advantage between the cracks was not affected by the BPs under the condition that the vertical stress was greater than the horizontal stress. Similar to the type of fracturing in a non-bedding formation, the stress interference was not significant at the beginning of the fracturing. As the crack expanded, the exterior cracks exhibited a distinct advantage. The inner crack was disturbed by the adjacent crack, and the expansion was suppressed.

Although the bedding has little impact on the competition and interference of multiple cracks under this condition, there is a certain amount of cracking at the intersection of the crack and the bedding (Figure 8F). Since the vertical stress on the bedding plane is greater than the horizontal stress on the fracture surface, the crack does not expand along the bedding plane. From the contour plots of Figures 8B–D, the x-direction stress is analyzed, and it can be observed that the stress interference region is more pronounced within the bedding. In Figure 8E, the interference stress of the cracks of f3–f5 is still large in the bedding. The

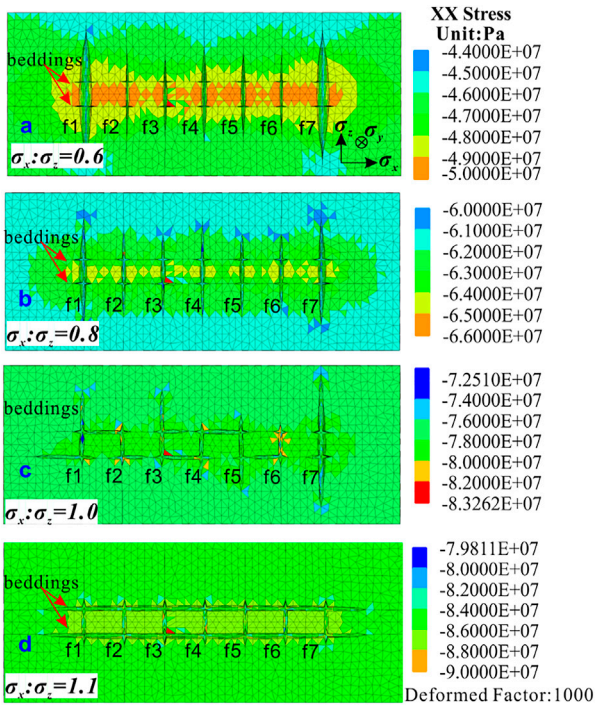

FIGURE 9
Propagation of multiple fractures under different stress states. **(A)** k = 0.6; **(B)** k = 0.8; **(C)** k = 1.0; **(D)** k = 1.1.

interference stress in other areas is chiefly caused by the external cracks of f1 and f7. The cracks of f2 and f6 are reclosed due to the interference stress caused by the exterior crack.

In summary, under the condition that the vertical stress was greater than the horizontal stress, the bedding had little impact on the multi-fracture competition. The fracture propagation in the formation with or without bedding was similar, that is, the interference between fractures was negligible at the initial stage of fracturing. As the fracturing time increased, the effects between bedding and cracks gradually appeared. Therefore, the shape difference of crack propagation at the initial stage of fracturing was small, and the research had to focus on the later stage of fracturing.

To understand the influence of the bedding plane under different stress states, we chose the fracture morphology at the late stage of k = *0.6/0.8/1.0/1.1*. The results are shown in Figure 9. First, by comparing Figures 9A,B, we found the width of the exterior cracks of f1 and f7 was smaller when k = 0.8. This indicates that the horizontal stress limits the width of the crack. In both cases, the fracture shape is consistent, and the vertical expansion advantage of the exterior crack is still obvious. Figure 9C shows the state in which the *in-situ* stress is uniform and the crack expands in the vertical direction as well as in the bedding direction. The bedding interferes with the vertical expansion of the crack, but it is not completely limited. The results of the horizontal stress greater than the vertical stress (k = 1.1) are exhibited in Figure 9D. At this time, the bedding plane becomes the dominant propagation path, which completely limits the vertical propagation. In short, when k < 1.0, the influence of the bedding plane on simultaneous multi-fracture fracturing is not significant. As the k value increases, the influence of the bedding plane becomes gradually obvious. When k > 1.0, the bedding plane will become the dominant channel, completely limiting the vertical expansion of each crack and eliminating the competitive advantage of expansion between the cracks. Thus, the degree of interference of the bedding plane on multi-crack simultaneous fracturing is related to the state of the *in-situ* stress.

3.2 Effect of distance from the wellbore to the bedding plane

Limiting the vertical expansion of the crack is the main effect of bedding on multi-fracture propagation. The distance from the bedding plane to the horizontal well also affects the fracture shape. We selected the distances of 1 m, 3 m, 6 m, and 9 m for simulation. The distance of 3 m was calculated in the base case. The results for different distances are presented in Figure 10. Figure 10A reveals that the hydraulic crack does not pass through the bedding but expands along the bedding plane when the distance is 1 m. Moreover, the bedding plane between two fractures is almost completely penetrated. Figure 10B shows the result for the 6 m distance. The exterior cracks of f1 and f7 turn into the bedding plane, and the cracks propagate along the bedding plane. The bedding between internal cracks also tends to penetrate through hydraulic cracks, such as the upper bedding plane between f4 and f5. Figure 10C displays the crack propagation pattern when the distance is 9 m. It also exhibits that the exterior cracks of f1 and f7 turn into the bedding. Therefore, the influence of the distance from the wellbore to the bedding on multi-fracture fracturing is very simple. Because of the influence of the bedding, the vertical extension of the crack is limited. Thus, the closer the distance is, the shorter the main crack is.

3.3 Effect of the number of bedding planes

In a real formation, there may be multiple BPs. Thus, we examined the effect of the different numbers of BPs on crack propagation. Figure 11 indicates that the number of BPs is sequentially increased on the outer side based on the base case. $k = \sigma_x/\sigma_z$ was defined as 1.0. The distance between each bedding plane was considered to be 3 m. The cases where the number of the single-sided BPs was from two to four were calculated separately and the results are shown in Figure 12.

Figure 12A depicts crack propagation with two BPs on one side, Figure 12B with three BPs on one side, and Figure 12C with

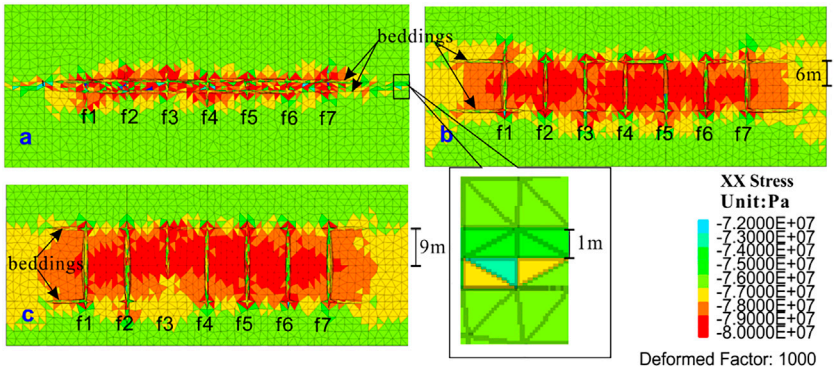

FIGURE 10
Propagation of the fracture with different distances between the BPs and wellbore. **(A)** distances of 1 m; **(B)** distances of 6 m; **(C)** distances of 9 m.

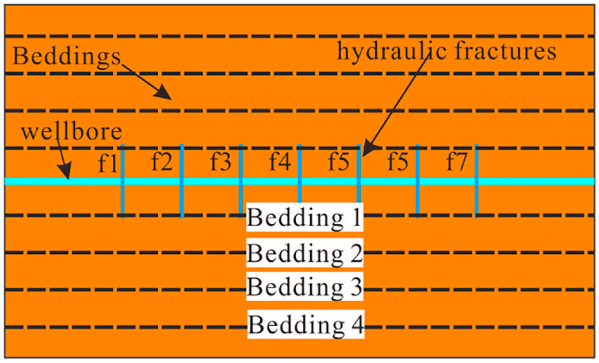

FIGURE 11
Model with multiple BPs.

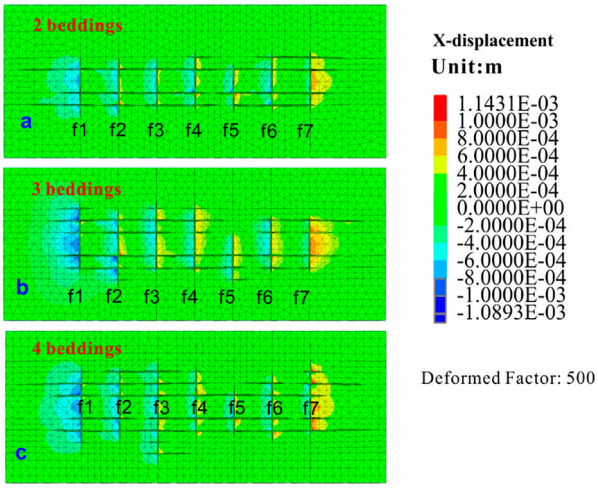

FIGURE 12
Fracture propagation with different numbers of BPs. **(A)** 2 beddings; **(B)** 3 beddings; **(C)** 4 beddings.

four BPs on one side. In each of these three cases, the crack may extend through the bedding plane while expanding the bedding plane, thereby moving the bedding plane farther from the wellbore. In general, the hydraulic fractures can penetrate bedding one and bedding 2, but bedding three and bedding four have only a few cracks (Figure 13). In the presence of multiple layers, the competitive advantage between cracks is no longer evident. However, as the number of BPs increases, the fracture network after fracturing becomes more complicated. As a result, an increase in the number of BPs will increase the complexity of the fracture network.

Only one of the sections of the block is shown in Figure 12C. Thus, the figure cannot characterize the three-dimensional spatial distribution of the crack. Therefore, the seven crack faces and the four bedding faces are shown separately in Figure 13. First, seven cracked faces were analyzed. Blue in the crack face indicates no cracking (set to the initial crack width), and other colors indicate different crack widths. As can be observed from the figure, the lateral expansion (y-direction, left and right for f1–f7, up and down for BPs of 1–4) morphology of the cracks between different BPs is very different. This has a close relationship with the crack connection of the bedding plane. It can be seen from the crack morphology on the bedding surface that the bedding plane between the cracks is penetrated on bedding one and bedding 2. However, only a portion of bedding three and bedding four is cracked. This suggests that the seven cracks can pass through bedding one and bedding 2, but only partially pass through bedding three and bedding 4. Furthermore, the farther the bedding plane is from the wellbore,

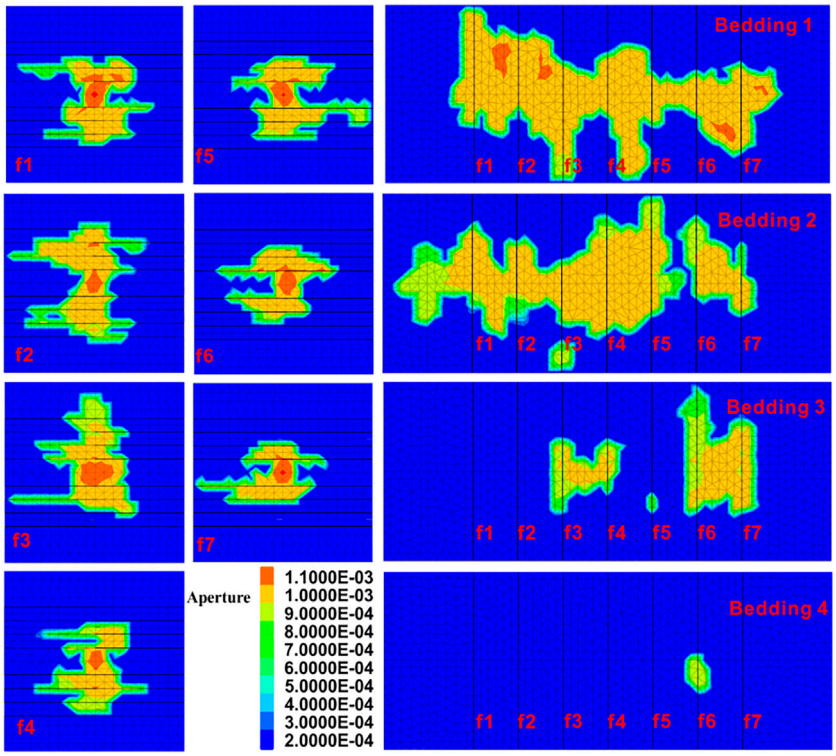

FIGURE 13
Fracture propagation in the presence of the seven preset fractures and four BPs.

the more difficult it is to pass through. The crack propagation on the bedding plane makes it easier to see the expansion of the crack face in the lateral direction (i.e., y-direction). Moreover, the expansion in the y-direction will vary depending on the nature of the rock formation. This also indicates that the two-dimensional multi-fracture fracturing simulation can lead to distortion of the analog information. The flow loss caused by the lateral crack propagation is unpredictable in the two-dimensional simulation, and the unevenness of the lateral expansion of the crack leads to a deviation in the results.

4 Discussion

4.1 How to make the fracture network more complex

Section 3.1 indicated that the *in-situ* stress state determines whether or not the BPs affect multi-crack propagation. When the horizontal stress is much smaller than the vertical stress, the bedding plane has little impact on the crack propagation. In this case, the difference in crack propagation is significant. When the horizontal stress is close to the vertical stress, the BPs will seriously interfere with the expansion of each crack and even thoroughly will limit the vertical expansion of each crack. In the general case, the horizontal stress is considered to be smaller than the vertical stress. However, during the vertical expansion of the crack, the fluid pressure in the crack acts on the crack surface. The pressure on the fracture surface is ultimately transmitted to the formation between the fractures, which leads to an increase in the horizontal stress of the rock mass. In the case where the vertical stress does not change much, the difference between the two decreases. The inhibition of the vertical crack propagation due to the hindering effect of the BPs is becoming more and more obvious.

The distance from a bedding plane to the wellbore primarily affects the length of the main crack. It can be stated that the greater the distance is, the greater the length of the main crack is. Therefore, in actual engineering, horizontal wells should be avoided in two BPs that are too close. When there is a bedding plane near the wellbore, the barrier of the bedding plane should also be reduced in some ways to increase the length of the main fracture. According to the experimental results of related literature (Beugelsdijk et al., 2000; Tan et al., 2017), it is believed that the increase in the injection rate and viscosity of the fracturing fluid can effectively increase the length of the main crack. Then the length of the main crack should be increased by performing some processes in the formation where the bedding is present.

Under the condition that the length of the main crack can be guaranteed, the BPs are conducive to the complexity of the fracture networks. It is clear that the increase in the number of BPs increases the complexity of the crack. Consequently, the influence of bedding on multi-fracture fracturing should be addressed controversially. On the one hand, the presence of bedding affects the vertical extension of the fracture and reduces the length of the main fracture. In this respect, the bedding is not conducive to fracturing. On the other hand, bedding connectivity can increase crack complexity. In cases where the length of the main crack can be ensured, the bedding is advantageous for well stimulation by hydraulic fracturing. As a result, the influence of bedding on well stimulation by hydraulic fracturing should be discussed according to the current situation. It is not logical to state confidently that the bedding is beneficial or not conducive to fracturing.

In short, to obtain a more complex fracture network in a formation with multiple BPs, there are two key points: the length of the main fractures and crack propagation in the BPs. However, the two are contradictory. First, the length of the main fracture should be obtained. This is a question about how cracks pass through more BPs. According to Section 3.1, *in-situ* stress may affect fracture propagation. Relevant studies (Li et al., 2017; Manríquez, 2018) have demonstrated that the *in-situ* stress can be changed by neighboring fractures or wells. Thus, stress intervention is a method to control *in-situ* stress. Then a longer main fracture may be obtained. Laboratory experiments (Beugelsdijk et al., 2000; Tan et al., 2017) showed that a larger injection rate and fluid viscosity were conducive to the propagation of the main fracture in formations with bedding. Furthermore, the approach angle between the fracture and the bedding plane also affects the propagation behavior. The study of Zheng et al. (2019b) indicated that a longer main fracture may form at a higher approach angle if the cementation of BPs is not weak. On the contrary, for fracture propagation in BPs, stress intervention, smaller injection rate, and smaller fluid viscosity are useful in general. The recommended road map for a complex network is to first acquire the long main fractures and then allow the fractures to expand within the BPs.

4.2 Grid meshing

In the real world, the rock mass is heterogeneous. Therefore, crack propagation has certain randomness (see Figure 6). A slight difference in the initial state of the crack results in a significant difference in the final shape of the crack. The slight difference in the meshing of the rock mass is not considered a critical shortcoming for the simulation. Instead, it can reflect the heterogeneity of rock mass. Through the slight difference in the meshing, we realized that under almost the same stress conditions, the shape of the crack would also be greatly different. Although the grid difference causes a difference in cracking, the damage discrimination mode used in the simulation is the same. Therefore, grid meshing is not a very critical issue.

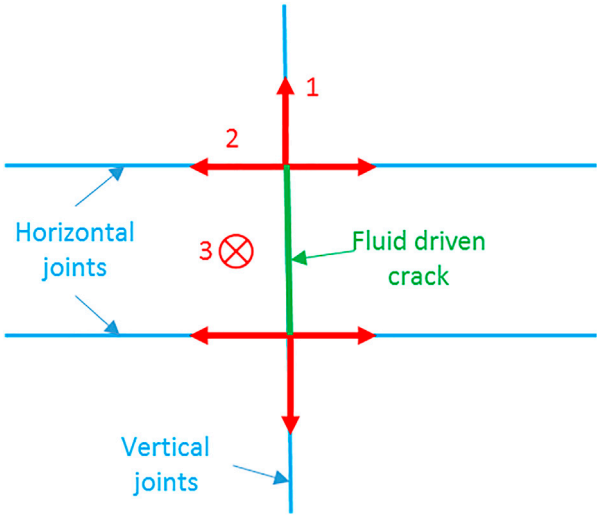

FIGURE 14
Schematic diagram of crack propagation direction.

Although the meshing difference can reflect the heterogeneity of rock mass, there are still some issues related to meshing that need further discussion. All we know is that the difference in the mesh causes the difference in the fracture initiation. The differences in the mesh which lead to the differences in the fracture initiation and the properties which these grid differences represent in the rocks remain unclear. Thus, they need to be studied in more detail.

For capturing the heterogeneity of rock mass, we should ensure the regular accuracy of the simulated results. We have already discussed the mesh dependency of the simulation results in our previous work (Zheng et al., 2019b). The size of the mesh is determined by the edge. Therefore, the edge lengths were selected as 0.5 m, 1.0 m, and 2.0 m for examining mesh dependency. The results showed that with the increase in mesh size, the fluctuation in the simulation outcomes was more obvious. In sum, the mesh should be small enough to ensure accurate results. However, to characterize the heterogeneity of the rock mass, the mesh must not be too small. To satisfy these two points, the edge size was considered 1.0 m. According to our previous work (Zheng et al., 2019b), the edge size of 2.0 m can ensure accurate results.

4.3 From two-dimensional analysis to three-dimensional analysis

In this study, we analyzed the three-dimensional shape of the crack. The two-dimensional or quasi-three-dimensional analysis

of crack propagation is performed only at a certain plane, and the height of the crack is assumed to be constant. Crack propagation under two-dimensional conditions is shown in Figure 14. When the hydraulic crack propagates to the joint surface, the crack can only continue to expand in one or two directions, and the other directions are ignored in the 2D calculations. But for three-dimensional propagation, the expansion direction of the crack has one more choice. The crack can be expanded in direction 3, which is called lateral expansion. The three-dimensional calculations suggest that the lateral expansion of the crack faces at different positions is not the same, and the height of the crack in the space is not the same too. Figure 13 indicates that the difference in crack height is very large. Under these conditions, the advantages of 3D analysis are well reflected. The three-dimensional hydraulic fracturing model can better represent the shape of hydraulic fractures more realistically.

We simulated the expansion of cracks on a three-dimensional scale. However, the crack was preset during the simulation. This situation did not take into account the deflection of the crack under stress interference. The numerical simulation method for the three-dimensional expansion of hydraulic fracturing remains to be developed. Although the relevant literature has simulated three-dimensional hydraulic fracturing, most of them are still simplified or need to meet special requirements. From the current literature, BDEM is one of the most effective methods for simulating three-dimensional hydraulic fracturing. Simulations for 3D hydraulic fracturing are expected to be simpler, more efficient, and more realistic.

5 Conclusion

1. When multiple cracks are simultaneously fractured, the expansion priority between the cracks is different due to stress interference between the cracks. The exterior crack has a greater vertical expansion compared to the inner crack. The internal crack is disturbed by the stress between the cracks, and the crack propagation is limited. Under high-stress conditions, internal cracks may close after cracking. Besides, the flow distribution of the crack is the same as the expansion of the crack.
2. The presence of the bedding plane will hinder the vertical expansion of the crack. The bedding plane reduces the difference in expansion between cracks. The smaller the stress difference, the more obvious the effect of the bedding plane. When the stress difference is large, the effect of the bedding plane on the crack advantage is not obvious.
3. The effect of the bedding plane on fracturing should be evaluated from two perspectives. On the one hand, the bedding plane impedes the vertical expansion of the crack and reduces the length of the crack. This will reduce the range of the well stimulation by hydraulic fracturing. This is not conducive to the hydraulic fracturing of the reservoir. On the other hand, the bedding plane increases the complexity of the fracture network after fracturing. This is beneficial for reservoir fracturing. Therefore, in the fracturing process of layered formations, the key issue is how to reduce the limitation of the length of the main cracks so that the cracks extend farther. This allows for a greater range of well stimulation by hydraulic fracturing.
4. The recommended workflow for a complex network is to first obtain the long main fractures and then allow the fractures to expand within the bedding plane. Stress intervention, the change of the injection rate and fluid viscosity, and adjustment of the approach angle between fracture and bedding plane can be applied to attain a more complex fracture network.

Data availability statement

The original contributions presented in the study are included in the article/Supplementary Material, further inquiries can be directed to the corresponding author.

Author contributions

YM completed the simulation and manuscript. DW helped on the manuscript and YZ helped on the simulation.

Funding

This research was funded by the China National Science and Technology Major Project (Grant No. 2017ZX05037001), the Liaoning Province Applied Basic Research Program (2022JH2/101300136), and by the Discipline Innovation Team Project of Liaoning Technical University (Grant No. LNTU20TD-11).

Acknowledgments

We would like to thank Liuke Huang, a visiting scholar at Tongji University, for his help in applying the block distinct element method. Besides, we are grateful to the International Science Editing (http://www.internationalscienceediting.com) for editing this manuscript.

Conflict of interest

The authors declare that the research was conducted in the absence of any commercial or financial relationships that could be construed as a potential conflict of interest.

Publisher's note

References

Beugelsdijk, L. J. L., de Pater, C. J., and Sato, K. (2000). "Experimental hydraulic fracture propagation in a multi-fractured medium," in *SPE asia pacific conference on integrated modelling for asset management* (Yokohama, Japan: Society of Petroleum Engineers), 8.

Cao, R., Cao, P., Fan, X., Xiong, X., and Lin, H. (2016). An experimental and numerical study on mechanical behavior of ubiquitous-joint brittle rock-like specimens under uniaxial compression. *Rock Mech. Rock Eng.* 49 (11), 4319–4338. doi:10.1007/s00603-016-1029-6

Chen, X., Li, Y., Zhao, J., Xu, W., and Fu, D. (2018). Numerical investigation for simultaneous growth of hydraulic fractures in multiple horizontal wells. *J. Nat. Gas Sci. Eng.* 51, 44–52. doi:10.1016/j.jngse.2017.12.014

Cundall, P. A. (1988). Formulation of a three-dimensional distinct element model—Part I. A scheme to detect and represent contacts in a system composed of many polyhedral blocks. *Int. J. Rock Mech. Min. Sci. Geomechanics Abstr.* 25 (3), 107–116. doi:10.1016/0148-9062(88)92293-0

Dontsov, E. V., and Peirce, A. P. (2017). A multiscale implicit level set algorithm (ILSA) to model hydraulic fracture propagation incorporating combined viscous, toughness, and leak-off asymptotics. *Comput. Methods Appl. Mech. Eng.* 313, 53–84. doi:10.1016/j.cma.2016.09.017

Hart, R., Cundall, P. A., and Lemos, J. (1988). Formulation of a three-dimensional distinct element model—Part II. Mechanical calculations for motion and interaction of a system composed of many polyhedral blocks. *Int. J. Rock Mech. Min. Sci. Geomechanics Abstr.* 25 (3), 117–125. doi:10.1016/0148-9062(88)92294-2

Kresse, O., and Weng, X. (2018). Numerical modeling of 3D hydraulic fractures interaction in complex naturally fractured formations. *Rock Mech. Rock Eng.* 12, 3863–3881. doi:10.1007/s00603-018-1539-5

Kumar, D., and Ghassemi, A. (2018). Three-dimensional poroelastic modeling of multiple hydraulic fracture propagation from horizontal wells. *Int. J. Rock Mech. Min. Sci.* 105, 192–209. doi:10.1016/j.ijrmms.2018.01.010

Li, X., Wang, J., and Elsworth, D. (2017). Stress redistribution and fracture propagation during restimulation of gas shale reservoirs. *J. Petroleum Sci. Eng.* 154, 150–160. doi:10.1016/j.petrol.2017.04.027

Li, Y., Chen, X., Zhao, J., Xu, W., Wu, J., and Fu, D. (2018). Influence of perforation erosion on multiple growing hydraulic fractures in multi-stage fracturing. *Nat. Gas. Ind. B* 5 (1), 8–15. doi:10.1016/j.ngib.2017.11.002

Manríquez, A. L. (2018). Stress behavior in the near fracture region between adjacent horizontal wells during multistage fracturing using a coupled stress-displacement to hydraulic diffusivity model. *J. Petroleum Sci. Eng.* 162, 822–834. doi:10.1016/j.petrol.2017.11.009

Maxwell, S. C. L. B. (2016). "Calibrated microseismic geomechanical modeling of a horn river basin hydraulic fracture," in The 50th US Rock Mechanics/Geomechanics Symposium.

Olson, J. E. (2008). "Multi-fracture propagation modeling: Applications to hydraulic fracturing in shales and tight gas sands," in The 42nd US rock mechanics symposium (USRMS), San Francisco.

Peirce, A., and Bunger, A. (2015). Interference fracturing: nonuniform distributions of perforation clusters that promote simultaneous growth of multiple hydraulic fractures. *SPE J.* 20 (02), 384–395. doi:10.2118/172500-pa

Roussel, N. P., and Sharma, M. M. (2011). Optimizing fracture spacing and sequencing in horizontal-well fracturing. *SPE Prod. Operations* 26 (02), 173–184. doi:10.2118/127986-pa

Salimzadeh, S., Usui, T., Paluszny, A., and Zimmerman, R. W. (2017). Finite element simulations of interactions between multiple hydraulic fractures in a poroelastic rock. *Int. J. Rock Mech. Min. Sci.* 99, 9–20. doi:10.1016/j.ijrmms.2017.09.001

Tan, P., Jin, Y., Han, K., Hou, B., Chen, M., Guo, X., et al. (2017). Analysis of hydraulic fracture initiation and vertical propagation behavior in laminated shale formation. *Fuel* 206, 482–493. doi:10.1016/j.fuel.2017.05.033

Tang, H., Wang, S., Zhang, R., Li, S., Zhang, L., and Wu, Y. S. (2019). Analysis of stress interference among multiple hydraulic fractures using a fully three-dimensional displacement discontinuity method. *J. Petroleum Sci. Eng.* 179, 378–393. doi:10.1016/j.petrol.2019.04.050

Wang, Y., ZhangLin, H. H., Zhao, Y., and Liu, Y. (2020). Fracture behaviour of central-flawed rock plate under uniaxial compression. *Theor. Appl. Fract. Mech.* 106, 102503. doi:10.1016/j.tafmec.2020.102503

Wick, T., Singh, G., and Wheeler, M. F. (2016). Fluid-filled fracture propagation with a phase-field approach and coupling to a reservoir simulator. *SPE J.* 21 (03), 0981–0999. doi:10.2118/168597-pa

Wu, K., and Olson, J. E. (2016). Mechanisms of simultaneous hydraulic-fracture propagation from multiple perforation clusters in horizontal wells. *SPE J.* 21 (031), 1000–1008. doi:10.2118/178925-pa

Wu, K., and Olson, J. E. (2015). Simultaneous multifracture treatments: fully coupled fluid flow and fracture mechanics for horizontal wells. *SPE J.* 20 (02), 337–346. doi:10.2118/167626-pa

Xie, S., Lin, H., Wang, Y., Chen, Y., Du, S., Zhao, Y., et al. (2020). A statistical damage constitutive model considering whole joint shear deformation. *Int. J. Damage Mech.* 4, 988–1008. doi:10.1177/1056789519900778

Xu, Y., Cavalcante Filho, J. S., Yu, W., and Sepehrnoori, K. (2017). Discrete-fracture modeling of complex hydraulic-fracture geometries in reservoir simulators. *SPE Reserv. Eval. Eng.* 20 (02), 403–422. doi:10.2118/183647-pa

Zeng, Q., Liu, W., and Yao, J. (2018). Numerical modeling of multiple fractures propagation in anisotropic formation. *J. Nat. Gas Sci. Eng.* 53, 337–346. doi:10.1016/j.jngse.2018.02.035

Zhang, F., and Dontsov, E. (2018). Modeling hydraulic fracture propagation and proppant transport in a two-layer formation with stress drop. *Eng. Fract. Mech.* 199, 705–720. doi:10.1016/j.engfracmech.2018.07.008

Zhang, F., and Mack, M. (2017). Integrating fully coupled geomechanical modeling with microsesmicity for the analysis of refracturing treatment. *J. Nat. Gas Sci. Eng.* 46, 16–25. doi:10.1016/j.jngse.2017.07.008

Zhao, W., Ji, G., Li, K., Liu, W., Xiong, L., and Xiao, J. (2022). A new pseudo 3D hydraulic fracture propagation model for sandstone reservoirs considering fracture penetrating height. *Eng. Fract. Mech.* 264, 108358. doi:10.1016/j.engfracmech.2022.108358

Zheng, Y., Liu, J., and Zhang, B. (2019b). An investigation into the effects of weak interfaces on fracture height containment in hydraulic fracturing. *Energies* 12 (17), 3245. doi:10.3390/en12173245

Zheng, Y., Liu, J., and Lei, Y. (2019a). The propagation behavior of hydraulic fracture in rock mass with cemented joints. *Geofluids* 15, 1–15. doi:10.1155/2019/5406870

Zhu, H., Shen, J., and Zhang, F. (2019). A fracture conductivity model for channel fracturing and its implementation with Discrete Element Method. *J. Petroleum Sci. Eng.* 172, 149–161. doi:10.1016/j.petrol.2018.09.054

Zou, Y., Ma, X., Zhang, S., Tong, Z., and Han, L. (2016a). Numerical investigation into the influence of bedding plane on hydraulic fracture network propagation in shale formations. *Rock Mech. Rock Eng.* 9, 3597–3614. doi:10.1007/s00603-016-1001-5

Zou, Y., Zhang, S., Ma, X., Zhou, T., and Zeng, B. (2016b). Numerical investigation of hydraulic fracture network propagation in naturally fractured shale formations. *J. Struct. Geol.* 84, 1–13. doi:10.1016/j.jsg.2016.01.004

frontiers | Frontiers in Earth Science

TYPE Original Research
PUBLISHED 23 February 2023
DOI 10.3389/feart.2023.1129104

OPEN ACCESS

EDITED BY
Yu Song,
China University of Mining and Technology, China

REVIEWED BY
Cun Zhang,
China University of Mining and Technology, China
Bo Zhao,
Taiyuan University of Technology, China
Xiaohan Yang,
University of Wollongong, Australia

*CORRESPONDENCE
Shiqi Yu,
2895648066@qq.com

SPECIALTY SECTION
This article was submitted to Economic Geology, a section of the journal Frontiers in Earth Science

RECEIVED 21 December 2022
ACCEPTED 10 February 2023
PUBLISHED 23 February 2023

CITATION
Rong H, Yu S, Song W, Tang G, Wang Y, Sun D and Huo B (2023), Research on disaster mechanism and correlation of natural earthquake and coal and gas outburst.
Front. Earth Sci. 11:1129104.
doi: 10.3389/feart.2023.1129104

Research on disaster mechanism and correlation of natural earthquake and coal and gas outburst

Hai Rong[1], Shiqi Yu[1]*, Weihua Song[1], Guoshui Tang[2], Yadi Wang[3], Dequan Sun[4,5] and Bingjie Huo[1]

[1]College of Mining, Liaoning Technical University, Fuxin, China, [2]Chouzhou Polytechnic, Chuzhou, China, [3]College of Environmental Science and Engineering, Liaoning Technical University, Fuxin, China, [4]Engineering Laboratory of Deep Mine Rockburst Disaster Assessment, Jinan, China, [5]Shandong Province Research Institute of Coal Geology Planning and Exploration, Jinan, China

In recent years, with the increasing of mining depth and mining intensity, coal and gas outburst has become one of the most destructive and harmful dynamic disasters in coal mines. Natural earthquakes are the most destructive natural disasters in the earth's crust. Both of coal and gas outbursts and natural earthquakes are caused by geo-dynamic processes. In order to research the correlation between coal and gas outburst and natural earthquake, in this manuscript, we took Pingdingshan eastern mining area as the research object. The principles of disaster prevention, seismology, statistics and geophysics were taken as the research basis, both the characteristics and laws of natural earthquakes, and the occurrence laws and characteristics of coal and gas outburst were systematically analyzed by geo-dynamic division method. At the same time, the relationship between the two disasters were established. The research results show that natural earthquake is the accumulation and release process of elastic properties in rock mass, which can induce the abnormal emission of gas in coal mines under specific conditions. Especially the "weak plane structure" in geological structure, which is more likely to lead to the occurrence of coal and gas outburst accidents. Tectonic activities and stress field changes have a unified mechanism for the occurrence of natural earthquake and coal and gas outburst, there are correlations between space and intensity. The research results can also provide new ideas for the prediction work of these two kinds of disasters.

KEYWORDS

coal and gas outburst, natural earthquake, geological structure zone, disaster causing mechanism, geo-dynamic division

1 Introduction

With the increasing of mining depth in coal mines and the increasing complexity of geological conditions in China, the number of coal and gas outburst coal mines in China has also increased year by year. The violent dynamic effect of coal and gas outburst has caused serious personnel and property losses to society and enterprises (Yu, 1979; Hu et al., 2008; Li and Lin, 2010; Shu et al., 2017; Luo et al., 2018). As the most serious disaster in nature, natural earthquake is also a problem that the scientific community has always been unable to solve (Li et al., 2014; Mao et al., 2019). However, after years of research by scholars all around

the world, it has been found that the occurrence of the two disasters are affected by geo-dynamic environmental factors such as tectonic activities and stress field changes (Chen et al., 2005; Zhu et al., 2018). If the influence law between the two disasters could be determined, it will have a far-reaching impact on the prediction and early warning of earthquakes and coal and gas outbursts.

The classic M8.1 earthquake in Mountain Kunlun was taken as an example. After the earthquake, gas accidents occurred in five adjacent coal mines (Chen et al., 2009). Since then, the corresponding relationship between coal and gas outburst accidents and natural earthquakes has been found in time and space. For example, the gas explosion in Fushun, Liaoning on 30 March 2003, and the gas explosion in Fuxin, Liaoning on 14 February 2005, which have attracted the attention of many researchers.

Chen et al. (2005) analyzed the change of gas emission in mining space from three aspects, which are rock stress concentration, stress release and seismic activity (rock burst) before and after the earthquake, and they concluded that gas accidents in coal mines may caused by seismic activity.

Li and Cai (2008) explored the possibility and mechanism of gas disaster nucleation caused in coal mines by seismic energy based on the field geophysical observation. The abnormal gas emission in coal mines boosted by earthquake, and the response mechanism of groundwater to far-field earthquake were taken as an analogy, which combined with the geophysical evidence of large-scale simultaneous crustal movement. The analysis results showed that the possibility of coal mine gas disaster could be increased by seismic energy.

He et al. (2018) established the corresponding index evaluation system based on the theory of realizing regional monitoring with microseismic monitoring technology, and conducted application tests in outburst coal mines. The results showed that to monitor coal mining disturbance and geological anomaly was of good effect by taking microseismic frequency index and energy index.

In order to research the microseismic precursor characteristics of coal and gas outburst, based on the optimized outburst physical model and with the help of COMSOL multiphysics, Zhu et al. (2018) constructed a three-dimensional model of spatial gradual change of mechanical properties of coal, and he analyzed the distribution and evolution law of original rock stress and mining stress before and after roadway excavation. The results show that the sharp change of mechanical properties of coal is accompanied by local high stress area, low stress area and large gradient stress distribution. Before the coal outburst caused by regional structure in the process of roadway excavation in coal mines, the evolution of microseismic signal will go through three stages, which are safety period, foreshock period and quiet period. The microseismic signal will gradually decrease with the gradual gradient of soft coal.

According to the principle that mine earthquakes and natural earthquakes are jointly affected by the regional stress field, Pan et al. (2003) put the mine into the regional stress field and the whole Chinese plate for research, and they discussed the correlation between mine earthquakes and the natural earthquakes in the nearby region.

Zhang (2003) believe that tectonic activities and stress field changes have a unified mechanism for the occurrence of natural earthquakes, coal and gas outbursts, mine earthquakes, rock burst and other dynamic disasters in coal mines. Dynamic disasters in coal mines are an accompanying phenomenon in the process of geological fault activities and development of different scales, which are the result of the breeding and formation of secondary faults and fissures.

Zhu et al. (2019) researched the temporal and spatial distribution and evolution law of microseisms during tunneling. They analyzed and obtained the microseismic response law of geological anomaly areas within the mining range. The results show that microseismic events are generally distributed around the roadway during the tunneling of the working face, and the dislocation of the hanging and footwall of the fault caused by mining causes the release of energy in the rock mass, which is the main reason for the fault activation type microseismic activity.

In order to solve the problem of lack of regional online detection and early warning technology in coal and gas outburst mines, Song et al. (2021) applied the microseismic technology, which could reflect the dynamic load and static load of the mine to coal and gas outburst mines. They studied the spatio-temporal evolution characteristics of microseismic signals induced by tunneling. Based on the seismic wave computed tomography technology, the distribution characteristics of regional stress field in heading face are inversed.

In this paper, Pingdingshan eastern mining area was taken as the research object, we divided the No. 8 coal mine, the No. 10 coal mine and the No. 12 coal mine area into grade I to V fault structures, and determined the distribution characteristics and interaction relationship of fault structures in this area. After that, we integrated many disciplines to connect coal and gas outburst and natural earthquake through the geo-dynamic environment, combined with the mechanism and characteristics of coal and gas outburst and natural earthquake, and analyzed the relationship between them in time and space. The research results can provide guidance for the prediction and control of coal and gas dynamic disasters in coal mines.

2 Analysis of occurrence mechanism of natural earthquake and coal and gas outburst

2.1 Type and occurrence mechanism of earthquake

Natural earthquakes can be divided into three types, which are tectonic earthquakes, volcanic earthquakes and subsided earthquakes. Tectonic earthquake is an earthquake caused by the rupture and dislocation of rock strata deep underground, which is also known as “fault earthquake” (Jiang et al., 2022; Li et al., 2022). The earthquakes usually mentioned by us are tectonic earthquakes, which account for more than 90% of the total number of earthquakes in the world, and tectonic earthquakes pose the greatest threat to mankind. In this paper, we will focus on the occurrence mechanism of tectonic earthquakes and the correlation between coal and gas outburst and tectonic earthquake.

The movement of geological structure will destroy and deform the rock, redistribute the original rock stress, produce high stress areas, and form accumulation and concentration of stress. When the continuously accumulated stress in the rock mass exceeds its ultimate strength, the rock mass will be sheared or tensioned.

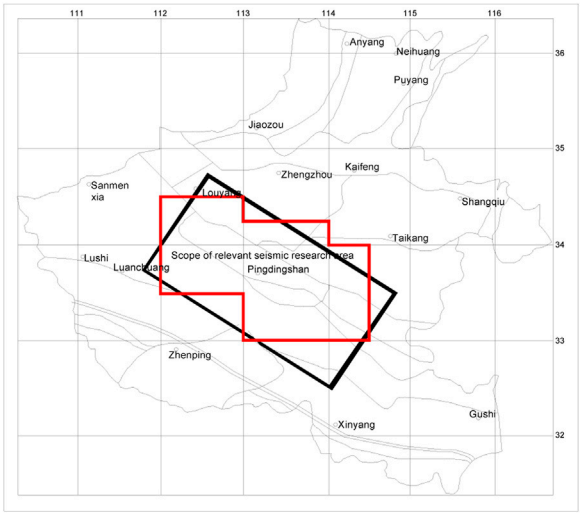

FIGURE 1
Scope of the research area.

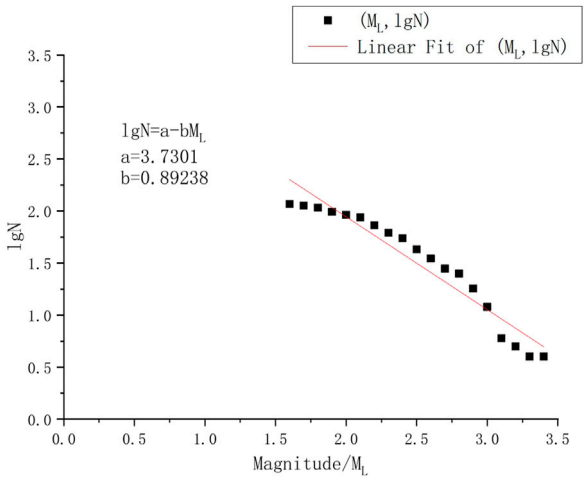

FIGURE 2
Fitting diagram of seismic b value in the research area.

The continuously increasing stress will force the rock mass to vibrate elastically and return to its original shape with its own elastic vibration. The energy released by the elastic vibration will cause earthquakes (Shang and Shi, 2022). This elastic recovery vibration mechanism is used to explain shallow earthquakes with focal depth less than 10 km. When the rock mass is dislocated and deformed, due to the uneven frictional resistance on the damaged structural surface and the stick-slip mechanism of viscosity and sliding during the dislocation process, a series of earthquakes are formed, and the focal depth of these earthquakes is within 20 km. During the tectonic movement, due to the difference in the stiffness of the upper and lower strata, pressure-induced tension fracture and roof breaking and empty lifting phenomenon were formed in the folding process. The deep old strata under high pressure moved up along the fault, igneous rock like dikes and rock discs invaded, and the extrusion mass invaded the surrounding rock, which led to the expansion and development of the fault and triggered the earthquakes. This is the diapiric tectonic development mechanism, but its focal depth is about the level of Conrad surface (About 20 km below the crust) and above the Conrad surface (Wu et al., 2021).

2.2 Mechanism of coal and gas outburst

Coal and gas outburst is a complex dynamic phenomenon and disaster in coal mines. After many scholars' long-term observation and research on a large number of coal and gas outburst phenomena in coal mines, we have basically mastered the causes, conditions and processes of coal and gas outburst, and made it clear that the coal, rock, gas and stress field involved in the outburst are a unified system. The elastic strain energy and gas internal energy accumulated in coal and rock mass are the energy sources of coal and gas outburst. The sudden change of ground stress and the disturbance of mining activities are the excitation factors of coal and gas outburst. If there are weak structural planes, external disturbances, and sudden brittle failure of coal and rock, it may lead to the instability of coal mass in the energy limit equilibrium zone. The elastic potential energy, gas internal energy accumulated in coal and rock mass and the gravity potential energy of unstable coal mass will be unstable, the coal mass will be broken and thrown out (or extruded), and the coal and gas outburst will occur (Gao et al., 2019).

To sum up, when the tectonic stress in the crust gradually accumulates beyond the ultimate bearing capacity of the weak surface of the geological structure, the stress and strain energy will be released in the form of earthquake to obtain a new balance. In the coal mines, the original tectonic stress and mining influence stress and gas pressure formed by mining activities are superimposed. When the stress of coal and rock mass exceeds its ultimate bearing capacity, the stress and energy will be released through coal and gas outburst to obtain a new balance.

2.3 Characteristics of seismicity in Pingdingshan eastern mining area

Pingdingshan eastern mining area is located in the Jiaxian—Pingdingshan fault depression area, and the generation and development of seismic activity in this area are controlled by fault activity. According to the requirements of relevant seismic research area, including the tectonic blocks and active faults that control the seismic activity in Jiaxian—Pingdingshan fault depression area where Pingdingshan eastern mining area is located. In order to analyze the correlation between coal and gas outburst and natural earthquake, the area shown in Figure 1 is selected as the scope of relevant seismic research area. In order to facilitate the selection of seismic data, the scope of relevant seismic research area is approximately a combination of three areas, which are (112°–113°E, 33.5°to 34.5°N), (113°–114°E, 33°to 34.25°N), and (114°–114.5°E, 33°to 34°N). In Figure 1, the area is indicated by the red and thick lines.

The seismicity parameter "b" has a clear physical meaning. High "b" value represents a large proportion of small earthquakes in the

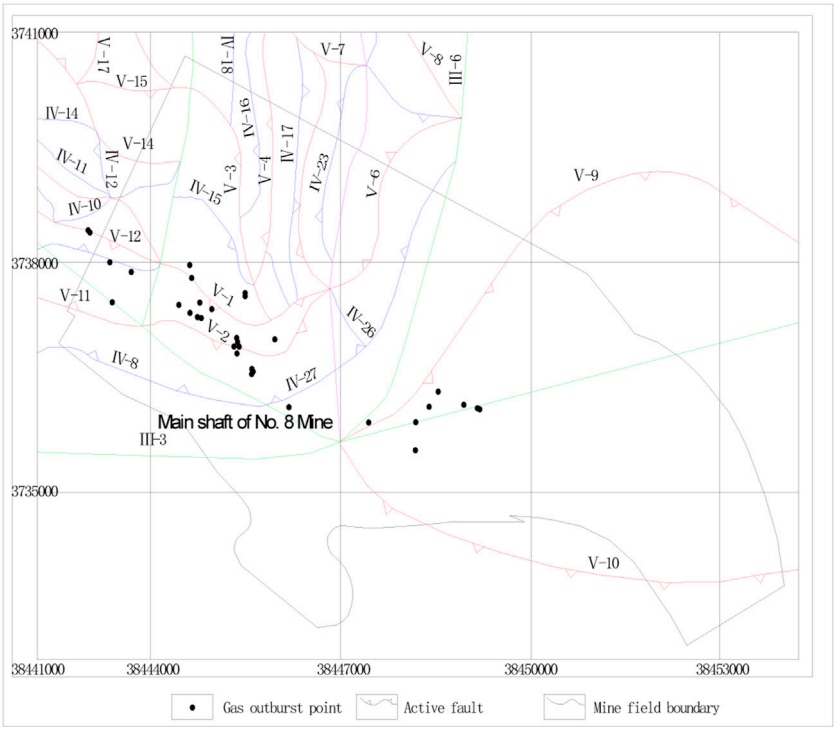

FIGURE 3
Grade VI fault map and spatial distribution map of coal and gas outburst in Pingdingshan No. 8 coal mine.

seismic sample, while low "b" value represents a large proportion of large earthquakes in the seismic sample (Guo et al., 2021). The "b" value is inversely proportional to the shear stress, and the low "b" value region has higher stress accumulation. Therefore, the magnitude of natural earthquake "b" value can be used as an index to measure the stress level of coal and rock mass in the region, thus to evaluate the type and risk of regional dynamic disasters in coal mines.

In order to ensure the reliability of "b" value, the minimum magnitude M_C=1.6 in the natural earthquake catalog is taken as the lower limit of the statistical sample, and the maximum magnitude M_C=3.4 with frequency>1 is taken as the upper limit of the statistical sample. The magnitude frequency relationship of the earthquake catalog is fitted by the least square method, so as to obtain the natural earthquake "b" value in the research area.

According to the calculation, the "b" value of natural earthquakes in the research area is 0.89238, which is higher than the "b" value of natural earthquakes in the whole North China region (0.798), which belonging to the region with relatively high "b" value distribution in North China region. The higher "b" value reflects that the crustal stress level in the research area in recent 30 years is lower than that in the whole North China region, so there are fewer rock burst and mine earthquakes that are more affected by the crustal stress. It is determined that coal and gas outburst are the main mine dynamic disasters in the research area, and the seismic "b" value fitting diagram of the research area is shown in Figure 2.

According to the above analysis results, the coal and gas outburst in the mining area and the occurrence of natural earthquake have internal correlation in terms of geo-dynamic conditions. Therefore, we use the geo-dynamic division method to divide the fault structures in Pingdingshan eastern mining area into grade I to V, and determine the high stress area, stress gradient area and low stress area, so as to build the relationship between the two disasters.

3 Geo-dynamic division of Pingdingshan eastern mining area

3.1 Geological structure characteristics of Pingdingshan eastern mining area

The geological structure of the mining area in the east of Pingdingshan is mainly distributed in NW direction and NE direction. In the NW direction, the geological structure is mainly subjected to compression and shear, while in the NE direction, the geological structure is mainly subjected to tension and shear. No. 8 coal mine, No. 10 coal mine and No. 12 coal mine in Pingdingshan eastern mining area are located in the structural complex area controlled by NW trending faults and folds. Coal and gas outbursts mainly occur near the structure.

The occurrence of dynamic disasters in Pingdingshan eastern mining area is controlled by the thrust nappe tectonic belt, which has a strong extrusion effect. Under the extrusion pressure, the porosity of the coal seam is reduced, and the ability of the coal seam to store gas is enhanced. Under the extrusion stress, the stress concentration and energy accumulation appear in the coal and rock mass. Pingdingshan mining area is located in the northeast edge of the thrust nappe structural belt, which is in the energy accumulation

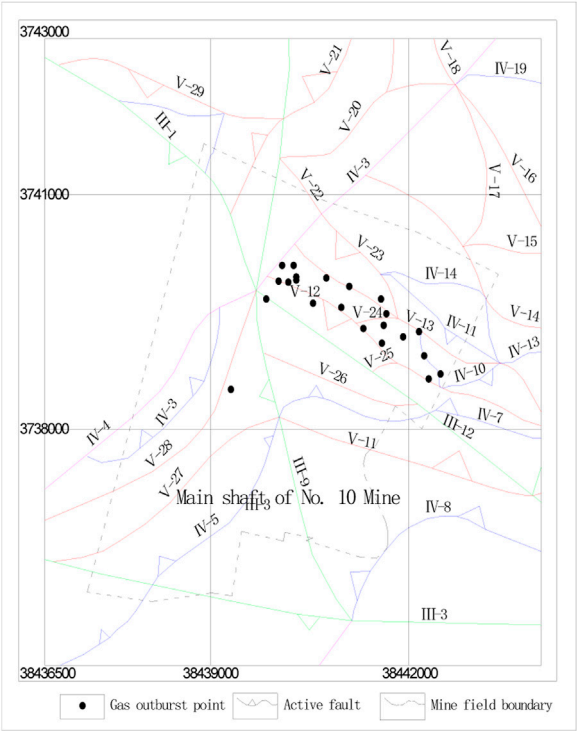

FIGURE 4
Grade VI fault map and spatial distribution map of coal and gas outburst in Pingdingshan No. 10 coal mine.

area. When the energy accumulated by coal and rock volume reaches the critical condition, under the disturbance of mining, the accumulated elastic energy will release in the weak surface of coal and rock mass, and coal and gas outburst will be formed.

3.2 Classification of grade IV and grade V fault structures in the mining area

Geo-dynamic division is an interdisciplinary subject, which is involved mining, geology, surveying mechanics, and computer technology. It is mainly based on the principle that the basic form and main characteristics of landform which are determined by the form of geological structure. Through the analysis of landform, the formation and development of regional faults could be found out, the stress state of rock mass could be determined, geological environment information for human engineering activities could be provided and the possible geological effects of engineering activities could be predicted (Zhang et al., 1998; Zhang et al., 2019).

In this paper, we use geo-dynamic division method to divide the research area into faults. On the basis of the division of grade I to grade III faults, we narrow the division scope to the research area with a larger scale. After that, we divide the grade IV and grade V faults. The division of regional geological structure is more specific than the actual fault, which can reflect the formation and development of the fault and reflect a trend. It is a structural model map of the research area based on the actual geological structure fault, mainly by drawing method, combined with the interpretation of aerial and satellite photos, trend surface analysis, earthquake and regional tectonic activity survey methods, so as to observe the relationship between fault structure and coal and gas outburst in location. No. 8 coal mine and No. 10 coal mine were taken as examples, the spatial distribution of active faults and coal and gas outbursts are shown in Figures 3, 4.

As shown in Figure 3, the coal and gas outburst in the western area of No. 8 coal mine is mainly controlled by active faults III-6, III-12, V-1, V-2, V-11, and V-12. Among the 24 coal and gas outbursts in Wu-9-10th coal seam, 19 were located between active faults III-12 and V-1, and active fault V-2 passed through the middle. 2 were located at the intersection of V-3 fault and VI-15 fault. 3 were located between III-12 and V-12 active faults, and 2 were distributed along VI-7 fault. 3 of the 18 coal and gas outbursts occurred near the intersection of III-6, III-12, and V-11 in Ji-15th coal seam. 1 was located at the intersection of III-12 fault and VI-27 fault, which was mainly affected by the active III-12 fault. In general, the western area of Pingdingshan No. 8 coal mine is affected by the III-12 large-scale active fault, and under the influence of the active faults V-1, V-2, and V-12, resulting in the frequent occurrence of coal and gas outbursts near the fault zone, and in the intersection area.

The coal and gas outburst events in No. 10 coal mine are mainly distributed near the north side of the III-12 fault. Among the 25 coal and gas outbursts in the Wu-9-10th coal seam, 14 occurred near the V-12 active fault. 4 were located near the V-13 fault zone, two times near the V-24 fault zone, and 3 near the VI-9 fault zone. It can be seen that the area is generally affected by active fault III-12. In this area, due to the strong activity of grade III active faults and the large distribution density of grade V active faults, the rock mass is highly fractured and the tectonic stress concentration is strong, resulting in the high frequency and intensity of coal and gas outburst. It shows that the geological fault structure is the energy source of coal and gas outburst.

3.3 Geo-dynamic division and seismic structure of mining area

The fault structure will form a local tectonic stress concentration area, and the concentration of tectonic stress will lead to the accumulation of elastic deformation potential of coal and rock mass. When underground engineering activities enter this area, due to the superposition of mining stress, the stress balance of coal and rock mass is destroyed, and the elastic potential accumulated in coal and rock strata is suddenly released. When the released elastic energy is greater than the consumed energy, it will lead to coal and gas outburst, rock burst and other mine dynamic disasters. Therefore, based on the view of geo-dynamic division, it is considered that tectonic activity and tectonic stress are the dynamic sources of mine geo-dynamic disasters, and engineering activity is the direct inducement of coal and gas outburst and rock burst. In order to analyze the specific relationship between earthquakes and fault structures in the mining area, earthquakes with magnitudes greater than 1.1 that have occurred near the mining area are linked to the grade III fault division map. The relationship between grade III

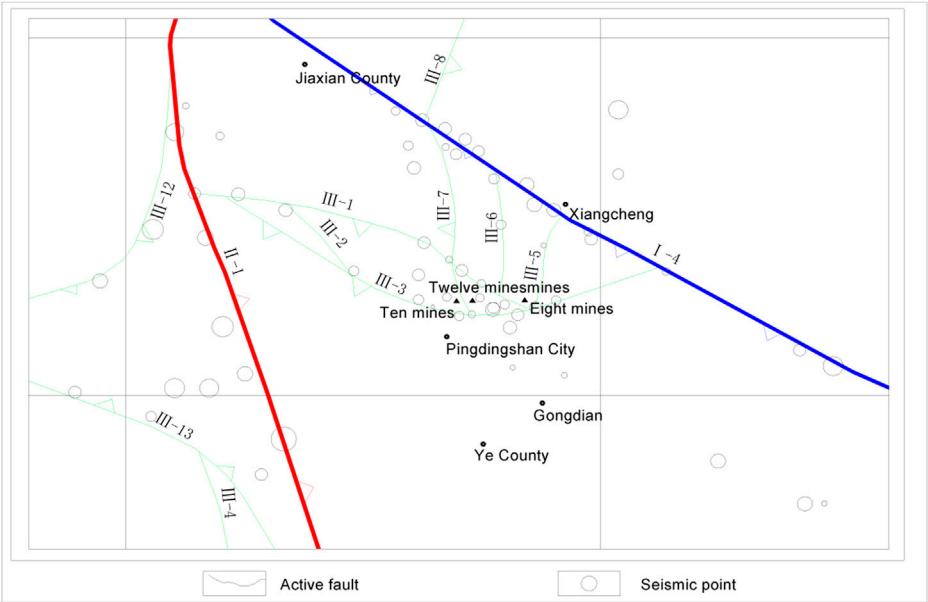

FIGURE 5
Grade III division and seismic distribution in the mining area.

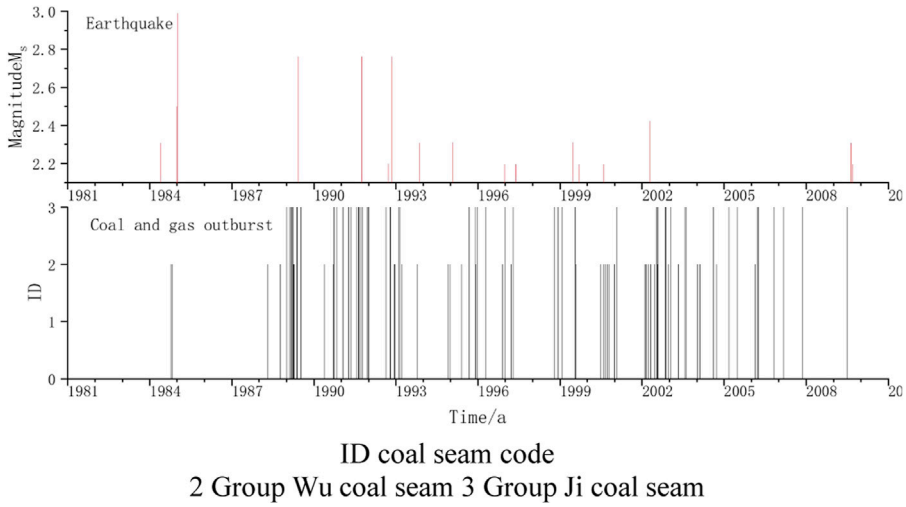

FIGURE 6
Time sequence comparison diagram of coal and gas outburst and natural earthquake (M_S>2.1) in Pingdingshan eastern mining area.

division and seismic distribution in the mining area is shown in Figure 5.

Among them, the major faults are I-4 and II-1, and the III-3 fault crosses between the two major faults. Earthquakes are also mostly distributed near this fault, so the above three fault zones play a leading role in the occurrence of earthquakes controlling, and the existence of the fault is easy to cause stress concentration and earthquake. The earthquake caused by the fault structure activity releases the energy of the fault structure, which is easy to cause mine geodynamic disasters such as coal and gas outburst.

4 Study on the correlation between natural earthquake and coal and gas outburst in Pingdingshan eastern mining area

4.1 Temporal correlation

Synchronicity specifically refers to that when Ms>2.1 earthquakes occur or are more frequent in the research area, coal and gas outbursts occur more or intensively in

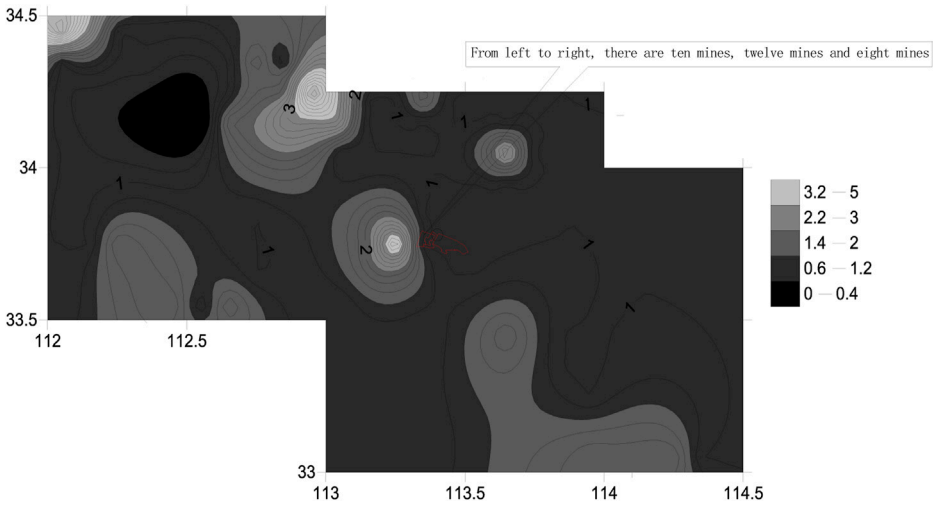

FIGURE 7
Isoline of seismic frequency in the research area.

Pingdingshan eastern mining area, and *vice versa*. The time sequence comparison of coal and gas outburst in Pingdingshan eastern mining area and natural earthquake (Ms≥2.1) in the research area is shown in Figure 6.

On 6 January 1985, an earthquake with M_S=3.0 occurred in Yichuan, Henan Province. There were also three earthquakes with Ms>2.1 in about half a year before the earthquake. These four earthquakes were the only earthquakes with Ms>2.1 from 1981 to 1987. During the four earthquakes, two coal and gas outbursts occurred in Pingdingshan eastern mining area for the first time since production, while no coal and gas outbursts occurred in the eastern mining area of Pingdingshan in 3 years after the four earthquakes. Coal and gas outburst and natural earthquake are close to synchronization in time. In addition, two coal and gas outbursts occurred before the Yichuan earthquake with M_S=3.0, and the other three earthquakes with M_S>2.1 appeared as "precursors" of larger earthquakes. There were three earthquakes with larger magnitudes from 1988 to 1993, all of which were magnitude, corresponding to three intensive coal and gas outbursts in Pingdingshan eastern mining area in 1989, 1991 and the end of 1992 (early 1993), At the same time, the M_S = 2.75 earthquake on 5 June 1989 also lagged behind that in 1988, and coal and gas outbursts also appeared as "precursors".

After 2008, the synchronization of coal and gas outburst and natural earthquake in Pingdingshan eastern mining area was highlighted again. On August 25th and 12 September 2009, earthquakes with M_S = 2.3 and M_S = 2.2 occurred in Yicheng and Yiyang, Henan, respectively. This was the first earthquake with M_S>2.1 since 2003. The mining area was highlighted in 2009, but not in the adjacent years.

As shown in Figure 6, although the coal and gas outburst in Pingdingshan eastern mining area and the natural earthquake in the research area have a certain degree of synchronization in the dense sparse time process, the synchronization is poor in some years (1994–2008), which reflecting that although the tectonic activity and stress field changes have a unified mechanism for the occurrence of natural earthquakes and coal and gas outbursts, and the two disasters are correlated, the occurrence of coal and gas outbursts is also affected by gas occurrence due to the influence of coal seam mining, outburst prevention and control activities and other factors, the degree of correlation varies from time to place.

4.2 Spatial distribution relevance

The research area is divided into evenly spaced grids with grid cell size of 0.1°×0.1°, count the frequency of seismic records in the grid unit, and using this as the frequency of seismic activity at the center of the unit to draw the seismic frequency contour. The natural earthquake frequency contour in the research area is shown in Figure 7.

According to the frequency contour, the spatial distribution characteristics of earthquake frequency in the research area are basically consistent with the spatial distribution characteristics of earthquake magnitude, showing the pattern of natural seismicity in the region. The mining area in Pingdingshan eastern mining area is located near the light colored area of the seismic frequency contour map, which is near the seismic high frequency area of the research area.

In terms of magnitude and frequency, the mining area in Pingdingshan eastern mining area belongs to the concentrated area of crustal energy release, and the stress field is relatively unstable. The spatial distribution characteristics of natural seismicity reveal that Pingdingshan eastern mining area is prone to dynamic disasters. The change of stress field of seismic response conforms to the characteristics of dynamic source of coal and gas outburst in the research area, and the two disasters are spatially correlated. In such a dynamic environment, coal and gas outbursts and other mine dynamic disasters will occur frequently in Pingdingshan eastern mining area.

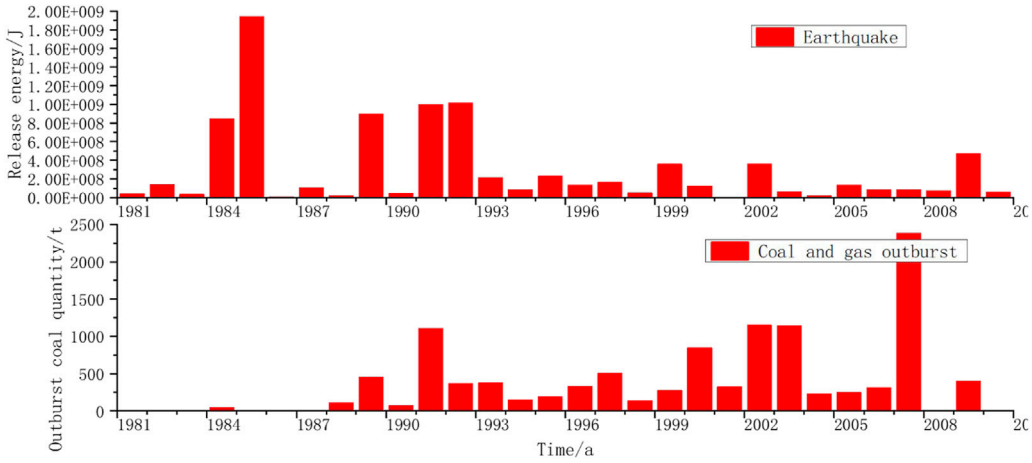

FIGURE 8
Comparison histogram of annual coal and gas outburst and annual energy released by natural earthquake in Pingdingshan eastern mining area.

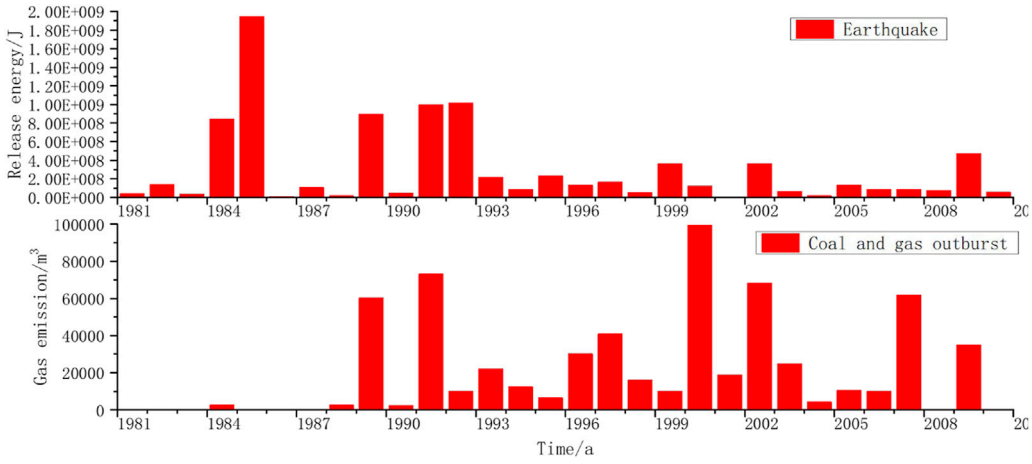

FIGURE 9
Histogram of annual outburst gas volume and annual release energy of natural earthquake of coal and gas outburst in Pingdingshan eastern mining area.

4.3 Strength relevance

The energy released by earthquakes depends on magnitude and frequency, and the annual energy released by earthquakes that combine magnitude and frequency reflects the intensity of seismic activity (Wangi et al., 2021). The intensity of coal and gas outburst is represented by the volume of outburst coal and the amount of gas emitted (Wang et al., 2022). According to the annual released energy of natural earthquakes in the research area and the annual coal and gas outburst volume and annual gas emission data of coal and gas outburst in Pingdingshan eastern mining area, Figures 8, 9 are drawn.

It can be seen from Figures 8, 9 that the annual activity intensity of coal and gas outburst and natural earthquake basically maintained the same trend before 1993, that is, in the year when the energy released by natural earthquake was large, the annual intensity of coal and gas outburst was also in the peak year. It shows that the natural earthquake and coal and gas outburst are affected by the tectonic activity and the change of stress field. The external manifestation of the effect is the natural earthquake or coal and gas outburst and other mine dynamic disasters. It also shows that the tectonic activity and the change of stress field before 1993 are the dominant factors inducing coal and gas outburst.

From 1994 to 2008, the annual energy released by natural earthquakes in the mining area generally showed a downward trend, while the coal and gas outburst generally showed an upward trend according to the judgment of the amount of outburst coal and gas emission. To analysis of the reasons, first, with the deepening of mining, mining disturbance plays a major role

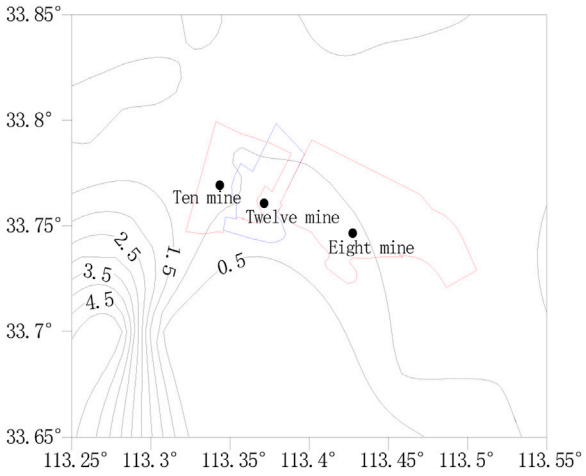

FIGURE 10
Comparison of mine dynamic disasters and natural earthquake frequency such as coal and gas outburst (M_S>2.1).

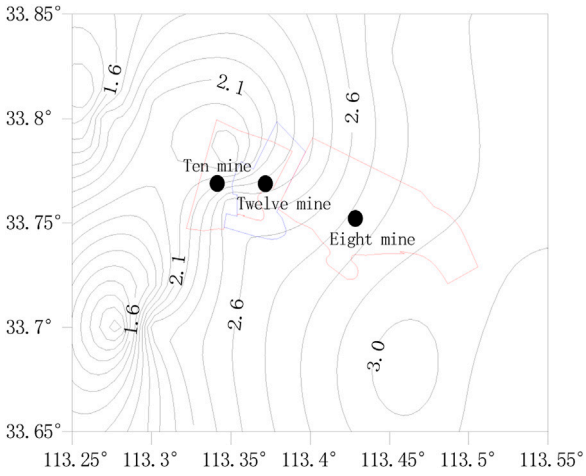

FIGURE 11
Comparison results of coal and gas outburst and other mine dynamic disasters with natural earthquake magnitude (M_S>2.1).

in the change of local stress field in a small range, and its influence ability has exceeded the self-regulation of regional tectonic stress field in a large range to a certain extent. Second, the gas content in the coal seam below 900 m is increasing with the increase of buried depth (according to the actual measurement), and the impact of high gas is greater. The intensity of energy released by natural earthquakes in 2007 is not large, which belongs to the medium level in the 30 years from 1981 to 2010, reflecting that the adjustment of regional tectonic stress field is not strong, and the tectonic activity is relatively calm. However, the amount of coal and gas outburst in 2007 reached the highest level in the history of outburst in the eastern mining area, indicating that the participation of tectonic stress in outburst was not high in 2007, and high gas and mining stress were the main factors of causing outburst.

The annual energy released by natural earthquakes showed an upward trend in 2009 and later. The annual energy released by earthquakes in 2009 reached the maximum value in the past 17 years, and the corresponding coal and gas outburst volume and gas emission volume were large. It shows that with the strengthening of regional tectonic activity and stress field, the influence of tectonic activity and stress field change on coal and gas outburst has begun to dominate.

It can be seen from the above analysis that the earthquake activity corresponding to the gas accident is generally at the magnitude of 2.5–4.5, rather than the magnitude of more than 5, which is specifically manifested in the destruction of gas reservoirs and coal seams caused by the earthquake. During the earthquake, the coal seam containing gas is loosened, the permeability of the coal seam is increased, the stress is released, and a large amount of gas is emitted.

4.4 Impact of natural earthquake on coal and gas outburst

In order to better reflect the impact of natural earthquakes on coal and gas outburst in the mining area, the comparison diagram between the frequency and magnitude of coal and gas outburst events and natural earthquakes in Pingdingshan eastern mining area is drawn, and the comparison results are shown in Figures 10, 11.

In Figures 10, 11, the spatial distribution of magnitude and frequency of natural earthquakes in Pingdingshan eastern mining area are reflected. The historical magnitudes of natural earthquakes in No. 8 coal mine, No. 10 coal mine and No. 12 coal mine are concentrated between 2.0 and 2.9, reflecting that the magnitude of natural earthquakes in Pingdingshan eastern mining area is relatively large and concentrated near the high value area.

The above analysis results show that the natural earthquake and coal and gas outburst in Pingdingshan eastern mining area have a certain correlation in time, space and intensity, and both of them are affected by the geological structure, with the same energy base and dynamic source. The seismic activity directly causes the physical damage of the gas reservoir, providing the conditions for the analysis and migration of the gas overflow in the coal mass. On the correlation between seismic activity and coal and gas outburst, tectonic movement plays a leading role, and coal and gas outburst is in a passive position. Tectonic movement causes coal and gas outburst and other mine dynamic disasters through stress disturbance.

5 Conclusions and suggestions

(1) The occurrence mechanism of coal and gas outburst and natural earthquake have been analyzed. Both of them are affected by tectonic activities and stress field changes. Tectonic activities and stress field changes have a unified mechanism for the occurrence of coal and gas outburst and natural earthquake.
(2) Pingdingshan eastern mining area and its surrounding areas are relatively high in North China (b value), and the tectonic stress level is lower than the average level of the whole North China region. The dynamic disasters in Pingdingshan eastern mining area are mainly coal and gas outbursts.
(3) Pingdingshan eastern mining area has been divided into Ⅰ to Ⅴ fault structures by geo-dynamic division method. The results

show that most of the earthquakes in the mining area are distributed near the fault structures, and the fault structures control the small earthquakes and microseismic events in the mining area.

(4) Natural earthquake and coal and gas outburst have certain relevance in time, space and intensity. The specific performance is that natural seismic activity affects the occurrence of coal and gas outburst events, the disturbance amplitude of *in situ* stress is the key role, tectonic movement is the leading role, and coal and gas outburst is in a passive position.

(5) According to the geological structure form and fault strike of the mining area, we should understand the influence of tectonic stress disturbance and mining pressure relief on the roof and gas release, find out the stress concentration area, and establish a standard ground pressure and gas monitoring system.

Data availability statement

The original contributions presented in the study are included in the article/supplementary material, further inquiries can be directed to the corresponding author.

Author contributions

HR and SY wrote the main manuscript text. WS and GT were responsible for geo-dynamic division in Pingdingshan mining area. YW, DS, and BH were responsible for figure making and data analysis. All authors reviewed the manuscript.

Funding

This project was supported by the National Natural Science Foundation of China Project No. 51904145, the Engineering Laboratory of Deep Mine Rockburst Disaster Assessment Open Project No. LMYK2021005, the Engineering Laboratory of Deep Mine Rockburst Disaster Assessment Open Project No. LMYK2020006, Anhui Provincial Academic Funding Program for Top Disciplines (Specialties) in Colleges and Universities No. gxbjZD2022134, Basic scientific research project (youth project) of Liaoning Provincial Department of Education in 2022 (LJKQZ20222322) and the announced bidding project of the Shanxi Provincial Science and Technology Plan No. 20191101015.

Conflict of interest

The authors declare that the research was conducted in the absence of any commercial or financial relationships that could be construed as a potential conflict of interest.

Publisher's note

References

Chen, B., Zheng, W. T., and Liang, H. D. (2005). Interaction of earthquake activity and gas accident in coal mining underground. *J. China Coal Soc.* 4, 447–450.

Chen, Y. H., Dong, Z. P., and Cheng, J. W. (2009). Preliminary discussion on the comprehensive characteristics and preparation process of the anomaly of the M8.1 earthquake in the west of Kunlun Mountain Pass. *Seismol. Geol.* 31 (02), 363–371. doi:10.3969/j.issn.0253-4967.2009.02.017

Gao, K., Qiao, G. D., and Liu, Z. D. (2019). On classification conception of coal and gas outburst mechanism and its application. *J. Min. Saf. Eng.* 36 (05), 1043–1051. doi:10.13545/j.cnki.jmse.2019.05.023

Guo, T. L., Liang, S. S., and Zou, L. Y. (2021). Using the microseismic template match and locate method to identify microseismic events in the Fushun mining area. *Liaoning Seismol. geomagnetic Observation Res.* 42 (06), 76–81. doi:10.3969/j.issn.1003-3246.2021.06.011

He, X. Q., Wang, A. H., and Dou, L. M. (2018). Technology of microseismic dynamic monitoring on coal and gas outburst-prone zone. *J. China Coal Soc.* 43 (11), 3122–3129. doi:10.3969/j.issn.1003-3246.2021.06.011

Hu, Q. T., Zhou, S. N., and Zhou, X. Q. (2008). Mechanical mechanism of coal and gas outburst process. *J. China Coal Soc.* 33 (12), 1368–1372. doi:10.13225/j.cnki.jccs.2008.12.018

Jiang, Z. S., Shao, Z. G., and Liu, X. X. (2022). Crustal deformation associated with seismogenic process of Chinese main land strong earthquakes and identification of approximation to seismogenic process in the late seismogenic stage [J]. *Geomatics Information Sci. Wuhan Univ.* 47 (06), 807–819. doi:10.13203/j.whugis20220204

Li, D. W., Chen, J. L., and Chen, G. F. (2014). Continental seismotectonic system: example from Qinghai-Tibet Plateau and its adjacent areas [J] Earth Science. *J. China Univ. Geosciences* 39 (12), 1763–1775. doi:10.3799/dqkx.2014.160

Li, T., and Cai, M. F. (2008). The mechanism of earthquake induced gas disaster nucleation in coal mines. *J. Coal Industry* 10, 1112–1116. doi:10.13225/j.cnki.jccs.2008.10.012

Li, X. J., and Lin, B. Q. (2010). Status of research and analysis on coal and gas outburst mechanism. *Coal Geol. Explor.* 38 (01), 7–13. doi:10.3969/j.issn.1001-1986.2010.01.002

Li, X. W., Zhang, G. G., and Xie, Z. J. (2022). The mechanism of M6.0 earthquake in Luxian County, Sichuan Province in 2021 and the temporal and spatial evolution characteristics of seismic activity. *Chin. J. Geophys.* 65 (11), 4284–4298. doi:10.6038/cjg2020Q0045

Luo, M. K., Fan, C. J., and Li, S. (2018). Failure criteria of the geological dynamic system of coal and gas outburst. *J. China Univ. Min. Technol.* 47 (01), 137–144. doi:10.13247/j.cnki.jcumt.000820

Mao, S. L., Cai, X. X., and Jiang, M. (2019). Discussion on the mechanism of tectonic earthquake formation - -introduction to the physical model of fracture bulge. *Sci. Technol. Inf.* 17 (31), 1–3. doi:10.16661/j.cnki.1672-3791.2019.31.001

Pan, Y. S., Li, Z. H., and Zhang, M. T. (2003). Disterbution, type, mechanism and prevention of rockbrust in China. *Chin. J. Rock Mech. Eng.* 11, 1844–1851.

Shang, Y. C., and Shi, B. P. (2022). The mechanism of the 2013 Qianguo earthquake swarm in Jilin base on the stressing rate and seismicity model. *Chin. J. Geophys.* 65 (01), 26–36. doi:10.6038/cjg2022p0125

Shu, L., Wang, K., Qi, Q., Fan, S., Zhang, L., and Fan, X. (2017). Key structural body theory of coal and gas outburst. *Chin. J. Rock Mech. Eng.* 36 (02), 347–356. doi:10.13722/j.cnki.jrme.2016.0598

Song, D. Z., He, X. Q., and Dou, L. M. (2021). Research on MS regional detection technology for coal and gas outburst hazard. *China Saf. Sci. J.* 31 (01), 89–94.

Wang, W., Wang, H. P., and Zhang, B. (2022). Experimental study on multi-factor influence law and energy criterion of coal and gas outburst. *J. Northeast. Univ. Nat. Sci.* 43 (04), 582–590. doi:10.12068/j.issn.1005-3026.2022.04.017

Wangi, Z. W., Cai, H. Y., and Chen, M. L. (2021). Spatio - temporal evolution characteristics of earthquake in "the Belt and Road"for over 100 years. *J. Nat. Disasters* 30 (01), 141–154. doi:10.13577/j.jnd.2021.0115

Wu, Z. H., Pan, P. Z., and Pan, J. F. (2021). Analysis of mechanism of rock burst and law of mining induced events in graben structural area. *Rock Soil Mech.* 42 (08), 2225–2238. doi:10.16285/j.rsm.2020.1732

Yu, B. F. (1979). On the mechanism of coal and gas outburst. *Coal Sci. Technol.* 8, 34–42. doi:10.13199/j.cst.1979.08.36.yubf.009

Zhang, H. W. (2003). Application of geodynamic zoning method in prediction of coal and gas outburst region. *Chin. J. Rock Mech. Eng.* 04, 621–624.

Zhang, H. W., Ma, Y. F., and Duan, K. X. (1998). Tectonic stress and mine earthquake. *J. Liaoning Tech. Univ. Nat. Sci.* 20 (01), 1–6.

Zhang, J. G., Lan, T. W., and Wang, M. (2019). Prediction method of deep mining dynamic disasters and its application in Pingdingshan mining area. *J. China Coal Soc.* 44 (06), 1698–1706. doi:10.13225/j.cnki.Jccs.2019.6037

Zhu, N. N., Zhang, L., and Shu, L. Y. (2018). Experimental study on microseismic precursory characteristics of coal and gas outburst and case analysis of early-warning. *Chin. J. Rock Mech. Eng.* 37 (06), 1419–1429. doi:10.13722/j.cnki.jrme.2017.1451

Zhu, Q. J., Li, Q. S., and Zhang, E. H. (2019). Study on microseismic characteristics of geologic anomaly region in coal and gas outburst seam induced by roadway excavation. *Coal Sci. Technol.* 47 (07), 39–46. doi:10.13199/j.cnki.cst.2019.07.003

frontiers | Frontiers in Earth Science

TYPE Original Research
PUBLISHED 28 February 2023
DOI 10.3389/feart.2023.1127995

OPEN ACCESS

EDITED BY
Yu Song,
China University of Mining and Technology, China

REVIEWED BY
Shiqi Liu,
China University of Mining and Technology, China
Junhong Yuan,
Inner Mongolia University, China

*CORRESPONDENCE
Yutong Fu,
fytxuzhidan@163.com

SPECIALTY SECTION
This article was submitted to Economic Geology, a section of the journal Frontiers in Earth Science

RECEIVED 20 December 2022
ACCEPTED 23 January 2023
PUBLISHED 28 February 2023

CITATION
Fu Y, Yuan W, Xu Z, Zhao R, Wu Y, Zheng H, Wang X, Guo X, Gou S and Ma C (2023), Geological adaptability of deep CBM fractured horizontal well in SLN block. *Front. Earth Sci.* 11:1127995. doi: 10.3389/feart.2023.1127995

Geological adaptability of deep CBM fractured horizontal well in SLN block

Yutong Fu[1]*, Weilin Yuan[1], Zhidan Xu[2], Ruosi Zhao[1], Yue Wu[3], Haibo Zheng[1], Xianqing Wang[1], Xudong Guo[1], Shiyong Gou[4] and Chunlin Ma[4]

[1]Sanya Institute of South China Sea Geology, Guangzhou Marine Geological Survey, China Geological Survey, Sanya, China, [2]Shiwen Software Co., Ltd., Xian, China, [3]No. 11 Oil Production Plant, PetroChina Changqing Oilfield Company, Qingyang, China, [4]Shaanxi Tiancheng Petroleum Technology Co., Ltd., Xian, China

The buried depth of the main coal beds in SLN Block is more than 1,500 m, and the gas content of the coal beds is high. However, the coal beds are generally in a high geostress environment, the permeability of the coal beds is generally low, and the development effect of conventional fractured straight wells is poor. Fractured horizontal well is an important technical means to improve the development effect of low permeability coalbed methane, but the investment cost is high. To reduce the investment risk of fractured horizontal wells, it is necessary to find out the gas production capacity and main control factors of the fractured horizontal wells, and determine the area suitable for the development of fractured horizontal wells. In the area with permeability higher than 0.28 md and gas content higher than 12.8 m^3/t, the daily gas production capacity of fractured horizontal well is 16,450–21500 m^3/d, and the development effect is good. The research results are of great significance to quickly evaluate the adaptability of fractured horizontal wells.

KEYWORDS

deep CBM, fractured horizontal well, numerical simulation, geological suitability, sln block

1 Introduction

China has abundant deep coalbed methane (CBM) resources. The total resources of CBM buried between 1,000 and 2,000 m is approximately 22.4 × 10^{12} m^3 (Luo et al., 2019; Xu et al., 2019). As of 2015, China has been developing CBM for more than 40 years, and 20,000 CBM wells have been drilled (Li et al., 2015; Mu et al., 2015; Yan et al., 2019). Due to the poor permeability of deep coal beds, the development effect of fracturing straight wells is not ideal (Fei et al., 2015; Cao et al., 2016; Ali et al., 2017; Su et al., 2018). How to improve the gas production is a major problem faced by China's deep CBM development (Song et al., 2015; Sun et al., 2016; Fan et al., 2018). The horizontal well is a very important stimulation technology, which has the advantages of small well pad area, large discharge area, high gas production of single well, and quick capital recovery (Liu et al., 2018). According to whether the horizontal section of horizontal well is fractured, it can be divided into non-fractured horizontal well and fractured horizontal well (Hoang et al., 2008; Gentzis. 2009). Different types of horizontal wells have different geological adaptation conditions. In order to maximize the development benefit, it is necessary to evaluate the geological conditions suitable for fractured horizontal wells. Scholars at home and abroad have conducted a lot of research on coal seam permeability, gas content, coal seam thickness, isothermal adsorption performance, coal structure, structural characteristics and fault development (Laubach and Gale. 2006; Zou et al., 2018). Unfractured horizontal wells are applicable to high permeability and high gas bearing areas with simple

structures and undeveloped faults, and fractured horizontal wells are applicable to medium low permeability and medium high gas bearing areas (Thararoop et al., 2012; Zhang et al., 2017). Predecessors' research results are mainly concentrated in the shallow coal beds with a depth of 1,000 m, the geostress is relatively low, and the physical properties of the coal beds are relatively good (Zhang 2014). The burial depth of the coal beds in SLN Block is generally more than 1,500 m, the ground stress of the coal beds is generally high, and the physical properties are generally poor. Whether the geological adaptability of horizontal wells is the same as that of the middle and shallow parts needs further study. On the basis of previous research results, this paper uses numerical simulation method to study the gas production of fractured horizontal wells under different coal seam physical properties and thicknesses, and determines the geological conditions of deep coal beds suitable for fractured horizontal wells according to the gas production.

2 Geological overview

2.1 Geological setting

The Ordos Basin is situated in central China and has an area of 25×10^4 km^2, which is composed of six structural units (Figure 1): Yimeng uplift, Weibei uplift, Western edge thrusting belt, Jinxi flexural fold belt, Tianhuan depression, and Yishan slope. The SSN Block covers an area of about 975 km^2, which is located in the southern area of Ordos Basin. It is adjacent to the Jinxi flexural fold belt in the middle north and Yishan slope in the West. Four main faults are developed in the area: Shilou East fault, Caocun fault, Caocun East fault, and Xixian East fault, forming six structural units, including Shilou anticline, Shilou East syncline, Caocun anticline, Caocun East syncline, Xixian anticline, and Xixian East syncline.

2.2 Geological characteristics

The coal-bearing deposits of the basin are composed of Pennsylvanian, Permian, and Triassic. From bottom to top, there are Carboniferous Benxi Formation and Taiyuan Formation, Permian Shanxi Formation, Shihezi Formation and Shiqianfeng Formation. The block mainly develops five layers of coal beds, including No. 4 and No. 5 coal beds in the Shanxi Formation of Permian (P1s), No. 7, No. 8, and No. 9 coal beds in the Taiyuan Formation of upper Carboniferous (C3t). The No. 9 coal seam is the target stratum for the coalbed methane (CBM) development.

The thickness of the No. 9 coal seam ranges from 2.2 to 8.5 m, with a mean value of 5.6 m. The buried depth of No. 9 coal Seam is 1,300–2,000 m, with an average of 1,650 m. The buried depth of the No. 9 coal seam is gradually deepened from the South to the North, while the thickness shows a contradict changes trend. The vitrinite reflectance is 1.70%–2.20%, with an average of 1.93%. The coal rank is dominated by lean coal and lean coal. The coal seam gas content of Shanxi Formation is 14.0–28.9 m^3/t, with an average of 16.8 m^3/t;

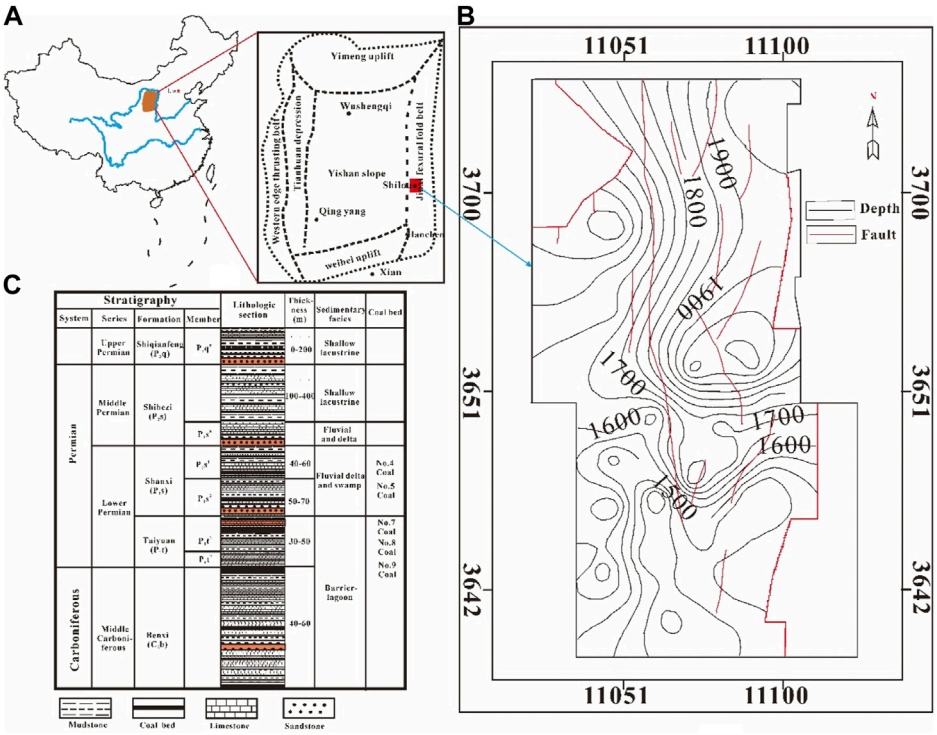

FIGURE 1
The location and geological setting of the SSN Block (revised from Tang et al., 2018), **(A)** and **(B)** are the geological structure map; **(C)** is the stratigraphic column.

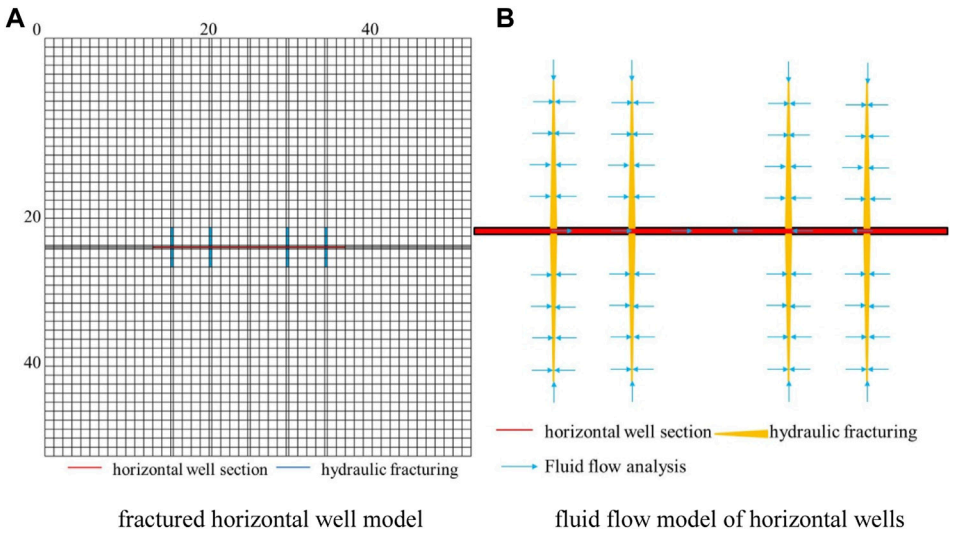

FIGURE 2
Fractured horizontal well model. **(A)** fractured horizontal well model, **(B)** fluid flow model of horizontal wells.

The gas saturation is 82.1%–97.6%, with an average of 92.6%. The coal seam gas content of Taiyuan Formation is 14.5–23.2 m^3/t, with an average of 18.8 m^3/t; Gas saturation is 68.2%–89.8%, with an average of 82.1%. The coal seam porosity is 1.79%–7.24%, with an average of 3.66%. The permeability of coal seams in this area varies greatly from 0.01 to 6.4 mD, which is not only affected by the change of coal seam burial depth, but also related to structural characteristics and coal quality.

3 Geological model of horizontal well

3.1 Simulation area and horizontal well model

The simulation area is 2,315 m × 2,235 m horizontal rectangular area (Figure 2A), the whole simulation area is divided into 49 × 51 grids. The 15th, 20th, 30th, 35th columns and the 25th, 26th, and 27th rows are densified grids, with grid sizes of 5 m × 50 m and 50 m × 5 m, other grid size is 50 m × 50 m. The grid permeability in line 26 is 0.005 mD, simulating the pollution zone around the wellbore.

The horizontal section of the horizontal well is 1,000 m long, located in the 26th row of the simulation area, and the midpoint of the horizontal section is located in the center of the simulation area. In the horizontal section, there are four pressure fractures with a length of 90 m and a half seam of 90° to the horizontal plane of the shaft, respectively in the 15th, 20th, 30th, and 35th columns. The fracture conductivity is 400 mD, and the fracture conductivity remains unchanged during drainage.

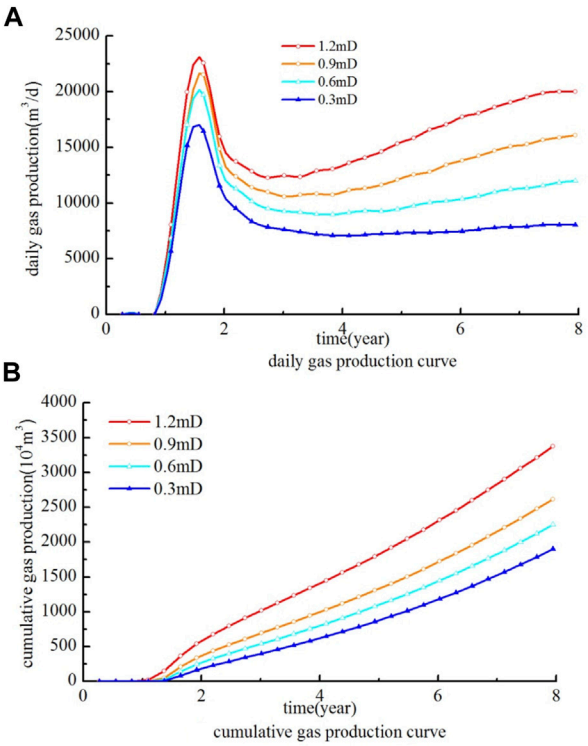

FIGURE 3
Gas production curve under different permeability conditions. **(A)** Daily gas production curve, **(B)** Cumulative gas production curve.

3.2 Initial and boundary conditions

According to the previous test data, the basic geological parameters of CBM in the model are respectively assigned as follows: the initial pressure of the coal bed is 14.85 MPa, the fracture porosity is 0.95%, the initial water saturation of the fracture is 100%, the coal seam density is 1.45 t/m^3, and the compressibility coefficient is 4.50 × 10^{-6}/KPa, diffusion coefficient 1.0 × 10^{-9} cm^2/s, Langmuir pressure 2.64 MPa, Langmuir volume 30.2 m^3/m^3, and coal seam vertical depth 1,650 m (Table 1).

TABLE 1 Basic parameters of coalbed methane reservoir.

Description	Value
Initial coal reservoir pressure, MPa	14.85
Initial fracture porosity of coal seam, %	0.95
Coal seam density, t/m^3	1.45
Compressibility coefficient, 10^{-6}kPa^{-1}	4.50
Diffusion coefficient, cm^2/s	1.0×10^{-9}
Langmuir pressure, MPa	2.64
Langmuir volume, m^3/m^3	30.2
Temperature of coal seams, K	313.15
Coal seam vertical depth, m	1,650

4 Geological suitability evaluation of horizontal well

Without considering the influence of engineering factors, the productivity of horizontal wells with gas pressure fractures in coal beds is mainly affected by three factors: single well controlled resources, seepage conditions and coal seam isothermal adsorption performance. As the adsorption performance of coal beds in the study area has little change, only single well control resources and seepage conditions need to be considered. The controlled resources of a single well are jointly affected by the gas content of the coal seam and the thickness of the coal seam. The seepage condition is the cleat fracture permeability of the coal seam.

4.1 Permeability

4.1.1 Gas production

When the simulated permeability is 0.3, 0.6, 0.9, and 1.2 mD, respectively, the fracturing horizontal well will discharge 3,000 days of gas production, coal seam pressure reduction effect, desorption gas volume and recovery factor. Permeability increased from 0.3mD to 1.2mD, and peak gas production increased from 16,450 m^3/d to 21,500 m^3/d (Figure 3A). From the shape of gas production curve, the higher the permeability is, the faster the gas production will decline after reaching the peak value. When the permeability is 0.3 mD, the gas production will be basically stable from the third year. When the permeability is>0.6 mD, the gas production will slowly increase from the third year. When the permeability increases from 0.3 to 1.2 mD, the cumulative gas production increases from 2,180 × 10^4 m^3/d increased to 4,240 × 10^4 m^3/d (Figure 3B).

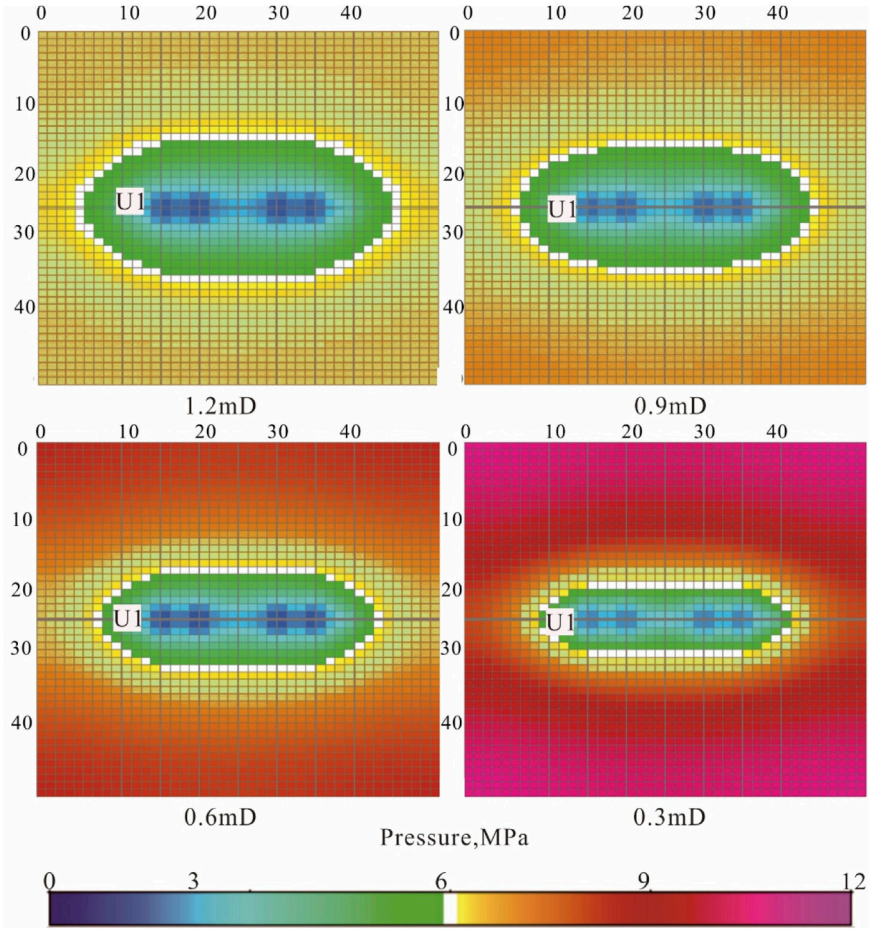

FIGURE 4
Plane distribution of coal seam pressure drop effect under different permeability conditions.

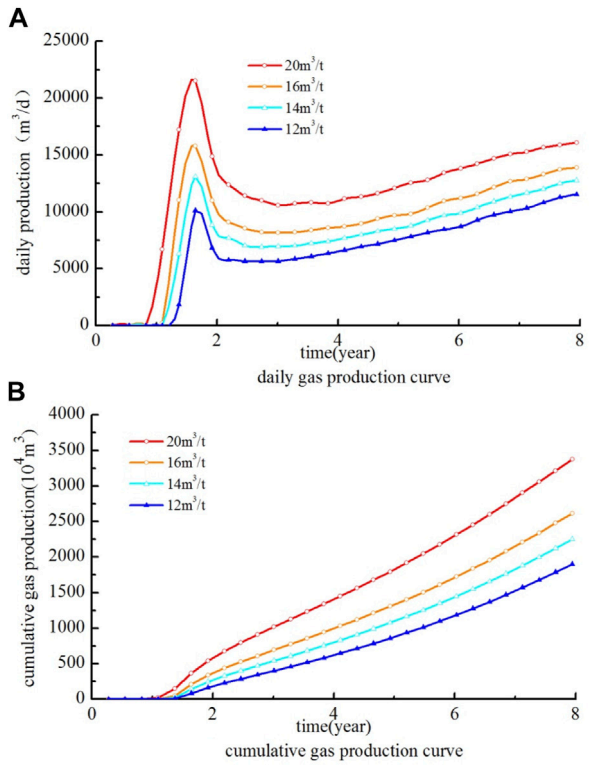

FIGURE 5
Variation curve of gas production with gas content. **(A)** daily gas production curve, **(B)** cumulative gas production.

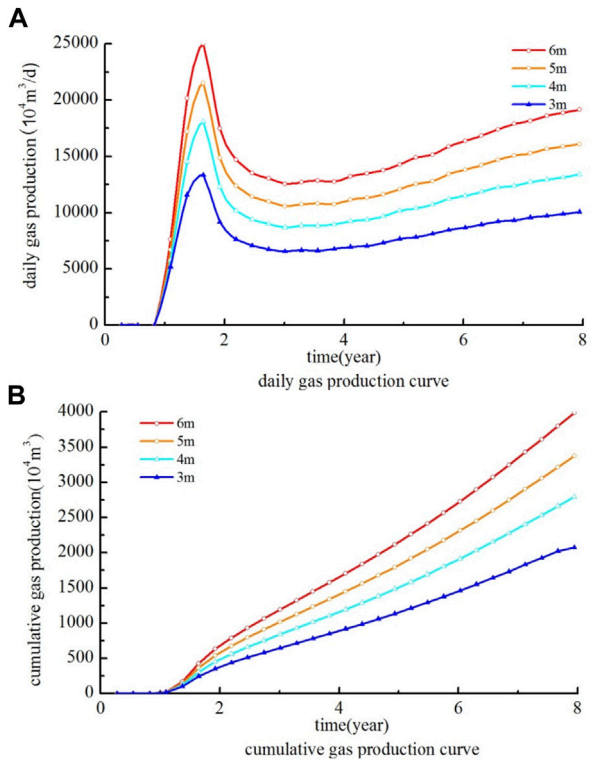

FIGURE 6
Variation curve of gas production with coal thickness. **(A)** daily gas production curve, **(B)** cumulative gas production.

There is a linear positive correlation between cumulative gas production and permeability, and the relationship between them is:

$$Q = 2280 * K + 1430$$

where, Q cumulative gas production, 10^4 m^3; K permeability, mD.

4.1.2 Depressurization effect and recovery factor

Under the same production time, the higher the coal seam permeability is, the larger the desorption radius of coalbed methane is, and the lower the average coal seam pressure is. Taking 8 years of drainage as an example (Figure 4), the permeability increases from 0.3 to 1.2 mD, the desorption radius increases from 225 to 810 m, and the desorption area increases from 0.41 to 2.35 km^2. The larger the coal seam desorption area is, the more free CBM is desorbed from the coal seam, which is more conducive to high and stable production of CBM horizontal wells. In the process of drainage and depressurization of coalbed methane horizontal wells, the higher the coal seam permeability is, the higher the pressure conductivity coefficient is, and the faster the pressure transmission is. Under the same pressure difference and production time conditions, the lower the average pressure of the coal seam is, the larger the drainage and depressurization area and desorption area are.

4.2 Gas content

The higher the coal seam gas content, the higher the coal seam gas saturation and desorption pressure, and the more conducive to the high production of coal seam gas wells. Other parameters remain unchanged, and the coal seam gas content is adjusted by adjusting the desorption pressure. The gas content is respectively 20, 16, 14, and 12 m^3/t for simulation. The simulation results show that (Figure 5): the gas content increases from 12 to 20 m^3/t, the peak gas production increases from 11,700 to 21,500 m^3/d, and the total gas production increases from 2,018 × 10^4 m^3 increased to 3,508 × 10^4 m^3. It can be seen that the higher the gas content, the earlier the gas production time, the higher the peak gas production, and the higher the cumulative gas production in the same production time.

The gas content and cumulative gas production meet the relationship.

$$Q = 2970 * \ln(Gc) - 5640$$

In the formula, the gas content of Gc coal seam, m^3/t.

The higher the coal seam gas content is, the earlier the coal seam desorption time is, and the smaller the area of discharge and pressure reduction before desorption. After desorption, the more coalbed methane is desorbed under the same pressure conditions, the higher the gas saturation in the coal seam barrier and the higher the relative permeability of the gas phase, which is not conducive to continuous drainage and depressurization. The lower the gas content, the lower the coal seam desorption pressure and the later the desorption time. After desorption, under the same pressure conditions, the smaller the amount of desorbed coalbed methane is, the lower the gas saturation in the coal seam bedding is, the higher the relative permeability of water phase is, and the greater the pressure conductivity coefficient is, which is more conducive to the pressure reduction of coal seam drainage, and

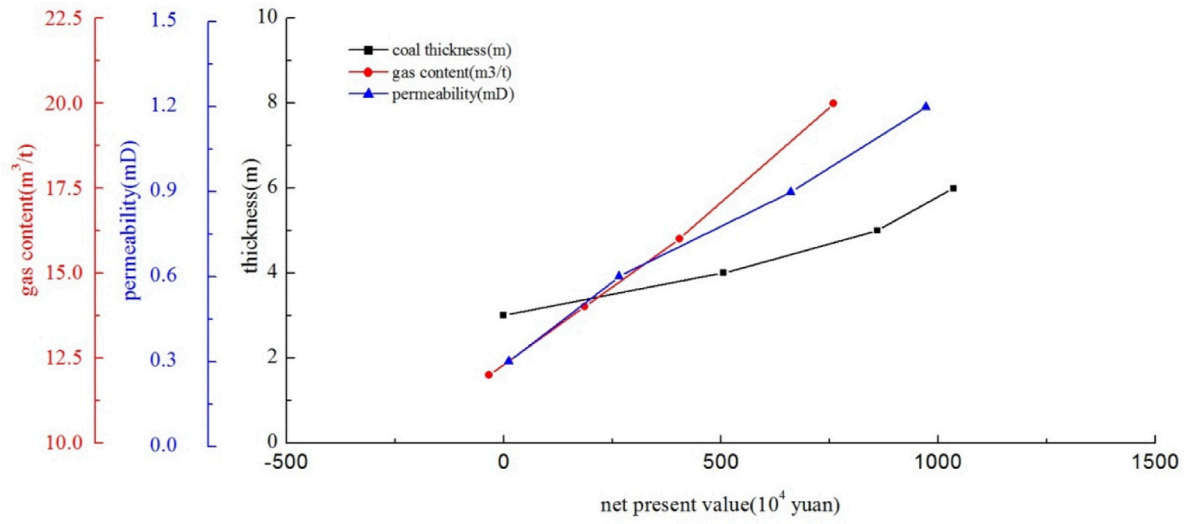

FIGURE 7
Variation curve of gas production with coal thickness.

the lower the average coal reservoir pressure. Therefore, although the drainage area of the coal seam is larger and the average pressure of the coal seam is lower under the condition of low gas content, the desorption radius is larger under the condition of high gas content, and the gas saturation of the coal seam partition is higher.

4.3 Coal seam thickness

When other geological parameters are the same, the thickness of coal seam is taken as 3, 4, 5, and 6 m, respectively for simulation. The simulation results show that the peak gas production, cumulative gas production and coal seam thickness are positively correlated.

When the thickness of the coal seam changes from 3 to 6 m, the peak gas production of the fractured horizontal well increases from 13,200 to 24,905 m^3/d, and the cumulative gas production increases from 2,010 × 10^4 m^3 increased to 4,180 × 10^4 m^3.

The relationship between cumulative gas production and coal seam thickness.

$$Q = 708 * h$$

In the formula, h is the coal seam thickness, m.

The greater the thickness of the coal seam, the more CBM can be desorbed from the coal seam under the same pressure drop conditions, and the higher the productivity of the CBM well (Figure 6; Figure 7).

4.4 Economic benefit evaluation

4.4.1 Economic benefit evaluation model

Economic benefit evaluation is the core content of horizontal well suitability evaluation. Economic evaluation indicators can be divided into two categories: first, investment value indicators, including net present value, cost limit, etc.; The second is the capital utilization efficiency index, including the rate of return, internal rate of return, etc. This paper mainly evaluates the economic feasibility of fracturing horizontal well development from two indicators: net present value and return on investment. If the net present value and return on investment of the first 8 years are greater than 0, fracturing horizontal well development technology can be adopted.

The calculation formula of NPV is:

$$NPV = \sum (CI - CO)(1 + i)^{-t}$$

CI refers to cash inflow, mainly including CBM sales revenue and financial subsidies; *CO* is cash outflow, including investment in horizontal well development, daily production and maintenance fees of horizontal well, and various taxes;

$(CI - CO)$ is the net cash flow in year *t*, *i* benchmark discount rate; The calculation formula of return on investment is:

$$NPM = \frac{NPV}{CO}$$

NPM is the net rate of return. The higher the NPM, the higher the unit investment income.

4.4.2 Economic benefit evaluation

According to Formula 4 and Formula 5, respectively calculate the net present value and rate of return of fractured horizontal wells under the conditions of different permeability, gas content and coal seam thickness. When the permeability increases from 0.3 to 1.2 mD, the NPV increases from 11,000 yuan to 97,24,000 yuan. When the gas content increases from 12 m^3/t to 20 m^3/t, the net present value increases from −3,43,000 yuan to 75,78,000 yuan. When the coal seam thickness increases from 3 to 6 m, the net present value increases from −5,90,000 yuan to 1,03,50,000 yuan.

It can be seen that the geological conditions of CBM suitable for fracturing horizontal well development are: permeability >0.28 mD, gas content >12.8 m^3/t, and coal seam thickness >3.1 m.

5 Conclusion

(1) The burial depth of coal beds in the study area is generally more than 1,500 m, which is characterized by high metamorphic

degree, high gas content, high reservoir pressure and low permeability.

(2) The numerical simulation results show that the gas production of fractured horizontal wells is positively correlated with the permeability, gas content and thickness of coal beds: the higher the permeability, the higher the coal seam pressure conductivity coefficient, the better the coal seam pressure reduction effect and the larger the desorption radius after the same production time; The higher the gas content is, the earlier the coal seam desorption time is. After the same production time, the higher the average pressure of the coal seam is, the larger the desorption radius is;

(3) Combined with the economic benefit evaluation model, it is found that the lower limit of geological conditions suitable for the development of fracturing horizontal wells is: permeability >0.28 mD, gas content >12.8 m^3/t, and coal seam thickness >3.1 m.

Data availability statement

The raw data supporting the conclusion of this article will be made available by the authors, without undue reservation.

Author contributions

YF: Conceptualization, methodology, first draft, numerical simulation. WY: Data curation, writing-review and editing. ZX, RZ, and YW: Mapping, data processing. HZ, XW, and XG: Supervision, writing—review and editing. SG and CM: Geological data collection. All authors contributed to the manuscript.

Funding

The research was supported by the project of Sanya Yazhou Bay Science and Technology City (Grant No: SCKJ-JYRC-2022-14).

Acknowledgments

Thanks Shaanxi Tiancheng Petroleum Technology Co., Ltd. for providing geological data.

Conflict of interest

Author ZX was employed by the company Shiwen Software Co., Ltd., author YW was employed by the company PetroChina Changqing Oilfield Company and authors SG and CM were employed by the company Shaanxi Tiancheng Petroleum Technology Co., Ltd.

The remaining authors declare that the research was conducted in the absence of any commercial or financial relationships that could be construed as a potential conflict of interest.

Publisher's note

All claims expressed in this article are solely those of the authors and do not necessarily represent those of their affiliated organizations, or those of the publisher, the editors and the reviewers. Any product that may be evaluated in this article, or claim that may be made by its manufacturer, is not guaranteed or endorsed by the publisher.

References

Ali, M., Paul, S., and Chatterjee, R. (2017). Cleat orientation from ground mapping and image log studies for *in-situ* stress analysis: Coal bed methane exploration in South Karanpura Coalfield, India. *Energy & Fuels* 31, 6812–6824. doi:10.1021/acs.energyfuels.7b00702

Cao, P., Liu, J., and Leong, Y. K. (2016). Combined impact of flow regimes and effective stress on the evolution of shale apparent permeability. *J. Unconv. Oil Gas Resour.* 14, 32–43. doi:10.1016/j.juogr.2016.01.004

Fan, Y., Deng, C., Zhang, X., Li, F., and Wang, X. (2018). Numerical study of multi-branch horizontal well coalbed methane extraction. *Energy Sources, Part A Recovery, Util. Environ. Eff.* 40, 1342–1350. doi:10.1080/15567036.2018.1476616

Fei, L., Luo, Z., Wang, Z., and Liu, P. (2015). Gas seepage rule and productivity analysis in designing coalbed methane wells. *Chem. Technol. Fuels Oils* 50, 516–524. doi:10.1007/s10553-015-0558-0

Gentzis, T. (2009). Stability analysis of a horizontal coalbed methane well in the Rocky Mountain Front Ranges of southeast British Columbia, Canada. *Int. J. Coal Geol.* 77 (3), 328–337. doi:10.1016/j.coal.2008.05.016

Hoang, S. K., Abousleiman, Y. N., and Al-Tahini, A. M. (2008). Multilaterals drilling and sustainable openhole production from theory to field-case studies. *SPE J.* 15, 878–892. doi:10.2118/116138-pa

Laubach, S. E., and Gale, J. F. W. (2006). Obtaining fracture information for low permeability (tight) gas sandstones from sidewall cores. *J. Pet. Geol.* 29 (2), 147–158. doi:10.1111/j.1747-5457.2006.00147.x

Li, T., Wu, C. F., and Liu, Q. (2015). Characteristics of coal fractures and the influence of coal facies on coalbed methane productivity in the South Yanchuan Block, China. *J. Nat. Gas. Sci. Eng.* 22, 625–632. doi:10.1016/j.jngse.2015.01.014

Liu, S., Tang, S., and Yin, S. (2018). Coalbed methane recovery from multilateral horizontal wells in Southern Qinshui Basin. *Adv. Geo-Energy Res.* 2, 34–42. doi:10.26804/ager.2018.01.03

Luo, C. J., Zhang, D. F., Lun, Z. M., Zhao, C. P., Wang, H. T., Pan, Z. J., et al. (2019). Displacement behaviors of adsorbed coalbed methane on coals by injection of SO2/CO2 binary mixture. *Fuel* 247, 356–367. doi:10.1016/j.fuel.2019.03.057

Mu, F. Y., Zhong, W. Z., Zhao, X. L., Che, C. B., Chen, Y. P., Zhu, J., et al. (2015). Strategies for the development of CBM gas industry in China. *Nat. Gas. Ind. B* 2 (4), 383–389. doi:10.1016/j.ngib.2015.09.013

Song, H., Cao, Y., Yu, M. X., Wang, Y., Killough, J. E., and Leung, J. (2015). Impact of permeability heterogeneity on production characteristics in water-bearing tight gas reservoirs with threshold pressure gradient. *J. Nat. Gas Sci. Eng.* 22, 172–181. doi:10.1016/j.jngse.2014.11.028

Su, X., Zhou, F., and Tyson, S. (2018). Numerical investigation of the potential contamination of a shallow aquifer in producing coalbed methane. *Energy Explor. Exploitation* 36 (2), 282–296. doi:10.1177/0144598717736629

Sun, X., Zhang, Y., Li, K., and Gai, Z. (2016). A new mathematical simulation model for gas injection enhanced coalbed methane recovery. *Fuel* 183, 478–488. doi:10.1016/j.fuel.2016.06.082

Thararoop, P., Karpyn, Z. T., and Ertekin, T. (2012). Development of a multi-mechanistic, dual-porosity, dual-permeability, numerical flow model for coalbed methane reservoirs. *J. Nat. Gas Sci. Eng.* 8, 121–131. doi:10.1016/j.jngse.2012.01.004

Xu, J. Z., Zhai, C., Ranjith, P. G., Sun, Y., and Qin, L. (2019). Petrological and ultra sonic velocity changes of coals caused by thermal cycling of liquid carbon dioxide in coalbed methane recovery. *Fuel* 249, 15–26. doi:10.1016/j.fuel.2019.03.089

Yan, J., Lu, Y. Y., Zhong, D. L., Zou, Z. L., and Li, J. B. (2019). Enhanced methane recovery from low-concentration coalbed methane by gas hydrate formation in graphite nanofluids. *Energy* 180, 728–736. doi:10.1016/j.energy.2019.05.117

Zhang, J. (2014). Numerical simulation of hydraulic fracturing coalbed methane reservoir. *Fuel* 136, 57–61. doi:10.1016/j.fuel.2014.07.013

Zhang, L. H., Shan, B. C., and Zhao, Y. L. (2017). Production performance laws of vertical wells by volume fracturing in CBM gas reservoirs. *J. Nat. Gas. Ind.* 36 (2), 36–44.

Zou, M., Wei, S., Huang, Z., Lv, X., and Guo, B. (2018). Simulations on recoverability performances for a coalbed methane field in SE edge of Ordos basin, China. *Fuel* 233, 354–360. doi:10.1016/j.fuel.2018.06.071

frontiers | Frontiers in Earth Science

TYPE Original Research
PUBLISHED 08 March 2023
DOI 10.3389/feart.2023.1131386

OPEN ACCESS

EDITED BY
Chaojun Fan,
Liaoning Technical University, China

REVIEWED BY
Xiangjun Chen,
Henan Polytechnic University, China
Jianwei Cheng,
China University of Mining and Technology, China

*CORRESPONDENCE
Huice Jiao,
pdsjhc@163.com

SPECIALTY SECTION
This article was submitted to Economic Geology, a section of the journal Frontiers in Earth Science

RECEIVED 25 December 2022
ACCEPTED 21 February 2023
PUBLISHED 08 March 2023

CITATION
Song W, Jiao H and Wang Y (2023), Crack closure effect during the impact coal seam with high-pressure air blasting and the influence of gas drainage efficiency. *Front. Earth Sci.* 11:1131386. doi: 10.3389/feart.2023.1131386

Crack closure effect during the impact coal seam with high-pressure air blasting and the influence of gas drainage efficiency

Weihua Song[1,2], Huice Jiao[2]* and Yingwei Wang[1]

[1]State Key Laboratory of Coking Coal Exploitation and Comprehensive Utilization, China Pingmei Shenma Corporation Group, Pingdingshan, Henan, China, [2]College of Mining, Liaoning Technical University, Fuxin, Liaoning, China

The crack closure in impact coal seams induced by high-pressure air blasting greatly affects gas drainage efficiency. The length of the crack closure was calculated and analyzed based on energy and elastic theories. The closure region was then determined to be 3.8 m from the blasting hole. The results of a high-pressure air blasting experiment in the underground of one coal mine in China showed that the effect of crack closure on gas drainage efficiency manifested as a decreased amplitude of gas emission in the crack closure region. At 1.0–4.0 m from the blasting hole, the amplitude of gas emission in the observation holes first increased and then decreased with increasing distance from the blasting hole. At 1.8–2.5 m from the blasting hole, the amplitude of the gas emission was maximal. At 4.0 m from the blasting hole, the crack was nearly closed, and the gas emission in the observation holes was minimal. The theoretical calculation had good consistency with the field test results; thus, it can provide an important reference for an appropriate arrangement of gas drainage boreholes.

KEYWORDS

high-pressure air blasting, impact coal seam, gas drainage, crack closure, gas emission

1 Introduction

The coal seams in China have large amounts of coal seam gas (Dai et al., 2019; Zou et al., 2019; Huang et al., 2022; Men et al., 2022). However, the existing coal seam gas has not been sufficiently utilized due to its low permeability in the rock mass, geological complexities, and equipment limitations. The Shenyang Coal Science Research Institute pioneered the development of the compressed air blast technique and equipment that has been widely used in China (Li, 2013; Li, 2015). The application of this technique in Huainan Mine showed that the predicted influential area resulting from the compressed air blast was inconsistent with real-world data. This might be attributed to the closure of the fractures, leading to difficulties in gas transport in the rock mass. More specifically, after the compressed air is released, fractures close to the elastic rock mass zone tend to close, resulting in a reduction of the flow channels for coal seam gas transport. These fractures can only be re-opened if the high-pressure gas is pumped through into the rock mass. The present work is a case study of the influence of compressed air blasts on the performance of coal seam gas drainage.

2 Coal failure mechanism due to compressed air blasts

After the compressed air blast, the resulting blasting wave and pressure jointly damage coal through compressive and tensile stresses. The borehole wall is heavily damaged and fractured into small pieces, whereas the rock mass in the distance to the borehole wall forms fractures due to tangential stress. The fracture propagates further into the rock mass and continuously consumes energy provided by the air blast. As a result, the blasting wave-induced energy tends to decrease as it propagates further, leading to formation of only elastic failure in the rock mass (Ning, 2012; Zhang et al., 2017; Gao et al., 2018; Yang et al., 2019).

2.1 Elastic energy consumption Et due to compressed air blasts

Beyond the fracture boundary, only elastic deformation occurs due to the wave blast. The elastic deformation in the unit volume of rock δ_t is according to the following formula (Cai et al., 2014; Li et al., 2018; Cheng et al., 2022):

$$\delta_t = \frac{1}{2}(\sigma_r\varepsilon_r + \sigma_\theta\varepsilon_\theta) = \frac{{\sigma_r}^2}{2E_m}(1+\lambda^2).$$

Thus, the energy consumed due to the elastic deformation is

$$E_t = \int_{r_1}^{R_E} 2\pi r\delta_E dr,$$

$$E_t = \frac{\pi(1+\lambda^2)(p_m r_m)^2}{2E_m(\alpha-1)}\left[\left(1-\frac{r_m}{R_E}\right)^{2(1-\alpha)}\right],$$

where ε_r and ε_θ are the strain along the radial and tangential directions, respectively, relative to the borehole, m and α are coefficients where $\alpha = 2 - \nu/(1-\nu)$, $\nu = 0.3$, $\alpha = 1.57$, E_m the Young's Modulus of coal, 4.6 GPa, $r_m = b_1/2$ is the radius of the fracture, λ is a coefficient equivalent to $\nu/(1-\nu) = 0.43$, R_E is the radius at which the elastic deformation starts to occur, $R_E = \frac{1+\nu}{E_m}\frac{(\sigma_t+\sigma_w){r_m}^2}{r}$, 4.0 m, σ_t is the tensile strength, and σ_w is the initial stress.

The immediate stress induced on coal when air blasting occurs is calculated according to the following equation:

$$p_m = \frac{\rho v_p \cdot \rho_{ky}{v_s}^2}{2\left(\rho v_p + \rho_{ky} v_s\right)},$$

where ρ is the coal density (1334 kg/m^3), v_p is the compressive wave velocity (1856 m/s) determined by laboratory testing, ρ_{ky} is the density of the compressed air (83.85 kg/m^3), and v_s is the compressed air velocity at the releasing nose (243.7 m/s) as determined by measurement.

2.2 Fracture closure

After the air blast, the fracture propagates to an extent beyond which the deformation remains elastic. Once the blasting wave energy is completely consumed, the fractures at the boundary between the fracture and elastic deformation zone tend to close under the action of load F. For ease of calculation, the friction is ignored and the closure of the fractures is elastic. The energy consumption time is very short (approx. 25 μs), and the length of the coal is l (Figure 1).

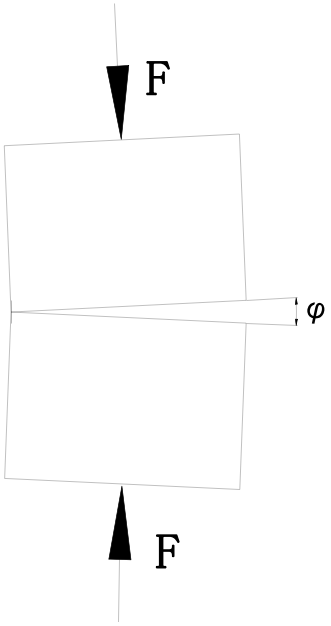

FIGURE 1
Schematic diagram of the fracture closure.

The probability of damage to the microelement of the coal is assumed to be the damage variable D according to

$$D = \int_0^J P(x)dx = 1 - \exp\left[-(J/J_0)^m\right].$$

If the rock microelement strength is J, then $\sigma_1 = \sigma_c$, $\varepsilon_1 = \varepsilon_c$ when the peak point gradient is 0, and the relevant microelement strength is J_c. When the rock at the closure zone has residual strength, $D = 1$; hence, $\exp[-(J/J_0)^m] = 0$. The strength parameters in the microelement, J, J_0, and m can be calculated as follows:

$$m = \frac{-(\sigma_c - 2\mu\sigma_3)}{(\sigma_c - 2\mu\sigma_3 - E\varepsilon_c + hE\varepsilon_c)\ln\left(\frac{\sigma_c - 2\mu\sigma_3 - E_m\varepsilon_c + \xi E_m\varepsilon_c}{hE_m\varepsilon_c}\right)},$$

$$J = \sigma_1^* + 2\sigma_3^* + \frac{\sin\varphi}{3\sqrt{3-\sin^2\varphi}}(\sigma_1^* - \sigma_3^*)^2,$$

$$J_0 = J_c\left[\frac{J_1(\sigma_c - 2\mu\sigma_3 - E_m\sigma_c + \xi E_m\varepsilon_c)}{\sigma_c - 2\mu\sigma_3}\right]^{1/J_1},$$

where σ_1^* and $2\sigma_3^*$ are the effective stresses of σ_1 and σ_3, respectively, and φ is the internal friction angle.

The fracture closure coefficient ξ can be calculated according to

$$\xi = 1 - \frac{\sigma_r - 2\mu\sigma_r}{E_m\varepsilon_r},$$

where μ is the Poisson's ratio, σ_r is the residual strength in MPa, and ε_r is the residual strain.

Considering the expansion of the fracture resulting from coal seam gas adsorption in the fracture, σ_z is the summation of closure stress in coal fractures σ_e (Meng and Li, 2015; Vyacheslav et al., 2016; Peng and Zheng, 2020; Liu et al., 2022) and expansion stress σ_p, and the expansion stress due to the coal seam gas adsorption in the fractures is calculated as follows (Xue et al., 2015; Chu et al., 2022):

$$\sigma_p = \left[2aRT\rho(1-2\nu)\ln(bp)\right]\Big/(3V),$$

where a and b are adsorption coefficients, p is the compressive stress of the coal seam gas (1.2 MPa), ν is the Poisson's ratio, ρ is the coal density (334 kg/m^3), R is the molar gas constant (8.31 J/(mol·K)), T is the absolute temperature (297.35 K), and V is the molar volume (22.41 L/mol).

The effective stress σ_e and actual stress σ_Z are as follows:

$$\sigma_Z = \sigma_e + \sigma_p,$$
$$\sigma_Z = \kappa\sigma_e,$$

where κ is the effective stress coefficient according to

$$\kappa = 1 - K/K_s,$$

where K is the water bulk modulus and K_s is the coal solid particle bulk modulus. κ is 0.7.

During the blasting, the decay of the blasting wave peak in the coal mass is calculated as follows:

$$p_E = p_E\left(\frac{r_m}{r_E}\right)^3.$$

Assuming the total force on the coal in the elastic zone results only from the blasting wave,

$$p_E = F.$$

Considering the conservation of energy, the energy in the elastic zone is not completely released, with most of the energy converted to kinetic energy, while a minor portion is stored in the elastic zone.

$$E_t = E_t^1 + Q_1.$$

The simplified form is

$$E_t^{'} = \eta E_t.$$

The energy from the elastic zone is assumed to contribute to the fracture closure according to

$$E_t^{'} = \eta E_t = Fl\sin\frac{\varphi}{2}\cos\frac{\varphi}{2},$$

where η is the energy coefficient, and it equals 1 when all energy is used for fracture closure.

The length of the fracture closure is

$$1 = \frac{\frac{\eta\pi\left(1+\lambda^2\right)\left(p_m r_0\right)^2}{2E_m(\alpha-1)}\left[\left(1-\frac{r_0}{R_E}\right)^{2(1-\alpha)}\right]}{p_m\left(\frac{r_m}{r_E}\right)^3\sin\frac{\varphi}{2}\cos\frac{\varphi}{2}}.$$

The effective closure length in the fracture is

$$l_y = \xi l.$$

After compressed air blasting, fractures form, leading to an increase in the gas flow channels. In contrast, the fractures close to the elastic zone tend to close, resulting in decreased gas flow channels. Therefore, the borehole for air blasting should be drilled within the fracture propagation zone. In addition, if the borehole height is more than the height of the fracture closure zone, the amount of coal seam drainage decreases greatly.

The effective drainage zone is assumed to be as far as L from the borehole according to

$$L = a_* + b_1 + b_2 - l_y,$$

where a_* is the blasting radius (0.094 m), b_1 is the thickness of the loose area, and b_2 is the thickness of the fracture propagation.

The diameter of the loosened area can be calculated as follows (Qian, 2010):

$$b_1 = \left(\frac{(1-2\nu)(1+\nu)}{3(1-\nu)}\frac{\rho {c_p}^2}{\sigma_*}\right)^{1/3}\frac{1}{2}\frac{0.61{E_z}^{1/3}}{\left(\rho c_p\sigma_*\right)^{1/9}}.$$

The diameter of the fracture propagation is calculated as follows (Qian, 2010):

$$b_2 = \left(\frac{\rho {c_p}^2}{4\left(\frac{1+\sin\theta}{1-\sin\theta}\right)\sigma_0}\right)^{1/3}\frac{1}{2}\frac{0.61{E_z}^{1/3}}{\left(\rho c_p\sigma_*\right)^{1/9}}.$$

As such,

$$L = 0.094 + \left(\frac{(1-2\nu)(1+\nu)}{3(1-\nu)}\frac{\rho {c_p}^2}{\sigma_*}\right)^{1/3}\frac{1}{2}\frac{0.61{E_z}^{1/3}}{\left(\rho c_p\sigma_*\right)^{1/9}} + \left(\frac{\rho {c_p}^2}{4\left(\frac{1+\sin\theta}{1-\sin\theta}\right)\sigma_0}\right)^{1/3}\frac{1}{2}\frac{0.61{E_z}^{1/3}}{\left(\rho c_p\sigma_*\right)^{1/9}} - \xi\frac{\frac{\eta\pi\left(1+\lambda^2\right)\left(p_m r_0\right)^2}{2E_m(\alpha-1)}\left[\left(1-\frac{r_0}{R_E}\right)^{2(1-\alpha)}\right]}{p_m\left(\frac{r_m}{r_E}\right)^3\sin\frac{\varphi}{2}\cos\frac{\varphi}{2}},$$

where ν is Poisson's ratio (0.3), ρ is the coal density (1334 kg/m^3), and c_p is the compressive stress velocity in the coal mass (1856 m/s). η is 0.75, E_Z is the energy resulting from the blast, σ_* is the compressive strength of the coal (28.63 MPa), σ_0 is the tensile strength (0.462 MPa), $\theta = \pi/18$, and $\varphi = 2\pi/45$. Substituting all these parameters into the equation mentioned previously leads to $L = 3.8m$.

3 Field testing

3.1 Site background

The field testing was conducted in the transport roadway in a single coal mine. The compressed air blasting was initiated in a coal seam with a thickness of 3.6 m. The stress from the coal seam gas was 1.6 MPa, and the gas intake was around 6.11 m^3/t. The seam was weak and the gas permeability was 0.0111 m^2/MPa^2·d. The roadway was reinforced by cable bolts and steel mesh.

3.2 Testing methodology

A 0.5-m-deep borehole was drilled into the seam, followed by the installation of the blasting detonation. When the stress

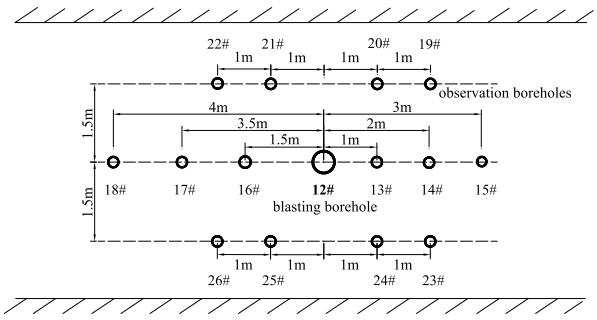

FIGURE 2
Borehole pattern.

reached 60 MPa, the compressed air was released. Two to three blasts were performed in each borehole. Eventually, one drainage borehole and 12 blasting boreholes were formed. In addition, adjacent to the blasting boreholes, another 14 boreholes were drilled for observation (Figure 2). The observation boreholes were drilled 0.5 m deep into the seam with a drill bit 94 mm in diameter. All these boreholes were sealed thereafter. Blasting boreholes were drilled similarly. As soon as the compressed air blasting occurred, the drainage borehole was connected to the gas drainage system. All gas drainage parameters were the same in each borehole. The variations in coal seam gas drainage volume during the drainage were measured. The gas drainage volumes measured in each observation borehole were used to aid in identifying the locations of fracture closure.

3.3 Testing results and analysis

As shown in Table 1 and Figure 3, blasting in 12 blasting boreholes showed increased gas flow in the observation boreholes. The observation boreholes within 2 m of the blasting holes had the largest gas flow. The gas flow decreased from the observation borehole 1 m (borehole 13) to that 1.5 m (borehole 16) from the blasting borehole. The flow then increased to the observation boreholes 1.8 m (boreholes 20, 21, 24, and 25) away from the blasting borehole before decreasing again to the observation boreholes 2 m (borehole 14) and 2.5 m (boreholes 19, 22, 23, and 26) away from the blasting borehole. The gas flow increase peaked at the observation borehole 3 m (borehole 15) from the blasting borehole and reached its minimum in the observation borehole 4 m (borehole 18) from the blasting borehole. The gas flow increase was more obvious in the zone within 3 m from the blasting borehole. The increasing rate of gas intake peaked in the zone 1.8–2.5 m from the blasting borehole. The increasing rate of gas flow peaked in the zone 1.5 m from the blasting borehole. The rate was as high as 55.56%, and the gas drainage was also enhanced most significantly in this area. The gas flow increase tended to decrease more than 2.5 m from the blasting borehole. The increasing rate reached its minimum in the zone 4 m from the blasting borehole, where it was close to the fracture closure zone.

After the air blasting, the rate of gas intake tended to increase and then decrease with distance from the blasting borehole. When approaching the fracture closure zone, the increasing rate reached its minimum. The increasing rate of the gas intake on the left-hand side of the blasting borehole was greater than that on the right-hand side. This might be attributed to the orientation of the *in situ* major

TABLE 1 Variation in coal seam gas flow before and after the compressed air blast.

Borehole no.	Before blasting		After blasting		Variation in coal seam gas flow/%
	Total gas flow/ ($mL \cdot min^{-1}$)	Coal seam gas volume percentage/%	Total gas flow/ ($mL \cdot min^{-1}$)	Coal seam gas volume percentage/%	
13	2232.55	98	3213.57	100	43.94
14	1545.87	99	2131.64	100	37.89
15	1225.61	99	1840.45	98	50.17
16	1108.60	97	1724.58	98	55.56
17	783.90	98	955.90	100	21.94
18	1382.67	98	1586.20	100	14.72
19	1487.45	97	2104.89	98	41.51
20	983.27	98	1422.99	99	44.72
21	1164.56	99	1705.73	98	46.47
22	1572.35	98	2291.81	99	45.74
23	1374.53	98	1611.08	98	17.21
24	1231.09	98	1632.79	99	32.63
25	1028.61	99	1397.06	99	35.82
26	792.54	99	923.94	98	16.58

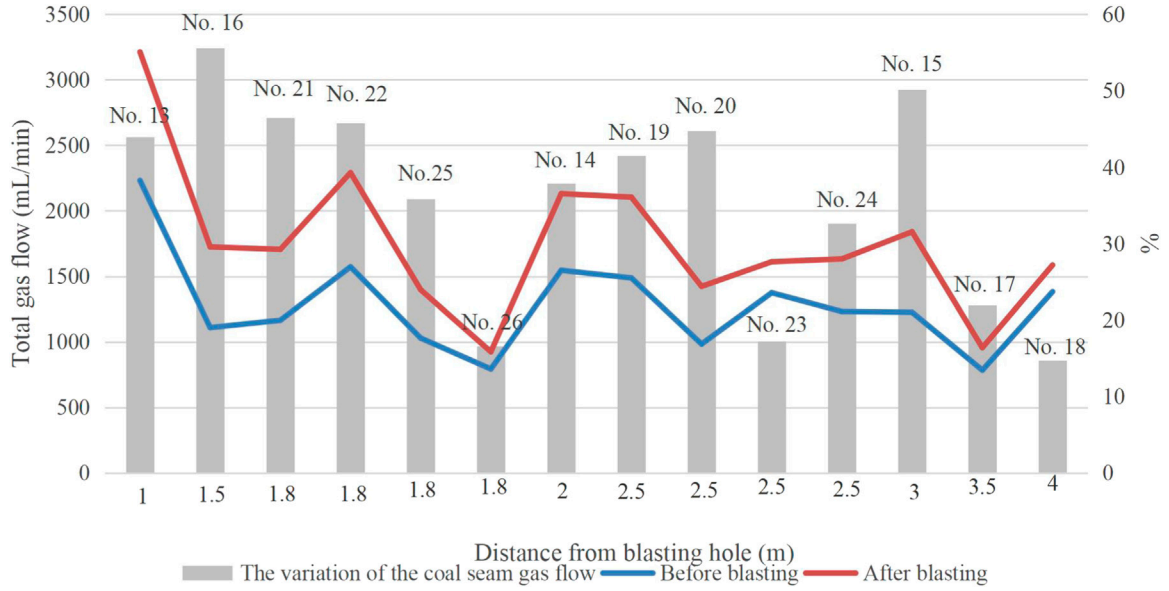

FIGURE 3
Schematic diagram of variations in coal seam gas flow.

principal stress. The observation boreholes above the blasting borehole (boreholes 19–22) had higher gas intake increase rates than those below the blasting borehole (boreholes 23–26). Although the induced stress level at the top and bottom of the blasting borehole by the blasting wave tended to be the same, the induced failure differed, with tensile and compressive failures dominating the top and bottom, respectively. As the tensile strength is always much less than the compressive strength, the influential area resulting from air blasting at the top would be much larger than that at the bottom.

4 Conclusions

a. As a result of compressed air blasting, the huge blasting wave induced extensive fractures that propagated into the coal mass, leading to increased gas flow channels. The gas intake above the air-blasting borehole was higher than that below. The difference in gas intake between the zones on the left and right was attributed to the *in situ* major principal stress.
b. The compressed air blasting propagated the fractures into the coal mass up to a certain extent, beyond which the coal mass remained intact. The fractures close to the boundary tended to close, leading to decreased gas flow channels. In other words, the real fracture length was always smaller than the theoretical fracture length.
c. The observations of gas flow and intake volumes confirmed that the fracture started closing 4 m from the blasting borehole, a finding consistent with the theoretical value of 3.8 m. This also demonstrated that the theoretical model proposed in this study could predict the fracture length and, hence, aid in coal seam gas drainage prediction. However, the gas migration in the coal seam had the characteristics of an unstable flow field and was also affected by factors such as the construction quality of the drainage hole and the gas flow in the hole. Therefore, further research is needed.

Data availability statement

The raw data supporting the conclusion of this article will be made available by the authors, without undue reservation.

Author contributions

WS wrote the main manuscript text. HJ and YW oversaw the editing of the manuscript. All authors reviewed the manuscript.

Funding

The authors declare that this study received funding from China Pingmei Shenma Corporation Group (Grant No. 41040220181107-2). The funder was not involved in the study design, collection, analysis, interpretation of data, the writing of this article, or the decision to submit it for publication. This project was supported by the Open Research Fund of State Key Laboratory of Coking Coal Exploitation and Comprehensive Utilization.

Conflict of interest

WS and YW were employed by the China Pingmei Shenma Corporation Group.

The remaining author declares that the research was conducted in the absence of any commercial or financial relationships that could be construed as a potential conflict of interest.

Publisher's note

References

Cai, F., Liu, Z. G., and Luo, Y. (2014). Propagation and attenuation characteristics of stress waves generated by explosion in high-gas coal-beds. *J. China Coal Soc.* 39 (1), 110–114. doi:10.13225/j.cnki.jccs.2013.0218

Cheng, S. F., Ye, Y., Zeng, Y. W., and Gao, R. (2022). Failure law of surrounding rock under underground explosion based on a new damage-virtual tensile crack model. *Explos. And Shock Waves* 42 (5), 055201. doi:10.11883/bzycj-2021-0414

Chu, H. B., Ren, Z. Q., Yan, S., Zhu, S. Y., Chen, Z., Ye, H. Y., et al. (2022). Experimental study on the propagation and attenuation laws of stress waves in coal under high-pressure gas impact. *J. Henan Polytech. Univ. Nat. Sci.* 9, 1–6. 1673-9787.2020100040. doi:10.16186/j.carolcarrollnki

Dai, J. X., Qin, S. F., Hu, G. Y., Ni, Y. Y., Gan, L. D., Huang, S. P., et al. (2019). Major progress in the natural gas exploration and development in the past seven decades in China. *Petroleum Explor. Dev.* 46 (06), 1100–1110. doi:10.1016/s1876-3804(19)60266-1

Gao, K., Liu, Z., and Liu, J. (2018). Propagation law and failure characteristics of blasting stress wave in structural belt coal-rock. *J. China Coal Soc.* 43, 79–86. doi:10.13225/j.cnki.jccs.2017.0798

Huang, Z. W., Li, G. F., Yang, R. Y., and Li, G. S. (2022). Review and development trends of coalbed methane exploitation technology in China. *J. China coal Soc.* 47 (9), 3212–3238. doi:10.13225./j.carolcarrollnkiJCCS.SS22.0669

Li, S. G. (2015). Key technology and equipment research and development of improving coal seam permeability by high pres`sure air blasting. *Coal Sci. Technol.* 43 (2), 92–95. doi:10.13199/j.cnki.cst.2015.02.021

Li, S. G. (2013). Numerical simulation of coal fracture caused by high-pressure air blasting. *Saf. Coal Mines* 44 (12), 163–165. doi:10.13347/j.cnki.mkaq.2013.12.053

Li, X. L., Li, Z. H., Wang, E. Y., Liang, Y. P., Niu, Y., and Li, Q. G. (2018). Spectra, energy, and fractal characteristics of blast waves. *J. Geophys. Eng.* 15 (1), 81–92. doi:10.1088/1742-2140/aa83cd

Liu, X. B., Xue, K. S., Luo, Y., Long, K., Liu, Y. N., and Liang, Z. M. (2022). The effect of pore pressure on the mechanical behavior of coal with burst tendency at a constant effective stress. *Sustainability* 14 (21), 14568. doi:10.3390/su142114568

Men, X. Y., Lou, Y., Wang, Y. B., Wang, Y. Z., and Wang, L. X. (2022). Development achievements of China's CBM industry since the 13th Five-Year Plan and suggestions. *Nat. Gas. Ind.* 42 (06), 173–178. doi:10.3787/j.issn.1000-0976.2022.06.015

Meng, Y., and Li, Z. P. (2015). Experimental study on the porosity and permeability of coal in net confining stress and its stress sensitivity. *J. China Coal Soc.* 40 (1), 154–159. doi:10.13225/j.cnki.jccs.2013.1518

Ning, J. G. (2012). *Explosion and impact dynamics*. Beijing: National Defense Industry Press.

Peng, Z., and Zheng, F. (2020). Modal properties of elastic surface waves in the presence of material anisotropy and prestress. *J. Sound Vib.* 485 (1–2), 115588. doi:10.1016/j.jsv.2020.115588

Qian, Q. H. (2010). *Impact and explosion effect in rock and soil*. Beijing: National Defense Industry Press.

Vyacheslav, N. R., Lauren, C. G., Sinisha, A. J., Yee, S., and Gino, A. I. (2016). Coal-gas interaction: Implications of changes in texture and porosity. *Int. J. Coal Sci. Technol.* 3 (1), 10–19. doi:10.1007/s40789-015-0098-6

Xue, J. H., Wang, H. P., Zhou, W., Ren, B., Duan, C., and Deng, D. (2015). Experimental research on overlying strata movement and fracture evolution in pillarless stress-reliefmining. *Int. J. Coal Sci. Technol.* 2 (1), 38–45. doi:10.1007/s40789-015-0067-0

Yang, R. S., Xu, P., and Chen, C. (2019). Interaction between blast stress waves and cracks. *Explos. And Shock Waves* 39 (8), 081102. doi:10.11883/bzycj-2018-0480

Zhang, S. C., Zhu, F. H., and Gao, K. (2017). Study on mechanism of deep-hole controlled blasting in coal seam. *China Saf. Sci. J.* 27 (9), 140–145. doi:10.16265/j.cnki.issn1003-3033.2017.09.024

Zou, C. N., Yang, Z., Huang, S. P., Ma, F., Sun, Q. P., Li, F. H., et al. (2019). Resource types, formation, distribution and prospects of coal-measure gas. *Petroleum Explor. Dev.* 46 (03), 451–462. doi:10.1016/s1876-3804(19)60026-1

Frontiers in Earth Science

Investigates the processes operating within the major spheres of our planet

Advances our understanding across the earth sciences, providing a theoretical background for better use of our planet's resources and equipping us to face major environmental challenges.

Discover the latest Research Topics

See more →

Frontiers

Avenue du Tribunal-Fédéral 34
1005 Lausanne, Switzerland
frontiersin.org

Contact us

+41 (0)21 510 17 00
frontiersin.org/about/contact